ulm university universität ulm

Advanced molecular tweezers as broad-spectrum antivirals

Dissertation submitted in partial fulfillment of the requirements for the degree of

Doctor rerum naturalium (Dr. rer. nat.)

of the International Graduate School in Molecular Medicine Ulm

Institute of Molecular Virology Ulm University

Heads: Prof. Dr. Frank Kirchhoff and Prof. Dr. Jan Münch

Author: Tatjana Corinna Weil

Born in Mutlangen (Germany)

2023

Current dean of the Medical Faculty:	Prof. Dr. Thomas Wirth
Current chairman of the Graduate School:	Prof. Dr. Bernd Knöll

Thesis Advisory Committee (TAC)

1st supervisor:	Prof. Dr. Jan Münch
2nd supervisor:	Prof. Dr. Holger Barth
3rd supervisor:	Prof. Dr. Tanja Weil

External reviewer:	Prof. Dr. Eva Herker
	Prof. Dr. Herre Jelger Risselada

Day doctorate awarded:	October 13, 2023

Results gained in my thesis have previously been published in the following publications:

- Weil, T.; Kirupakaran, A.; Le, M.-H.; Rebmann, P.; Mieres-Perez, J.; Issmail, L.; Conzelmann, C.; Müller, J. A.; Rauch, L.; Gilg, A.; Wettstein, L.; Groß, R.; Read, C.; Bergner, T.; Pålsson, S. A.; Uhlig, N.; Eberlein, V.; Wöll, H.; Klärner, F.-G.; Stenger, S.; Kümmerer, B. M.; Streeck, H.; Fois, G.; Frick, M.; Braubach, P.; Spetz, A.-L.; Grunwald, T.; Shorter, J.; Sanchez-Garcia, E.; Schrader, T.; Münch, J. **Advanced Molecular Tweezers with Lipid Anchors against SARS-CoV-2 and Other Respiratory Viruses**. JACS Au 2022, 2, 9, 2187-2202. https://doi.org/10.1021/jacsau.2c00220.
  License: CC BY-NC-ND 4.0

- Weil, T.*; Lawrenz, J.*; Seidel, A.; Münch, J.; Müller, J. A. **Immunodetection Assays for the Quantification of Seasonal Common Cold Coronaviruses OC43, NL63, or 229E Infection Confirm Nirmatrelvir as Broad Coronavirus Inhibitor**. Antiviral Res. 2022, 203, 105343. https://doi.org/10.1016/j.antiviral.2022.105343.
  *shared first-authorship; License: CC BY-NC-ND 4.0

- Weil, T.*, Groß, R.*, Röcker, A.*, Bravo-Rodriguez, K.*, Heid, C., Sowislok, A., Le, M.-H., Erwin, N., Dwivedi, M., Bart, S. M., Bates, P., Wettstein, L., Müller, J. A., Harms, M., Sparrer, K., Ruiz-Blanco, Y. B., Stürzel, C. M., von Einem, J., Lippold, S., Read, C., Walther, P., Hebel, M., Kreppel, F., Klärner, F.-G., Bitan, G., Ehrmann, M., Weil, T., Winter, R., Schrader, T., Shorter, J., Sanchez-Garcia, E. & Münch, J. **Supramolecular Mechanism of Viral Envelope Disruption by Molecular Tweezers.** J. Am. Chem. Soc. 2020, 142, 17024–17038. https://doi.org/10.1021/jacs.0c06400.
  *shared first-authorship; License: ACS AuthorChoice/Editors' Choice

Table of contents

Abbreviations

°C	Degrees celsius
229E	Student specimen code 229E
ACE2	Angiotensin-converting enzyme 2
AD	Alzheimer´s disease
AIDS	Acquired immune deficiency syndrome
ALI	Air-liquid interface culture
ANOVA	Analysis of variance
APN	Aminopeptidase N
ARDS	Acute respiratory distress syndrome
ATCC	American Type Cell Culture Collection
AUC	Area under the curve
Aβ	Amyloid beta
BCA	Bicinchoninic acid
CC_{50}	50 % cytotoxic concentration
Chol	Cholesterol
Chol ester	Cholesteryl oleate
CLR01	CLEAR 01
CM	Camostat mesylate
CoV	Coronavirus
COVID-19	Coronavirus disease 2019
CPE	Cytopathic effect
CTG	CellTiter-Glo™ Luminescent Cell Viability Assay
DDP4	Dipeptidyl peptidase 4
DENV	Dengue virus
DLS	Dynamic light scattering
DMEM	Dulbecco's modified Eagle medium
DMSO	Dimethylsulfoxide
DOPC	1,2-dioleoyl-sn-glycero-3-phosphocholine
dpi	Days post infection
EBOV	Ebola virus

EC_{50}	50 % effective concentration
E-protein	Envelope protein
ELISA	Enzyme-linked immunosorbent assay
ERGIC	Endoplasmic reticulum-Golgi-intermediate complex
EtOH	Ethanol
FACS	Fluorescence-activated cell sorting
FCS	Fetal calf serum
FFU	Focus forming unit
g	Gram(s)
h	hours
GaMD	Gaussian accelerated Molecular Dynamics
GFP	Green fluorescent protein
GUVs	Giant unilamellar vesicles
hCoV	Human coronavirus including hCoV-229E, -OC43, -NL63 and -HKU1
HA	Hemagglutinin
HCMV	Human cytomegalovirus
HEPES	4-(2-hydroxyethyl)-1-piperazineethanesulfonic acid
HIV-1	Human immunodeficiency virus type 1
HRP	Horseradish peroxidase
HSV-1	Herpes simplex virus type 1
HSV-2	Herpes simplex virus type 2
IAV	Influenza A virus
IC_{50}	50 % inhibitory concentration
ISG	Interferon stimulated gene
kDa	Kilodalton
LTR	Long terminal repeat
LyPC	Lysophosphatidylcholine
LyPE	Lysophosphatidylethanolamine
LyPS	Lysophosphatidylserine
M-protein	Matrix protein
mABs	Monoclonal antibodies

MEM	Minimum Essential Medium
MeOH	Methanol
MERS-CoV	Middle East respiratory syndrome coronavirus
MeV	Measles virus
min	Minute(s)
mM	Millimolar
MOI	Multiplicity of infection
N-protein	Nucleocapsid protein
NL63	Netherland 63
NIBSC	National Institute for Biological Standards and Control
nM	Nanomolar
NTA	Nanoparticle tracking analysis
OC43	Organ culture 43
OD	Optical density
ORF	Open reading frame
PA	Phosphatidic acid
PAP	Prostatic acidic phosphatase
PBS	Phosphate-buffered saline
PC	Phosphate clip
PC	Phosphatidylcholine
PCA	Principle component analysis
PD	Parkinson´s disease
PE	Phosphatidylethanolamine
PFA	Paraformaldehyde
PFU	Plaque forming unit
PG	Phosphatidylglycerol
PI	Phosphatidylinositol
PM	Plasma membrane
PS	Phosphatidylserine
RBD	Ribosome binding domain
RdRp	RNA-dependent RNA polymerase
RLU/s	Relative light units per second

RNA	Ribonucleic acid
rpm	Rotations per minute
RPMI-1640	Roswell Park Memorial Institute Medium
RSV	Respiratory syncytial virus
RT	Room temperature
SARS-CoV	Severe acute respiratory syndrome coronavirus
SARS-CoV-2	Severe acute respiratory syndrome coronavirus type 2
SD	Standard deviation
Sec	Seconds
SEM	Standard error of the mean
SEM1/2	Semenogelins 1 and 2
SEVI	Semen-derived Enhancer of Virus Infection
SM	Sphingomyelin
TCA	Trichloroacetonitrile
$TCID_{50}$	Tissue culture infectious dose 50
TEM	Transmission electron microscopy
TMB	3,3',5,5'-Tetramethylbenzidine
TMPRSS2	Transmembrane protease serine subtype 2
TX	Triton X-100
UV	Ultraviolet
v/v	Volume / volume ratio
VOC	Variants of concern
w/v	Weight/volume ratio
× g	Times gravitational acceleration
YFV	Yellow fever virus
ZIKV	Zika virus
β-gal	Beta-galactosidase
µM	Micromolar

1 Introduction

1.1 Broad-spectrum antivirals for pandemic preparedness

In the past, the most devastating threats to the global health can be traced back to RNA viruses originating from zoonotic spillovers[1]. RNA viruses can replicate in numerous host species and have a high mutation rate supporting fast adaptation and evasion from the host response[2]. The influenza pandemic from 1918 to 1919, caused by the H1N1 strain, was responsible for the loss of 20 to over 50 million lives[3]. Later in time, human immunodeficiency virus 1 (HIV-1), the causative virus of the acquired immune deficiency syndrome (AIDS) pandemic, was discovered[4]. These events were followed by several emergences of highly pathogenic viruses, such as the Ebola virus (EBOV)[5], the coronavirus severe acute respiratory syndrome coronavirus (SARS-CoV)[6], the Middle East respiratory syndrome coronavirus (MERS-CoV)[7] or more recently SARS-CoV-2[8]. All of the mentioned viruses have a zoonotic origin. Overall 75 % of all emerging pathogens are derived from animals, primarily wildlife hosts, such as bats[9]. Bats comprise more than 1,400 species and are the main natural reservoir of viruses[10]. The high population density of bats in their habitat, their long lifespan, and their immune system tolerating the presence of viruses without symptomatic disease favor frequent spillovers to other mammalian species[10]. Besides coronaviruses, viruses of the (families) *paramyxoviridae* and *rhabdoviridae* have been found in bats[11] and led to emergence of other highly pathogenic viruses such as Nipah, measles and lyssa virus. In sum, zoonotic spillovers pose a constant threat to the human population. Arboviruses are transmitted by arthropod vectors and represent another group causing viral epidemics. For example, the flaviviruses such as Zika virus (ZIKV), yellow fever virus (YFV) and dengue virus (DENV) are transmitted via mosquitos, infect up to 400 million people annually[12] and led to several outbreaks in the recent past[13,14]. The climate change enables virus carrying mosquitos to expand into new habitats, and also the spread of less-known arboviruses is a constant concern[12].

As a counter measurement and preparedness for further (re-)emerging viruses, antiviral therapies are needed. Broad-spectrum antivirals have the ability to inhibit multiple virus families by targeting a common characteristic. These fast adaptable and broadly acting treatments or protective antiviral measures provide a promising option, which is time effective and cost saving, achieving one strategy for pandemical preparedness[2]. The current SARS-CoV-2 pandemic is highlighting this need for broad-spectrum antivirals, especially for respiratory viruses. These viruses comes along with a high transmission rate and contribute significantly to morbidity and mortality worldwide[15].

1.2 *Coronaviridae*

The family of *Coronaviridae* is divided into two subfamilies; *Letovirinae* and *Orthocoronavirinae*, which comprises four genera: *alpha*-, *beta*-, *gamma*- and *deltacoronavirus*[16]. Today seven coronaviruses (CoVs) are known to infect humans[17]. In the 1960s the first coronaviruses, hCoV-229E (named after a student specimen code 229E)[18] and hCoV-OC43 (Organ Culture 43)[19] were discovered, followed by hCoV-NL63 (NetherLand 63)[20] and hCoV-HKU1 (Hong Kong University 1)[21], more recently in 2004 and 2005, respectively[22]. These low pathogenic coronaviruses cause mild to moderate upper-respiratory tract infections, while circulating endemically in the human population with annual peaks during the winter term[23–25]. The most prominent members of the coronavirus family are SARS-CoV[6], MERS-CoV[7] and SARS-CoV-2[8], which emerged in late 2002, 2012 and more recently in late 2019, respectively. These three representatives belong together with HCoV-OC43 and -HKU1 to the genus of *betacoronavirus*[26]. Along with *alphacoronaviruses* hCoV-229E and -NL63 representatives of both genera are able to infect mammalian species[26] and originate from bats or rodents[26–29], while viruses belonging to *gamma*- and *deltacoronavirus* are found to infect birds, fishes and in few cases mammals[30,31].

1.2.1 Coronavirus structure

Coronaviruses contain a single-stranded, positive-sense RNA genome with a length of 26 to 32 kb[32,33]. The virions are enveloped and of spherical or pleomorphic shape with a diameter from 80 to 120 nm[8,22]. The characteristic spike protein (S-protein) measures 9 to 12 nm, surrounds the viral envelope and gives the virus the eponymous corona (Figure 1a)[8]. The S-protein is a homotrimeric transmembrane protein consisting of the two domains, S1 and S2 (Figure 1b)[34]. S1 facilitates receptor binding, whereas S2 is required for cellular and viral membrane fusion[34–37]. CoVs employ a variety of cellular receptors for entry such as aminopeptidase N (APN, used by hCoV-229E)[38], angiotensin converting enzyme 2 (ACE2, used by hCoV-NL63, SARS-CoV and SARS-CoV-2)[39,40], dipeptidyl peptidase 4 (DPP4, used by MERS-CoV)[41] or glycan-based receptor carrying 9-*O*-acetylated sialic acid (used by hCoV-OC43 and -HKU1)[22]. This receptor usage determines the cell tropism. Proteolytic cleavage of the S-protein at the S1/S2 interface and within the S2 domain is necessary for S-protein activation and further fusion. The priming is mediated by cellular proteases

(transmembrane protease serine subtype 2 (TMPRSS2), cathepsin and/or furin), depending on the respective coronavirus[42].

Further structural proteins of CoVs are the membrane protein (M-protein) and the envelope protein (E-protein) (Figure 1b). The M-protein is the most abundant structural protein, coordinates the viral assembly by binding to the nucleocapsid protein (N-protein), E-protein and S-protein and thereby determines the shape of the envelope[43–45]. The small E-protein contributes in assembly and envelope formation as well as in budding by inducing membrane curvature[43,46]. Packing and stabilizing of the viral genome is accomplished by the N-protein, which also enhances transcription efficiency of the virus[47,48]. Some *betacoronaviruses* including hCoV-OC43 and -HKU1 contain also the structural protein hemagglutinin-esterase (HE-protein), functioning as co-factor of viral attachment to the cell[22,43,49].

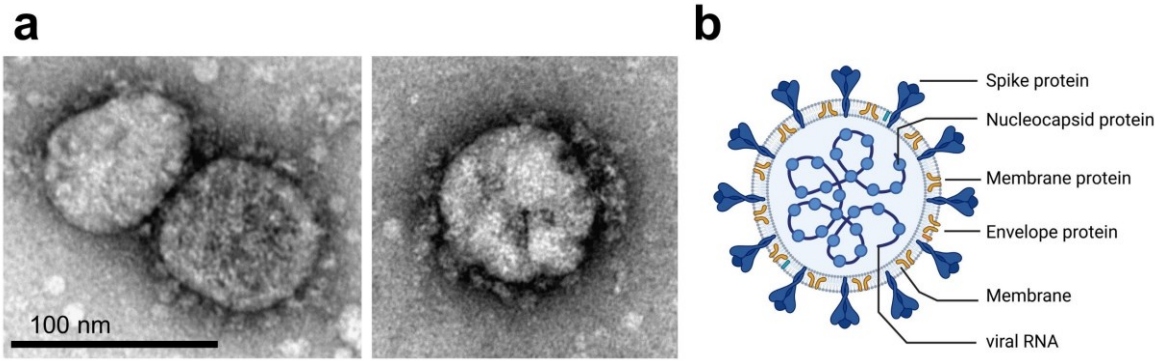

Figure 1. **Structure of coronaviruses. a)** Negative stained transmission electron micrograph of SARS-CoV-2 visualizing spike protein corona. Scale bar indicate 100 nm (kindly provided by Tim Bergner). **b)** Schematic structure of a coronavirus. Nucleocapsid protein covered RNA genome surrounded by a lipid bilayer. Structural proteins spike, membrane and envelope are located in the viral membrane. Hemagglutinin-esterase is only present in hCoV-OC43 and -HKU1 (b) Figure was created with BioRender.com. Printed with permission according to Biorender Academic License Terms (https://biorender.com/terms/).

1.2.2 Transmission, spread, and emergence of coronaviruses

For more than fifty years, CoVs infecting humans are known, but attention has only recently been paid to them due to three outbreaks of SARS-CoV, MERS-CoV and SARS-CoV-2 in the past two decades. These accumulated emergences in a short period of time demonstrate the potential threat to the human population. All of the aforementioned highly pathogenic and seasonal coronaviruses are the result of zoonotic spillovers from bats or rodent reservoirs[26,28]. To enter the human population, many of the viruses took advantage of intermediate hosts. In case of SARS-CoV, MERS-CoV, hCoV-OC43 and -229E, civet cats, camels, ungulates or camelids likely function as intermediate hosts, respectively[26,28,50–52]. For hCoV-NL63, -HKU1 and SARS-CoV-2 the definite intermediate host remains unclear.

All coronaviruses are transmitted (from human to human) by droplets, contact and fomites[27]. The particles can remain stable in aerosols for hours and infectious on surfaces for up to days; as it has been demonstrated for SARS-CoV-2[53].

After the emergence of SARS-CoV, about 8000 people became infected in 2002 to 2003, while no new cases have been reported until today[26]. Since the identification of MERS-CoV in the Middle East, over 2600 infected individuals in 27 countries were reported[54]. In this region, the major livestock are dromedary camels, which contain a reservoir of the pathogen leading frequently to new case reports[13].

The latest emerged coronavirus, SARS-CoV-2, causes the coronavirus disease 2019 (COVID-19), was firstly detected in Wuhan, China[8] and resulted in a pandemic that is still not under control. The global spread resulted in around 670 million reported cases over the past 3 years[55]. This fast spread is accomplished by high transmissibility of the virus and it is postulated that the acquisition of the polybasic furin cleavage site enhances the infection and expands the cell tropism, a major differences to SARS-CoV[34,56,57]. Additionally, transmission of SARS-CoV-2 occurs also through asymptomatic contacts[58], because viral loads in asymptomatic and symptomatic patients are similar[59]. In contrast, SARS-CoV infected patients are infectious only upon onset of symptoms[60]. These benefits contributed to the increased transmission of SARS-CoV-2 leading to high case rates and the occurrence of new mutations, even though the virus encodes a polymerase with proof-reading activity[61]. The first predominant mutation, D614G, found in the S-protein of SARS-CoV-2 was detected in February 2020 and is associated with higher viral loads due to enhanced replication and infectivity[62,63]. This mutation is conserved in all subsequent variants of concern (VOC) alpha, beta, gamma, delta, and omicron, which are equipped with several mutations allowing them to outcompete previous variants.

The alpha variant (lineage B.1.1.7) was firstly reported in the United Kingdom in December 2020 and became the dominant variant due to an increased affinity towards ACE2, mediated by the N501Y mutation (in comparison to the original SARS-CoV-2)[64,65]. The beta variant (lineage B.1.351), firstly reported in South Africa, and the gamma variant (lineage P.1), detected in travelers from Brazil, also demonstrated enhanced ACE2 binding due to the N501Y mutation and furthermore lower susceptibility to convalescent sera or vaccine induced antibodies[66]. In late 2021, the delta variant (lineage B.1.617.2) outcompeted pre-circulating strains due to further reduced sensitivity towards neutralization and higher replication efficiency than B.1.1.7[67]. The fifth VOC named omicron (lineage B.1.1.529) was reported in November 2021 in South Africa and possesses more than 50 mutations, of

which 32 are located in the S-protein[68]. These mutations lead to increased infectivity and immune escape compared to other VOCs[69]. However, the pathogenicity of omicron is associated with milder symptoms, decreased hospitalization rates, and lower fatality rates[70].

1.2.3 Clinical pathology

HCoVs are endemic viruses in the human population causing relatively mild, common cold-like symptoms in the upper respiratory tract, however they are associated with 15 – 30 % of all common cold cases[71,72]. In addition, hCoVs are responsible for hospitalization in children and immunocompromised adults with respiratory illness in 10 – 20 % of cases, where they might lead to bronchiolitis, pneumonia and even neurological diseases[26,73]. The repeated acquisition of hCoV infections suggest a high likelihood of reinfection and a lack of long-lasting protective immunity[22].

On the contrary, the three highly pathogenic CoVs can lead to severe disease(s), along with increased mortality[74]. MERS-CoV, SARS-CoV and SARS-CoV-2 cause symptoms in the respiratory tract such as cough, sore throat, shortness of breath, but also fever, headache, myalgia and gastro intestinal symptoms[58,75,76]. Diarrhea is more frequently occurring in patients infected with SARS-CoV than SARS-CoV-2 (16-73 % for SARS-CoV and 7.4 % for SARS-CoV-2[77]). Fatality rates are ranging from ~ 1%, for SARS-CoV-2[75] to 9.6 % for SARS-CoV[60] and are even higher for MERS-CoV, with a mortality rate of 35 %[78]. Even though the fatality rate for SARS-CoV-2 is comparatively low, 3 - 20 % of people suffering from COVID-19 require hospitalization[75]. Differences in severity of the diseases can be explained by the tropism of the viruses. SARS-CoV and MERS-CoV replicate mainly in the lower respiratory tract[79], while SARS-CoV-2 is found preferentially in the upper airway tract[34]. However, in severe cases, SARS-CoV-2 can also disseminate to the lower respiratory tract through lack of clearance by the immune system and further propagation[75]. This can result in the infection and destruction of alveolar type 2 (AT2) cells[80,81], leading to alveolar collapse and the development of acute respiratory distress syndrome (ARDS). The syndrome is characterized by inflammation, pulmonary lung injury, and loss of aerated lung tissue[75].

1.2.4 Therapy and protective measures

Until today, a standardized and effective drug treatment against hCoV infection is not available[22]. Initial attempts have studied various drugs for antiviral therapy in cell culture

systems, targeting viral RNA-dependent RNA polymerase (RdRp), viral fusion machinery or cellular proteases responsible for entry. Few direct acting antiviral drugs are approved and applied up to now, however only effective upon early treatment[82,83]. Besides direct antiviral therapy, COVID-19 patients are also treated with heparin[84] and systemic corticosteroids against virus induced inflammation and thrombosis[85,86].

The first potential pan-coronavirus drug remdesivir (GS-5734) was approved by the FDA in 2020. Remdesivir is an adenosine analog targeting the viral RdRp, and its antiviral activity was firstly reported against EBOV in nonhuman primates[87]. During the SARS-CoV-2 pandemic, studies showed activity of remdesivir against SARS-CoV-2 *in vivo*[88] and it is now being used in the clinics to treat COVID-19, however only controversial results are reported[89]. Further studies have demonstrated a broad-spectrum activity of remdesivir against the coronaviruses MERS-CoV, SARS-CoV, hCoV-229E, -OC43, -NL63 and several bat CoVs[90]. Another nucleoside analogue targeting the viral RdRp, called molnupiravir, has been described to have broad activity against multiple CoVs[91–93]. Lately, PAXLOVID, containing nirmatrelvir, a viral protease inhibitor, and ritonavir responsible for increasing the bioavailability of nirmatrelvir, was approved for COVID-19 therapy in patients with increased risk of severe outcome[94,95]. Additionally, nirmatrelvir activity has also been confirmed against hCoV-229E, SARS-CoV and MERS-CoV *in vitro*[96]. Further approaches for CoV restriction are dealing with the prevention of cell entry. This includes, for example, fusion inhibitors such as EK1 inactivating the viral fusion peptide[91,97] or protease inhibitors such as camostat mesylate (CM), which suppress S-protein priming by blocking the cell protease TMPRSS2[39]. However, studies on EK1 were only carried out in cell culture systems and in a mice model. Additionally, a clinical trial to investigate the efficacy of CM in COVID-19, showed no clinical benefit[98]. Currently, another trial is conducted with an increased dose of CM for administration[99]. Targeting the virus directly can also be achieved with antibodies. Monoclonal antibodies (mABs) against the S-protein showed effective treatment against SARS-CoV-2[100]. mABs bamlanivimab, imdevimab and casivirimab are used for COVID-19 patients with mild to moderate symptoms, who are at risk of a severe outcome[89]. However, with the emergence of VOC, mABs showed reduced susceptibility or completely lost their neutralizing activity, especially against the currently dominant variant omicron[91,100,101].

Prevention of virus infection can be achieved by vaccination. A massive roll-out campaign after the emergence of SARS-CoV-2 resulted in effective vaccines protecting from moderate and symptomatic infection plus lowering the risk of hospitalization and death[102–104].

However, vaccine-induced antibodies show lower neutralization against VOC capable of immune escape, in particular for the VOC omicron[105,106]. Besides, initial studies on vaccines to prevent infection of SARS-CoV and MERS-CoV were also carried out, but none of them are approved until this date[107,108].

1.3 Broad-spectrum antivirals targeting the viral envelope

Most epidemic or pandemic viruses are membrane-enveloped[4,5,12,109–111]. The viral envelope is derived from cell membranes, which consist out of a phospholipid bilayer with hydrophobic fatty acid tails that are faced inwards and hydrophilic lipid head groups that are facing outwards[112]. Membranes are assembled heterogeneously and contain different types of lipids and transmembrane proteins, which allow trafficking and signal transduction[113]. Furthermore, membranes function as protection surrounding the cell, enable compartmentalization within the cell, and play an important role in cell division[114]. However, cell-derived membranes are also crucial for the infectivity of enveloped viruses. During viral egress, these viruses bud from an infected cell to obtain their envelope[115]. This lipid bilayer protects the viral genetic material and harbors the viral glycoproteins, which are essential for infecting a new host cell[115]. Consequently, compounds targeting the viral membrane not only possess broad-spectrum antiviral activity, but also pose a high resistance barrier for viral escape mutations[116,117].

Previous publications have described existing bacterial peptides, named labyrinthopeptins, which bind to phosphatidylethanolamine (PE) lipids in the viral membrane and subsequently disrupt the virus[118]. Another synthetic peptide, called AH, is capable of destroying particles with less than 160 nm in diameter by forming pores into the membrane, whereupon the virus is lysed[119]. Both peptides demonstrated broad antiviral activity against flaviviruses, HIV-1 and herpes simplex viruses (HSV-1 and HSV-2), but not against influenza strains or members of the coronavirus family[120].

1.4 Molecular Tweezers

Prof. Dr. Thomas Schrader and Prof. Dr. Frank-Gerrit Klärner designed a novel compound harboring an electron-rich, torus-shaped cavity and two anionic phosphate groups at the central bridge (Figure 2a)[121]. These properties enable the so-called molecular tweezer CLR01 the binding of lysine (K_D of ~10 µM) and of arginine with 5 - 10-fold lower affinity[122]. While the electron-rich side walls of CLR01 include the butylene chain of lysine

into the cavity, which gives rise to a strong hydrophobic effect, the phosphate group of CLR01 forms an ion pair with the ε-NH_3^+ group of lysine (Figure 2b)[123,124]. The negative control CLR03 is equipped with two phosphate groups at the central bridge but lacks the side walls of CLR01 and thus is unable to bind either lysine or arginine[125].

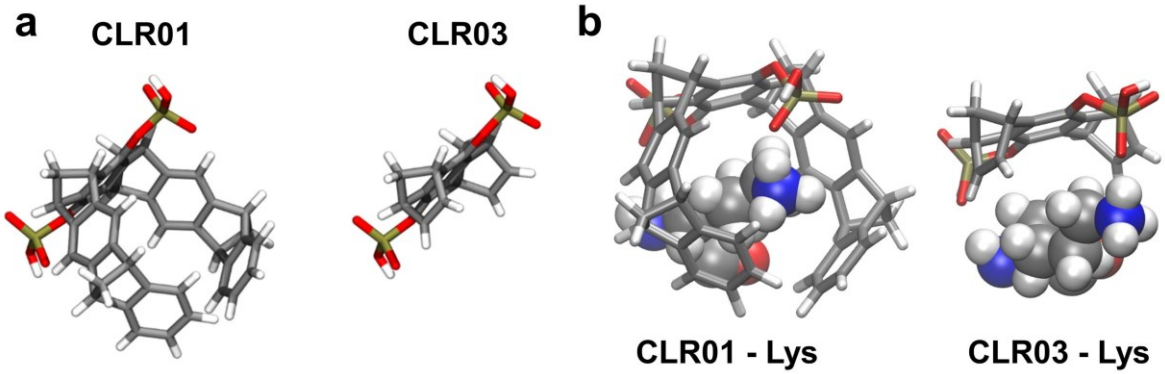

Figure 2. Structure of molecular tweezers and inclusion of lysine. a) CLR01 consist of a torus-shaped carbon backbone with two phosphate groups linked to the centre. Tweezer CLR03 has a truncated backbone. **b)** CLR01 binds the butylene chin of lysine into tweezer cavity and forms an ion pair between the phosphate groups of CLR01 and the ε-NH3+ group of lysine. P atoms are in gold, O atoms in red, H atoms in white, N atoms in blue and C atoms in grey. Obtained from Röcker 2018[126] with permission (created by Kenny Bravo-Rodriguez) and Lump et al. 2015[127] (created by Kenny Bravo-Rodriguez and Elsa Sánchez-García; CC BY 4.0; https://creativecommons.org/licenses/by/4.0/, Copyright© 2015, Lump et al.)

1.4.1 Anti-amyloid activity

Various proteinopathies are known today, with Alzheimer´s disease (AD) and Parkinson´s disease (PD) being the most prominent representatives. These diseases are characterized by misfolded and self-assembling amyloidogenic proteins, which potentially form large fibrillar aggregates[128]. Recent studies suggest that oligomeric fibril precursor may contribute to the pathogenesis[129–131], however the exact mechanism leading to proteinopathies are still elusive[132,133]. Interestingly, when forming amyloids, the misfolded proteins tend to face the amino acids lysine and arginine outwards, which serves as perfect target for the molecular tweezer[134]. In the native confirmation, these positive charged amino acids are hidden due to salt bridge interactions, resulting in high selectivity of CLR01 towards the misfolded proteins[124]. A further advantage of the molecular tweezer is its labile interaction and high on-off rate with lysine and arginine[122,135]. Due to this binding mode, weak interactions that are important for the formation of misfolded amyloidogenic proteins or toxic oligomers are interfered with[135]. The inhibition of amyloid beta (Aβ), α-synuclein, tau fibril formation and the assembly of ~20 other amyloidogenic proteins by CLR01 were previously demonstrated *in vitro* and *in vivo* in mice, rate, zebra fish and lamprey model, without showing any side effects[124,136–140]. Furthermore, CLR01 is able to disassemble pre-formed

fibrils allowing its administration for treatment in later stages of the diseases[140]. Therefore, the molecular tweezer CLR01 serves as promising treatment option in neurodegenerative diseases and other proteinopathies.

Amyloid fibrils are also found in the seminal fluid contributing to HIV-1 transmission[141]. In this process, cationic fibrils capture virus particles to overcomes electrostatic repulsion of the negatively charged viral and cellular membranes[142,143]. Fibril forming fragments of the prostatic acidic phosphatase (PAP; PAP248-286 and PAP 85-120) and semenogelins 1 and 2 (SEM 1 and SEM 2) are found to increase the attachment of HIV-1 to the target cell and enhance the infection by several orders of magnitude[141,144,145]. These semen derived fragments possess lysine and arginine in their sequence, thus serving as perfect target for CLR01 to inhibit their fibrillation. Surprisingly, CLR01 not only abrogated enhancement of infection, but also inhibited HIV-1 infection entirely, suggesting a direct activity towards the virus[127]. This result was not achieved during CLR03 treatment, showing that the side walls are essential for the anti-amyloid and antiviral activity.

1.4.2 Antiviral activity

The virucidal effect of CLR01 has been demonstrated for HIV-1 and other enveloped viruses such as HSV-1 and 2, human cytomegalovirus (HCMV), EBOV, ZIKV, but also for respiratory viruses such as measles (MeV) or influenza A (IAV) virus[127,146,147]. This establishes the molecular tweezer CLR01 as broad-spectrum antiviral agent. Interestingly, the infection of non-enveloped viruses is not interfered with, indicating that CLR01 targets the viral lipid bilayer[127]. To investigate the exact anti-viral mechanism of the molecular tweezer, a new tweezers called CLR05, harboring a methylene carboxylate groups instead of hydrogen phosphate substitutes, and the phosphate clip PC, with planar naphthalene sidewalls were developed (Figure 3)[147].

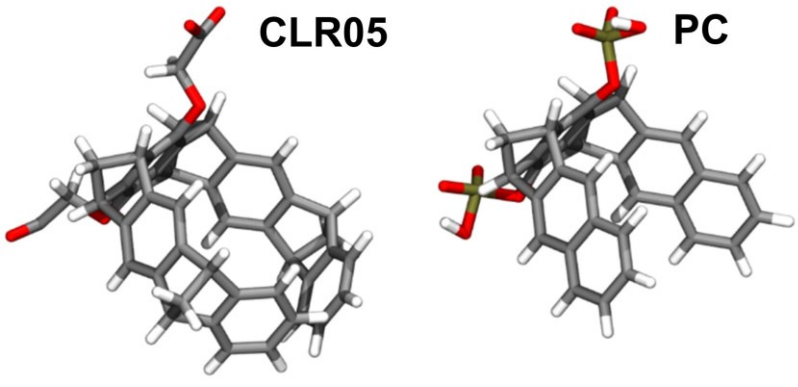

Figure 3. Structure of carboxylate tweezer CLR05 and phosphate clip PC. CLR05 consists of a torus-shaped carbon backbone with two carboxylate groups linked to the centre. Phosphate clip PC harbours

almost parallel naphthalene sidewalls with two phosphate groups at the centre. P atoms are in gold, O atoms in red, H atoms in white and C atoms in grey. Obtained from Röcker 2018[126] with permission (created by Kenny Bravo-Rodriguez).

The replacement of the phosphate groups by methylene carboxylate groups in CLR05 resulted in a weaker binding profile to lysine (K_D of ~643 µM)[122]. On the other hand, PC favors aromatic guests binding, and thus aliphatic cationic guests as lysine and arginine are bound only with low affinity[123,148]. Consequently, PC and CLR05 do not inhibit amyloid assembly. However, CLR05 reduced infection of HIV-1 resulting from direct anti-viral activity[147]. Further analysis showed that CLR01, CLR05 and PC include the head group of lipids, which form the viral membrane, into their cavity. Binding of tweezer and lipid head group is accomplished by attraction of the polar ammonium moiety from the membrane lipids phosphatidylcholine (PC) or sphingomyelin (SM) into the cavity of the tweezer. After lipid binding, only CLR01 and CLR05 are able to change the lipid head orientation allowing the penetration of the tweezer into the outer membrane leaflet (Figure 4). The insertion of the tweezer into the viral membrane results in increased surface tension, destabilization of the membrane and abrogates infectivity of the virus particle with activity in the micromolar range[147].

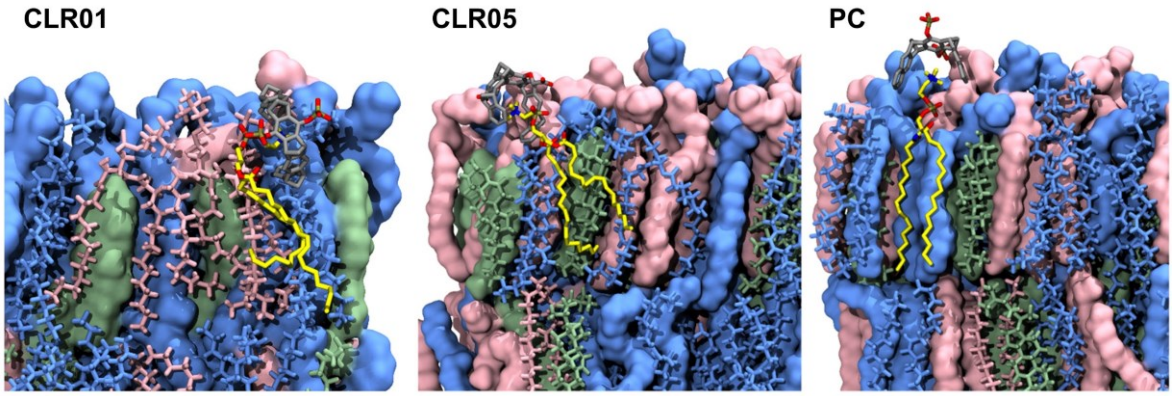

Figure 4. Visualization of tweezer/phosphate clip interaction with the membrane. Inclusion of lipid head group into cavity takes place for tweezers and clip. CLR01 and CLR05 alter lipid orientation perpendicular with respect to the normal lipid axis, resulting in penetration of the tweezers into the membrane and increased surface tension. DOPC is visualized in blue, SM in pink, Chol in green and tweezers in grey. The lipid interacting with clip or tweezers is highlighted in yellow. (DOPC = 1,2-dioleoyl-sn-glycero-3-phosphocholine, SM = sphingomyelin, Chol = cholesterol) Obtained from Röcker 2018[126] with permission (created by Kenny Bravo-Rodriguez).

1.5 Scope of the study

With the emerge of SARS-CoV-2, the interest in understanding coronavirus biology and prevention of infection tremendously increased[149]. Many assays were established to quantify SARS-CoV-2 infection in a high throughput manner. However, studies investigating the highly pathogenic coronaviruses requires BSL-3 laboratories. Human coronaviruses (hCoVs) are members of the coronavirus family and low pathogenic viruses. Similarities in the structural proteins and viral enzymes as the RNA-dependent RNA polymerase (RdRp) and the 3C-like protease allow translation of results obtained with hCoVs towards highly pathogenic coronaviruses[73,150,151]. Moreover, working with hCoVs is allowed in BSL-2 facilities and therefore simplifies studies on the coronavirus family. Common methods to study the hCoV biology are qRT-PCR, western blotting, plaque assay or fluorescent staining[93,152–154]. These methods are time consuming, laborious and involve increased workload for large sample quantities. Thus, my first aim was to establish and validate high throughput and specific detection methods of authentic hCoVs.

Emerging and re-emerging viruses pose a constant threat to the public health. The COVID-19 pandemic and the threat of SARS-CoV-2 highlighted the need for new antiviral agents, in particular broad-spectrum antivirals, which can be readily administered when encountering a novel virus as a measure of pandemic preparedness[2,117,155]. Molecular tweezers are synthetical compounds that inhibit enveloped viruses. Binding to lipid head groups leads to a orientational change of the lipids and allows penetration of the tweezers into the membrane[147]. This results in increased tension and disruption of the viral membrane. Previously, inhibition of several enveloped viruses such as HIV-1 and ZIKV was reported[127,146]. However, the tweezer does not inhibit viral infection in the presence of serum[146], in which aforenamed viruses are detected and potentially transmitted[156,157]. Nevertheless, anogenital tissue might still be amenable for tweezer application. Moreover, respiratory viruses are opening another treatment perspective, including the coronavirus family. Therefore, we set out to develop improved tweezer derivatives and to explore their broad antiviral activity particularly on respiratory viruses.

2 Material and Methods

2.1 Materials

2.1.1 Bacteria cells

E. coli XL-2 blue^{TM}	Chemically competent *Escherichia coli* (*E. coli*) cells. Genotype: Δ(mcrA)183 Δ(mcrCB hsdSMR-mrr)173 endA1 supE44 thi-1 recA1 gyrA96 relA1 lac [F proAB lacIqZΔM15 Tn10 (Tetr) Amy Camr]*, Agilent Technologies

2.1.1.1 Bacteria culture media

Lysogeny both (LB)	1 % (w/v) Bacto-tryptone, 0.5 % (w/v) Bacto yeast extract, 1 % (w/v) NaCl. Selection media contained 100 µg/ml ampicillin.
LB agar	LB + 1.5 % (w/v) agar
S.O.C. Medium	Thermo Fischer Scientific

2.1.2 Eukaryotic cells

2.1.2.1 Cell lines

Caco-2	Adherent human colorectal carcinoma cell line. Cells were kindly provided by Prof. Holger Barth, Institute of Pharmacology and Toxicology, Ulm University, Ulm.
Huh-7	Adherent hepatocyte-derived carcinoma cell line. Cells were kindly provided by Dr. Anna-Laura Kretz, Department for General and Visceral Surgery, Ulm University, Ulm.
Vero E6	Adherent African green monkey derived epithelial kidney cell line. Cells were obtained from American Type Cell Culture Collection (ATCC).
TMPRSS2 expressing Vero E6	Vero E6 cell line stably expressing TMPRSS2 were kindly provided by National Institute for Biological Standards and Control (NIBSC).
A549	Adherent human lung cancer cell line was purchased from ATCC.
MDCK	Adherent Madin-Darby canine kidney cell line were obtained from ATCC.

TZM-bl	Adherent human cervical carcinoma reporter cell line expressing CD4, CCR5 and CXCR4. β-galactosidase and firefly luciferase gene expression under the control of HIV-1 long terminal repeat (LTR) promotor. Cell were obtained from National Institutes of Health AIDS Research and Reference Reagent Program.
ELVIS	Adherent hamster kidney cell line obtained from ATCC. Upon infection with the trans-activator ICP10, lacZ gene is expressed.
Calu-3	Adherent human non-small-cell lung adenocarcinoma cell line. Cells were obtained from ATCC.
LLC-MK2	Adherent rhesus monkey kidney epithelial cell line. Cells were kindly provided by Prof. Lia van der Hoek, Institute for Infection and Immunity, Amsterdam University, Amsterdam.
HCT-8	Adherent human ileocecal adenocarcinoma cell line. Cells were obtained from ATCC.
HEK 293T	Adherent human embryonal kidney cell line, expressing the simian virus 40 (SV40) large T-antigen[158]. Cells were obtained from ATCC.

2.1.2.2 Primary cells

HAECs	Human airway epithelial cell (HAECs) were derived from primary human basal cells. Provided by Dr. Giorgio Fois, Institute of General Physiology, Ulm University, Ulm. Tissues were obtained from donors who gave informed consent. Ethical approval by the Ethics committees of Ulm University (application number 126/19) and Medical School Hannover (application number 2699-2015).

2.1.2.3 Eukaryotic cell culture media

Fetal calf serum (FCS) was heat inactivated at 56 °C for 1 h prior to usage.

Caco-2	Dulbecco´s Modified Eagle Medium (DMEM) supplemented with 10 % (v/v) FCS, 2 mM L-glutamine, 100 U/ml penicillin, 100 µg/ml streptomycin, 1 mM sodium pyruvate, 1× non-essential amino acids.

Huh-7	DMEM, supplemented with 10 % (v/v) FCS, 2 mM L-glutamine, 100 U/ml penicillin, 100 µg/ml streptomycin.
Vero E6	DMEM, supplemented with 2.5 % (v/v) FCS, 2 mM L-glutamine, 100 U/ml penicillin, 100 µg/ml streptomycin, 1× non-essential amino acids.
TMPRSS2 expressing Vero E6	DMEM, supplemented with 10 % (v/v) FCS, 2 mM L-glutamine, 100 U/ml penicillin, 100 µg/ml streptomycin, 1 mg/ml geneticin.
A549	See Huh-7
MDCK	See Huh-7
TZM-bl	See Huh-7
ELVIS	See Huh-7
Calu-3	Minimum Essential Medium (MEM), supplemented with 20 % (v/v) FCS, 100 U/ml penicillin, 100 µg/ml streptomycin, 1 mM sodium pyruvate, 1× non-essential amino acids.
LLC-MK2	MEM, supplemented with 8 % (v/v) FCS, 100 U/ml penicillin, 100 µg/ml streptomycin, 2 mM L-glutamine, 1× non-essential amino acids.
HCT-8	Roswell Park Memorial Institute Medium (RPMI-1640) supplemented with 10 % (v/v) FCS, 100 U/ml penicillin, 100 µg/ml streptomycin.
HEK 293T	See Huh-7
HAECs	Culture medium: Airway epithelial cell basal medium supplemented with airway epithelial cell growth medium supplement pack (Promocell). Differentiation medium: 1:1 mixture of DMEM and LHC basal medium (Thermo Fischer) supplemented with airway epithelial cell growth medium supplement pack.

2.1.3 Viruses

2.1.3.1 Viral pseudoparticles

LV(Luc)-CoV-2	Lentiviral pseudoparticle (pp) lacking *env*, *vif*, *vpu* and *vpr*. Encodes luciferase reporter gene and harbors SARS-CoV-2 S-protein.

2.1.3.2 Replication competent viruses

SARS-CoV-2 Wuhan/Hu-1	BetaCoV/France/IDF0372/2020 (#014V-03890), obtained from European Virus Archive.
SARS-CoV-2 Wuhan/Hu-1	BetaCoV/Germany/BavPat1/2020p.1 strain used in mice study was obtained from Dr. Jasmin Fertey, Fraunhofer Institute for Cell Therapy and Immunology Leipzig.
SARS-CoV-2 B.1.1.7 (alpha)	hCoV-19/Netherlands/NoordHolland_20432/2020 (014V-04031), obtained from European Virus Archive.
SARS-CoV-2 B.1.351 (beta)	2102-cov-IM-r1-164, was kindly provided by Prof. Dr. Michael Schindler, Institute for Medical Virology and Epidemiology of Viral Diseases, Tübingen University.
SARS-CoV-2 B.1.617.2 (delta)	Kindly provided by Prof. Dr. Hendrik Streeck, Institute of Virology, Bonn University Medical Center, Bonn[159].
hCoV-NL63	Kindly provided by Prof. Lia van der Hoek, Institute for Infection and Immunity, Amsterdam University.
hCoV-229E	VR-740™ purchased from ATCC.
hCoV-OC43	CR-1558™ purchased from ATCC.
IAV	Strain A/PR/8/34, H1N1 was obtained from ATCC.
MeV	Recombinant eGFP-encoding measles virus, vac2 strain[160]. Kindly provided by Dr. Christian Pfaller und Dr. Konstantin Sparrer.
RSV	Recombinant eGFP-encoding respiratory syncytial virus[161].
HIV-1	Lab-adapted HIV-1 NL4-3_92TH014-12 strain.
ZIKV	Asian ZIKV strain FB-GWUH-2016[162] was kindly provided by Olli Vapalahti, Department of Virology, University of Helsinki.

HSV-1	Recombinant eGFP-encoding herpes-simplex-virus 1, strain F, kindly provided by Benedikt Kaufer, Free University of Berlin.
HSV-2	Recombinant eGFP-encoding herpes-simplex-virus 2, strain 333, kindly provided by Patricia Spear, Northwestern University, USA.

2.1.4 Nucleic acid

2.1.4.1 Primers

SARS-CoV-2-ORF1b-*nsp14* fwd.	5'-TGGGGYTTTACRGGTAACCT-3'
SARS-CoV-2-ORF1b-*nsp14* rev.	5'-AACRCGCTTAACAAAGCACTC-3'
SARS-CoV-2-ORF1b-*nsp14* probe	5'-FAM-GCAAATTGTGCAATTTGCGG-TAMRA-3'
Mus musculus-TBP fwd.	5'-CTACCGTGAATCTTGGCTGTAA-3'
Mus musculus-TBP rev.	5'-GTTGTCCGTGGCTCTCTTATT-3'
Mus musculus-TBP-Cy5 probe	5'-Cy5-AATCCCAAGCGATTTGCTGCAGTC-BBQ-3'
Mus musculus-RIG-I fwd.	5'-CAGAACTGGAACAGGTCGTTTA-3'
Mus musculus-RIG-I rev.	5'-GCTTCTCTGTCTCCTTCATCAG-3'
Mus musculus-RIG-I-ROX probe	5'-ROX-AGGAAAGTGGCATCCCGGACTTC-BBQ-3'
Mus musculus-ISG15 fwd.	5'-CACAGTGATGCTAGTGGTACAG-3'
Mus musculus-ISG15 rev.	5'-CTGCGTCAGAAAGACCTCATAG-3'
Mus musculus-ISG15-FAM probe	5'-6FAM-AGCATCCTGGTGAGGAACGAAAGG-BHQ2-3'
Mus musculus-OAS1 fwd.	5'-GCTGAAGGAGGTGAAGTTTGA-3'
Mus musculus-OAS1 rev.	5'-CACTGATGAGATTGGCGTAGAA-3'
Mus musculus-OAS1-HEX probe	5'-HEX-TCCAGTAAATCATAGGCTGGCAGCAC-BHQ2-3'
Mus musculus-MX1 fwd.	5'-GAATTACCAGGGTGGCTGTAG-3'
Mus musculus-MX1 rev.	5'-CCAGGTTGATGGTCTCTTGTT-3'
Mus musculus-MX1-TAMRA probe	5'-5TAMRA-TGCAGACATAGGACGCCAGATCAA-BBQ-3'

2.1.4.2 RNA

SARS-CoV-2 RNA standard	Twist Bioscience

2.1.4.3 Plasmid DNA

All plasmids encoding an ampicillin resistance gene.

pBR_NL4-3_92TH014-12 (R5)	Plasmid encoding HIV-1 NL4-3 provirus in BR322 vector. V3-loop is replaced by V3-loop of the CCR5-tropic 92th014.12 isolate[163].
pCMVdR8.91	Plasmids encodes replication deficient HIV-1 provirus lacking *env*, *vif*, *vpu* and *vpr*. Plasmid was kindly provided by Christian Buchholz, Molecular Biotechnology and Gene Therapy, Paul-Ehrlich Institute, Langen.
pSEW-luc2	Plasmids a encodes firefly luciferase, which is flanked by HIV-1 long terminal repeats. The 3'-LTR harbors a self-inactivation (SIN) mutation. Together with pCMVdR8.91 and pCG1-SARS-CoV-2 lentiviral pseudoparticles are produced (see 2.1.3.1). Plasmid was kindly provided by Christian Buchholz, Molecular Biotechnology and Gene Therapy, Paul-Ehrlich Institute, Langen.
pCG1-SARS-CoV-2 SΔ18	Plasmid encodes S-protein of SARS-CoV-2 based on the Wuhan/Hu-1/2019 isolate[39,56] and C-terminal truncation of 18 (Δ18) amino acids residues for increased incorporation into pseudoparticles[164]. Plasmid was kindly provided by Prof. Stefan Pöhlmann, Infection Biology Unit, German Primate Center, Göttingen.

2.1.5 Proteins

2.1.5.1 Antibodies

hCoV immunodetection assay and flow cytometry

hCoV-229E N rabbit antibody	40640-T62, SinoBiological
hCoV-OC43 N rabbit antibody	40643-T62, SinoBiological
hCoV-NL63 N rabbit antibody	40641-T62, SinoBiological

Goat anti-rabbit IgG (H+L) secondary antibody, HRP	#31460, Thermo Fischer Scientific
Goat anti-rabbit IgG (H+L) secondary antibody, Alexa Fluor 647	#A32733, Thermo Fischer Scientific
SARS-CoV-2 immunodetection assay	
SARS-CoV-2 N-protein mouse antibody	40143-MM05, SinoBiological
SARS-CoV-2 S-protein mouse antibody 1A9	GTX-GTX632604, Biozol
Goat anti-mouse IgG (H+L) secondary antibody, HRP	#A16066, Thermo Fischer Scientific
Western Blot	
SARS-CoV-2 N-protein rabbit antibody	40143-R001, SinoBiological
StarBright 520-coupled anti-rabbit secondary antibody	12005869 Bio Rad
Tubulin hFAB Rhodamine antibody	12004165 Bio Rad
ZIKV immunodetection assay	
Flavivirus protein E 4G2 mouse antibody	#Ab00230-2.0, Absolute Antibody

2.1.6 Buffer

Antibody buffer	0.3 % (v/v) Tween-20, 10 % (v/v) FCS in PBS
ELISA washing buffer	0.3 % (v/v) Tween-20 in PBS
FACS buffer	1 % (v/v) FCS in PBS
HEPES buffer	10 mM HEPES, 150 mM NaCl, 0.05 % (v/v) Tween-20, pH 7.5
Lysis buffer (10x)	10 % (v/v) Triton X-100,10 % (v/v) SDS and 1:50 protease inhibitor
PBS	137 mM NaCl, 2.7 mM KCl, 10 mM Na_2HPO_4, 1.8 mM KH_2PO_4
PBST 0.05 %	0.05 % (v/v) Tween-20 in PBS
MES buffer	32.5 mM MES monohydrate and 4 mM $CaCl_2$ dihydrate
Western blot transfer buffer	10 % (v/v) Semi dry blot transfer buffer, 20 % (w/v) MeOH in dH_2O
Western Blot blocking buffer	50 % (v/v) Casein Blocker™ in 0.05 % (v/v) PBST
Western Blot antibody buffer	10 % (v/v) Casein Blocker™ in 0.05 % (v/v) PBST

2.1.7 Chemicals

2.1.7.1 General reagents

1 kb Plus DNA ladder	Thermo Fischer Scientific
4× Protein Sample Loading Buffer	LI-COR Biosciences GmbH
Agar	BD Bioscience
Agarose	Thermo Fischer Scientific
Ampicillin	Ratiopharm GmBH
Avicel cellulose RC-581	FMC Corporation
Bacto™ Tryptone	BD Biosciences
Bacto™ Yeast Extract	BD Biosciences
Blocker™ Casein in PBS	Thermo Fischer Scientific
Carboxyfluorescein	Sigma-Aldrich
Calcium chloride dihydrate	PanReac AppliChem
Chloroform	Sigma-Aldrich
Crystal violet	Sigma-Aldrich
Dimethylsulfoxid (DMSO)	Merck KGaA
Distilled H_2O (HPLC grade)	VWR
DNA/RNA Shield™	Zymo Research
Dulbecco´s Modified Eagle Medium (DMEM)	Thermo Fischer Scientific
Dulbecco´s Phosphate Buffered Saline (PBS)	Thermo Fischer Scientific
Ethanol (EtOH)	Merck KGaA
FACS clean solution	Beckman Coulter
FACS Sheath Fluid	Beckman Coulter
Fetal calf serum (FCS)	Thermo Fischer Scientific
FIX&PERM® Kit 1000	Nordic-MUbio
GelRed® Nucleic Acid Gel Stain	Biotium
Geneticin	Fischer Scientific
HEPES Buffer Solution (1 M)	Thermo Fischer Scientific
Human serum	Sigma-Aldrich
Incidin® Plus	ECOLAB Healthcare
Isopropanol	VWR
L-Glutamine	Thermo Fischer Scientific
MES SDS Running Buffer (20×)	Thermo Fischer Scientific
MES	Thermo Fischer Scientific

Methanol (MeOH)	Sigma-Aldrich
Minimum essential medium (MEM)	Thermo Fischer Scientific
MUNANA (4-methylumbelliferyl-N-acetylneuraminic acid)	Thermo Fischer Scientific
Non-essential amino acids (NEAA, 100×)	Thermo Fischer Scientific
OptiMEM Reduced Serum Media	Thermo Fischer Scientific
Paraformaldehyde (PFA)	Merck KGaA
Penicillin-Streptomycin	PAN-Biotech GmbH
PK Digestion Buffer	Zymo Research
Polyethylenimine (PEI)	Merck KGaA
Precision Plus Protein™ Kaleidoscope™ Prestained	Bio-Rad Laboratories Inc.
Protease inhibitor cocktail	Merck KGaA
Proteinase K Set	Zymo Research
Roswell Park Memorial Institute Medium (RPMI-1640)	Thermo Fischer Scientific
Semi dry blot transfer buffer (10×)	Alfa Aesar
Small Airway Epithelial Cell Growth Medium	PromoCell
Sodium chloride (NaCl)	Sigma-Aldrich
Sodium dodecyl sulfate (SDS)	Fluka BioChemika
Sodium hydroxide (NaOH)	Merck KGaA
Sodium Pyruvate (100 mM)	Thermo Fischer Scientific
Sulfuric acid (H_2SO_4)	Sigma-Aldrich
TAE buffer (50×)	Carl Roth GmbH & Co. KG
TMB peroxidase substrate	Thermo Fischer Scientific
TransIT®-LT1 Transfection Reagent	Mirus Bio LLC
Tris(2-carboxyethyl) phosphine HCl (0.5 M)	Merck KGaA
Triton X-100	Sigma-Aldrich
Trypsin/EDTA (0.05 %)	PAN-Biotech GmbH
Tween®-20	Sigma-Aldrich
Uranyl acetate	Merck KGaA
X-VIVO 15	Lonza

2.1.7.2 Lipids

1,2-Dioleoyl-sn-glycero-3-phosphocholine (DOPC)	Avanti® Polar Lipids

Ceramide from egg	Avanti® Polar Lipids
Cholesterol (Chol) from ovine wool	Avanti® Polar Lipids
Cholesteryl oleate (Chol ester) 18:1	Avanti® Polar Lipids
Phosphatidic acid (PA) from egg	Avanti® Polar Lipids
Phosphatidylcholine (PC) from egg	Avanti® Polar Lipids
Phosphatidylethanolamine (PE) from egg	Avanti® Polar Lipids
Phosphatidylglycerol (PG) from egg	Avanti® Polar Lipids
Phosphatidylinositol (PI) from soy	Avanti® Polar Lipids
Phosphatidylserine (PS) from porcine brain	Avanti® Polar Lipids
Sphingomyelin (SM) from egg	Avanti® Polar Lipids
Lyso-PC 18:1	Avanti® Polar Lipids
Lyso-PE 18:1	Avanti® Polar Lipids
Lyso-PS 18:1	Avanti® Polar Lipids

2.1.7.3 Antiviral substances

Bamlanivimab	Eli Lilly
Camostat mesylate (CM)	Merck KGaA
Casivirimab	Roche
E-64d	Selleckchem
Imdevimab	Roche
Molnupiravir (EIDD-2801)	Selleckchem
Nirmatrelvir (PF-07321332)	Selleckchem
Remdesivir (GS-5734)	Selleckchem

Molecular Tweezers

CLR01	7.4 mM stock in PBS	CP012	4 mM stock in PBS
CLR03	7.4 mM stock in PBS	CP013	1 mM stock in 5 % DMSO, PBS
CLR05	4 mM stock in water	CP015	4 mM stock in PBS
PC	4 mM stock in PBS	CP018	4 mM stock in PBS
p-CH200	4 mM stock in PBS	CP019	4 mM stock in PBS
p-CH201	4 mM stock in PBS	CP020	2 mM stock in 2 % DMSO, PBS
p-CH202	4 mM stock in PBS	CP021	4 mM stock in PBS
p-CH203	4 mM stock in PBS	CP022	4 mM stock in PBS
p-CH204	4 mM stock in PBS	CP023	4 mM stock in PBS

p-CH205	4 mM stock in PBS	CP024	4 mM stock in PBS
p-CH206	1 mM stock in 2 % DMSO, PBS	CP025	4 mM stock in PBS
p-CH192	1 mM stock in 2 % DMSO, PBS	CP026	4 mM stock in PBS
p-CH193	1 mM stock in 2 % DMSO, PBS	CP027	4 mM stock in PBS
CP002	4 mM stock in PBS	CP033	2 mM stock in 2 % DMSO, PBS
CP005	4 mM stock in PBS	CP036	4 mM stock in PBS
CP006	2 mM stock in 2 % DMSO, PBS	CP037	4 mM stock in PBS
CP007	4 mM stock in PBS	CP038	4 mM stock in PBS
CP008	4 mM stock in PBS	CP041	4 mM stock in PBS
CP009	4 mM stock in PBS	CP049	4 mM stock in PBS

2.1.8 Consumables

Amicon Ultra-15 100 kDa MWCO filters	Millipore
Cell culture flask (T175, T75, T25)	Thermo Fischer Scientific
Cell Crown™	Sigma-Aldrich
Cell scraper	Sarstedt and VWR
Copper grids G2300C Cu square 300 mesh	PLANO
Filter supports	Avanti® Polar Lipids
gentleMACS M tubes	Miltenyi Biotec
Gloves	VWR
Headspace Glass Vial 10 ml	SUPELCO
Immobilon®-FL PVDF-Membrane	Merck KGaA
Luna™ Counting slide	Logos biosystems
Nunc™ F96 Microwell™ Polystyrol plate, opaque	Thermo Fischer Scientific
Nunc™ cell culture dish 100 mm	Thermo Fischer Scientific
NuPAGE™ 4-12 % Bis-Tris, 1.0 mm	Thermo Fischer Scientific
Polycarbonate Membrane 0.05, 0.1, 0.2, 0.4, 0.8 µm	Avanti® Polar Lipids
PCR-plate 96-well	Brand
Pipette tips 100-1000 µl, 2-200 µl, 1-10 µl	Sarstedt
QIAcuity Nanoplate 96 well	Qiagen
Reaction tube 1.5 ml, 2 ml	Sarstedt
Reagent reservoirs 50 ml	VWR
Serological pipettes	Sarstedt
Syringe filter 0.45 µM	Merck Millipore

Syringes 1 ml	B. Braun
Syringes 5 – 50 ml	Becton Dickinson
TC plate 6-well, Standard F	Thermo Fischer Scientific
TC plate 12-well, Standard F	Thermo Fischer Scientific
TC plate 24-well, Standard F	Thermo Fischer Scientific
TC plate 96-well, Standard F	Thermo Fischer Scientific
TC plate 96-well, Standard, R	Thermo Fischer Scientific
TC plate 96-well, Standard, V	Thermo Fischer Scientific
Tube 15 ml, 50 ml	Sarstedt
Whatman filter paper	Whatman

2.1.9 Kits

CellTiterGlo® Luminescence Cell Viability Assay	Promega Corporation
Detach Kit	Promocell
Gal-Screen™ β-Galactosidase Reporter Gene Assay	Thermo Fisher Scientific
Luciferase Assay System	Promega Corporation
Pierce Rapid Gold BCA Protein Assay Kit	Thermo Fisher Scientific
PD-10 Desalting Columns Sephadex G-25	Cytiva
PrimeScript RT Reagent Kit	Takara
QIAamp Viral RNA Mini Kit	Qiagen
Quick-RNA™ Miniprep Kit	Zymo Research
TaqMan Fast Virus 1 Step	Thermo Fisher Scientific
Wizard® Plus Midipreps DNA Purification System	Promega Corporation

2.1.10 Technical equipment

Autoclave HX-150 2D	Systec GmbH
Avanti Mini Extruder	Avanti® Polar Lipids
Cell counter Luna II	Logos Biosystems
Centrifuge 5430 R	Eppendorf AG
Centrifuge 5810 R	Eppendorf AG
Centrifuge Rotor 96 plate A-2-MTP	Eppendorf AG
Centrifuge Rotor A4 81	Eppendorf AG
Centrifuge Rotor F45 30 11	Eppendorf AG
CytoFLEX flow cytometer	Beckman Coulter
Explorer™ semi micro scale	OHAUS

Gel Caster Sub-Cell GT	Bio-Rad
Gel imaging system ChemiDoc MP	Bio-Rad
GentleMACS Octo Dissociator	Miltenyi Biotec
Heat block ThermoMixer C	Eppendorf AG
Incubator Forma Steri-Cult™ CO_2	Thermo Fischer Scientific
Incubator MaxQ6000	Thermo Fischer Scientific
JEOL JEM-1400 transmission electron microscope	JEOL GmbH
Laminar Flow Hood Herasafe™ KSP	Thermo Fischer Scientific
Light microscope DMi1	Leica Camera AG
Luminometer Orion II	Titertek Berthold
Microplate reader Asys Expert 96 UV	Biochrom
Microplate reader Versa max	Molecular Devices LLC
Mini-Sub Cell GT, Wide	Bio-Rad
Multichannel pipette Transferpette S12 (20-200 µl)	Brand GmbH & Co. KG
Multichannel pipette Transferpette S12 (5-50 µl)	Brand GmbH & Co. KG
Nanophotometer® NP80	IMPLEN GmbH
OSMOMAT 3000	Gonotec
pH-meter SevenCompact pH/Cond S312-Std Kit	Mettler Toledo
Pipette controller Macroman	Gilson Inc.
Pipette Pipetman L, P10L, P20L, P200L, P1000L	Gilson Inc.
Power Supply PowerPac™ HC	Bio-Rad
QIAcuity Digital PCR System	Qiagen
Semi-Dry-Blotter PerfectBlue	VWR
Synergy™ H1 microplate reader	BioTeK Instruments GmbH
Thermocycler StepOnePlus™ Real-Time PCR System	Thermo Fischer Scientific
UV-Transparent Tray, Fixed Height Combs	Bio-Rad
ZetaSizer Nano	Malvern Panalytical
ZetaView® Twin Particle Tracking Analyzer Z-NTA	Scientific Instruments

2.1.11 Software

Biorender	BioRender
ChemDraw Prime 21.0.0.	PerkinElmer

CytExpert 2.3	Beckmann Coulter Inc.
DigiRead 1.26	Biochrom
Gen5 3.04	BioTek Instruments
ImageJ 1.53c	National Institute of Health (Wayne Rasband)
Microsoft Office	Microsoft
Simplicity 4.20	Berthold Technologies GmbH & Co. KG
SoftMax Pro 7	Molecular Devices LLC
Step One 2.3	Thermo Fischer Scientific
ZetaView® and ZetaView® Analyze, 8.05.12 SP1	Particle Metrix

2.2 Methods

2.2.1 Cell culture

All cell lines were cultured in a ventilated 175 ml flask with respective media specified in 2.2.2.3, at 37 °C and with 5 % CO_2 in a humidified incubator. Upon reaching 100 % confluence, cells were trypsinized, resuspended in respective media and split at ratio of 1:2 - 1:10.

In case of differentiated air-liquid interface (ALI) cultures of human airway epithelial cells (HAEC), generation was performed by the group of Prof. Manfred Frick, Institute of General Physiology, Ulm University, Ulm. Briefly, human basal cells were cultured in a 175 ml flask until reaching 90 % confluence. Cells were detached using the Detach Kit and 3.5 x 10^4 cells were seeded onto 6.5 mm Transwell filters. Medium was added to apical and basolateral side for 72-96 h, before medium of the apical side was removed and the medium of basolateral side exchanged with differentiation medium. Lifting of the apical side set day 0 of ALI culture. After 14 days of culturing accumulated mucus on the apical side was removed and collected every 3 days[165].

2.2.2 Cell viability assay

Compounds were tested for their effect on cellular metabolic activity by CellTiterGlo Luminescence Cell Viability Assay. To assess cytotoxicity of tested antivirals, cells were treated with concentrations corresponding to that used in the respective infection assay. Afterwards, Cell Viability Assay was performed according to manufactures protocol. Briefly, supernatant was removed from cells after indicated days of incubations and 100 µl of PBS-substrate mix (ratio 1:1) was added. Cells were incubated for 10 minutes in the dark before luminescence measurement in an Orion II Microplate Luminometer. Untreated cells as control were set to 100 % viability[159].

2.2.3 Plasmid preparation

2.2.3.1 Transformation of bacteria

Plasmid DNA was amplified in chemical competent *E. coli* XL-2 blue™. Therefore, bacteria were incubated with 1 µl of plasmid DNA for 20 min on ice, before heat shocking for 45 sec at 42 °C and a 5 min cooling on ice. Bacteria were cultured in 500 µl of S.O.C. medium for 1 h at 37 °C with vigorous agitation (400 rpm) for recovery and plated afterwards on agar

places containing 100 µg/ml ampicillin as selection marker. Plates were incubated at 37 °C for additional 12 – 16 h and single clones were picked for plasmid preparation.

2.2.3.2 Culture of bacteria

To enrich bacterial biomass and increase plasmid yield, single colony was inoculated in 150 ml LB medium supplemented with 100 µg/ml ampicillin and incubated for 12-16 h at 37 °C with vigorous agitation (160 rpm).

2.2.3.3 Plasmid DNA isolation and characterization

Plasmid DNA was extracted from bacteria by the Wizard® Plus Midipreps DNA Purification System according to the manufacturer's instructions. DNA concentration was determined using Nanophotometer® NP80 at an absorption of 260 nm. Additionally, correctness of plasmid DNA was controlled by restriction digestion using respective endonucleases and buffers according manufacturer's instructions. Digested DNA was separated on an 1 % (w/v) agarose gel containing GelRed® Nucleic Acid Gel Stain (1:10 000), in TAE buffer. Before loading, samples were mixed with 5 µl of 5× DNA loading dye. The agarose gel was run at 120 V for 45 min and DNA bands were visualized using a DNA ChemiDoc Gel imaging system.

2.2.4 Synthesis and purification of tweezers

Tweezer were designed, synthesized and purified by the group of Thomas Schrader, Faculty of Chemistry, University of Duisburg-Essen as described in Weil et al.[159].

2.2.5 Virological methods

2.2.5.1 Severe acute respiratory syndrome coronavirus 2 (SARS-CoV-2) propagation

Propagation of all SARS-CoV-2 strains was performed on Caco-2 or Vero E6 cells. To this end, cells were seeded in a 75 cm^2 flask to reach 70-90 % confluence on the next day. Medium was removed and 3.5 ml serum free medium together with the virus strain at an MOI of 0.03-0.1 was used for inoculation. After 2 h incubation at 37 °C, additional 20 ml respective cell medium supplemented with 15 mM HEPES was added. Cells were observed and harvested when strong cytopathic effect (CPE) became visible. Cell debris were

removed by centrifugation for 5 min at 1,000 × g and virus stocks were stored as aliquots at -80 °C[159].

2.2.5.2 SARS-CoV-2 infection and immunodetection assay

Detection of N-protein of SARS-CoV-2 was accomplished with an in-cell ELISA. To this end, 25.000 Caco-2 cells were seeded in 100 µl medium in a 96 well plate. At the next day, serial dilution of tweezer was mixed with SARS-CoV-2 Wuhan/Hu-1 at an MOI of 0.01 or 0.0007. After incubation for 2 h, 44 µl medium and 36 µl tweezer-virus mixture was added on cells. Two days post infection, immunodetection assay was conducted. To this end, cells were fixed for 30 min with final 4 % paraformaldehyde (PFA) at room temperature (RT), followed by permeabilization with 0.1 % Triton X-100 for 5 min and a PBS washing step. PBS was aspirated and S-protein or N-protein stained with 1:5000 diluted 1st antibody in antibody buffer for 1 h at 37 °C. Cells were washed two times with 0.3 % Tween-20 in PBS and stained with 2nd anti-mouse HRP coupled antibody for 1 h at 37 °C. Cells were washed three times with 0.3 % Tween-20 in PBS and incubated for 5 min in 50 µl TMB peroxidase substrate. Afterwards, 50 µl H_2SO_4 was added and the optical density recorded with Asys Expert 96 UV at 450 nm with 620 nm background subtraction[159].

2.2.5.3 $TCID_{50}$ endpoint titration

Infectivity of virus stocks was determined by Tissue Culture Infection Dose 50 ($TCID_{50}$). To this end, respective cell line (20,000 for Vero E6, 25,000 for Huh-7, 30,000 for HCT-8, 25,000 for Caco-2) was seeded in 96 well plates in 100 µl respective medium, before 62 µl medium was added on the next day (for infectivity determination of hCoVs respective medium was supplemented with 2 % FCS). Titrated virus stock (5-fold or 10-fold) or tweezer samples were inoculated onto cells at a volume of 18 µl. Cells were incubated for 5 to 7 days and monitored for CPE[159,166]. $TCID_{50}$/ml was calculated according to Reed and Muench[167].

2.2.5.4 Transmission electron microscopy

SARS-CoV-2 Wuhan/Hu-1 stock produced in serum free medium was mixed with tweezers and incubated for 30 min at 37 °C, before fixation with PFA (2 % final concentration for 30 min at 37 °C and further 30 min at RT). The samples were negatively stained for transmission electron microscopy. Therefore, 10 µl sample was applied onto carbon

reinforced formvar film covered copper grids and incubated for 10 min at RT. Grids were washed three times with dH_2O and stained with 0.5 % uranyl acetate in dH_2O. Images were acquired with a JEOL JEM-1400 transmission electron microscope operated at 120 kV[159]. Electron microscopy experiments were performed by the group of Clarissa Read, Central Faculty for Electron Microscopy, Ulm University.

2.2.5.5 Human coronavirus (hCoV) stock generation

Propagation of hCoV strains was performed on LLC-MK2 (hCoV-NL63), Huh-7 (hCoV-229E), HCT-8 or TMPRSS2 expressing Vero E6 cells (hCoV-OC43). To this end, respective cell line was seeded in a 75 cm^2 flask to reach 70-90 % confluence on the next day. Medium was removed and 10 ml 2 % FCS containing medium together with the respective virus strain at an MOI of 0.1 was used for inoculation. After 1day of incubation at 33 °C, cells were washed with PBS and 10 ml respective medium supplemented with 2 % FCS was added. Cells were observed and harvested when strong CPE became visible (3dpi in case of hCoV-229E, 4 pi in case of hCoV-OC43 and 5 dpi for hCoV-NL63). Cell stocks were clarified from debris by centrifugation for 5 min at 1,300 rpm and virus stocks were stored as aliquots at -80 °C[166].

2.2.5.6 hCoV infection and immunodetection assay

To draw conclusion of hCoV infection an in-cell ELISA was established to detect N-protein. In brief, 25,000 Huh-7 (hCoV-229E and -OC43) or Caco-2 cells (hCoV-NL63) were seeded one day prior in respective medium supplemented with 2% FCS. 62 µl medium was added together with 18 µl of 2- or 10-fold titrated virus stock. Cells were incubated at 33 °C for 2 h, and 2, 3, 4, or 6 days followed by fixation with 180 µl 8 % PFA for 30 min. Permeabilization was achieved by incubation in 0.1 % Triton X-100 for 5 min. Afterwards, cells were washed once with PBS and stained using 50 µl of 1st antibody targeting the respective N-protein in antibody buffer (1:5,000, 1:7,500 or 1:10,000) for 1 h at 37 °C. Subsequently, cells were washed with 0.3 % Tween-20 in PBS twice and incubated for additional hour at 37 °C in 2nd anti-rabbit HRP coupled antibody (1:7,500, 1:10,000 or 1:15,000). Cells were washed three times with 0.3 % Tween-20 in PBS and incubated for 5 min in 50 µl TMB peroxidase substrate. Afterwards, 50 µl H_2SO_4 was added and optical density measured with Asys Expert 96 UV at 450 nm with 620 nm background subtraction[166]. Susceptibility of Huh7 (25,000), Caco-2 (25,000), Calu-3 (40,000) and

Vero E6 (20,000) cells towards hCoV infection was investigated by the established in-cell ELISA. Virus stocks were titrated as stated and used for inoculation of the respective cell line. Immunodetection analysis was performed as described in Table 2. Testing of antiviral activity of various compounds was performed as described above and setting was chosen as stated in Table 2. Application of each compound is indicated in the figure legend.

2.2.5.7 Plaque assay of hCoVs

Cells were seeded on day prior to infection in 12 well plates to reach confluent monolayer (700,000 of Huh-7 and Caco-2 cells or 400,000 of LLC-MK2 cells). At the next day, cells were washed once with PBS and 400 µl PBS was added. Virus was titrated in respective medium and used for inoculation on cells (100 µl). Cells were incubated for 2 h at 33 °C while swirling the plates every 20 min. Afterwards, the cells were overlaid with 1.5 ml 0.6 % Avicel containing medium and incubated at 33 °C until staining was performed at day 4 (hCoV-229E) or 5 (hCoV-NL63, -OC43). Therefore, cells were fixed with 1 ml 8 % PFA for 45 min and washed once with PBS. Cells were covered with 0.5 % crystal violet in 0.1 % Triton X-100 for 20 min, washed with H_2O, dried and plaques were counted[166].

2.2.5.8 hCoV infection and detection via flow cytometry

Establishment of viral human coronavirus detection via flow cytometry was accomplished in 96 well format. Briefly, Huh-7 or Caco-2 cells (25,000) were seeded in 100 µl medium supplemented with 2 % FCS. Virus stocks were titrated 5-fold and 18 µl together with 62 µl medium were used for inoculation. Cells were incubated at 33 °C for 2 h and 2, 3, or 4 days until detachment with 50 µl 0.05 % trypsin and subsequent fixation by incubation in 50 µl 8 % PFA for 30 min. Subsequently, cells were transferred in a V-well plate, centrifuged for 1 min at 3,000 rpm and permeabilized and stained in one step. Therefore, cells were incubated in 50 µl 1:5,000 or 1:10,000 diluted 1st antibody targeting respective N-protein in buffer B (Nordic-MUbio) for 40 min at 4 °C, followed by washing twice with FACS buffer. Cells were stained in 50 µl 2nd anti-rabbit AlexaFluor 647 coupled antibody (1:5,000, 1:10,000 and 1:15,000 diluted in FACS buffer) for 30 min at 4 °C. After two washing steps in FACS buffer and transfer into PBS, cells were analyzed by flow cytometry[166]. Antivirals were evaluated as described above and conditions set as stated in Table 1.

2.2.5.9 Lentiviral pseudoparticle production

Adherent HEK 293T cells ($9x10^5$ cells/well) were seeded in 6-well plate one day prior to transfection. Afterwards, 1 µg of DNA containing 2 % pCG1-SARS-CoV-2 SΔ18, 49 % pCMVdR8.91 and 49 % pSEW-luc2 were mixed with Opti-MEM reduced serum medium, followed by addition of TransIT-LT1. Transfection mixture was incubated for 20 min before dropwise addition onto cells in fresh medium. Cells were incubated for 8 h at 37 °C, washed once with PBS and coverred with DMEM containing 2.5 % FCS. Two days post transfection, virus stock was clarified from cell debris by centrifugation for 5 min at 1,500 rpm and aliquots were stored at -80 °C[159].

2.2.5.10 Lentiviral SARS-CoV-2 pseudoparticle inhibition assay

Antiviral activity of tweezer was assessed using lentiviral, replication incompetent pseudoparticles harboring the SARS-CoV-2 S-protein. The expression of a luciferase reporter gene upon transduction of a cell, allows the determination of the transduction rate. In brief, increasing concentrations of tweezers and lentiviral SARS-CoV-2 pseudoparticles were mixed and incubated for 30 min at 37 °C prior to transduction of Caco-2 cells (10,000 cells seeded one day ahead in 96 well plate). Four hours post transduction medium was refreshed. Luciferase activity was measured 2 days later using a Luciferase Assay System. Briefly, the supernatant was removed, cells washed once with PBS and 40 µl lysis buffer was added. 30 µl of the cell lysates were transferred to Nunc™ 96 well white plates and mixed with 50 µl substrate. Luciferase activity was measured in a Orion II Microplate Luminometer [159].

2.2.5.11 ZIKV infection and immunodetection assay

Propagation of Zika virus (ZIKV) strain FB-GWUH-2016 was performed on Vero E6 cells as described[168]. Antiviral activity of tweezers against ZIKV was assessed with in-cell ELISA detecting the flavivirus E-protein. Briefly, rising concentration of tweezers were mixed with the same volume of ZIKV to reach a final MOI of 0.15. After incubation period of 30 min at 37 °C, 40 µl of the mixture was used for infection of Vero E6 cells, seeded on day ahead (6,000 cells in 160 µl medium). Cells were incubated for 2 days, until supernatant was removed and cells fixed with 100 µl 4 % PFA for 20 min after washing once with PBS. PFA was aspirated, cells permeabilized using ice cold methanol for 5 min and further washed with PBS. Subsequently, cells were stained with 50 µl of 1:10,000 diluted flavivirus E-

protein E 4G2 antibody in antibody buffer for 1 h at 37 °C, prior to washing three times with 0.3 % Tween-20 in PBS. The 2nd anti-mouse HRP coupled antibody (1:20,000) was added for 1h at 37 °C. Subsequently, cells were washed four times with 0.3 % Tween-20 in PBS and incubated for 5 min in 50 µl TMB peroxidase substrate. Afterwards, 50 µl H_2SO_4 was added and optical density was recorded with Asys Expert 96 UV at 450 nm with 620 nm background subtraction[168].

2.2.5.12 HIV-1 infection and β-galactosidase assay

HIV-1 NL4-3_92TH014-12 strain was produced by transfection of HEK 293T cells using TransIT®-LT1 Transfection Reagent. To this end, HEK 293T (3.5 x 10^6 cells/10 cm dish) were seeded in 20 ml medium. At the next day, 15 µg of pBR_NL4-3_92TH014-12 (R5) was mixed with Opti-MEM reduced serum medium, followed by addition of TransIT-LT1. The transfection mixture was incubated for 20 min before dropwise addition onto cells. Cells were incubated for 8 h at 37 °C, washed once with PBS and covered with DMEM containing 2.5 % FCS. Two days post transfection, virus stock was clarified from cell debris by centrifugation for 5 min at 1,500 rpm and aliquots stored at -80 °C.

For inhibition assay, increasing concentrations of tweezers were incubated with HIV-1 for 10 min at 37 °C. TZM-bl cells (10,000) seeded one day before were inoculated with 20 µl of the tweezer mixture. Three days post infection, infectivity of HIV-1 was measured in cellular lysate by detecting β-galactosidase activity. To this end, supernatant was aspirated and cells covered with 40 µl 1:4 diluted Gal-Screen™ β-Galactosidase Reporter Gene substrate in PBS. After incubation for 40 min at RT, 35 µl sample was transferred into white 96 well plates and luminescence of samples was recorded using an Orion II Microplate Luminometer[159].

2.2.5.13 HSV-1 and HSV-2 infection and β-galactosidase assay

GFP expressing HSV-1 strain F and HSV-2 strain 333 were propagated as previously described[169]. For antiviral testing, 10,000 ELVIS cells were seeded in 100 µl respective medium. At the next day, medium was replaced by 144 µl X-VIVO 15 supplemented with 2 mM L-glutamine, 100 U/ml penicillin and 100 µg/ml streptomycin. Escalating concentrations of tweezers were incubated either with HSV-1 or HSV-2 for 15 min at 37 °C, before 36 µl sample was used for infection of ELVIS cells, resulting in an MOI of 0.05. Two

days afterwards, infectivity was measured in cellular lysates by detecting β-galactosidase activity (described in detail in 2.2.5.12)[170].

2.2.5.14 IAV infection and MUNANA assay

Influenza A virus (IAV) PR8 was propagated on MDCK cells as described[169]. Antiviral activity of tweezers against IAV was analyzed with a MUNANA assay. In brief, 20,000 Caco-2 cells were seeded on day prior to infection in 100 µl cDMEM (DMEM, supplemented with 7.5 % (v/v) BSA, 2 mM L-glutamine, 100 U/ml penicillin, 100 µg/ml streptomycin, 25 mM HEPES). At the next day, escalating concentrations of tweezers were incubated with IAV (MOI 0.0007) for 30 min and 40 µl mixture was used for inoculation together with additional 60 µl cDMEM. After 48 h, infectivity was assessed by measuring neuraminidase activity. Briefly, cells were washed once with PBS, lysed in 1% Triton X-100 for 30 min and diluted 1:2 in MES buffer. 20 µl of the sample and 30 µl 100 µM MUNANA substrate (4-methylumbelliferyl)-N-acetylneuraminic acid) was transferred into black 96 well plate and incubated for 4 h at 37 °C with gentle agitation. Afterwards, 150 µl stop solution was added (0.1 M glycine and 25% ethanol) and fluorescence was recorded with a Synergy™ H1 microplate reader at excitation of 360 nm and an emission at 455 nm[159].

2.2.5.15 MeV infection and detection via flow cytometry

Measles virus (MeV) vac2 strain expressing eGFP was propagated as described[160]. To assess antiviral effect of tweezers, MeV with an MOI of 0.1 was incubated with serial titration of tweezers for 30 min at 37 °C. A549 cells (20,000 cells seeded on day earlier) were washed once with PBS before infection with 40 µl of the tweezer-virus mix. After 1 h incubation, 160 µl medium was added and cells were incubated for further 48 h. Infection was determined by quantification of GFP positive cells. Therefore, cells were washed once, trypsinized until detachment and mixed with medium. Cells were transferred into a 96 V well plate, washed again, fixed in 2 % PFA and analyzed by flow cytometry[159].

2.2.5.16 RSV infection and detection via flow cytometry

Propagation of respiratory syncytial virus (RSV) expressing eGFP was performed as described[161]. Testing of antiviral activity was carried out on A549 cells (2.5×10^4) seeded in 48 well plates on day ahead. Rising concentrations of tweezers were mixed with RSV resulting in an MOI of 1. After incubation for 30 min at 37 °C, samples were used for

infection. After incubation for 24 h, cells were trypsinized and infection rates were assessed of detached cells using flow cytometry[159]. Experiments were performed by the group of Anna-Lena Spetz, Department of Molecular Bioscience, Stockholm University.

2.2.6 *In vivo* experiments

Transgenic K18-hACE2 male mice (14 weeks old) were randomized into groups of 6 animals. Experiments were performed under BSL3 conditions and in accordance to EU Directive 2010/63/EU with approval of local authorities. Body weight and clinical scored were assessed daily. For investigation of antiviral activity of tweezers on SARS-CoV-2 in mice, tweezers (150 µM) or PBS were mixed with 300 focus-forming unit (FFU) of SARS-CoV-2 Wuhan/Hu-1 and incubated for 1 min at 37 °C. The mixture (50 µl) was administered intranasally under isoflurane anesthesia. Seven hours post infection, mice were treated again with the same dose of tweezers or PBS. In the prophylactic set-up, tweezers (150 µM) or PBS was applied intranasally 1 h and 10 min prior to infection with 300 FFU SARS-CoV-2 Wuhan/Hu-1 (40 µl) intranasally under isoflurane anesthesia. Two days post infection, mice were euthanized and lung collected in gentleMACS M tubes, together with 2 ml PBS. Lungs were homogenized using GentleMACS Octo Dissociator and supernatant harvested after centrifugation at 2000 × g for 5 min at 4 °C[159]. Experiments were performed by the group of Thomas Grunwald, Fraunhofer Institute for Cell Therapy and Immunology, Leipzig.

2.2.6.1 Quantitative real-time PCR (RT-qPCR)

Supernatant of mice lung homogenates described in 2.2.6 were used to determine viral load of SARS-CoV-2. RNA was isolated with the QIAamp Viral RNA Mini Kit according to manufacturer´s instructions. Isolated RNA (5µl) was added to a mixture of TaqMan Fast Virus 1-Step 4x (5µl), primer fwd. (10 µM, 1 µl), primer rev. (10 µM, 1 µl), probe (10 µM, 0.5 µl) and RNAse free H_2O (7.5 µl). The sequences of primer and probe are stated in 2.1.4.1. Sample containing wells were sealed with foil, followed by addition of titrated RNA Standard of SARS-CoV-2 RNA and complete cover of the plate. The reaction was carried out in technical duplicates and performed in a OneStepPlus Real-Time PCR System with the following set-up:

Temperature (°C)	Time (mm:ss)	Round of cycles
50	05:00	1
95	00:20	
95	00:05	40
60	00:30	

Threshold for RNA detection was set at cycle threshold (C_t) of 35[159]. Experiments were performed by group of Thomas Grunwald, Fraunhofer Institute for Cell Therapy and Immunology, Leipzig.

2.2.6.2 Digital droplet PCR

The expression level of interferon stimulated genes (ISG´s) was measured using digital droplet PCR. As initial step, supernatant of mice lung homogenates described in 2.2.6 were mixed with RNA/DNA shield for viral inactivation and stored at -80 °C until further usage. Samples were treated with Proteinase K in respective enzyme buffer for 30 min at RT, before RNA was isolated using Quick-RNA™ Miniprep Kit according to the manufacturer´s instructions. Afterwards, RNA concentrations were determined with a nanodrop spectrometer and re-transcribed into cDNA with PrimeScript RT Reagent Kit. In brief, RNA (0.56 µg, 5µl) were added to 5 µl master mix containing final concentration of 5x PrimeScript buffer (2µl), oligo primer (50 µM, 0.5 µl), random 6mers (100 µM, 2 µl) and PrimeScript enzyme mix I (0.5 µl). The mixture was incubated in a thermal cycler for 15 min at 37 °C for reverse transcription, followed by enzyme inactivation through incubation at 85 °C for 5 sec and storage at 4 °C. For analysis of ISG5, RIG-I, MX1, OAS1 and housekeeping gene TBP expression level, 1.2 µl cDNA were added to 10.8 µl master mix containing final concentration of 4x Probe PCR Master Mix (3 µl), primer-probe set of each gene (1.2 µl in total, with 4 µM probe and 8 µM primer) and 1.8 µl RNAse free H_2O in a regular PCR plate. Primer and probe sequence are listed in 2.1.4.1. The design of probe and primers was performed on the mRNA level of each gene including, if possible, on exon spanning sequences. Each probe is equipped with a different fluorophore and respective blackhole quencher. Samples were mixed and 11 µl was transferred into a QIAcuity Nanoplate 96 well plate. Reaction was performed in technical duplicates using QIAcuity Digital PCR System under the following conditions:

Temperature (°C)	Time (mm:ss)	Round of cycles
95	02:00	1
95	00:15	40
60	00:30	

2.2.6.3 BCA assay

Protein content were determined using the Pierce™ Rapid Gold BCA Protein Assay Kit according to the manufacturer´s instructions. The protein-dependent reduction of copper ions allows the formation of BCA/copper complexes, which were detected at 480 nm in the Versa max microplate reader. The preparation of a BSA serial dilution serves as standard curve and enables the quantification of the protein contents.

2.2.6.4 SDS-PAGE

Proteins of the supernatant from mice lung homogenates described in 2.2.6 were separated via SDS-PAGE and viral N-protein were detected by Western blot. For lysis, 270 µl per sample was mixed with 30 µl 10x lysis buffer, vortexed for 30 sec and incubated for 5 min at 4 °C. Samples were centrifuged for 20 min at 21,000 × g and supernatants were transferred into fresh tubes. Protein concentrations were determined using Pierce Rapid Gold BCA Protein Assay Kit and adjusted to the sample with lowest concentration (for unified concentration). Samples were prepared by treatment with 4× Protein Sample Loading Buffer supplemented with 50 mM TCEP and heated for 10 min at 70 °C. 15 µg protein of each sample was loaded along with ladder onto NuPAGE™ 4-12 % Bis-Tris and separated in MES buffer for 30 min at 200 V[159].

2.2.6.5 Western Blot analysis

For Western Blot, SDS-PAGE was performed as described in 2.2.6.4. Afterwards, the proteins were transferred onto a MeOH activated PVDF membrane. Transfer was accomplished in a semi-dry blotter at 30 V for 30 min. The PDVF membrane was incubated in blocking buffer for 1 h at RT, followed by staining with 1st anti-rabbit antibody targeting SARS-CoV-2 N-protein (1:5000 diluted in antibody buffer), at 4 °C overnight. The membrane was washed three times for 5 min with 0.05 % PBST, before incubation with 2nd StarBright 520-coupled anti-rabbit antibody (1:5000 diluted in antibody buffer) and anti-Tubulin hFAB Rhodamine-coupled antibody (1:10,000 diluted in antibody buffer) for

1 h at RT. The membrane was washed for four times, before being imaged using a ChemiDoc MP imaging system[159].

2.2.7 Lipid particles – liposomes and giant unilamellar vesicles (GUVs)

2.2.7.1 Generation and characterization of liposomes

Liposomes were prepared by thin-film hydration and extrusion. Lipids were mixed at indicate ratios in glass vials with end concentration of 5 mM. The solvent chloroform was evaporated by applying nitrogen stream and the resulting lipid film was re-hydrated in a 50 mM isoosmolar 5(6)-carboxyfluorescein solution with 50 % PBS, adjusted to pH of 7.4 with NaOH. The glass vials were shaken at 60 °C with agitation of 160 rpm for 1 h. Liposomes were prepared by extrusion for at least 20 x through a polycarbonate membrane with 0.05 to 0.8 µm pore size in a Mini Extruder, placed on a heating platform at 60 °C. Non-encapsulated dye was removed with size-exclusion filtration using PD midiTrap Sephadex G-25 columns, performed twice. Liposomes were characterized by nanoparticle tracking analysis (NTA) using Zeta View Twin or dynamic light scattering (DLS, using Zeta Sizer Nano). In case of NTA measurements, samples were diluted in PBS and videos of the scattering particles were recorded with the following settings: 25 °C, 11 positions, 1 cycle, sensitivity 85 – 90, shutter 100, 15 fps, 2 s videos/positions, 3 – 5 measurements. Between the samples, the chamber was flushed with PBS. For DLS, samples were diluted in PBS and measured in a cuvette with automated settings for attenuator and position. 3 independent acquisitions were performed per sample[147,159].

2.2.7.2 Generation and characterization of GUVs

Virus-like giant unilamellar vesicles (GUVs) were produced based on a previous publication[171]. Briefly, lipids were mixed in a glass flask at a final concentration of 5 mM. The lipid mix was applied on Whatman Grade 1 paper sandwiched between CellCrown24 inserts in a 24 well plate. Chloroform solvent was evaporated by applying nitrogen stream and the lipid film was re-hydrated in 1.5 ml isoosmolar 50 mM 5(6)-carboxyfluorescein solution (in 50 % PBS, adjusted to pH of 7.4 with NaOH). The plate was shaken at 60 °C with agitation of 160 rpm for 1h. For further detachment of the GUV´s from the paper, membrane was puffed with an empty pipet and free-dye was removed by size-exclusion filtration using PD midiTrap Sephade×G-25 columns, performed twice. Size and concentration were measured using Luna II Cell Counter at three positions.

2.2.7.3 Dye leakage assay

Tweezer activity against liposomes or GUV´s was tested in a dye leakage assay. To this end, 90 µl of stated concentrations from liposomes or GUV´s were added into 96-well plates. Baseline was generated by measuring fluorescence at excitation 485 nm and emission at 528 nm for 5 min in a Synergy H1 plate reader, before 10 µl tweezer solution in escalating concentrations was added and fluorescence recorded for 30 min with measurement every minute. Maximum dye leakage was achieved by addition of Triton X-100 at a final concentration of 1 % and fluorescent measurement after for 5 min[147,159]. Background signals were subtracted from measured values, and normalized on the values of final Trion-induced fluorescence. Area under the curve (AUC) was calculated from each concentration and plotted accordingly.

2.2.8 Biomolecular modelling

Biomolecular modelling of molecular tweezers on membranes was performed by the group of Elsa Sanchez-Garcia, Computational Biochemistry, University Duisburg-Essen, described in Weil et al.[159].

2.2.9 Statistical analysis

For infection assays, values from untreated, uninfected cells were subtracted as baseline from measured infected, treated cells and untreated infected controls were set to 100 % infection. Half-maximal inhibitory concentration (IC_{50}) or half-maximal effective concentration (EC_{50}) of tested compound was calculated with a non-linear regression model (inhibitor vs. normalized respond, variable slope). Plaques were quantified using ImageJ 1.53c by assessing number of pixels occupied by plaques. Correlation analysis was assessed by Spearman Correlation, two-tailed p value. Further statistical analysis was either performed with ordinary one-way ANOVA with Dunnett´s Pairwise Multiple Comparison Procedures or nonparametric Mann-Whitney test. All statistical tests were performed in GraphPad Prism (9.4.0). Principal component analysis (PCA) was conducted using R version 4.1.2[172]. In brief, IC_{50} and EC_{50} values of tweezers against viruses or liposomes were used for PCA. To account for the impact of missing values and enable comparison of the different tweezers, viruses and synthetic vesicles, missMDA package version 1.18[173] was used to impute the missing values and remove their impact on the PCA. PCA was done

using the factoMineR package version 2.4[174] and results were extracted using the factoextra package version 1.0.7[175]. The first two dimensions were plotted with the tidyverse package collection[176] using the extracted dimensions.

3 Results

3.1 Establishment of high-throughput methods for human coronaviruses (hCoVs) detection

3.1.1 Detection of hCoV-NL63 and -229E by plaque assay

In order to study hCoV infection a plaque assay was applied[177–179]. To this end, cells were infected with a 10-fold virus dilution series and overlaid with Avicel containing medium after 2 hours of incubation. After 4 or 5 days, cells were fixed and stained with crystal violet. The virus induced cytopathic effect (CPE) in cell culture manifests plaque formation, which can be used to quantify infectivity. Plaques induced by hCoV-229E were visible after 4 days on Huh-7 cells, or after 5 days in the case of hCoV-NL63 on Caco-2 cells (Figure 5). Resulting plaque forming units (PFU) were assessed by eye (2.6×10^6 PFU/ml for hCoV-229E and 3.1×10^6 PFU/ml for -NL63) and were comparable with the counted plaques from software analysis (1.8×10^6 PFU/ml for hCoV-229E and 4.5×10^6 PFU/ml for -NL63). In addition, the application of the software allowed the calculation of the total plaque area. Thus, the plaque assay can be used for antiviral drug testing as it allows the efficient determination of virus induced plaque numbers and their size. Infection of a monkey cell line, called LLC-MK2, with hCoV-NL63 lead to detachment of cells in presence of the virus and no clear plaque formation (Supplementary Figure 1). The hepatocyte-derived carcinoma Huh-7 cells were described to be permissive for hCoV-OC43, however no plaques were observed in the plaque assay (Figure 5c). Hirose et al. previously reported infection of hCoV-OC43 only induced morphological changes in some cell lines, but no CPE, explaining the result[153,180]. Taken together, the plaque assays can be used as a platform to study infectivity of hCoV-229E and -NL63. However, the assay is not suitable for quantification of hCoV-OC43, can only be used as an end-point analysis, and is in addition inappropriate for large sample quantities.

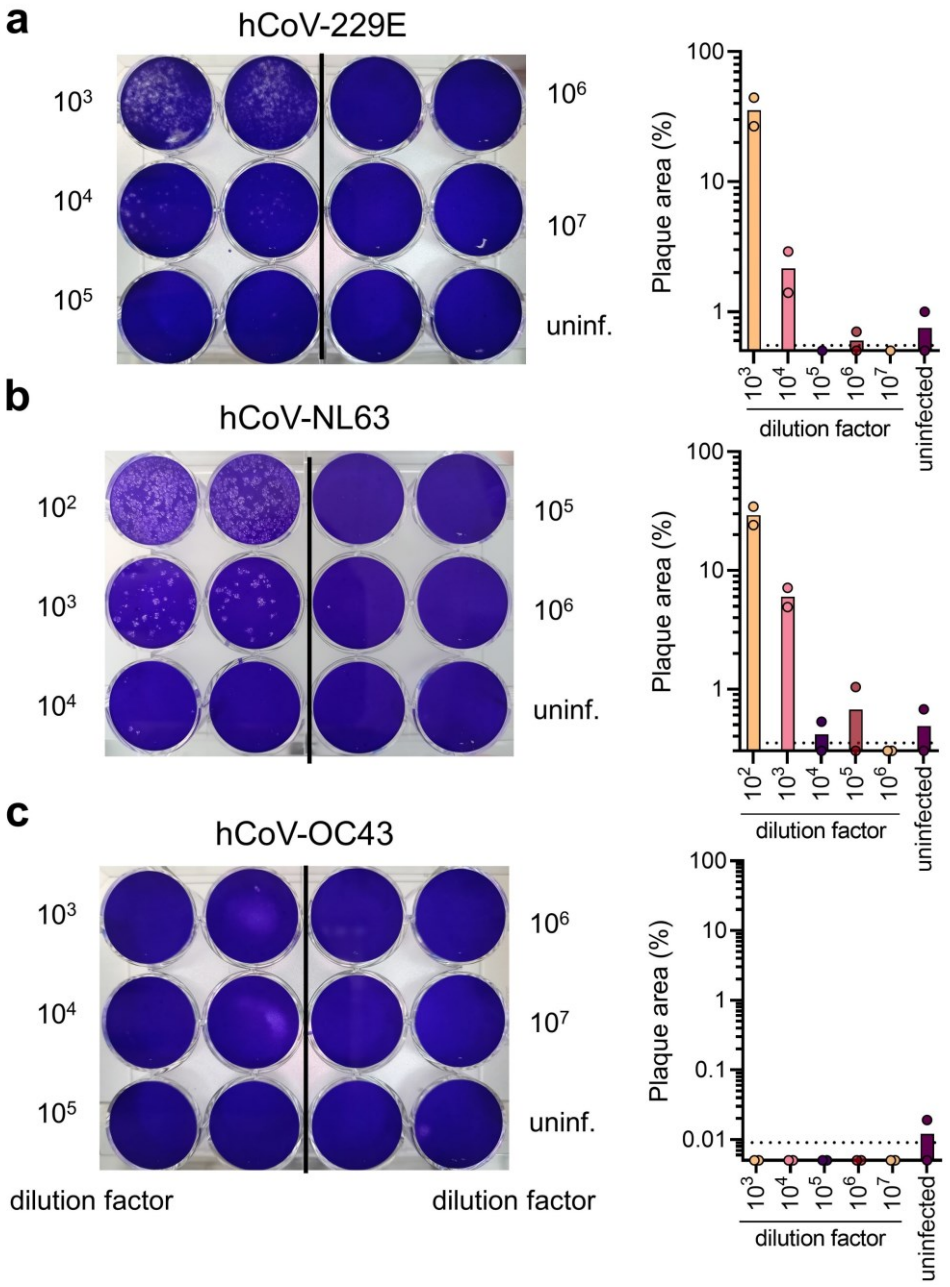

Figure 5. Quantification of hCoV-229E, -NL63 and -OC43 infectiousness by plaque analysis. Serial dilution of each virus was added on respective target cells. After incubation for 2 hours at 33 °C cells were overlaid with cellulose containing medium and incubated until visualization of plaques. After removal of cellulose containing medium and washing, remaining cells were stained with crystal violet. Plaques were quantified with ImageJ. **a)** plaque assay of hCoV-229E was carried out on Huh-7 cells and stained 4 days post infection (dpi). **b)** hCoV-NL63 plaque assay was performed on Caco-2 cells and stained 5 dpi. **c)** plaque assay of hCoV-OC43 was conducted on Huh-7 cells and stained 5 dpi. Shown are means from a single experiment performed in duplicates. Dashed lines indicate limit of detection. Data was generated together with Jan Lawrenz, Institute of Molecular Virology, Ulm University Medical Center. Modified from the master thesis of Jan Lawrenz and from Weil and Lawrenz et al. 2022[166] (CC BY-NC-ND 4.0; https://creativecommons.org/licenses/by-nc-nd/4.0/, Copyright© The Authors, permission to remix and transform was obtained from the creator).

3.1.2 Quantification of hCoV replication via flow cytometry

Sensitive quantification of virus infection on a single cell level and in a high throughput system can be achieved by flow cytometry. Besides detection of viral proteins, expression

levels of cellular factors can also be analyzed with this method. Permissive cell lines used for the plaque assays (Figure 5) were inoculated with an increasing multiplicity of infection (MOI) of hCoV and fixed at indicated days post infection (dpi) to determine the ideal viral inoculum and incubation time. Signals originating from the virus inoculum were excluded by a background control, which was fixed 2 h after infection ensuing the measurement of only newly translated nucleocapsid protein (N-protein). Subsequent antibody targeting of the viral N-protein, followed by addition of a fluorescently labeled secondary antibody, allowed the detection of hCoV infection (Figure6a-c). To maximize signal intensity, varying dilutions of primary and secondary antibodies were employed. The maximum infection rates varied from 62 % for hCoV-NL63 and -OC43 to 97 % for hCoV-229E, and increased with incubation time. Furthermore, the increase in MOI resulted in higher number of infected cells until a saturation was reached. Table 1 shows the assay conditions that were established for flow cytometry analysis of hCoV infection. To validate the integrity of the assay, the small molecule remdesivir, which shows broad antiviral activity against several coronaviruses[154,181,182], was tested in the selected settings. Remdesivir inhibited the three coronaviruses dose-dependently with IC_{50} values of 0.06 µM for hCoV-229E, 0.023 µM for -NL63 and 0.19 µM for - OC43 (Figure 6d), comparable with the literature and demonstrate reliability of the quantification method[154,180,181].

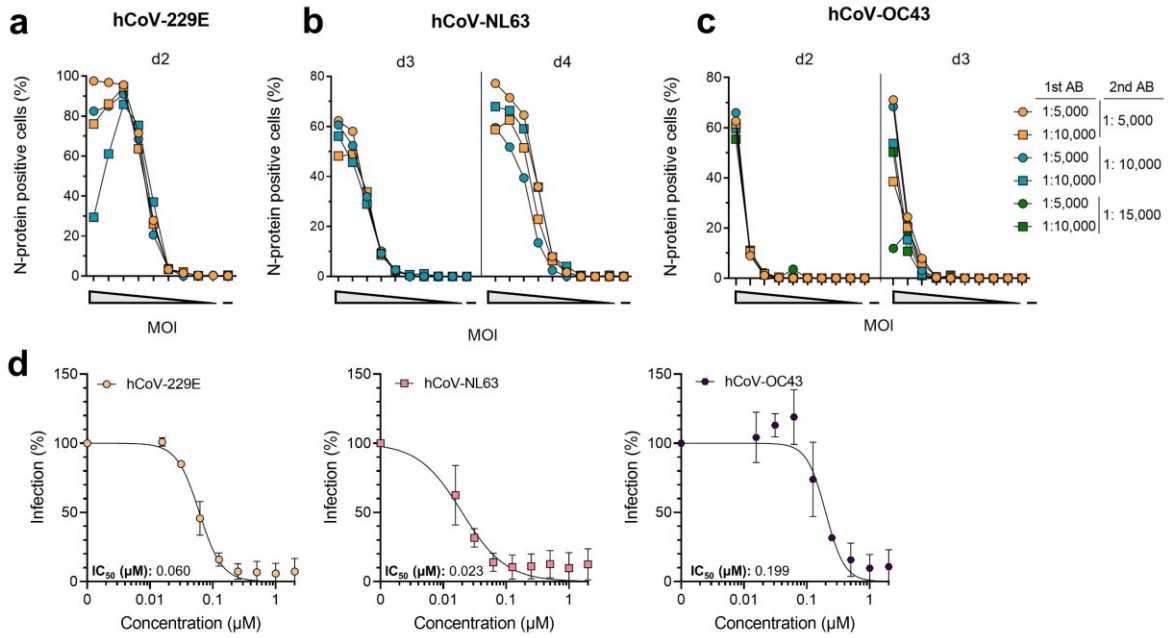

Figure 6. Detection of N-protein expression of hCoVs in target cells via flow cytometry. a) hCoV-229E was titrated 5-fold starting at an multiplicity of infection (MOI) of 0.7 and inoculated onto Huh-7 cells. **b)** hCoV-NL63 with starting MOI of 0.45 was titrated 5-fold and added onto Caco-2 cells. **c)** 5-fold titrated hCoV-OC43 strain with maximum MOI of 0.04 was inoculated onto Huh-7. After 2 h, 2, 3 or 4 dpi cells were fixed and stained by N-protein specific antibody followed by AlexaFluor647 coupled secondary detection

antibody at indicated concentrations. Data are derived from one experiment in pooled duplicates. Signals of input control (fixed 2 hpi) were subtracted. **d)** Respective target cells were treated with serial dilution of remdesivir for 10 min before infection with virus (hCoV-229E MOI 0.028, hCoV-NL63 MOI 0.018 and hCoV-OC43 MOI 0.008). At 2 (hCoV-229E) or 3 (hCoV-NL63, -OC43) dpi, cells were fixed and stained as described in Table 1. Shown are mean values ± SD of two independent experiments performed in triplicates. Data was generated together with Jan Lawrenz, Institute of Molecular Virology, Ulm University Medical Center. Obtained from the master thesis of Jan Lawrenz and from Weil and Lawrenz et al. 2022[166] (CC BY-NC-ND 4.0; https://creativecommons.org/licenses/by-nc-nd/4.0/, Copyright© The Authors, permission to remix and transform was obtained from the creator).

Table 1. Parameters to perform hCoV infection analysis by flow cytometry. Modified from the master thesis of Jan Lawrenz and from Weil and Lawrenz et al. 2022[166] (CC BY-NC-ND 4.0; https://creativecommons.org/licenses/by-nc-nd/4.0/, Copyright© The Authors, permission to remix and transform was obtained from the creator).

Virus	Cell line	dpi	MOI	1st antibody	2nd antibody
hCoV-229E	Huh-7	2	0.028	1:5,000	1:5,000
hCoV-NL63	Caco-2	3	0.018	1:5,000	1:5,000
hCoV-OC43	Huh-7	3	0.008	1:5,000	1:5,000

3.1.3 Establishment of hCoV high-throughput immunodetection assay

A further commonly used method for specific quantification of viral infections in a high throughput manner is immunodetection of a viral protein by an in-cell ELISA[183,184]. To establish the conditions for hCoVs detection in this assay, permissive cell lines previously used for flow cytometry, were infected with escalating concentrations of hCoVs and fixed at indicated days of incubation. The N-protein expression was determined by using an anti-N-protein primary antibody staining followed by an HRP-coupled secondary antibody, at varying concentrations to detect the ideal antibody ratios. To ensure the detection of only newly produced N-protein, the background signals from 2 h post-infection were subtracted. The measured optical density (OD) increased dose-dependently with increasing virus inoculum (Figure 7a-c). At the maximum applied MOIs signal intensities were reduced, as the cells detached due to virus-induced cell death. This was particularly prominent for hCoV-229E and -OC43. The detection of N-protein was possible after two days for all hCoVs, and increased over time even at lower MOI. hCoV-NL63 replication was the slowest, suggesting an analysis is only possible after 6 days of incubation. Selection of 1:5,000 dilution of the primary antibody and high dilution of the HRP-coupled secondary antibody (1:10,000 or 1:15,000) resulted in highest OD. For a more sensitive quantification, an extended serial dilution of hCoV-229E and -OC43 was performed (Figure 7d) and provides together with hCoV-NL63 data (Figure 7c), parameters for quantification of hCoV

infection by in-cell ELISA. The selected parameters for hCoV detection in bulk analysis are stated in Table 2 and result in high signal to noise ratios (6.81 – 22.56) and high ODs after shortest possible incubation time.

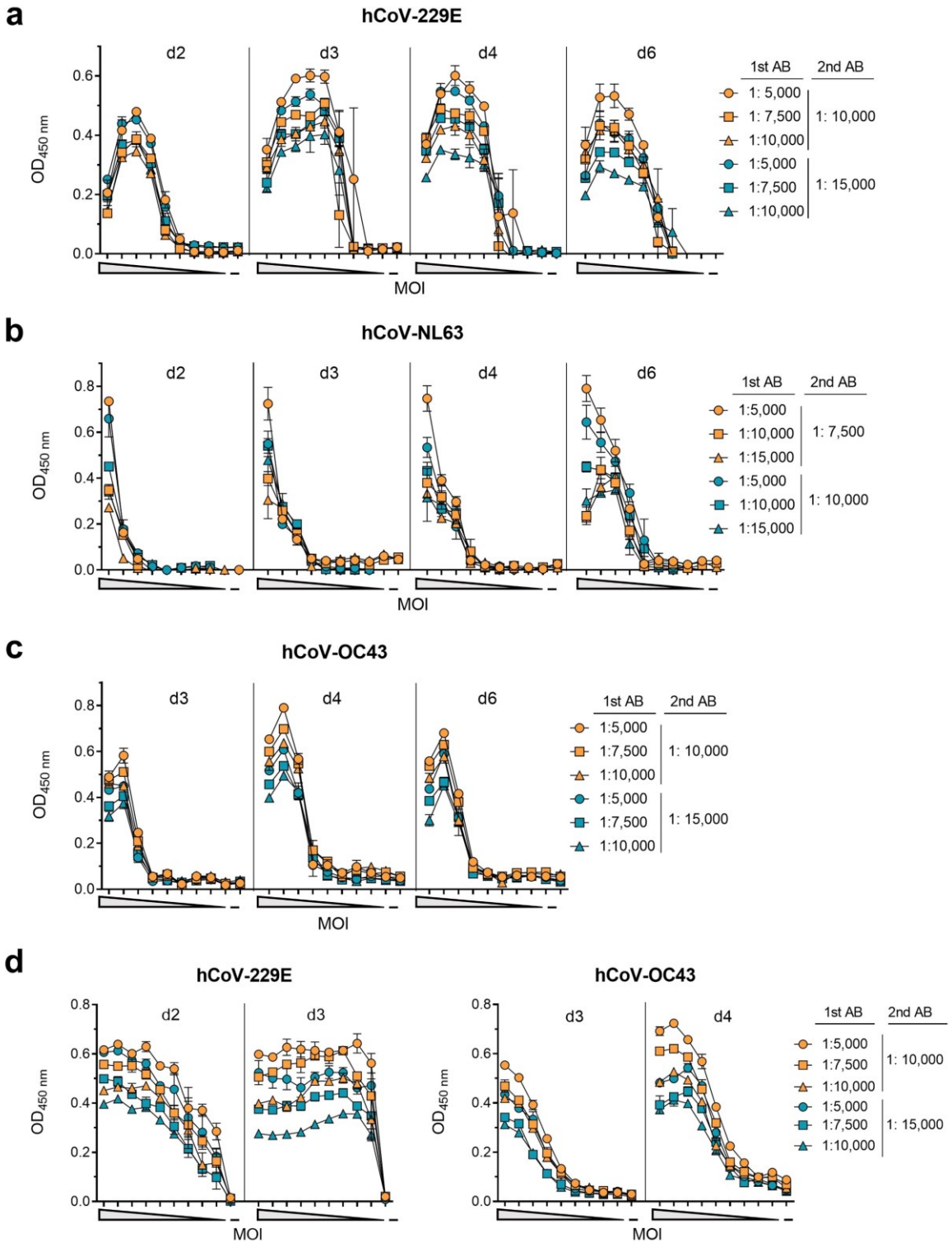

Figure 7. Establishment of an immunodetection assay for detection of hCoV infection. a) 10-fold dilution of hCoV-229E (maximum MOI of 0.44) were added on Huh-7, **b)** hCoV-NL63 (maximum MOI of 1.6) added on Caco-2 and **c)** hCoV-OC43 (maximum of MOI of 0.35) added on Huh-7cells. **d)** 2-fold dilution of hCoV-229E and -OC43 (starting MOI 0.004 or 0.006, respectively) were used for inoculation of Huh-7 cells. At indicated time points, cells were fixed, permeabilized and stained with anti-nucleocapsid antibody and secondly with HPR-coupled detection antibody at stated concentrations. Optical density (OD) was recorded at

450 nm and baseline corrected at 620 nm. Signals of input control (fixed 2 hpi) were subtracted. Data show mean values of one experiment in duplicates ± range. Data was generated together with Jan Lawrenz, Institute of Molecular Virology, Ulm University Medical Center. Obtained from the master thesis of Jan Lawrenz and from Weil and Lawrenz et al. 2022[166] (CC BY-NC-ND 4.0; https://creativecommons.org/licenses/by-nc-nd/4.0/, Copyright© The Authors, permission to remix and transform was obtained from the creator).

Table 2. Parameters to perform hCoV infection analysis with in-cell ELISA. Modified from the master thesis of Jan Lawrenz and from Weil and Lawrenz et al. 2022[166] (CC BY-NC-ND 4.0; https://creativecommons.org/licenses/by-nc-nd/4.0/, Copyright© The Authors, permission to remix and transform was obtained from the creator).

Virus	Cell line	dpi	MOI	1st antibody	2nd antibody	S/N ratio
hCoV-229E	Huh-7	2	0.002	1:5,000	1:15,000	22.56
hCoV-NL63	Caco-2	6	0.01	1:5,000	1:10,000	6.81
hCoV-OC43	Huh-7	3	0.006	1:5,000	1:10,000	21.75

In the next step, a set of cell lines were investigated by the in-cell ELISA to determine whether they support replication of hCoVs. Vero E6, Calu-3, Caco-2 and Huh-7 cells were infected with increasing concentrations of each virus, and the in-cell ELISA was performed according to Table 2. Viral replication of hCoV-229E was only detectable in Huh-7 cells, reaching high signals even at the lowest MOI of 0.000015 (Figure 8a). The in-cell ELISA performed with hCoV-NL63 showed replication of the virus in Caco-2 and Calu-3 cells, with an increase of the signal when proloning incubation times from 4 to 6 dpi (Figure 8b). The signal of hCoV-NL63 on Calu-3 cells was lower compared to Caco-2, indicating poor susceptibility. N-protein signals of hCoV-NL63 detected in Huh-7 cells, did not exceed the background. hCoV-OC43 was able to infect Huh-7 and Vero E6 cells, but not Caco-2 or Calu-3 cells (Figure 8c). These findings are consisitent with the literature[153,177,179,185,186] and demonstrate that the hCoV in-cell ELISA is feasible for studing cell tropism of hCoVs.

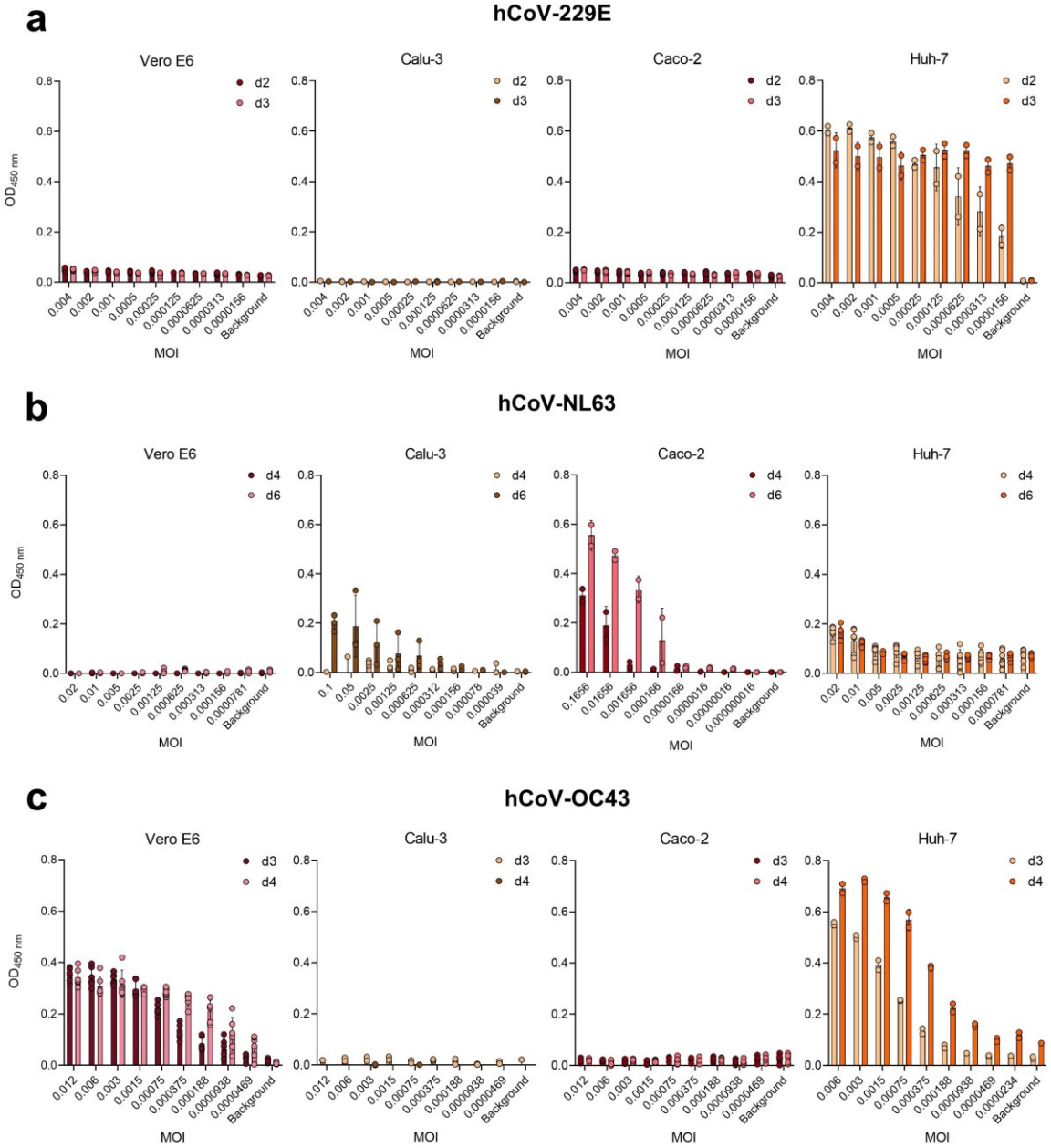

Figure 8. Application of in-cell ELISA to determine cell line susceptibility for hCoVs. Cell lines Vero E6, Calu-3, Caco-2 and Huh-7 were infected with 2-fold serial dilutions of **a)** hCoV-229E, **b)** -NL63 and **c)** -OC43. At indicated timepoints cells were fixed and stained according to Table 2. Signals of input control (fixed 2 hpi) were subtracted. Data show mean values ± SD of one experiment in 2 – 6 replicates. Data was generated together with Jan Lawrenz, Institute of Molecular Virology, Ulm University Medical Center. Obtained from the master thesis of Jan Lawrenz and from Weil and Lawrenz et al. 2022[166] (CC BY-NC-ND 4.0; https://creativecommons.org/licenses/by-nc-nd/4.0/, Copyright© The Authors, permission to remix and transform was obtained from the creator).

3.1.4 Remdesivir, Molnupiravir and Nirmatrelvir function as broad-spectrum anti-coronavirals

During the SARS-CoV-2 pandemic, several antiviral drugs were brought into the spotlight. The compounds remdesivir, molnupiravir and nirmatrelvir target viral enzymes such as the RdRp or the 3C-like protease, while the small molecules camostat mesylate (CM) and E-64d

restrict host proteases important for spike processing. The antiviral activity of remdesivir on hCoVs was previously observed by flow cytometry (Figure 6) and could later be confirmed by in-cell ELISA, yielding similar IC_{50} values (ranging from 0.041 to 0.218 µM) without showing any cytotoxicity (Figure 9a, Supplementary Figure 2). In this analysis, the adenosine analog remdesivir was again 10-fold less effective against hCoV-OC43 compared to -229E and -NL63, although still in the low micromolar range. Another nucleoside analog used in COVID-19 therapy[92,93], molnupiravir, also abrogated viral infection of all hCoVs tested. However, the drug achieved higher IC_{50} values (ranging from 1.62 to 25.40 µM) compared to remdesivir. The 3C-like protease inhibitor nirmatrelvir has been described to inhibit SARS-CoV-2 and hCoV-229E infection and to reduce proteolytic activity of all hCoV proteases, indicating a broad-spectrum activity[96]. By applying the developed immunodetection assay, inhibition of replication efficient hCoV-NL63 and -OC43 by nirmatrelvir was proven with IC_{50} of 4.1 and 0.16 µM, respectively (Figure 9a). The TMPRSS2 inhibitor CM was only able to suppress hCoV-NL63 infection (IC_{50} = 13.21 µM), whereas the cathepsin B/L inhibitor E-64d displayed activity over 0.19 µM (hCoV-229E) and 28.08 µM (hCoV-OC43), and only a slight effect on hCoV-NL63 infection. The virus hCoV-229E was most sensitive to the treatment with E-64d. For E-64d, a slight cytotoxic effect was observed at the highest applied concentration on Huh-7 and Caco-2 cells, which was not observed for CM (Supplementary Figure 2). A further therapeutic approach to treat COVID-19 is the usage of monoclonal antibodies targeting the S-protein of SARS-CoV-2[187]. Testing the antibodies Imdevimab, Bamlanivimab and Casivirimab showed no cross neutralization of hCoV infection (Figure 9b).

In sum, the established methods for hCoV detection support investigation on a bulk or single cell level in a high-throughput manner. The assays are feasible to test the susceptibility of cell lines and can be used for antiviral testing and screening.

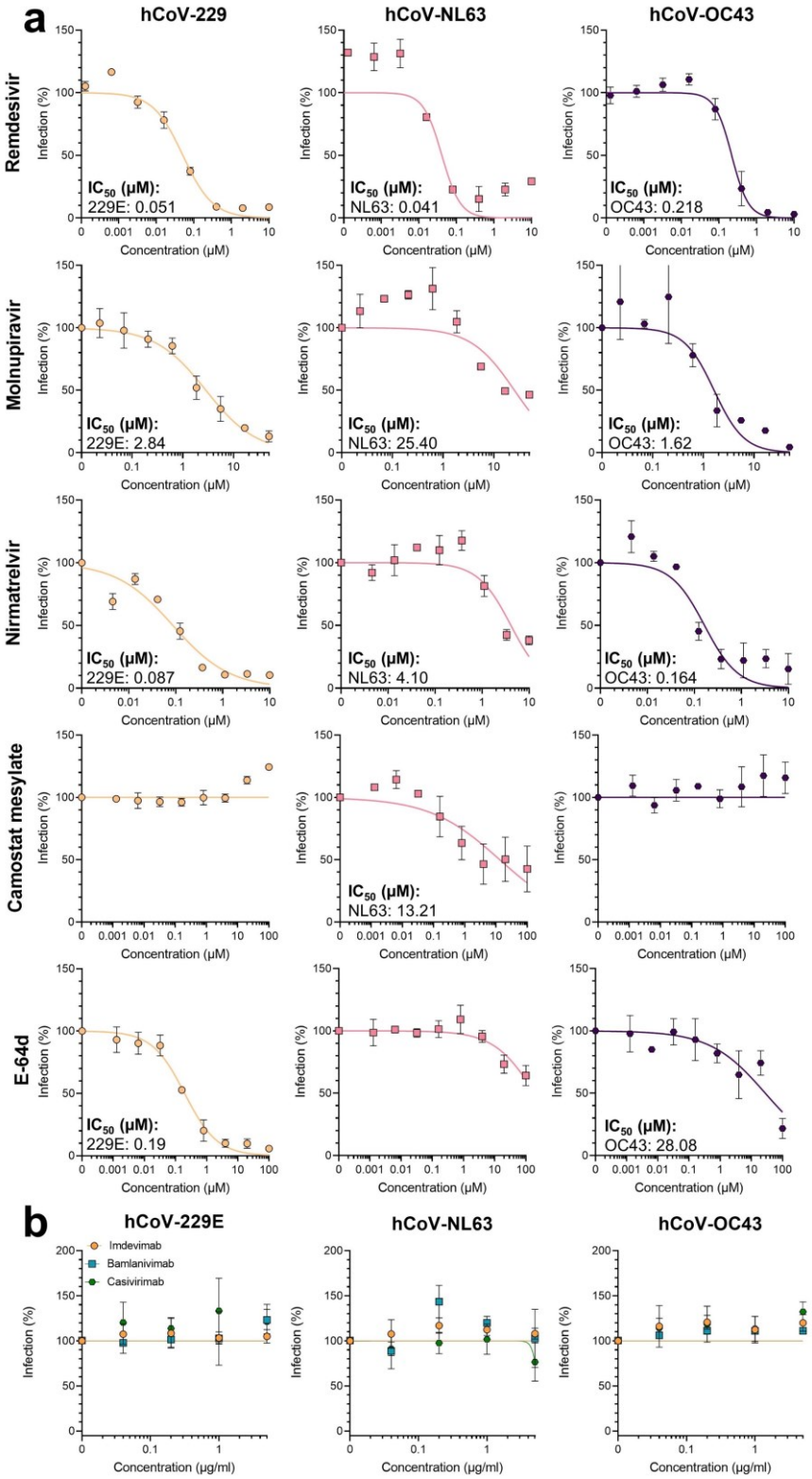

Figure 9. Evaluation of antivirals against hCoVs by in-cell ELISA. a) RNA-dependent RNA polymerase inhibitor remdesivir and molnupiravir, 3C-like protease inhibitor nirmatrelvir, small molecule TMPRSS2 inhibitor camostat mesylate and small molecule cathepsin inhibitor E-64d were titrated and added to target cells before infection with hCoVs. **b)** Monoclonal antibodies were mixed with respective virus and incubated for 30 min at 33 °C before addition on cells. Experiments were carried out according to Table 2. Graphs represent mean ± SD or SEM of one (for b), two or three independent experiments performed in triplicates. Data was generated together with Jan Lawrenz, Institute of Molecular Virology, Ulm University Medical Center. Modified from the master thesis of Jan Lawrenz and from Weil and Lawrenz et al. 2022[166] (CC BY-NC-ND 4.0; https://creativecommons.org/licenses/by-nc-nd/4.0/, Copyright© The Authors, permission to remix and transform was obtained from the creator).

3.2 Advanced molecular tweezers with lipid anchor as broad-spectrum antivirals

3.2.1 Molecular tweezers CLR01 and CLR05 inhibit coronavirus infection

With the emergence of SARS-CoV-2, broad-spectrum antivirals such as the molecular tweezers gained more attention since they might be fast and easily repurposed for COVID-19 treatment[155]. To verify the antiviral activity of tweezers against SARS-CoV-2, replication deficient pseudoparticles harboring the structural SARS-CoV-2 S-protein were used. With this system, the SARS-CoV-2 entry can be measured and direct acting inhibitors analyzed. To test the antiviral activity of molecular tweezers, pseudoparticles were mixed with tweezers and then added to cells. CLR01 and CLR05, but not the truncated tweezer CLR03, inhibited the entry of lentiviral SARS-CoV-2 pseudoparticles without being cytotoxic to Caco-2 cells at the applied concentrations (Figure 10a, b). IC_{50} values reached the micro molar range, with 35.5 µM and 33 µM for CLR01 and CLR05, respectively. Time dependent experiments demonstrated a decrease in transduction rates when increasing the incubation period of CLR01 with the pseudoparticles (Figure 10c). As indicated before, tweezers abrogated viral infection by direct disruption of the viral membrane (1.4.2). To investigate tweezer activity mechanistically a liposome dye leakage was performed. The assay is based on liposomes filled with a reporter dye that becomes fluorescent upon liposomes disruption (for detailed description see 3.2.5). In agreement with the proposed mechanism, the molecular tweezer CLR01 destroyed synthetic liposomes, which resemble the viral membrane dose-dependently (Figure 10d). Thereby, increasing the number of liposomes required a higher concentration of CLR01 for complete disruption, which is also observed when increasing the amount of lentiviral SARS-CoV-2 pseudoparticle (Figure 10e).

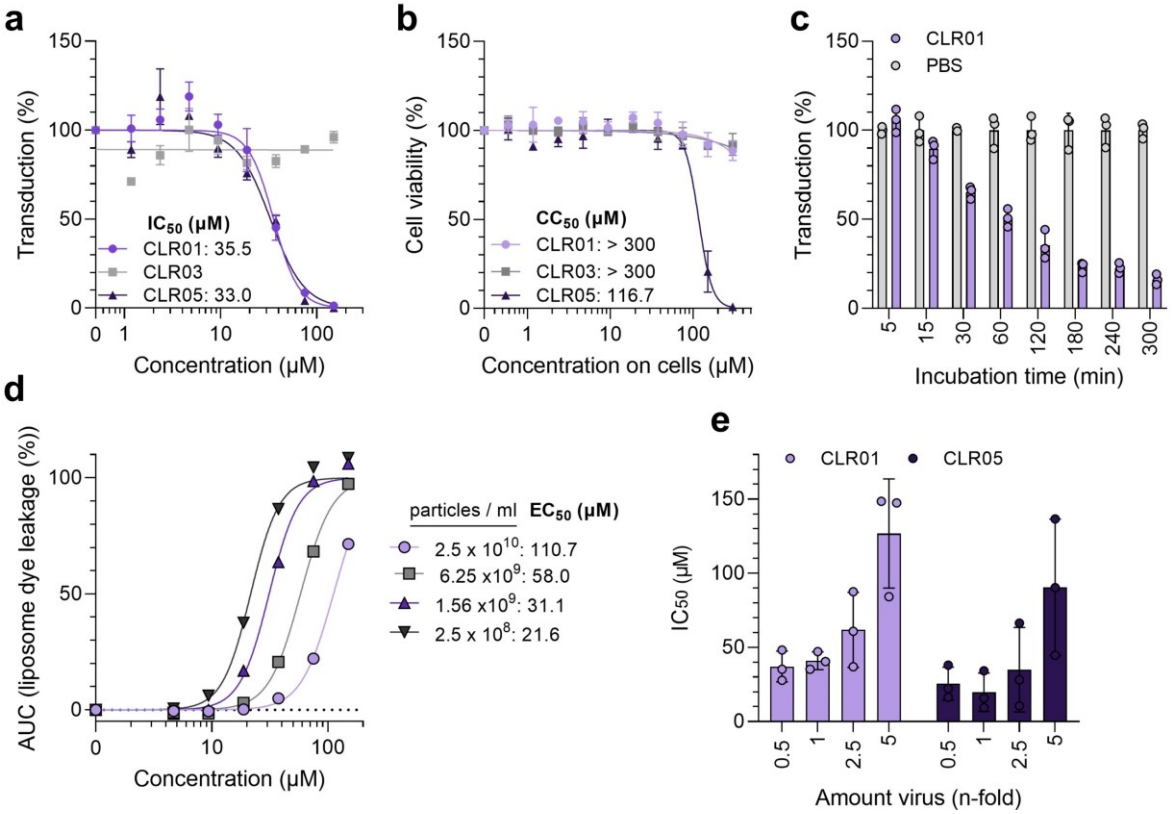

Figure 10. Molecular tweezers CLR01 and CLR05 inhibit lentiviral SARS-CoV-2 spike mediated entry. **a)** Serial dilutions of tweezers were mixed with lentiviral pseudoparticles carrying the S-protein of SARS-CoV-2 Wuhan/Hu-1 and used for inoculation of Caco-2 after 30 min incubation at 37 °C. Graph represents mean values ± SEM of three independent experiments performed in triplicates. **b)** Cytotoxicity of tweezers on Caco-2 cells was assessed by measuring of ATP level in CellTiterGlo Luminescent cell viability assay. Therefore, tweezers were added on cells at indicated concentrations for 2 days. Shown are mean values ± SD of three experiments each performed in duplicates. **c)** CLR01 (100 µM) or PBS was mixed with lentiviral pseudoparticles carrying S-protein of SARS-CoV-2 Wuhan/Hu-1 for indicated time prior to stopping the reaction by addition of 20 % FCS. Afterwards, Caco-2 cells were transduced with the mix. Shown are mean values ± SD from one experiment conducted in triplicates. **d)** Listed amounts of 200 nm sized virus-like liposomes (1,2-dioleoyl-sn-glycero-3-phosphocholine (DOPC)/ sphingomyelin (SM)/ cholesterol (Chol); (45/25/30 mol%)) filled with 50 mM carboxyfluorescein were incubated with escalating concentrations of CLR01 for 30 min after measuring baseline fluoresce for 5 min. Dye leakage was recorded by measuring fluorescence every minute at 485 nm excitation and 528 nm emission. To ensure complete leakage, 1 % Triton X-100 was added and fluorescence was recorded as described for 5 min. Shown values were corrected for baseline, normalized to maximum fluorescence and area under the curve was calculated. Experiment was performed once in triplicates. **e)** Dilutions of lentiviral pseudoparticles carrying S-protein of SARS-CoV-2 Wuhan/Hu-1 were mixed with serial dilution of tweezers for 30 min at 37 °C before transduction of Caco-2 cells. Shown are calculated IC_{50} values ± SD of three experiments each performed in triplicates. For a, c and e, cells were washed once 4 h after transduction and fresh medium was added. Entry rates were assessed 2 days post transduction (dpt) by measuring luciferase activity in cells lysates. Modified from Weil et al. 2022[159] (CC BY-NC-ND 4.0; https://creativecommons.org/licenses/by-nc-nd/4.0/, Copyright© The Authors; permission to remix and transform was obtained from the creator) and Weil, Groß, Röcker and Bravo-Rodriguez et al. 2020[147] (permission was obtained from the publisher, Copyright© 2020 American Chemical Society, https://pubs.acs.org/doi/10.1021/jacs.0c06400; permissions related to the material excerpted should be directed to the ACS; This is an unofficial adaptation of an article that appeared in an ACS publication. ACS has not endorsed the content of this adaptation or the context of its use).

After the antiviral activity of tweezers on SARS-CoV-2 pseudoparticles was shown, the ability to inhibit replication competent SARS-CoV-2 was studied. Treatment of virus particles with CLR01, negative control CLR03, or CLR05 and subsequent infection of

Caco-2 cells confirmed the tweezers activity, reaching IC_{50} values of 76.7 µM for CLR01 and 167.3 µM for CLR05 (Figure 11a). Visualization of the membrane disruption by the tweezer was analyzed by transmission electron microscopy (TEM). Of note, the high numbers of viral particles required for TEM analysis also raise the need for increased concentration of tweezers, compared to cell culture experiments. SARS-CoV-2 virions treated with PBS or CLR03 exhibited the reported spherical structure with spike peplomers, surrounding the membrane (Figure 11b)[188]. On the other hand, virus particles incubated with CLR01 or CLR05 showed notches, deformations, and sometimes the presence of uranyl acetate dye inside of the virus, indicating membrane rupture (Figure 11b, c).

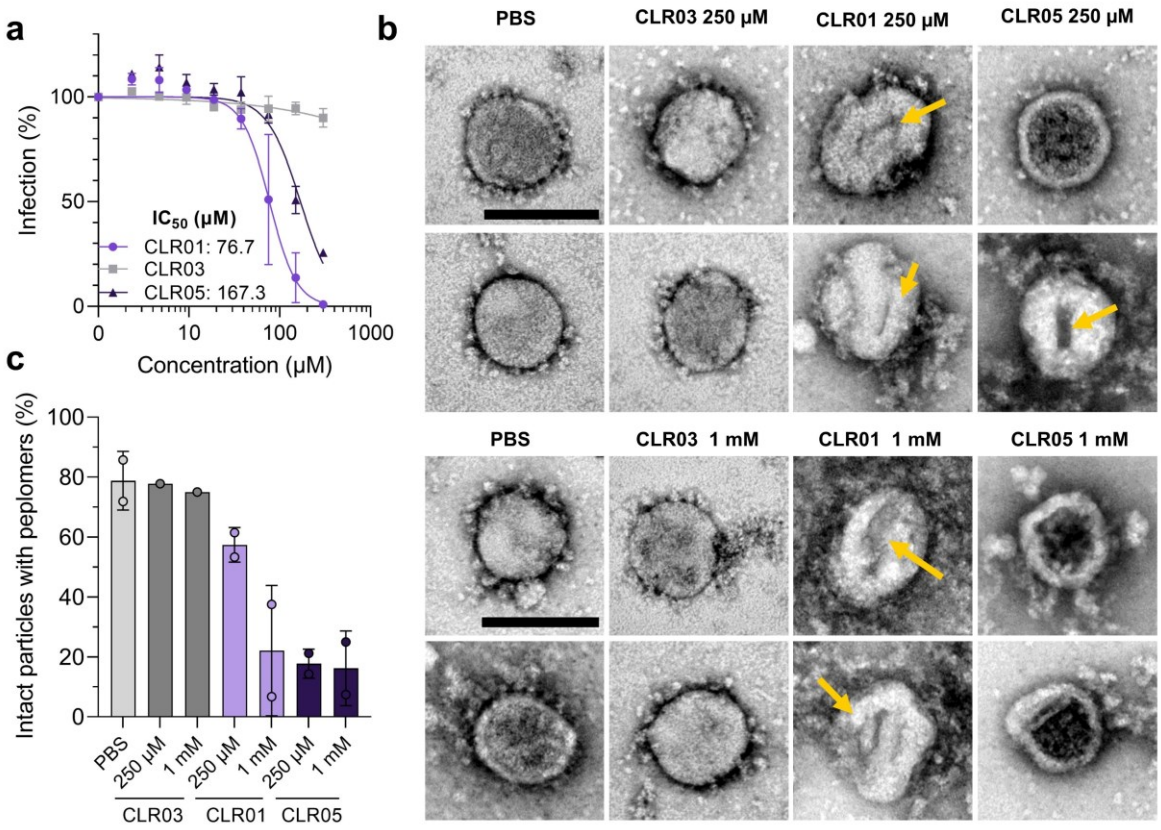

Figure 11. Tweezer disrupt replication competent SARS-CoV-2. a) Serial dilutions of molecular tweezers were mixed with SARS-CoV-2 Wuhan/Hu-1 isolate for 2 h at 37 °C (MOI 0.01) and mixtures were used to infect Caco-2 cells. Infection rates were assessed by in-cell ELISA measuring S-protein. Graphs represent mean values ± SEM of two independent experiments performed in triplicates. **b)** Tweezers at indicated concentrations or PBS were mixed with serum-free SARS-CoV-2 Wuhan/Hu-1 isolate (1.2 x 10^6 PFU/ml), incubated for 30 min at 37 °C and fixed. Virions were stained with uranyl acetate and visualized by TEM. Scale bar indicates 100 nm and yellow arrows notches in the viral envelope induced by tweezer treatment. **c)** Quantification of intact virions with peplomers from b). Shown are mean values ± SD of two independent experiments (for CLR03 one) with at least 35 virions analyzed of each sample. Experiments were conducted by Janis Müller and Carina Conzelmann, Institute of Molecular Virology, Ulm University Medical Center and Clarissa Read with Tim Bergner, Central facility of Electron Microscopy, Ulm University. Modified from Weil et al. 2022[159] (CC BY-NC-ND 4.0; https://creativecommons.org/licenses/by-nc-nd/4.0/, Copyright© The Authors, permission to remix and transform was obtained from the creator).

By taking advantage of the newly established hCoV in-cell ELISA, tweezers were tested against common cold coronaviruses of the alpha and beta genera. As observed for SARS-CoV-2, CLR01 and CLR05 suppressed the infection upon direct viral treatment of hCoVs (Figure 12a-c). Curiously, the treatment of hCoV-NL63 with low concentrations of CLR01 seems to enhance the infection maybe due to increased fusogenicity of membrane, and only the highest applied concentrations achieved complete inhibition. The IC_{50} values were in the middle to high micromolar range, similar to those against SARS-CoV-2 (Figure 12d).

In sum, molecular tweezers CLR01 and CLR05 inhibit infection of members from the *Coronaviridae* with IC_{50} values in the middle to high micromolar range, leaving room for further improvement.

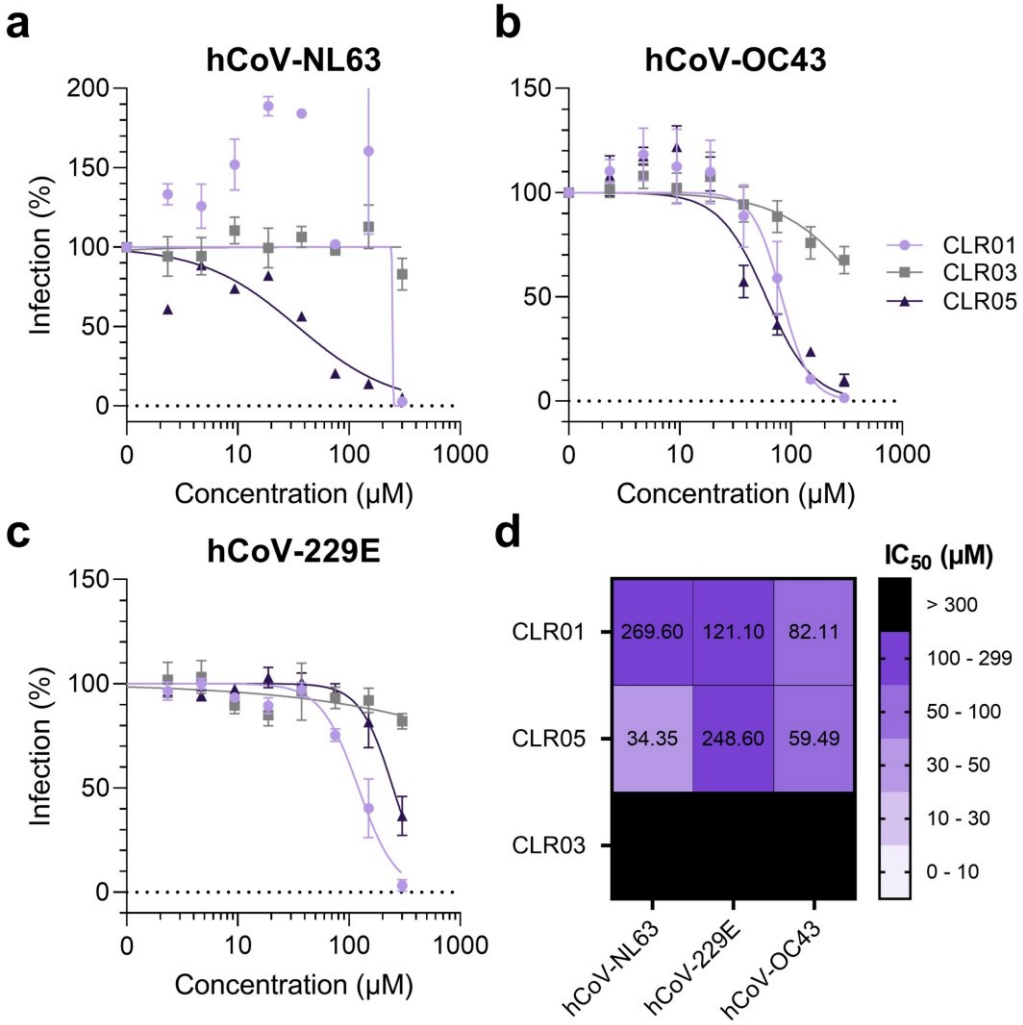

Figure 12. Ancestral tweezers CLR01 and CLR05 suppress hCoV infection. Escalating concentrations of tweezers were incubated with **a)** hCoV-NL63 (MOI 0.01), **b)** hCoV-OC43 (MOI 0.006) or **c)** hCoV-229E (MOI 0.002) for 30 min at 33 °C before inoculation onto Caco-2 (hCoV-NL63) or Huh-7 cells (hCoV-OC43 and -229E). Infection rate was measure by in-cell ELISA analyzing N protein expression 2 (-229E), 3 (-OC43) or 6 (-NL63) dpi. Shown are mean values ± SEM of three independent experiments conducted in triplicates. **d)** IC_{50} values derived from a) to c). Data was generated together with Jan Lawrenz (Master thesis), Institute of Molecular Virology, Ulm University Medical Center.

3.2.2 Introduction of alkyl and aromatic moieties to CLR01 enhance antiviral activity against SARS-CoV-2

Having demonstrated the activity of tweezers to abrogate infection of CoVs with relatively high IC_{50} values, further improvement of tweezers is warranted. To accomplish this task, a set of aliphatic and aromatic side chains mimicking lipid components were introduced onto both phosphate groups of CLR01 by the team of Prof. Dr. Thomas Schrader at the University of Essen-Duisburg (Figure 13). As rationale, hydrophobic moieties might be inserted into the viral membrane and further enhance viral envelope destabilization. CLR01 was selected since it shows improved activity in comparison to CLR05 and no cytotoxicity at the tested concentrations (Figure 10b, Figure 11a). The coupling of side chains was achieved by phosphate activation with pyridine and trichloroacetonitrile (TCA) of CLR01 in its diphosphoric acid form, followed by addition of the alcoholic side chain and neutralization with NaOH (Figure 13a). A selection of 34 moieties ranging from C1 to C18 alkyl chains with branched or linear orientation were attached (Figure 13b). To increase the rigidity, alkene or alkyne moieties were introduced and in addition aromatic units, which harbor a flat and rigid π-system. Furthermore, tweezers with charged side arms were generated in order to facilitate interactions with choline or phosphate head groups of lipids.

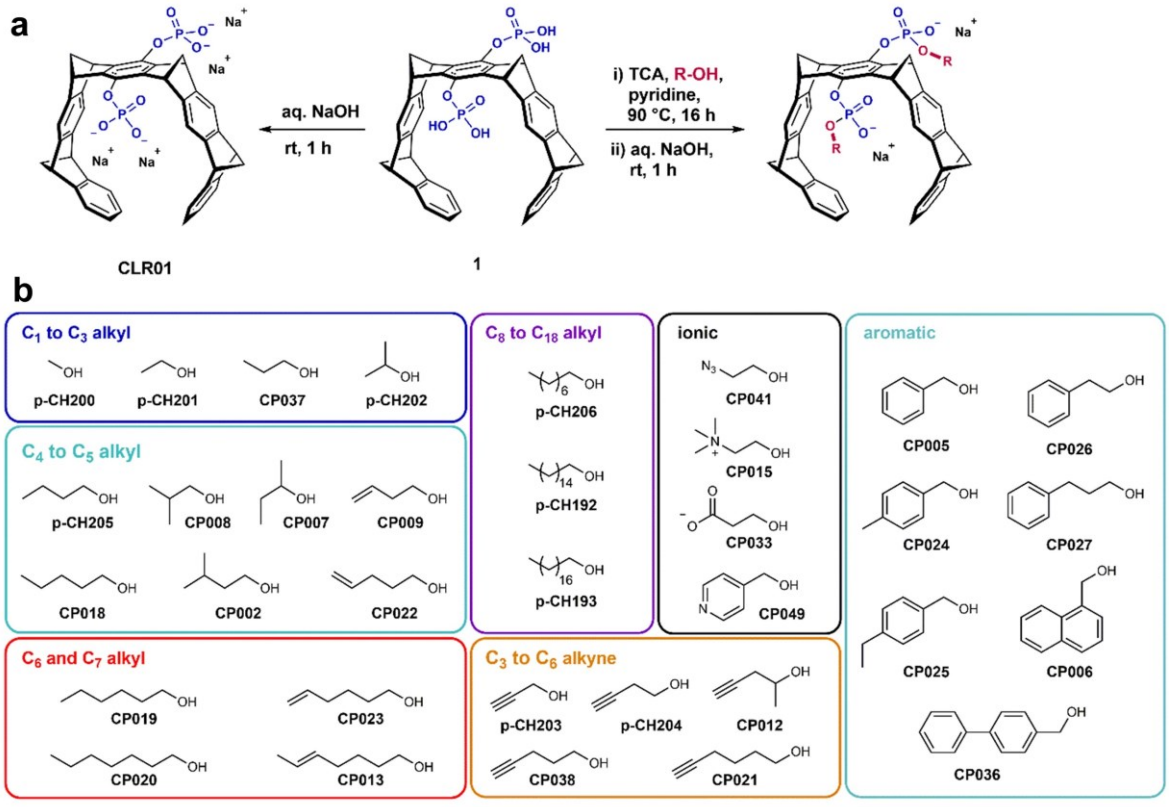

Figure 13. Generation of advanced tweezers harboring side arms. a) Conversion of the free diphosphoric acid "1" either to CLR01 or to dialkyl diphosphate tweezers by TCA- mediated esterification and neutralization. **b)** Overview of alkyl or aromatic alcohols coupled to CLR01. Schematic reaction (a) was

illustrated by Thomas Schrader (Faculty of Chemistry, University of Duisburg-Essen). Categorized according to the chemical properties. Obtained from Weil et al. 2022[159] (CC BY-NC-ND 4.0; https://creativecommons.org/licenses/by-nc-nd/4.0/, Copyright© The Authors, permission to remix and transform was obtained from the creator).

The activity of the new tweezer panel was investigated using the lentiviral SARS-CoV-2 pseudoparticle system. Subsequently, new tweezers were mixed with pseudoparticles before transduction of Caco-2 cells. Screening of the advanced tweezers revealed increased antiviral activity of nearly all second-generation tweezers, in comparison to CLR01 (IC_{50} = 35.5 µM) (Figure 14a). The most active tweezers belong to the C6/C7 alkyl and aromatic groups with IC_{50} ranging from 1.0 to 16.8 µM, with the C7 alkyl tweezer CP020 being as the most potent derivative. The antiviral activity of tweezers increases in dependency of the alkyl arm length meaning with every elongation step of the alkyl arm IC_{50} values decreases, and peaks with the C7 alkyl tweezer. The C8 alkyl arms (p-CH206) or longer alkyl chains (C16 = p-CH192 and C18 = p-CH193) only slightly improved the tweezer activity (IC_{50} from 14.9 to 40.6 µM). Tweezers with ionic arms inhibited transduction similar to CLR01, while CP015 equipped with a choline group was not antivirally active. In parallel, the cytotoxic effect of advanced tweezers was observed and CC_{50} values were calculated (Supplementary Figure 3, Figure 14b). Most tweezers showed no toxic effect or only at the highest concentration equivalent to 300 µM on cells. The aromatic tweezer group also impacted the cell viability at lower concentrations. Nevertheless, the resulting selectivity indices (SI) of second-generation tweezers ranged from 5.2 (CP008) to 213 (CP020) indicating a wide therapeutic window for therapeutic application.

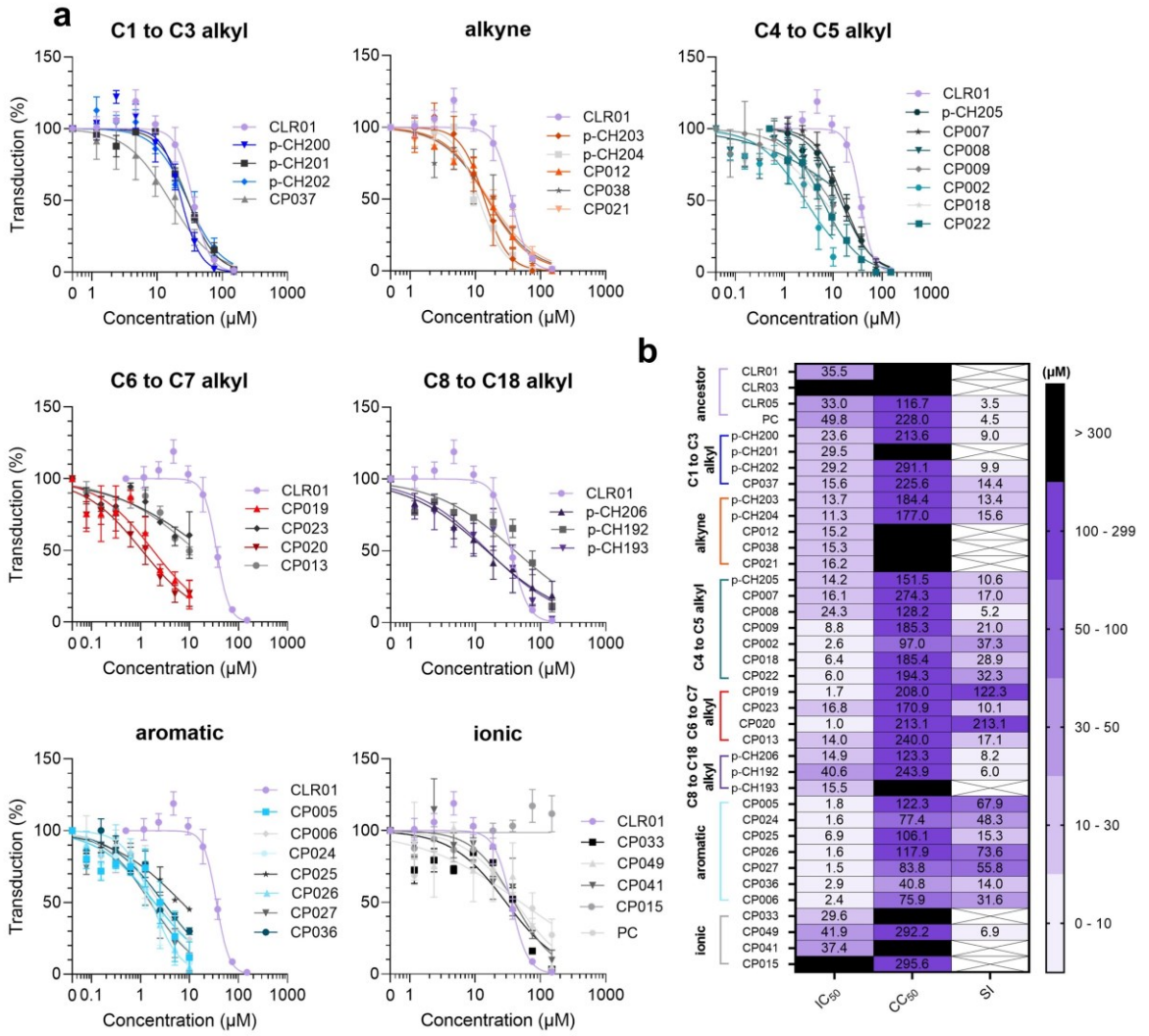

Figure 14. Introduction of side arms reduce lentiviral SARS-CoV-2pp mediated entry. a) Lentiviral pseudoparticles carrying the S-protein of SARS-CoV-2 Wuhan/Hu-1 were mixed with indicated concentrations of tweezers and used for inoculation of Caco-2 cells after 30 min incubation at 37 °C. Cells were washed once 4 h after transduction and fresh medium was added. Transduction rates were assessed 2 dpt by measuring luciferase activity in cells lysates. Graph represents mean values ± SEM of three independent experiments performed in triplicates. **b)** IC_{50} and CC_{50} values were derived from a), Figure 10 and Supplementary Figure 3, and plotted in regard to the chemical category of the tweezers. The selectivity index (SI) is defined as the quotient of CC_{50} and IC_{50}. Modified from Weil et al. 2022[159] (CC BY-NC-ND 4.0; https://creativecommons.org/licenses/by-nc-nd/4.0/, Copyright© The Authors, permission to remix and transform was obtained from the creator).

Plotting the generated CC_{50} against IC_{50} values demonstrated a structure-activity relationship of tweezers in dependency of their attached side arms (Figure 15). Antiviral activity of C1 to C3 alkyl (blue), C4 and C5 alkyl (green) and C6 and C7 alkyl (red) tweezer groups increases in comparison to ancestor tweezers CLR01 and CLR05, and also with concomitant increase in their alkyl arm length. However, elongation of the alkyl arms also slightly enhances the cytotoxicity. Alkyne tweezers (orange) showed a reduced cytotoxicity but similar or lower activity against lentiviral SARS-CoV-2 pseudoparticles than their alkyl

counterparts (CP037, p-CH205, CP018 and CP019). The C6 and C7 alkyl tweezers CP019 and CP020 achieve high antiviral activity with only slight impairment on the cell viability, as demonstrated by their high SI. The second promising group, the aromatic tweezers, show even more potent inhibition of pseudoparticle entry, but at the expense of cell damage.

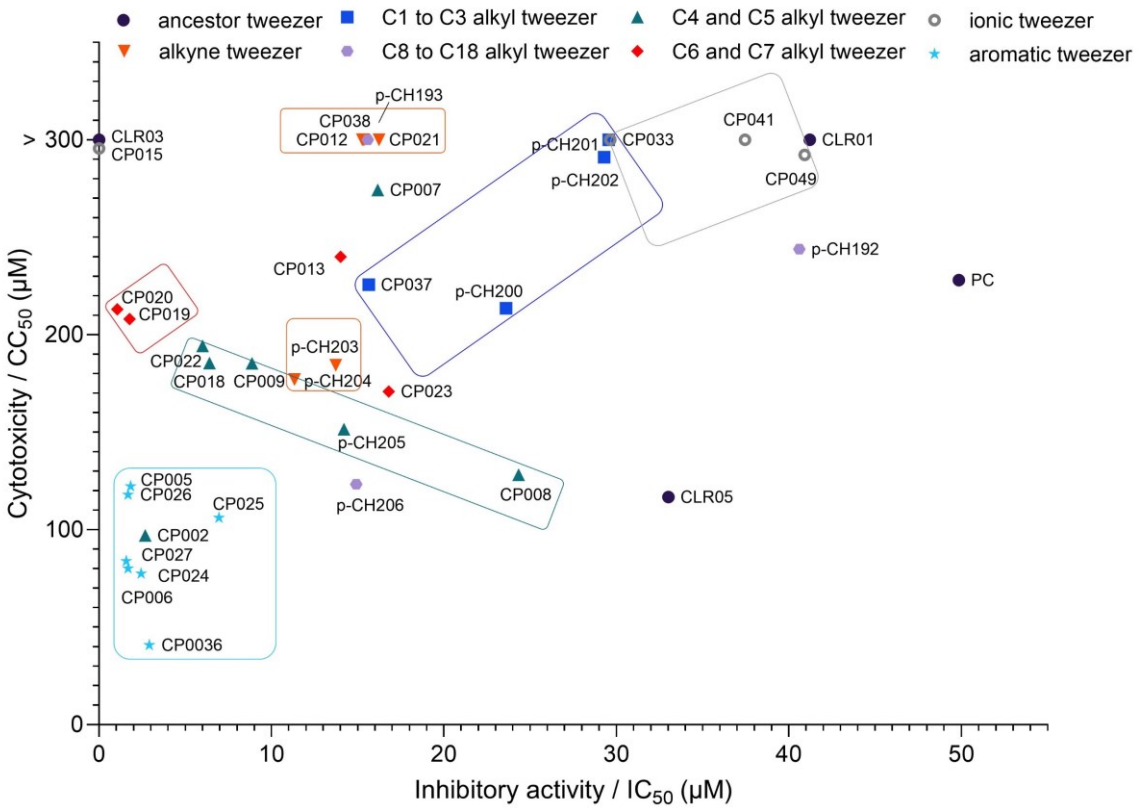

Figure 15. Relation of antiviral activity and cytotoxicity of molecular tweezers. IC_{50} and CC_{50} values of each tweezer derived from Figure 10 and Figure 14 are plotted. Clusters of tweezers with chemically similar side arms are marked. Modified from Weil et al. 2022[159] (CC BY-NC-ND 4.0; https://creativecommons.org/licenses/by-nc-nd/4.0/, Copyright© The Authors, permission to remix and transform was obtained from the creator).

The most promising candidates evaluated in the lentiviral SARS-CoV-2 pseudoparticle screen were tested against authentic SARS-CoV-2 infection on Caco-2 cells using an in-cell ELISA (Figure 16a-c). The branched C4 alkyl tweezer CP002 and the alkene C5 alkyl tweezer CP022 inhibited SARS-CoV-2 more efficiently then CLR01, with an IC_{50} of 8.2, 19.9 and 26.5 µM, respectively. In comparison to pseudoparticles experiments, alkyne tweezers (CP012, CP021 and CP038) did not reach higher activity as ancestor tweezer CLR01. However, C6/C7 alkyl and aromatic tweezers were still the most potent tweezer groups with IC_{50}s from 0.2 to 8.5 µM. In this context, the SI was further increased and reached values up to 532 for CP020. Visualization of membrane disruption by advanced tweezer on SARS-CoV-2 virions was performed by TEM analysis. The treatment with CLR01 and two representatives of the most potent aromatic and C6/C7 alkyl tweezers groups

demonstrated morphological deformation of SARS-CoV-2 virions and the appearance of an electron-dense center, caused by uranyl acetate stain penetration through the damaged lipid bilayer (Figure 16d). Furthermore, the number of destroyed virus particles was increased upon incubation with advanced tweezers CP019, CP020, CP024 and CP025 (Figure 16e). With the emergence of the SARS-CoV-2 variants of concerns (VOCs) and changes in the viral properties such as immune escape and faster replication, the activity of tweezers had to be re-evaluated. Treatment of the ancestral SARS-CoV-2 Wuhan/Hu-1 strain and VOCs alpha, beta or delta with tweezers confirmed lasting antiviral activity of advanced tweezers and suggests that upcoming strains of SARS-CoV-2 are not resistant against molecular tweezers (Figure 16f).

In sum, structure activity relationship study revealed C6/C7 alkyl and aromatic tweezers as promising groups with increased SI. Selected advanced tweezers demonstrated high efficiency in SARS-CoV-2 inhibition considering these candidates for *in vivo* evaluation.

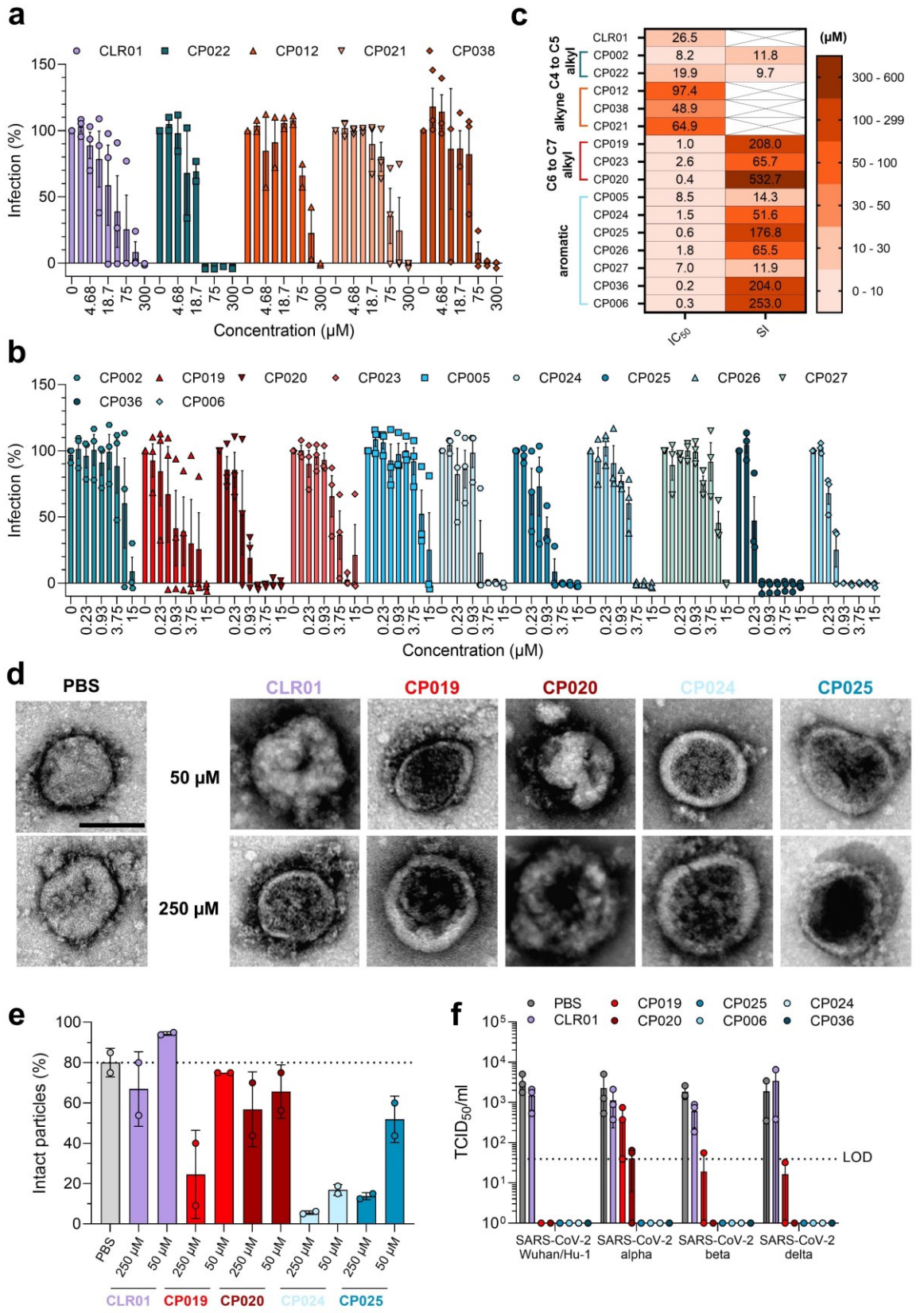

Figure 16. Advanced tweezers inhibit SARS-CoV-2 infection. a), b) SARS-CoV-2 Wuhan/Hu-1 isolate (MOI 0.0007) was mixed with a serial dilution of selected tweezers for 2 h at 37 °C and used to infect Caco-2 cells. Infection rates were assessed by in-cell ELISA measuring N-protein. Graphs represent mean values ± SEM of two or three independent experiments performed in triplicates. **c)** IC_{50} values derived from a) and b) are plotted and ordered according to the side arm category of tweezers. The selectivity index (SI) is defined as the quotient of CC_{50} and IC_{50}. (CC_{50} values are listed in Figure 14). **d)** Tweezers at indicated concentrations or

PBS were mixed with serum-free SARS-CoV-2 Wuhan/Hu-1 isolate (1.2 x 10^6 PFU/ml), incubated for 30 min at 37 °C and fixed. Virions were stained with uranyl acetate and visualized by TEM. Scale bar indicates 100 nm. **e)** Quantification analysis of d) Shown are mean values ± SD of two independent experiments with at least 31 virions analyzed of each sample. **f)** SARS-CoV-2 isolates alpha (B.1.1.7), beta (B.1.351), delta (B.1.617.2) and Wuhan/Hu-1 were mixed with tweezers (50 µM) and incubated for 2 h at 37 °C. Compound-virus mix was titrated 2-fold and used for infection of Vero E6 cells. Cytopathic effect was determined 5 – 7 dpi and $TCID_{50}$ calculated according to Reed and Muench[167]. LOD: Limit of detection of $TCID_{50}$ analysis. Shown are mean values ± SD of two (delta) or three independent experiments. Data were generated with the help of Carina Conzelmann, Institute of Molecular Virology, Ulm University Medical Center and TEM analysis was conducted by Clarissa Read with Tim Bergner, Central facility of Electron Microscopy, Ulm University. Modified from Weil et al. 2022[159] (CC BY-NC-ND 4.0; https://creativecommons.org/licenses/by-nc-nd/4.0/, Copyright© The Authors, permission to remix and transform was obtained from the creator).

3.2.3 Tweezers are active and stable in mucus from primary airway cells

Serum interferes with the activity of CLR01 as mentioned previously (1.5). To determine whether this loss of function also applies to advanced tweezers, the ancestral tweezer CLR01, the C6 alkyl tweezer CP019 and the aromatic tweezers CP006 and CP025 were incubated with 40 % serum or PBS and the membranolytic activity was recorded in a liposome dye leakage assay (Supplementary Figure 4). For all tested tweezers, disruption of liposomes was abolished when serum was present. For prevention or treatment of respiratory viruses, tweezers might also be applied topically on mucosal tissues. To test this, SARS-CoV-2 pseudoparticles were spiked into mucus derived from cultures of differentiated primary airway epithelial cells mimicking the conditions of the airways and contained a total protein concentration of around 165 µg/ml (Supplementary Figure 5). Addition of tweezers CLR01 or C6/C7 alkyl tweezers CP019 and CP020 to pseudoparticles with subsequent transduction of Caco-2 cells showed no impairment of the tweezer activity even up to 45 % mucus (Figure 17).

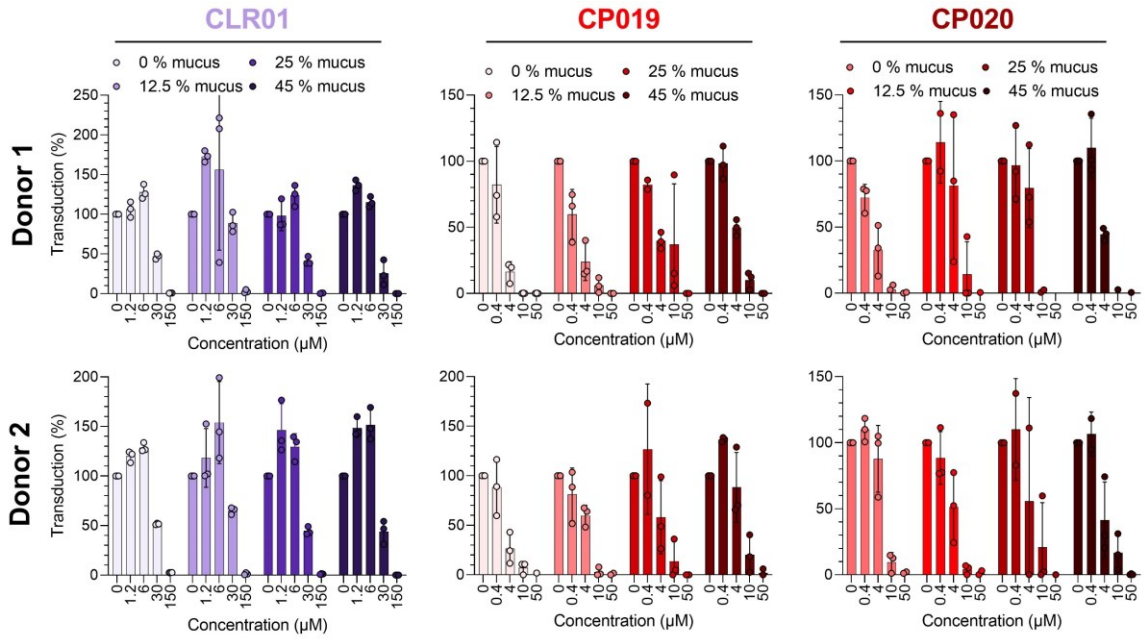

Figure 17. Mucus secreted by primary human airway epithelial cells (HAEC) does not impair antiviral activity of tweezers. Lentiviral pseudoparticles carrying the S-protein of SARS-CoV-2 Wuhan/Hu-1 were mixed with mucus derived from HAEC cultures and incubated for 10 min. Tweezers were added at indicated concentrations and incubated for 30 min at 37 °C, with subsequent transduction of Caco-2 cells. Cells were washed once 4 h after transduction and fresh medium was added. Transduction rates were assessed 2 dpt by measuring luciferase activity in cells lysates. Graph represents mean values ± SD of one experiment performed in triplicates. Modified from Weil et al. 2022[159] (CC BY-NC-ND 4.0; https://creativecommons.org/licenses/by-nc-nd/4.0/, Copyright© The Authors, permission to remix and transform was obtained from the creator).

3.2.4 Advanced tweezers abrogate SARS-CoV-2 infection *in vivo*

Finally, advanced tweezers were investigated against SARS-CoV-2 infection in an *in vivo* experiment with transgenic K18-hACE2 mice by the team of Prof. Dr. Thomas Grunwald at the Fraunhofer-Institute in Leipzig. Briefly, tweezers or PBS were mixed with SARS-CoV-2 (300 FFU) and applied intranasally after 1 min incubation. After seven hours, the mice received a second intranasal dose of PBS or tweezers CP019, CP025 and CP006, respectively (Figure 18a). Clinical scores and body weights were recorded daily, showing neither signs of viral infection nor impairment by the tweezer treatment (Figure 18b). Two days post infection, mice were sacrificed and the lungs were removed, homogenized and the viral genomic RNA and N-protein expression was quantified by qPCR and Western blot, respectively (Figure 18c, d). Mice treated with tweezers showed no infection with SARS-CoV-2, while 5 out of 6 PBS treated mice displayed high viral RNA loads (in average 7.3 x 10^7copies/ml), indicating a strong course of infection. Detection of the N-protein via Western blot analysis was only possible in the PBS treated control group, confirming the qPCR data. In addition, virus-induced expression of common interferon stimulated genes (ISGs) was analyzed[189] via a digital droplet-PCR to gain insight on the inflammatory

response. As expected, RNA levels of all four investigated ISGs, ISG15, RIG-I, MX1 and OAS1, were elevated in the infected control mice (Figure 18e). Mice with abrogated viral infection due to tweezer treatment did not display an increase of ISG expression. Consequently, presence of tweezers in mice abrogate infection and accompanying inflammation, while the tweezer treatment itself did not induce any ISG response.

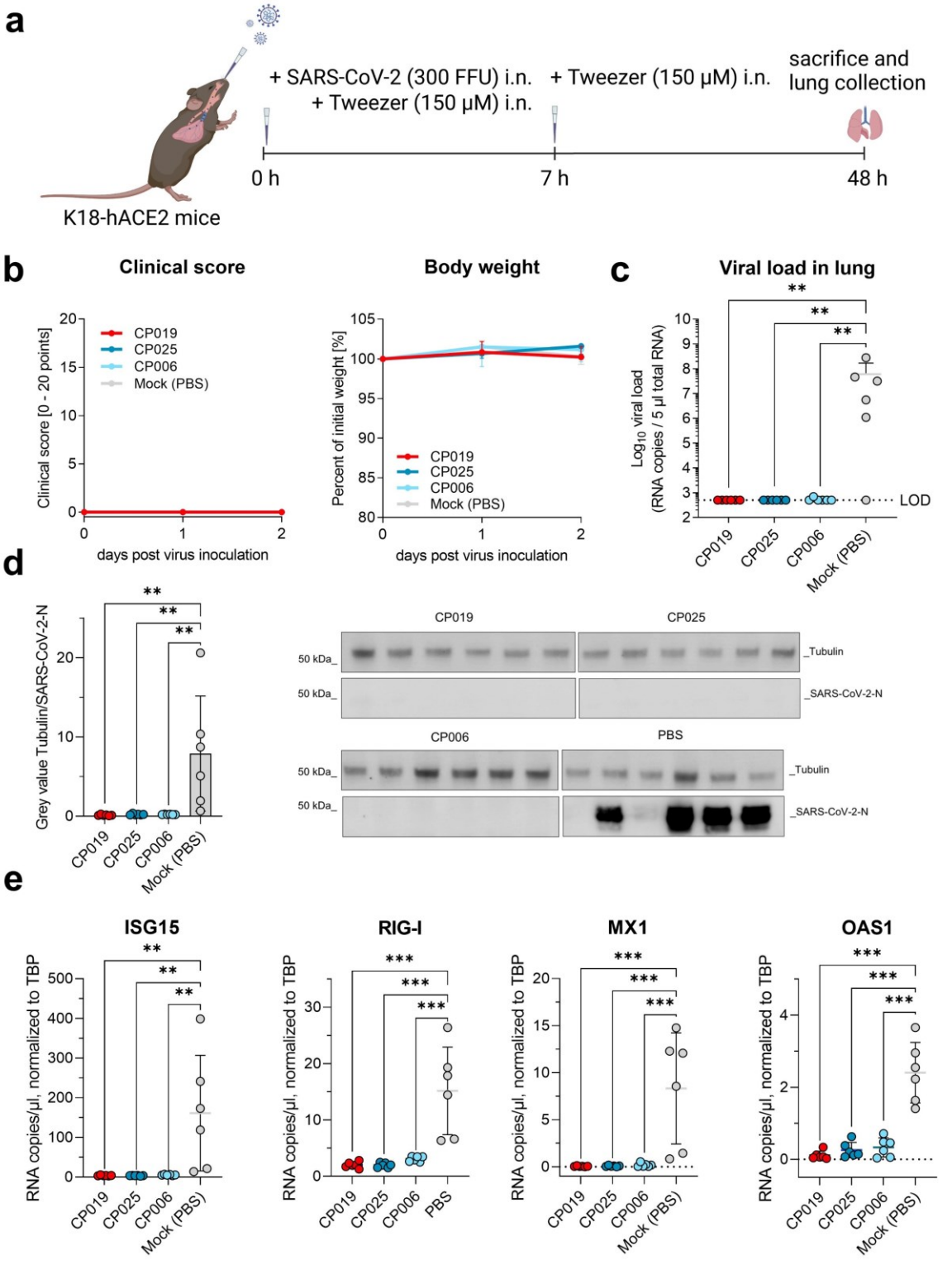

Figure 18. Advanced tweezers CP019, CP025 and CP006 inhibit SARS-CoV-2 infection in mice. a) Schematic illustration of experimental set-up. Transgenic K18-hACE2 mice (n = 6 per group, male) treated

intranasally with 50 µl tweezer (150 µM) or PBS mixed with SARS-CoV-2 Wuhan/Hu-1 isolate (300 FFU) after 1 min incubation. Seven hours later, mice were treated with tweezers or PBS again (50 µl, 150 µM). **b)** Body weight and clinical score were observed daily. **c)** Two days after infection, mice were sacrificed and the lungs were collected and homogenized. Viral RNA load of lungs analyzed by RT-qPCR. LOD: limit of detection. Shown are mean values ± SD. Statistical analysis was performed with one-way analysis of variance (ANOVA) with Kruskal-Wallis test and Dunn´s Pairwise Multiple Comparison Procedures as post hoc test (** = $p < 0.01$, *** = $p < 0.001$). **d)** Western blot analysis of SARS-CoV-2 N-protein and tubulin in mice lung homogenates. Band intensity was quantified by Fiji. **e)** mRNA expression level of interferon stimulating genes (ISG´s) normalized on housekeeping gene TATA-binding protein (TBP) in mice lung homogenates and analyzed in technical duplicates with digital droplet PCR. In case of d and e, graphs show mean values ± SD. Statistical analysis was performed with ordinary one-way ANOVA with Dunn´s Pairwise Multiple Comparison (** = $p < 0.01$, *** = $p < 0.001$). Mice experiments were carried out by Leila Issmail, Nadja Uhlig and Valentina Eberlein (Fraunhofer Institute for Cell Therapy and Immunology, Leipzig). Western blot analysis was performed by Rüdiger Groß (Institute of Molecular Virology, Ulm University Medical Center) and digital PCR was performed together with Lennart Koepke (Institute of Molecular Virology, Ulm University Medical Center). Modified from Weil et al. 2022[159] (CC BY-NC-ND 4.0; https://creativecommons.org/licenses/by-nc-nd/4.0/, Copyright© The Authors, permission to remix and transform was obtained from the creator). a) Figure was created with BioRender.com. Printed with permission according to Biorender Academic License Terms (https://biorender.com/terms/).

In a follow-up study, the activity of C6 alkyl tweezer CP019 and aromatic tweezer CP025 to inhibit SARS-CoV-2 infection was investigated in a prophylactic setting. Therefore, mice received 150 µM of tweezers 1 h and 10 minutes prior to infection with SARS-CoV-2 (300 FFU) (Figure 19a). The body weights and clinical scores were assessed daily until mice were sacrificed at day 2. Data of the body weight demonstrated no changes while the clinical score displayed a minor increase in the PBS treated control group (Figure 19b). The prophylactic treatment of tweezers did not abrogate the viral infection resulting in high level of viral RNA in all groups (Figure 19c). Only the group receiving aromatic tweezer CP025 showed slight reduction in the viral load, but without reaching significance. These results were reflected in detection of the N-protein by Western blot analysis (Figure 19d).

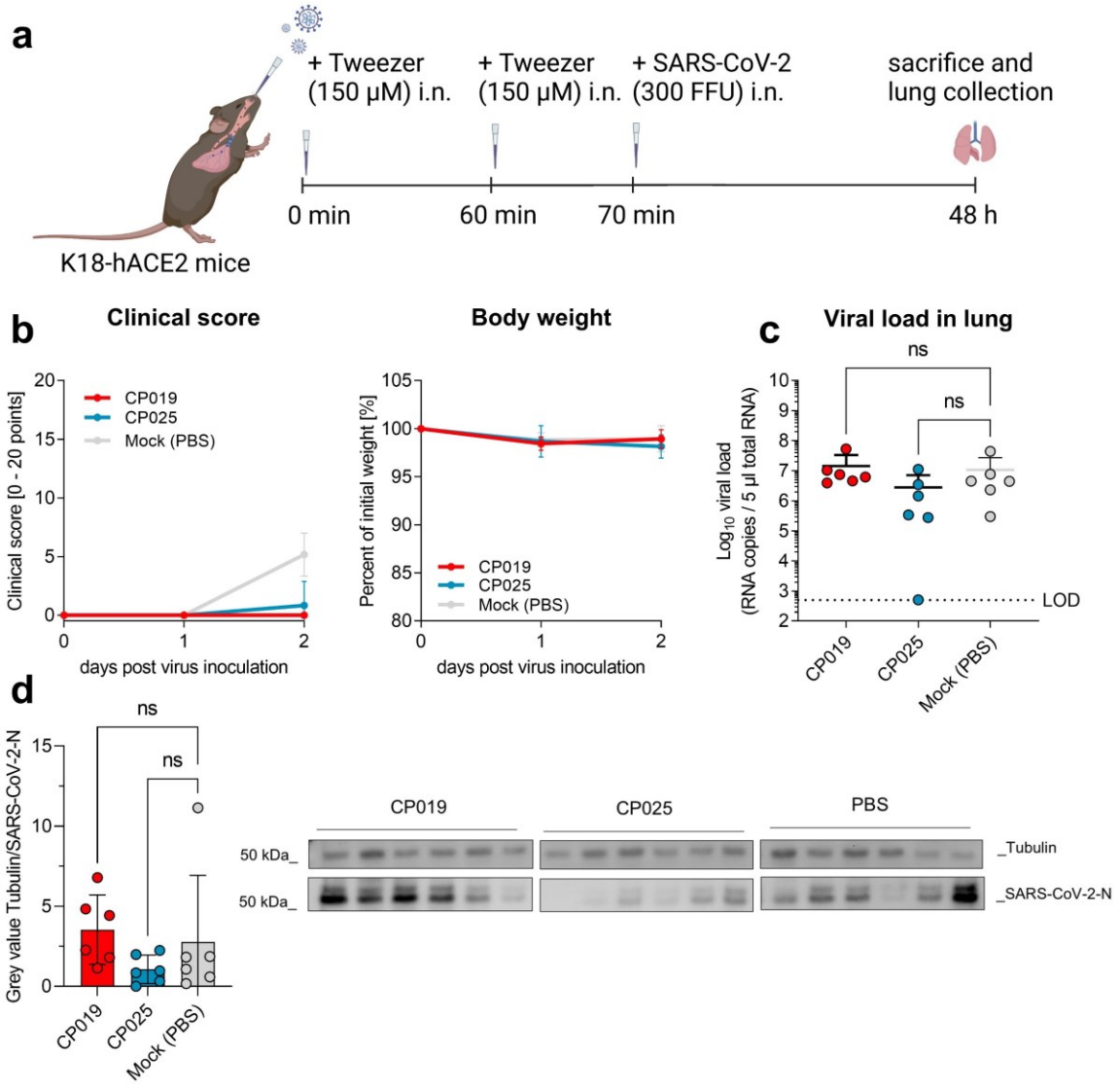

Figure 19. Prophylactic tweezer treatment of SARS-CoV-2 does not abrogate infection in mice. a) Schematic illustration of experimental set-up. Transgenic K18-hACE2 mice (n = 6 per group, male) treated intranasally with 50 µl tweezer (150 µM) or PBS 1 h and 10 min prior to infection with SARS-CoV-2 Wuhan/Hu-1 isolate (300 FFU, 40 µl). **b)** Body weight and clinical score were observed daily. **c)** Two days after infection, mice were sacrificed and the lungs were collected and homogenized. Viral RNA load of lungs analyzed by RT-qPCR. LOD: limit of detection. Shown are mean values ± SD. Statistical analysis was performed with one-way analysis of variance (ANOVA) with Kruskal-Wallis test and Dunn´s Pairwise Multiple Comparison Procedures as post hoc test (** = $p < 0.01$, *** = $p < 0.001$). **d)** Western blot analysis of SARS-CoV-2 N-protein and tubulin in mice lung homogenates. Band intensity was quantified by Fiji. Graph shows mean values ± SD. Statistical analysis was performed with ordinary one-way ANOVA with Dunn´s Pairwise Multiple Comparison (** = $p < 0.01$, *** = $p < 0.001$). Mice experiments were carried out by Leila Issmail, Nadja Uhlig and Valentina Eberlein (Fraunhofer Institute for Cell Therapy and Immunology, Leipzig). Western blot analysis was performed by Rüdiger Groß (Institute of Molecular Virology, Ulm University Medical Center). a) Figure was created with BioRender.com. Printed with permission according to Biorender Academic License Terms (https://biorender.com/terms/).

3.2.5 Side arms of tweezers increase membranolytic activity by additional insertion into the membrane

Having demonstrated improved antiviral activity of advanced tweezers, their mode of action was investigated to answer how the attached side arms to CLR01 increase the antiviral

activity. Firstly, the membranolytic potency of the novel tweezers was examined in a liposomes dye leakage assay. It is well established that certain lipids are enriched in viral membranes, derived from the cellular plasma membrane[190]. Therefore, to simulate the composition of a viral membrane, liposomes consisting of 1,2-dioleoyl-sn-glycero-3-phosphocholine (DOPC), sphingomyelin (SM) and cholesterol (Chol) were generated[190]. This lipid mixture was loaded with a solution of the self-quenching dye carboxyfluorescein and forced through a membrane with a pore size of 200 nm, yielding liposomes of size and composition comparable to a virus (Figure 20a). After removal of the non-encapsulated dye, a distinct number of liposomes was incubated with tweezers. Upon disruption of the lipid particle, carboxyfluorescein leaks out and gets diluted below the self-quenching concentration, resulting in a detectable fluorescence signal (Figure 20a). Testing of the advanced tweezers in the liposome dye leakage assay revealed disruption of the virus-like liposomes in a dose-dependent manner as demonstrated for CLR01, proposing a conserved inactivation mechanism (Figure 20b). However, all advanced derivatives were more potent than CLR01, in accordance to the antiviral data (Figure 14 and Figure 16). CP002, CP019 and CP020 showed highest activity for alkyl tweezers with half-maximal effective concentrations (EC_{50}) of 4.4, 6.5, and 4.4 µM, respectively. More potent in disruption of liposomes were the aromatic tweezers CP024 (EC_{50} = 3.0 µM) and CP026 (EC_{50} = 2.6 µM).

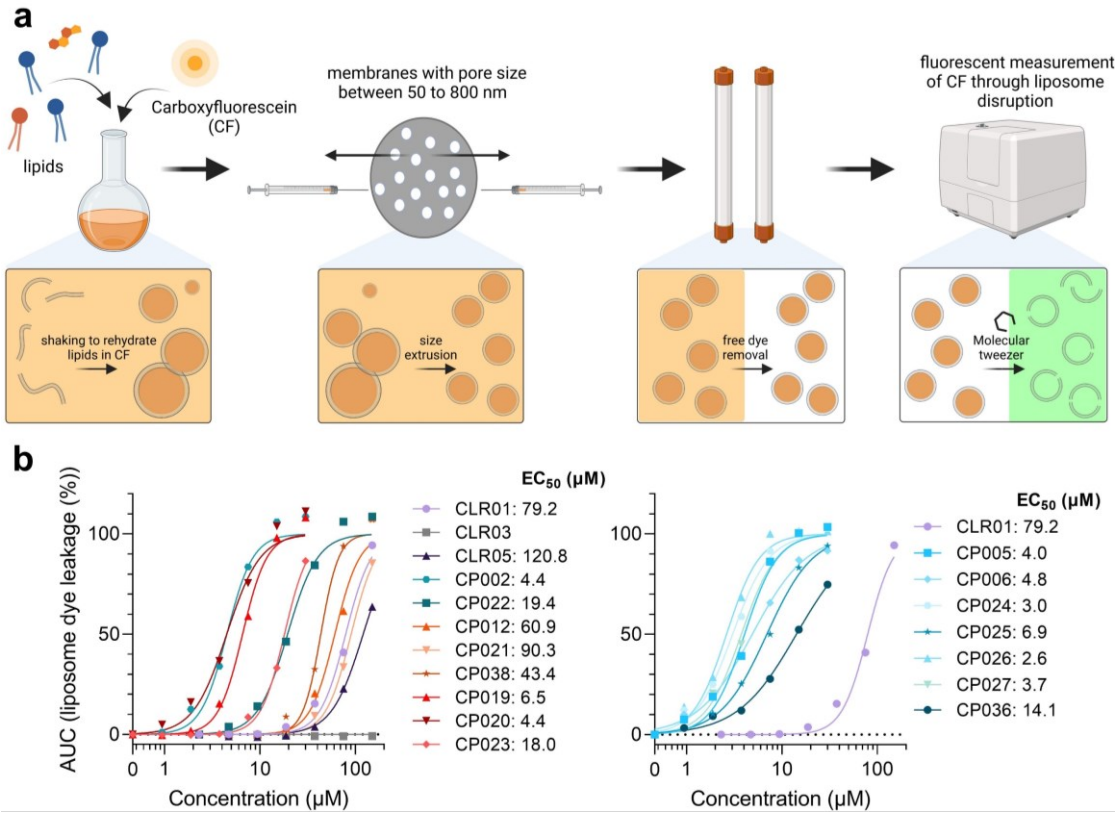

Figure 20. Advanced tweezers disrupt virus-like liposomes. a) Production of liposomes to measure membranolytic activity of tweezers. Lipids were mixed in glass vials and re-hydrated with 50 mM

self-quenching dye carboxyfluorescein (CF) in 50 % PBS, after the solvent chloroform was evaporated. The glass vials were shaken for one hour at 60 °C with agitation of 160 rpm. Liposomes were prepared by extrusion through a polycarbonate membrane with 0.05 to 0.8 µm pore size in a Mini Extruder. Non-encapsulated dye was removed with size-exclusion filtration, performed twice. Activity of tweezers were tested on a distinct number of liposomes. Upon membrane rupture, carboxyfluorescein leaks out and got diluted, resulting in a detectable fluorescence signal. **b)** Escalating concentrations of tweezers were incubated with 200 nm sized liposomes (DOPC 45/SM 25/Chol 30 mol %, 2.5 x 10^{10} particles/ml) filled with self-quenching dye carboxyfluorescein for 30 min after measuring baseline fluorescence for 5 min. Dye leakage was recorded every minute at 485 nm excitation and 528 nm emission. To ensure complete liposome disruption, 1 % Triton X-100 was added and dye leakage recorded for 5 min. Graphs show area under the curve of each tweezer concentration after baseline subtraction and normalization and data of one experiment performed in triplicates. Modified from Weil et al. 2022[159] (CC BY-NC-ND 4.0; https://creativecommons.org/licenses/by-nc-nd/4.0/, Copyright© The Authors, permission to remix and transform was obtained from the creator). a) Figure was created with BioRender.com. Printed with permission according to Biorender Academic License Terms (https://biorender.com/terms/).

Previously, the mechanism of CLR01 was studied, showing the inclusion of the choline head group of phosphatidylcholine (PC) and SM into the tweezer cavity[147]. As consequence, the orientation of the bound lipid changes, enabling the tweezers to penetrate into the outer membrane leaflet. Presence of the molecular tweezers thus induces an enhanced tension and finally disrupts the viral envelope. For further mechanistical insight into the advanced tweezers, aromatic tweezer CP024 and alkyl tweezer CP020, found as highly potent derivatives, were examined in biomolecular modelling approach. A virus-like membrane consisting of DOPC, SM and Chol (54:30:36 ratio) with a total of 120 lipid molecules per leaflet was set-up to investigate tweezer-lipid complexation with Gaussian accelerated Molecular Dynamics (GaMD). The simulation showed binding and inclusion of tweezers to lipids in all three replicates (Table 3, Figure 21a).

Table 3. Maximum number of tweezer molecules (CP020 or CP024) forming complexes with the membrane lipids during GaMD simulation. Modified from Weil et al. 2022[159] (CC BY-NC-ND 4.0; https://creativecommons.org/licenses/by-nc-nd/4.0/, Copyright© The Authors, permission to remix and transform was obtained from the creator).

		Number of tweezers forming inclusion complexes		
Tweezer	Number of tweezers	Replica 1	Replica 2	Replica 3
CP020	9	5	5	4
CP024	9	4	6	5

In the next step, the mechanistic ability of advanced tweezers to alter the lipid alignment was examined. The frequency of lipids in a certain tilt angle was measured for free lipids and compared to CP024 bound lipids. Most unbound lipids showed tilt angles of around 50 – 80 °, while tilt angles of lipids bound to CP024 shifted to 70 – 100 ° (Figure 21b).

During the simulations, an insertion of the introduced side arms from CP020, CP024 and CP026 into the membrane was observed (Figure 21c). The side arm insertion was achieved by one and also for both C7 alkyl or aromatic side arms supposedly increases the membrane tension further.

Taken together, the new generation of tweezers disrupt virus-like liposomes even at a lower concentration than CLR01. The binding to lipid head groups and alteration of the lipid tilt angle, as demonstrated for ancestor tweezers, was also observed for CP020 and CP024. Moreover, the simulations showed insertion of the side arms into the membrane potentially explaining the increased antiviral activity.

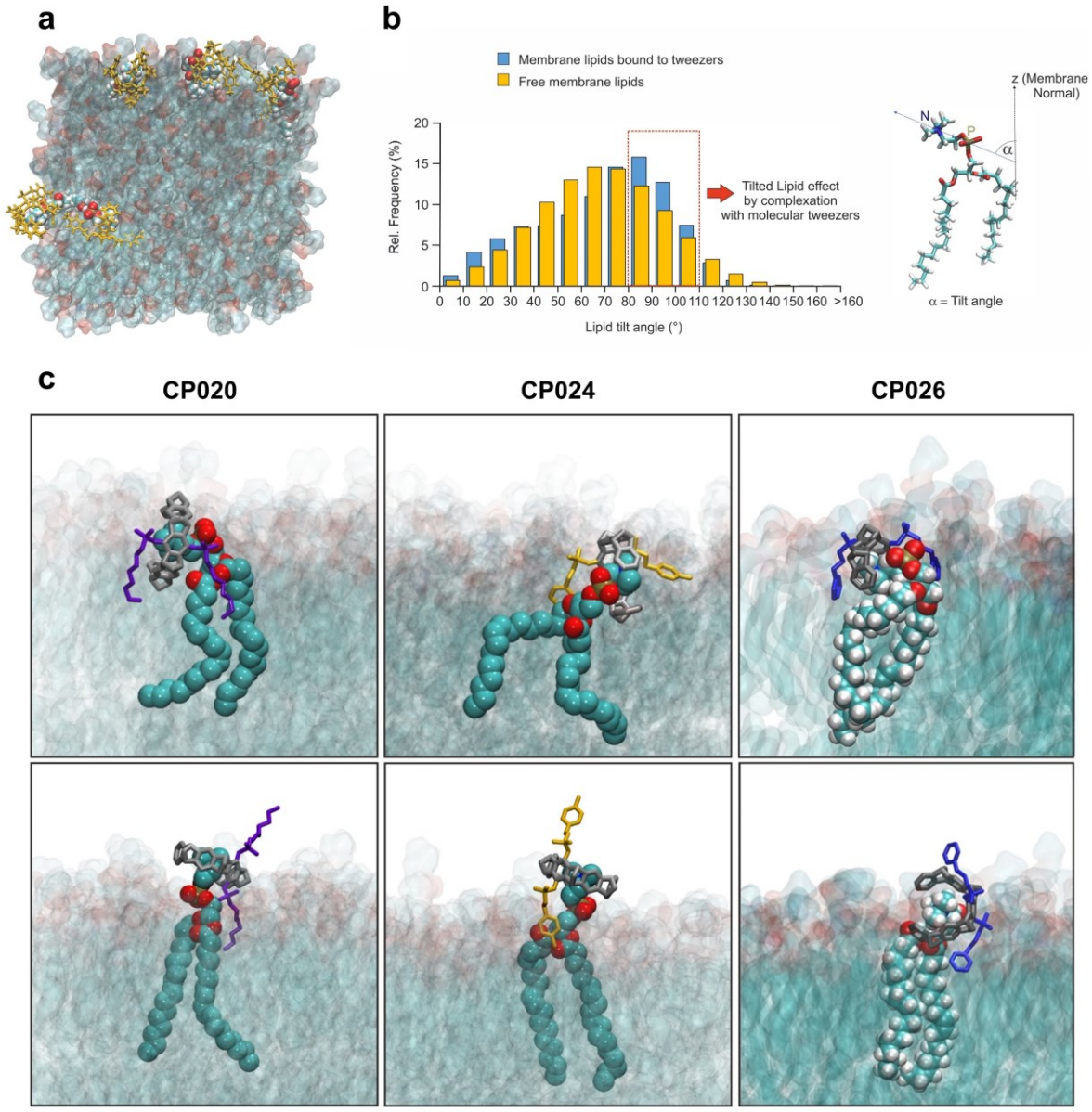

Figure 21. Aromatic and alkyl side arms of tweezers penetrate into membrane. a) Complex formation of membrane lipids and tweezers investigated by Gaussian accelerated Molecular Dynamics (GaMD). **b)** Distribution of lipid head orientation from free lipids and bound lipids to tweezer CP024. Tilt angle is defined as angle between the axis perpendicular to the membrane and the vector defined by P and N atoms of the lipid head. Bars correspond to the range of angles degree defined by the x-axis values on both sides of the bars. **c)**

Single tweezer-lipid complex. Side arms are highlighted in violet (CP020), yellow (CP024) or blue (CP026) and tweezer scaffold in grey. In case of a) and c), tweezer-lipid complex is highlighted in van der Waals representation, and the membrane is rendered transparent to allow visualization of complexes. Data was generated by Joel Mieres-Perez (Institute of Computational Biochemistry, University of Duisburg-Essen). Modified from Weil et al. 2022[159] (CC BY-NC-ND 4.0; https://creativecommons.org/licenses/by-nc-nd/4.0/, Copyright© The Authors, permission to remix and transform was obtained from the creator).

3.2.6 Advanced tweezers remain broadly active against enveloped viruses

Molecular tweezers CLR01 and CLR05 demonstrated broad-spectrum activity against several enveloped viruses in previous studies[146,147]. To verify this function for advanced tweezers and to understand the extend of optimization, selected candidates were tested against a panel of enveloped viruses, including influenza A virus (IAV), measles virus (MeV), respiratory syncytial virus (RSV), human immunodeficiency virus 1 (HIV-1), hCoVs, Zika virus (ZIKV) and herpes simplex viruses HSV-1 and HSV-2. All tweezers of the second generation suppressed the infection of each tested enveloped virus dose-dependently (Figure 22a, Supplementary Figure 6 and Supplementary Figure 7). Most advanced tweezers abrogated viral infection even at concentrations lower than CLR01, as already seen for SARS-CoV-2 pseudoparticles and authentic SARS-CoV-2 (Figure 14 and Figure 16). The C6/C7 alkyl and aromatic tweezer groups demonstrated highest activity with IC_{50} values in the low micromolar and high nanomolar ranges (Figure 22b). Interestingly, ZIKV was inhibited with IC_{50} values in the nanomolar range, even by CLR01. In contrast, hCoV inhibition required a relatively high dosage of tweezers.

Cytotoxicity of tweezers were assessed on the respective cells used for viral infection, A549 and TZM-bl cells, in addition to Caco-2 cells (Supplementary Figure 8 and Supplementary Figure 9). None of the tweezers interfered with the cell viability at the concentrations applied for the virus inhibition assay. Achieved CC_{50} values ranged from 29.1 to > 300 µM. As previously seen for Caco-2 cells, most tweezers showed cytotoxic effects at a concentration of 300 µM and for the aromatic tweezers also at lower concentrations.

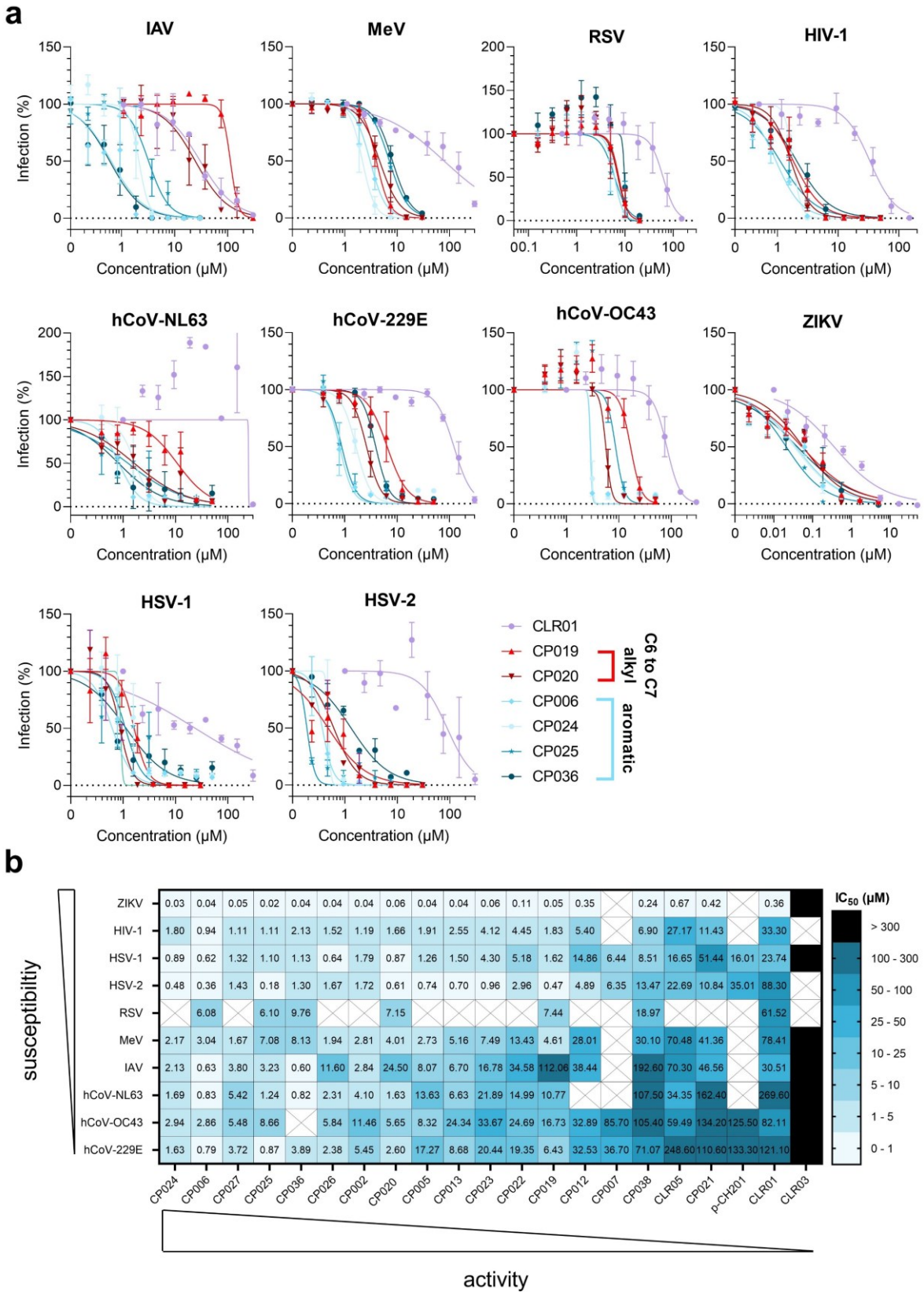

Figure 22. Broad-spectrum antiviral activity of advanced tweezers. a) To investigate activity of tweezers against IAV, titrated tweezers were mixed with IAV (MOI 0.0007), incubated for 30 min at 37 °C and added on Caco-2 cells. Infection rates were determined two days later by measuring neuraminidase activity in cellular lysates with a MUNANA assay. For MeV (MOI 0.1) and RSV (MOI 1) GFP reporter viruses, tweezers were incubated with the viruses for 30 min at 37 °C and added on A549 cells. One (for RSV) or two (for MeV) dpi, infection rate was measured with flow cytometry. Escalating concentrations of tweezers were incubated with hCoV-NL63 (MOI 0.01), hCoV-OC43 (MOI 0.006), hCoV-229E (MOI 0.002) for 30 min at 33 °C before

inoculation onto Caco-2 (hCoV-NL63) or Huh-7 cells (hCoV-OC43 and -229E). Infection rate was measured by in-cell ELISA analyzing N protein expression 2 (-229E), 3 (-OC43) or 6 (-NL63) dpi. ZIKV (MOI 0.15) was incubated for 30 min at 37 °C with titrated tweezers. Mixture was added on Vero E6 cells and two days later in-cell ELISA detecting flavivirus protein E was performed. For testing of tweezers on HSV-1 (MOI 0.05), HSV-2 (MOI 0.05) or HIV-1, viruses were incubated together with tweezers at indicated concentrations for 10 (in case of HIV-1) or 15 min at 37 °C and inoculated onto TZM-bl (for HIV-1) or ELVIS reporter cells. Infections rates were determined two days later by quantification of β-galactosidase activity in cellular lysates. Shown are mean values ± SEM of two (in case of MeV, HSV-1 and HSV-2) or three independent experiments conducted in triplicates. **b)** Overview antiviral activity of tweezers against various viruses, derived from a), Supplementary Figure 6 and Supplementary Figure 7. Data of IAV, MeV, RSV was generated by Lena Rauch-Wirth (Institute of Molecular Virology, Ulm University Medical Center), Andrea Gilg (Institute of Molecular Virology, Ulm University Medical Center) and Sandra Axberg Pålsson (Department of Molecular Bioscience, Stockholm University), respectively. Data of tweezers on hCoV-229E, -NL63 and ZIKV was generated by Jan Lawrenz (Master thesis), Institute of Molecular Virology, Ulm University Medical Center. Modified from Weil et al. 2022[159] (CC BY-NC-ND 4.0; https://creativecommons.org/licenses/by-nc-nd/4.0/, Copyright© The Authors, permission to remix and transform was obtained from the creator).

3.2.7 Inverse correlation of tweezer activity and particle size

Analyzing the activity of advanced tweezers against different viruses revealed a particularly high effectivity against ZIKV (Figure 22). Additionally, comparing previously conducted time course experiments of CLR01 against ZIKV and SARS-CoV-2 pseudoparticles demonstrated faster disruption of ZIKV (Figure 10)[146]. ZIKV belongs to the *Flaviviridae*, a family of viruses that display a particle diameter of only 40 – 60 nm[191] and is therefore the smallest virus used in the assays. This raised the question if the size of a virus influences the tweezer effectiveness. As a model system, a set of virus-like liposomes with defined sizes was generated by extrusion through membranes with pore diameters of 50 – 800 nm and characterized by dynamic light scattering (DLS) (Figure 23a). CLR01 and the most promising advanced tweezers, CP020 (C7 alkyl) and CP024 (aromatic) were incubated with this liposome-set and the membranolytic activity was assessed in the liposome dye leakage assay. Interestingly, all three tweezers showed an increased membranolytic activity with decreasing liposome size (Figure 23b). This observation also holds true when normalizing the number of tweezers required to destroy one particle to the number of input particles (Figure 23c), thus confirming that tweezer activity is increased against smaller particles.

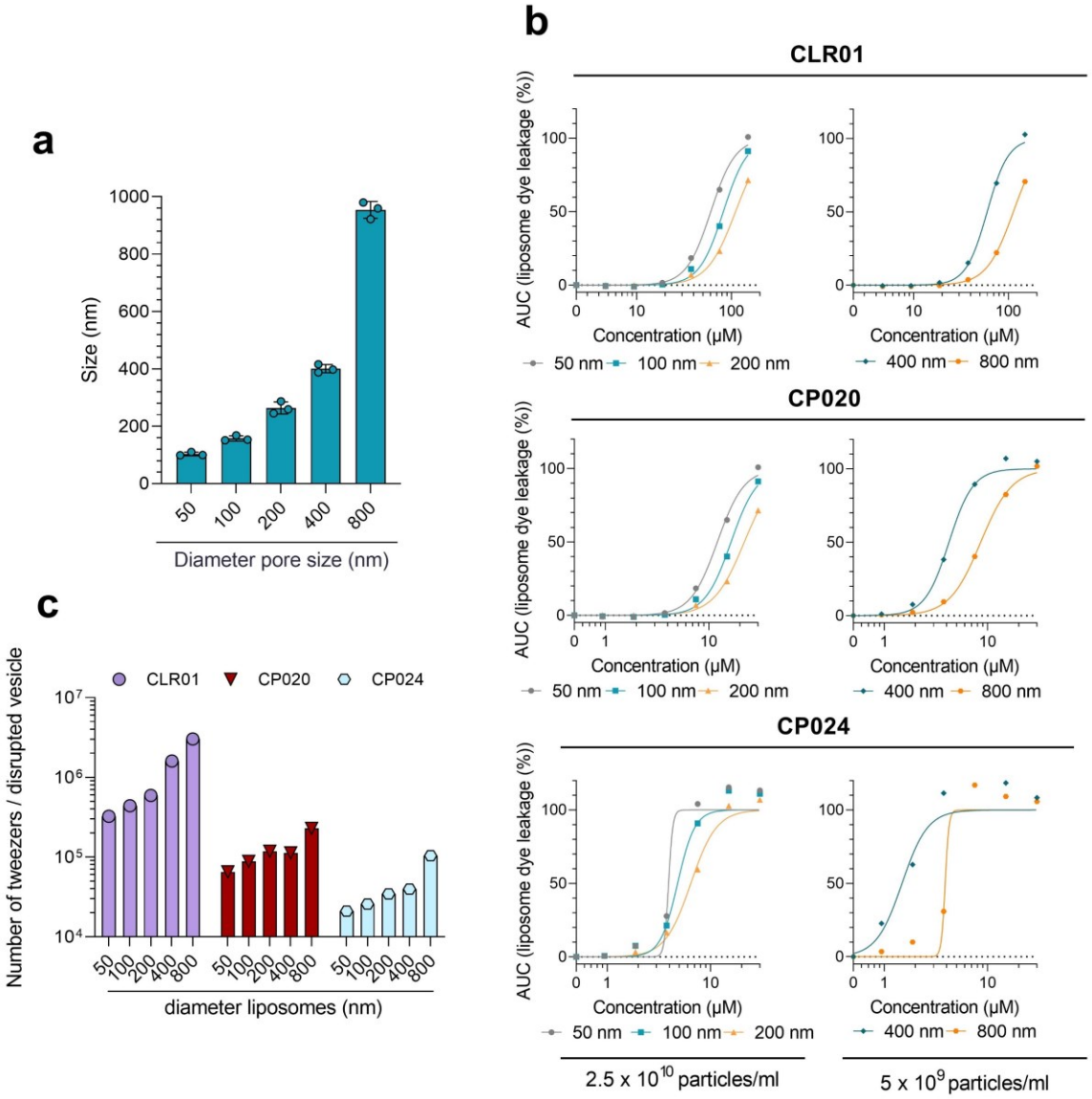

Figure 23. Tweezers disrupt particles with decreased diameter more efficiently. a) Membranes with pore diameter of 50 to 800 nm were used to form virus-like liposomes (DOPC 45/ SM 25/ Chol 30 mol %) filled with self-quenching dye carboxyfluorescein. Particle size was measured using dynamic light scattering (DLS) and graph shows mean of z average ± SD of three acquisitions. **b)** Titrated tweezers were incubated for 30 min with defined number of liposomes with different sizes and dye leakage was recorded every minute at 485 nm excitation and 528 nm emission. Baseline was measured for 5 min in absence of tweezers and maximum fluorescence was recorded after addition of 1 % Triton X-100. Graphs show area under the curve of each tweezer concentration after baseline subtraction and normalization. Experiment was performed once in triplicates. **c)** Calculated number of tweezers needed to disrupt one particle based on EC_{50} values of b).

To further evaluate the size dependency of the tweezer, giant unilamellar vesicles (GUVs) were produced. These vesicles consist of the same lipid composition as the synthetic virus-like liposomes (DOPC 45/SM 25/Chol 30 mol %) and are also filled with the self-quenching dye carboxyfluorescein. On the contrary, the produced GUVs had a size of 5.7 µm in average (Figure 24a), and thus similar to small cells, for example erythrocytes[192,193], whereas liposomes displayed a size diameter of only 162 nm in average (Figure 20). Several of the tweezers that were already analyzed against virus-like liposomes

were tested for GUV lysis in the dye leakage assay. Of note, the total lipid amount used for GUV and liposome production before sizing was equal and thus resulted in lower GUV particle number (1.0×10^{04} particles/ml), as compared to liposomes (2.5×10^{10} particles/ml). All tweezers, except for the negative control CLR03, disrupted the GUVs in a dose-dependent manner (Figure 24b). The carboxylate tweezer CLR05 and the alkyne tweezer CP021 did not reach full leakage at their highest applied concentration. Aromatic tweezers were the most potent group, with EC_{50} values between 0.3 to 3.2 µM. The EC_{50} values of tweezers against GUVs and liposomes correlated and were not significantly different to each other (Figure 24c and d). However, the number of vesicles employed in the GUV and liposome assays needs to be accounted for, to allow comparison. When calculating the number of tweezers to destroy one particle, a 2.2×10^{5}-fold increased activity towards liposomes is revealed, demonstrating once again the higher efficiency of tweezers towards smaller particles (Figure 24d). Interestingly, the tweezers even displayed a 260-fold increased activity for liposomes when normalizing to the number of single lipids in each vesicle preparation, indicating that other factors than the lipid amount influences the tweezer activity. A side by side comparison of the individual tweezer activities against liposomes and GUVs demonstrated the lowest selectivity for liposome lysis for aromatic tweezer (26.3 to 96.4-fold differences), and a medium selectivity for ancestor, C6/C7 alkyl and alkyne tweezer CP019, CP023, CP038, CP020, CLR05 and CLR01 (from 107.5 to 237.9-fold) (Figure 24e). The tweezer CP021 containing a C6 alkyne moiety exhibited the most remarkable selectivity towards liposome lysis, with a 613-fold observed difference. This differences in selectivity towards small particles are also reflected in the SI values of tweezers (Figure 14 and Figure 16).

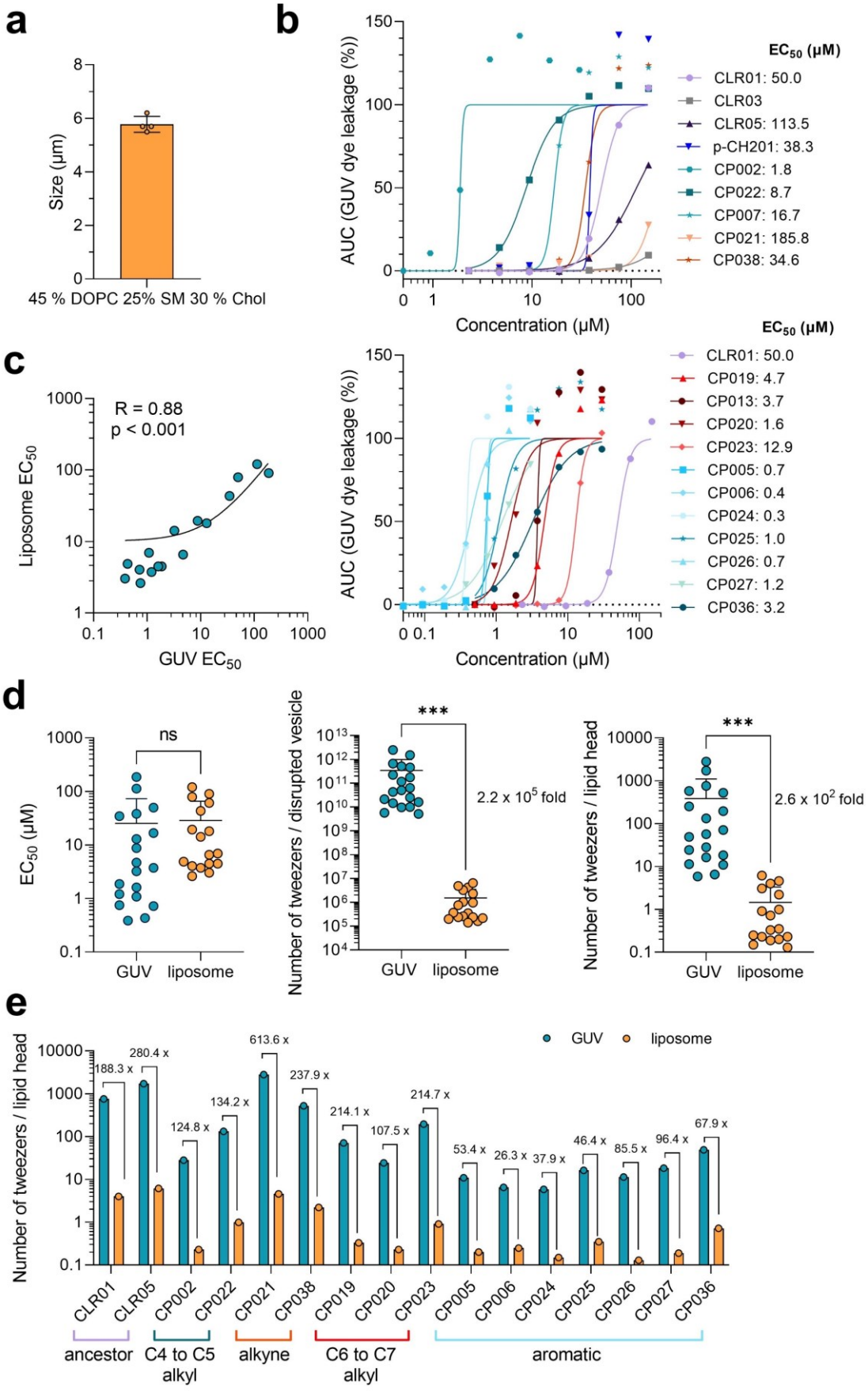

Figure 24. Disruption of giant unilamellar vesicles (GUVs) by molecular tweezers. a) Virus-like GUVs (DOPC 45/ SM 25/ Chol 30 mol %) were produced by the PAPYYRUS method[171] and filled with 50 mM

self-quenching dye carboxyfluorescein. Shown are mean values of GUV diameter ± SD in quadruplicates. **b)** Serial dilutions of tweezers were incubated for 30 min with GUVs (1.0 x 10^{04} particles/ml) and fluorescence was recorded every minute at 485 nm excitation and 528 nm emission. Baseline was measured for 5 min in absence of tweezers and maximum fluorescence was recorded after addition of 1 % Triton X-100. Graphs show area under the curve of each tweezer concentration after baseline subtraction and normalization. Shown values are derived from one experiment performed in triplicates. **c)** Correlation analysis of EC_{50} values derived from b) and Figure 20. Analysis was assessed by Spearman Correlation, two-tailed p value. **d)** Mean EC_{50} values of b) and Figure 20; number of tweezers required to induce leakage of one GUV or liposomes; number of tweezers per lipid head for particle disruption. Statistical analysis was performed using nonparametric Mann-Whitney test (*** = $p < 0.001$). **e)** Individual comparison of tweezer activity against GUVs and liposomes derived from d).

3.2.8 Antiviral activity of molecular tweezers depends on the viral budding site

Advanced tweezers displayed a broad-spectrum activity against enveloped viruses by targeting their membrane (Figure 22). However, at first glance, the analysis of the tweezer activities against individual viruses did not reveal any obvious commonalities or clusters (Figure 22b). In a principal component analysis (PCA), the IC_{50} and EC_{50} values against tested viruses and vesicles were analyzed to identify patterns that might explain the differences in virus susceptibility towards tweezers (Figure 25). All coronaviruses, except for hCoV-OC43, clustered together. Curiously, all of these viruses are budding from the endoplasmic-reticulum Golgi intermediate complex (ERGIC)[22,34,188,194]. In contrast, viruses budding through the plasma membrane (PM) including HIV-1[195], or lentiviral SARS-CoV-2 pseudoparticles, MeV[196] and RSV[197] were located in a separated cluster. The virus-like liposomes, simulating viruses deriving their envelope from the PM[190], were in close proximity to those viruses budding through the PM. GUVs harboring the same lipid composition as virus-like liposomes were not located close to the virus-like liposomes. This might be due to the impact of particle size on tweezer activity, as shown previously (Figure 24e). ZIKV and herpes simplex viruses, HSV-1 and HSV-2, which obtain their membrane from the ER[198,199] or the Golgi[200], clustered on the middle left side. Interestingly, all of the budding sites (PM, ERGIC, ER and Golgi) vary in their lipid composition[114]. Therefore, this analysis suggests that tweezer activity might be influenced by the viral budding site and consequently by the lipid composition of the viral envelope.

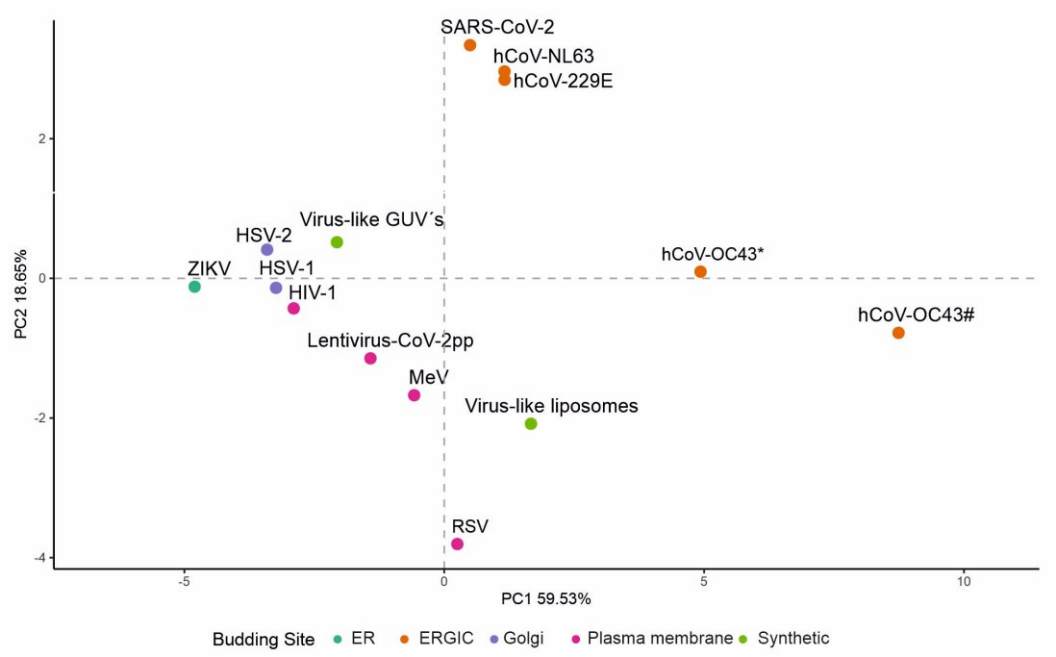

Figure 25. Principal component analysis of tweezer activity on various viruses and virus-like particles. IC_{50} and EC_{50} values used in a principal component analysis are derived from Figure 14, Figure 16, Figure 20, Figure 22, Figure 24 and Figure 26**.** # hCoV-OC43 was produced on HCT-8 cells, * hCoV-OC43 was produced on TMPRSS2 expressing Vero E6 cells. Analysis was performed by Victoria Hunszinger (Institute of Molecular Virology, Ulm University Medical Centre).

The viruses shown in the PCA were produced in various cell lines, which were derived from different human or even primate tissue. To analyse whether the producer cell line affected antiviral tweezer activity, hCoV-OC43 was propagated on human HCT-8 cells and used to test a selection of advanced tweezers, under the same conditions. The results were then compared to previously generated data using hCoV-OC43 that was produced on primate TMPRSS2 expressing Vero E6 cells (Figure 22, Supplementary Figure 6 and Supplementary Figure 7). All tweezers inhibited the hCoV-OC43 produced on HCT-8 cells with IC_{50} values from 4.11 – 148.30 µM (Figure 26a and b). Upon comparison, the resulting IC_{50} values obtained for the inhibition of TMPRSS2 expressing Vero E6 cells generated hCoV-OC43 did not differ from hCoV-OC43 that was generated in HCT-8 cells (Figure 26b), as confirmed by a correlation analysis with $r = 0.93$, $p = < 0.001$ (Figure 26c). This demonstrated high similarity of tweezer activity against viruses even when produced on different cell lines.

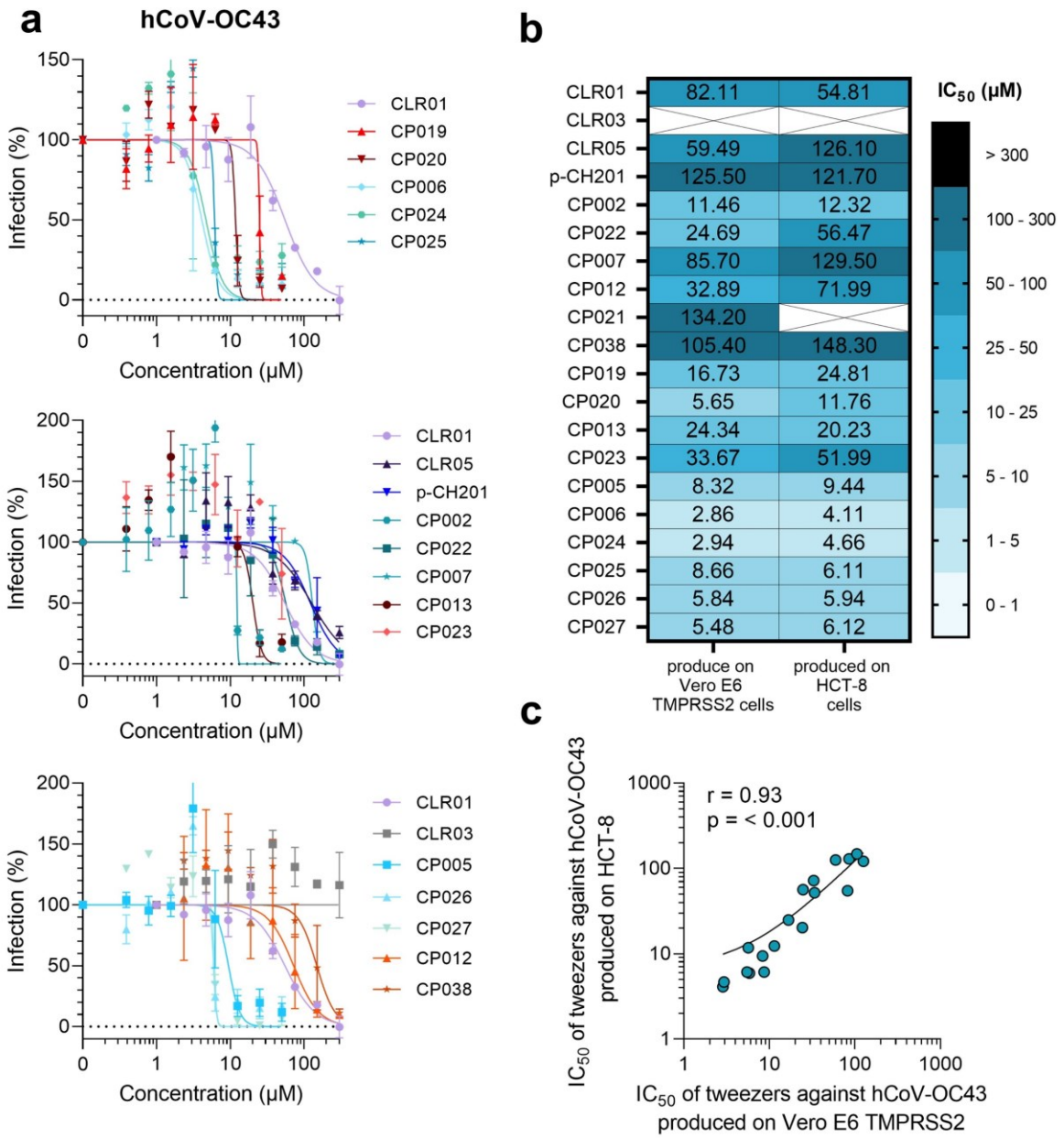

Figure 26. hCoV-OC43 produced in cell line of different species does not impair tweezer activity. a) Escalating concentrations of tweezers were incubated with hCoV-OC43 (MOI 0.006) produced on HCT-8 for 30 min at 33 °C before inoculation onto Huh-7 cells. Infection rate was measured by in-cell ELISA analyzing N-protein expression 3 dpi. Shown are mean values ± SEM of two independent experiments conducted in triplicates. **b)** Overview of antiviral activity of tweezers against hCoV-OC43 produced on Vero E6 expressing TMPRSS2 (derived from Figure 22, Supplementary Figure 6 and Supplementary Figure 7) or HCT-8 cells (derived from a)). **c)** Correlation analysis of tweezer activity against hCoV-OC43 produced on HCT-8 and Vero E6 expressing TMPRSS2 cells. IC_{50} values from b) were analyzed by Spearman Correlation. Two-tailed p value.

3.2.9 Generation of uniform or mixed liposomes

The membranolytic activity of tweezers may not only be affected by the size of particles, but also by the lipid composition of the viral envelope, as the PCA suggested (Figure 25). To explore the mechanistical activity of tweezers with regard to lipid selectivity, uniform or

mixed liposomes were generated. An assembly of 13 lipids representing the most commonly found lipids in cellular membranes, was selected[114,201]. This includes phospholipids, sphingolipids and sterols (Figure 27a). Homogenous liposomes from PC (phosphatidylcholine), PG (phosphatidylglycerol), PS (phosphatidylserine), PA (phosphatidic acid), PI (phosphatidylinositol) and heterogenous liposomes containing PC in combination with PE (phosphatidylethanolamine), sphingolipids sphingomyelin (SM) and ceramide or sterols cholesterol (Chol) and Cholesteryl oleate (Chol ester) were produced by extrusion through a membrane with 100 nm pore size and filled with carboxyfluorescein as previously described (Figure 20a). Of note, production of only homogenous liposomes from PE, SM, ceramide, Chol ester and Chol was not possible due to their physical properties. Therefore, the lipids were mixed with 50 mol% of PC, the most abundant cellular lipid[202]. The liposome size was verified by nanoparticle tracking analysis (NTA) and revealed uniform particle populations with similar sizes (105.7 to 146.8 nm) (Figure 27b, c). The measured zeta potential varied from 1.03 mV (for PC liposomes) to -39.65 mV (for PG liposomes), while PC liposomes demonstrated a slightly positive zeta potential and heterologous PC/PE and PC/Chol ester liposomes a slight negative value (Figure 27c). The remaining liposomes displayed a moderate to strong negative zeta potential of above -8.95 mV. This outcome was expected, since PC and PE are neutral lipids while PS, PG, PA and PI lipids contain negatively charged head groups[203]. Furthermore, rising concentrations of Chol were described to lower the zeta potential of phospholipid membranes and SM containing liposomes were reported with a negative zeta potential of – 11.4 mV[204,205].

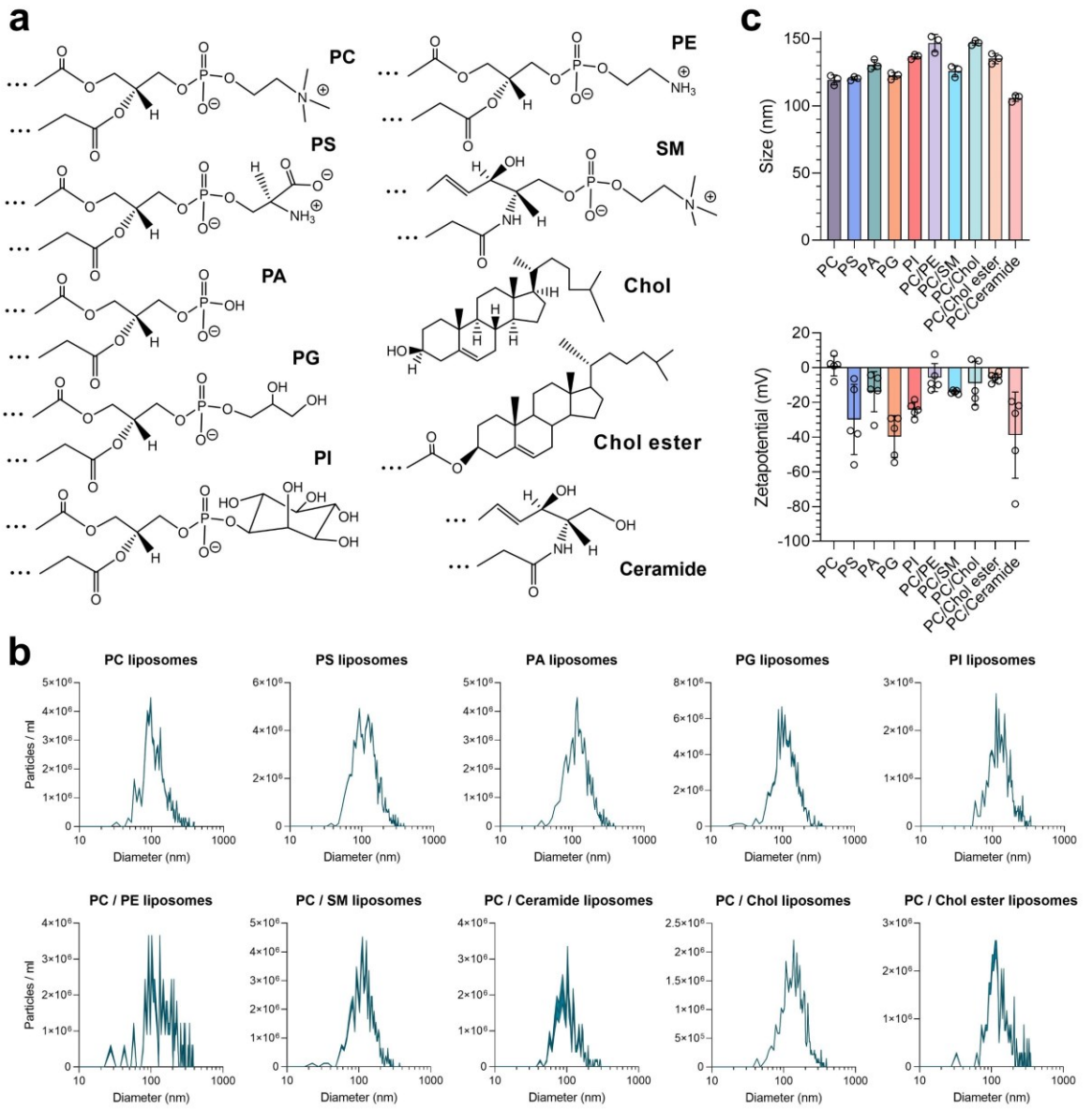

Figure 27. Characterization of uniform or mixed liposomes. a) Chemical structure of lipid head groups. **b)** Particle size and number of 100 nm sized uniform or mixed (50/50 % mol) liposomes, filled with 50 mM self-quenching dye carboxyfluorescein were analyzed by NTA. Shown are mean values ± SD in shaded lined of 3 acquisitions. **c)** Mean particle size from b) and zeta potential were assessed by NTA. Shown are mean values ± SD of 3 (size) or 5 (zeta potential) acquisitions. PC: phosphatidylcholine, PE: phosphatidylethanolamine, PS: phosphatidylserine, PI: phosphatidylinositol, PA: phosphatidic acid, PG: phosphatidylglycerol, Chol ester: Cholesteryl oleate, SM: sphingomyelin, Chol: Cholesterol.

3.2.10 Advanced tweezers show broad membranolytic activity on various lipid types

After generation and characterization of homo- and heterologous liposomes (Figure 27), promising tweezer representatives of each groups were selected and incubated with each liposome type. The tweezer activity was recorded by fluorescence measurement in the liposome dye leakage assay. All advanced tweezers, except C6 alkyne tweezer CP021, showed broad activity and disrupted nearly all types of liposomes in a dose-dependent manner (Figure 28). Ancestor tweezer CLR03 had no activity as expected, while CLR01,

CLR05 and CP021 were only able to induce more than 50 % leakage on PC/SM, PC, PC/Chol ester and PC/Ceramide liposomes (Figure 28 and Figure 29). All tweezers performed best on PC/SM liposomes with EC_{50} values ranging from 1.31 to 32.30 µM, while disruption of PC/Chol liposomes required the highest tweezer concentrations (EC_{50} = 10.51- 189.20 µM) and were often not fully lysed (Figure 29). Interestingly, the presence of SM increased activity of all tweezers, except for the aromatic tweezer CP025. Evaluation of the EC_{50} values from CP025 revealed high activity on phospholipid liposomes, but not in the presence of cholesterols or sphingolipids (Figure 29). Compared to PC/SM liposomes, other heterogenous liposomes such as PC/Chol ester or PC/ceramide were inhibited with lower effectiveness, and even lower than PC only. Tweezer activity against phospholipids PG, PC/PE, PI, PS and PA liposomes were even lower. Aromatic tweezer CP024 and branched C4 alkyl tweezer CP002 showed highest activity on all tested liposomes (EC_{50} of CP024 = 1.61 – 13.72 µM and EC_{50} of CP002 = 1.95 – 14.50), but also other aromatic (CP026, CP005, CP006, CP027) and C6/C7 alkyl tweezers, as CP020 and CP019, showed increased activity on various liposomes (Figure 29). In sum, advanced tweezers displayed a broader activity on various liposome types compared to ancestor tweezer CLR01 and CLR05, suggesting that this ability increase furthermore the efficiency on virus inhibition.

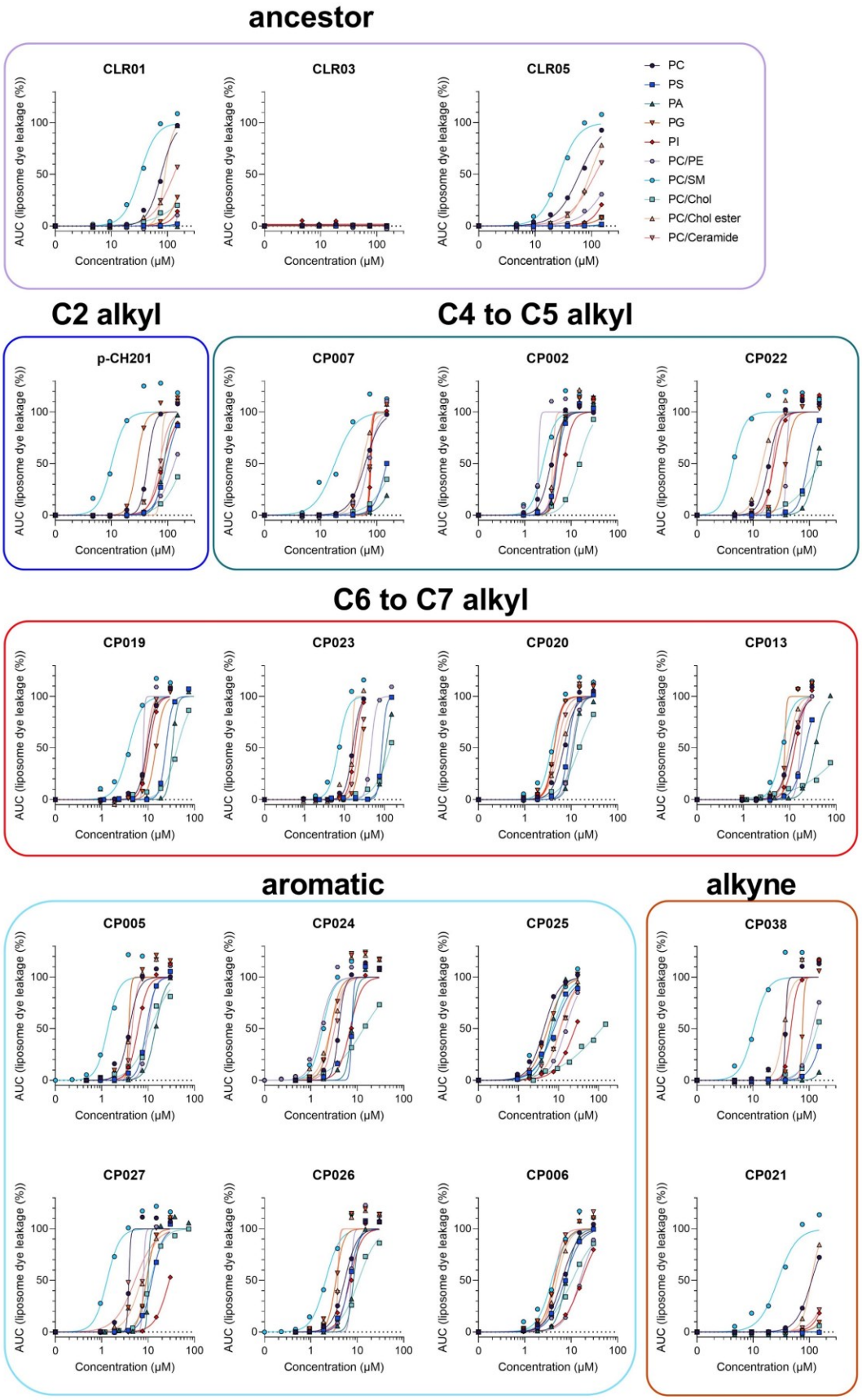

Figure 28. Advanced tweezers disrupt liposomes with varying lipid composition. Liposomes characterized in Figure 27 (2.5 x 10^{10} particles/ml) were incubated with increasing concentrations of tweezers for 30 min and fluorescence was recorded every minute at 485 nm excitation and 528 nm emission. Baseline was measured for 5 min in absence of tweezers and maximum fluorescence was recorded after addition of 1 % Triton X-100.

Graphs show area under the curve of each tweezer concentration after baseline subtraction and normalization. Data is derived from one experiment performed in triplicates.

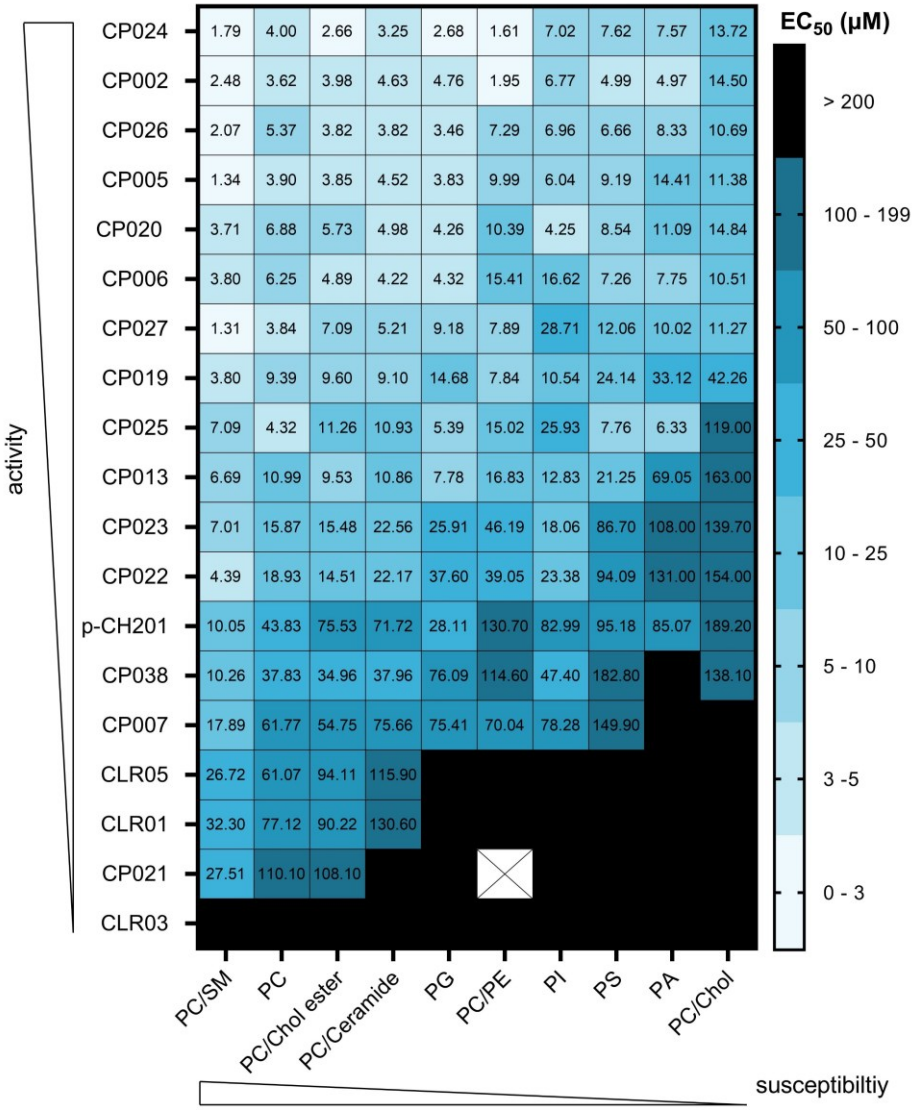

Figure 29. Advanced tweezers disrupt liposomes with varying lipid composition. Overview of tweezer activity against various liposome types from Figure 28.

Lyso-lipids harbour only one fatty acid tail and are found in the mammalian cell membrane[206]. Three lyso-lipids, named lyso-PC, lyso-PS and lyso-PE were used to generate heterogenous liposomes in a ratio of 5/95 mol % with PC, the main lipid of the cellular membrane[202]. Since lyso-lipids tend to form micelles at exceed concentrations, they were used at a concentration of 5 mol%, which is consistent with the amount found in cellular membranes[206]. Liposomes were produced under the same conditions as before (Figure 27), resulting in uniformly sized liposome populations, with different zeta potentials (Figure 30a, b, c). PS is equipped with a negatively charged head group and therefore represented the highest negative value (-42.64 mV), but presence of lyso-lipids decreased the zeta potential in general. All lyso-lipid containing liposome types were disrupted

dose-dependently by tweezers, except of CLR03 (Figure 30d). Activity of tweezers were increased against all lyso-lipid containing liposomes in comparison to EC_{50} values of homogenous PC liposomes. As example, the EC_{50} values of uniform PC liposomes ranged from 3.62 to 110.10 µM, while the EC_{50} values against PC/lyso PC liposomes were lower (0.94 to 67.52 µM) (Figure 30e). Furthermore, lyso-PC liposomes were most susceptible to tweezer disruption, followed by lyso-PE and final lyso-PS, as also shown for their respective two-tailed lipid counterpart (Figure 29).

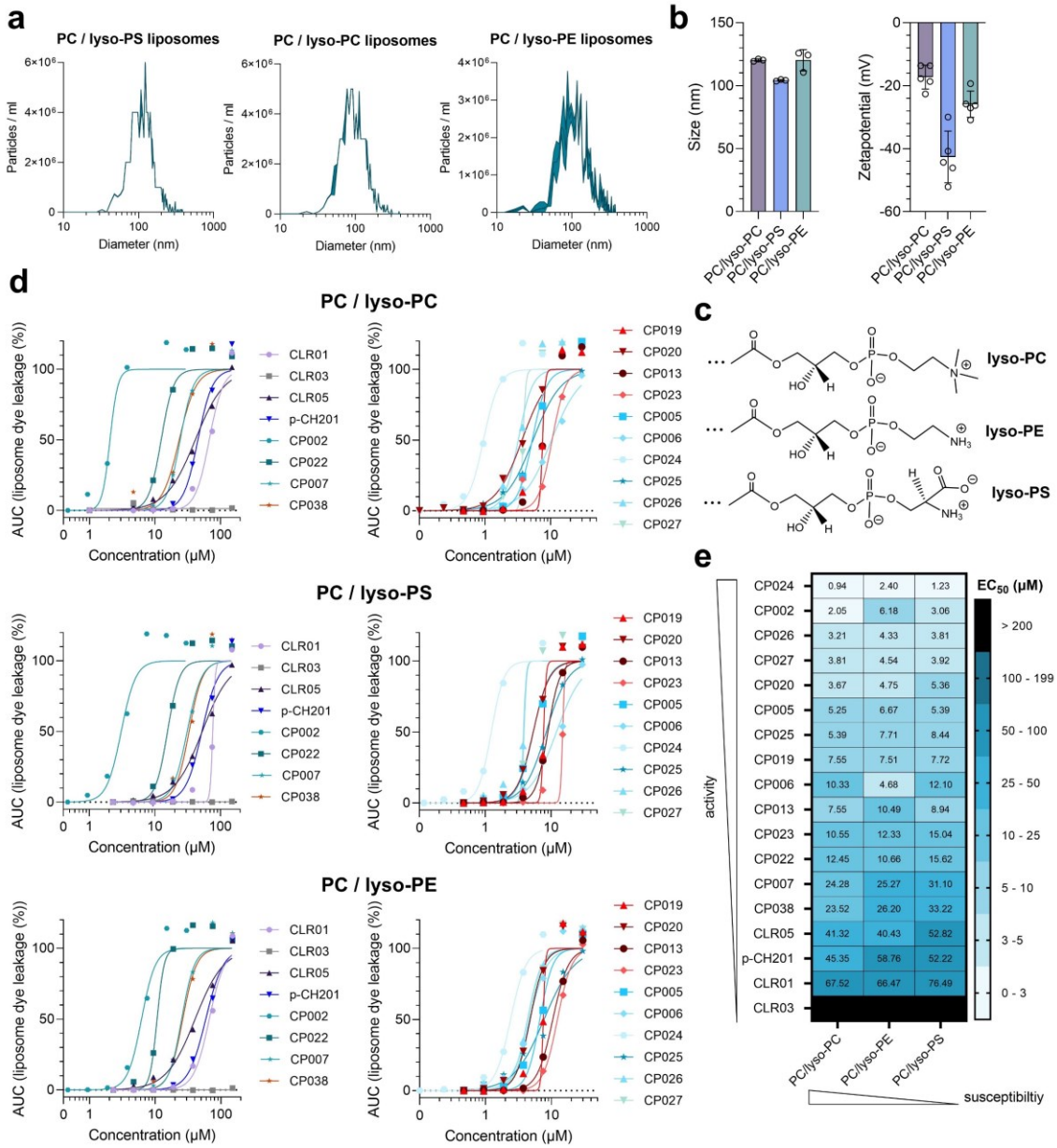

Figure 30. Presence of lyso lipids in liposomes tends to increased tweezer activity. a) Particle size and number of 100 nm sized mixed (95/5 % mol) liposomes, filled with self-quenching dye carboxyfluorescein were analyzed by NTA. Shown are mean values ± SD in shaded lines of 3 acquisitions. **b)** Mean particle size from a) and zeta potential were assessed by NTA. Shown are mean values ± SD of 3 (NTA) or 5 (zeta potential) acquisitions. **c)** Chemical structure of lyso-lipid head groups. **d)** Liposomes of b) (2.5 x 10^{10} particles/ml) were incubated with increasing concentrations of tweezers for 30 min and fluorescence was recorded every minute at 485 nm excitation and 528 nm emission. Baseline was measured for 5 min in absence of tweezers and maximum fluorescence was recorded after addition of 1 % Triton X-100. Values were corrected for baseline

and normalized. Graphs show mean values of area under the curve from one experiment performed in triplicates. **e)** Overview tweezer activity against various liposome types from d).

The screen for lipid selectivity on various liposome compositions showed differences in the tweezer activity. To interpret virus inhibitory data based on the liposome measurements, another PCA analysis was conducted, which incorporated the information obtained from both antiviral and liposome leakage data (Figure 25, Figure 29 and Figure 30). All phospholipid liposomes, PS, PI, PA, PG and PE, but not PC, cluster on top and with the smallest distance to coronaviruses hCoV-229E, -NL63, and SARS-CoV-2 (Figure 31). The group of PM budding viruses (HIV-1, MeV, RSV and lentiviral SARS-CoV-2 pseudoparticle), but also ER and Golgi budding viruses were found near to PC and PC/SM liposomes, whereas the data point of PC/Chol liposomes was placed with great distance. This was expected since the tweezer activity on PC/Chol liposomes was very weak. All three lyso-lipid liposomes were located in close proximity to each other and to PC liposomes.
Taken together, advanced tweezers showed broader activity on several liposome types indicating that binding is not limited to SM and PC, as it is for ancestor tweezer CLR01 and CLR05. Furthermore, the tweezers demonstrated a selective lipid specificity, which might help to gain further insight in the viral membrane composition in accordance to their respective budding sites.

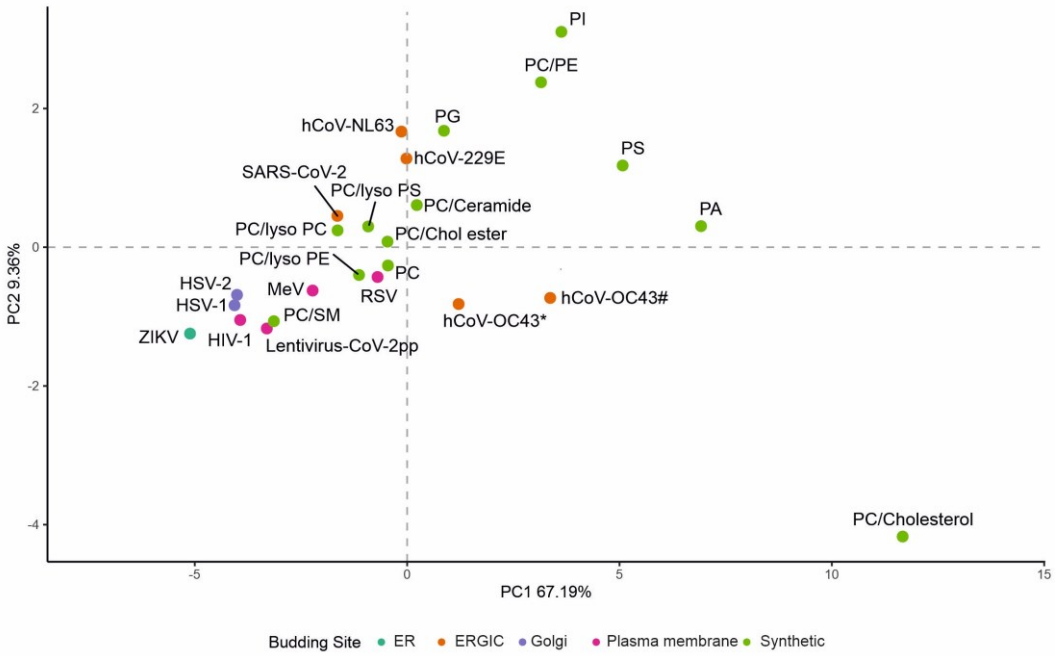

Figure 31. Principal component analysis of tweezer activity on various viruses and lipid particles. IC_{50} and EC_{50} values used in a principal component analysis are derived from Figure 14, Figure 16, Figure 20, Figure 22, Figure 24, Figure 26, Figure 29 and Figure 30. # hCoV-OC43 was produced on HCT-8 cells, * hCoV-OC43 was produced on TMPRSS2 expressing Vero E6 cells. Analysis was performed by Victoria Hunszinger (Institute of Molecular Virology, Ulm University Medical Center).

4 Discussion

4.1 Immunodetection assays for hCoV quantification

Highly pathogenic coronaviruses SARS-CoV, MERS-CoV and SARS-CoV-2 represent only one part of coronaviruses capable of infecting humans[17]. Low pathogenic hCoVs lead to seasonal waves of infection, which can also result in increased hospitalization rates[26,73] and thereby have an impact on health and economy[207,208]. However, the available detection and quantification methods for hCoVs, especially in a high-throughput manner, are minor and outdated[209].

The first aim of this study was to establish and quantify hCoV infection *in vitro*, through single cell (flow cytometry) and bulk (in-cell ELISA) high-throughput analysis. The methods were verified and used to test cell susceptibility of various cell lines towards hCoVs and potential antivirals against hCoVs. Both methods were successfully developed for hCoV-229E, -NL63 and -OC43 and resulted in virus-specific and sensitive assays, with high signal to noise ratios allowing a fast and convenient readout (Figure 6 and Figure 7). The established methods detect coronaviruses from both genera, *α*- and *β-coronaviruses*, but not the fourth hCoV infecting humans, hCoV-HKU1. This virus was not included in the study, since only primary human ciliated epithelial cells support its replication, but not the immortalized cell lines[210]. In comparison to flow cytometry and in-cell ELISA, the well-established plaque assay of hCoVs performed herein determines infectivity through virus induced cell death, however only in a small scale and after a longer incubation period until the final read-out (Figure 5)[211]. Thus, flow cytometry and in-cell ELISA represent methods with a faster and more sensitive output.

The established in-cell ELISA was then used to determine susceptibility of cells to hCoV infection (Figure 8). In accordance to literature, hCoV-229E is only able to infect hepatocyte-derived Huh-7 cells[185,212,213] of cell lines examined herein, while hCoV-OC43 infects Huh-7 and the primate kidney-derived Vero E6 cells[213,214]. HCoV-NL63 replication in Caco-2 cells is well described[152,177] and investigations here showed that human lung-derived Calu-3 cells also support the infection, as these cells express the receptor ACE2 utilized by hCoV-NL63 for entry[215]. These results demonstrated differences between hCoVs regarding their cell tropism and replication efficiency in dependency of the used target cells (Figure 8). Besides the cell susceptibility, the efficiency of anti-coronaviral compounds was evaluated by flow cytometry and in-cell ELISA (Figure 6 and Figure 9). The drug remdesivir targeting the viral RdRp was approved for COVID-19 treatment in 2020

and represents a potential antiviral for other coronaviruses. The measured IC_{50} values of remdesivir were 0.06 and 0.051 µM for hCoV-229E, 0.023 and 0.041 µM for hCoV-NL63, and 0.199 and 0.21 µM for hCoV-OC43, respectively by flow cytometry and in-cell ELISA, which is comparable between both methods and confirm those in the literature[154,180,216]. This finding is consistent for the use of another nucleoside analogue called molnupiravir und the protease inhibitor nirmatrelvir against hCoV infection[93,96]. Antiviral activity of nirmatrelvir against hCoV-NL63 and -OC43 was not reported so far and only suggested through described antiprotease activity[96]. With the investigations herein, antiviral activity of nirmatrelvir against mentioned authentic coronaviruses was demonstrated (Figure 9). Other drugs, frequently used during the SARS-CoV-2 pandemic, are monoclonal SARS-CoV-2 antibodies bamlanivimab, imdevimab and casivirimab, which did not displayed activity on hCoVs. This is expected, as monoclonal antibodies bind specifically to the receptor binding domain (RBD) of the SARS-CoV-2 S-protein, which shares only minor great similarity to the RBDs of the hCoVs S-protein[187,217,218].

Next, host-directed antivirals targeting cellular proteases that are important for the viral entry were studied for impairment of hCoV infection. The proteases TMPRSS2 and cathepsins, which process the S-protein of hCoVs during entry at the cell membrane or through the endosomal route[42], can be inhibited by CM or E-64d, respectively. The in-cell ELISA demonstrated that only hCoV-NL63 is substantially impaired by CM and slightly in the presence of E-64d, which is consistent with the published finding that this strain favors a TMPRSS2 dependent route of entry[215,219]. Testing of CM and E-64d against hCoV-229E and -OC43 was performed on Huh-7 cells, which do not express TMPRSS2[220]. Therefore, no inhibition by CM was expected. On the contrary, E-64d inhibited hCoV-229E infection completely, while hCoV-OC43 replication was strongly reduced, showing the dependency of both viruses on the cathepsin-mediated uptake. Interestingly, clinical isolates of hCoV-229E and -OC43 were reported to be susceptible to TMPRSS2 inhibition[221–223]. This result is reinforced by another study describing an effect of CM on a clinical isolate of hCoV-OC43, but not for the laboratory-adapted strain, which was also used herein[221]. These results show that the activity of hCoV entry inhibitors requires confirmation using clinical isolates.

Taken together, the developed methods can be applied to detect and quantify hCoV infection. Flow cytometry and in-cell ELISA are suitable for high-throughput manner and are easily adaptable towards other strains. Furthermore, the assays enable antiviral testing and screening of new coronavirus inhibitors.

4.2 Attachment of lipid anchors to tweezers improves their antiviral activity

Broad-spectrum antivirals possess the potential to treat newly emerging and re-emerging viruses. Application of these drugs with the potential to target the viral membrane as countermeasure is time-effective and cost-saving, making them a crucial element of pandemic preparedness[2]. The molecular tweezers represent one promising group of broad-spectrum antivirals abrogating viral infection by disrupting the viral membrane. Inhibition of several enveloped viruses, including ZIKV and HIV-1 by the molecular tweezers was reported previously[127,146].

In the second part of this study, molecular tweezers were studied against respiratory viruses, especially the newly emerged SARS-CoV-2 and other human-pathogenic members of the *Coronaviridae*. The ancestor tweezers CLR01 and CLR05 inhibit SARS-CoV-2 and hCoVs without exhibiting cytotoxicity, while IC_{50} vales reach the micromolar range (Figure 10, Figure 11 and Figure 12). These results infer the application of molecular tweezers to treat COVID-19 and makes them interesting candidates for further development. Subsequently, improvement of the antiviral activity of molecular tweezers was realized by introduction of different alkyl and aromatic side chains onto the phosphate groups of CLR01 resulting in a set of advanced tweezers. These alkyl and aromatic side chains were chosen to mimic fatty acid chains and sterols in membranes (Figure 13). Evaluation of the virucidal activity against SARS-CoV-2 pseudoparticle in a structure activity relationship study revealed C6/C7 alkyl (CP019 and CP020) and aromatic (CP025, CP024, CP026 and CP006) tweezers as the most potent groups (Figure 14 and Figure 15). This finding holds true when using authentic SARS-CoV-2 and other enveloped viruses, confirming the enhanced potential of advanced tweezers to supress viral infection, with IC_{50} values in the high nanomolar range (Figure 16 and Figure 22). In comparison to CLR01, already the addition of a C1 alkyl chain (p-CH200) enhanced the antiviral activity, which increased constantly with the length of the introduced alkyl chains. However, tweezers with C-8 (p-CH206) or longer alkyl chains (p-CH192, p-CH193) demonstrated only slightly increased activity, which might be due to constant inclusion of long side arms into the tweezer cavity, resulting in lower affinity of the side arms towards the membrane. Additionally, steric hinderance by the large alkyl arms might deny the interaction of the tweezer cavity with a lipid head group. In brief, supplementation of the tweezer CLR01 with C6 or C7 alkyl arms yielded tweezers with peak antiviral activity and highest SI values. However, further elongation of the side arms or presence of aromatic groups diminished the solubility of tweezers in aqueous physiologic solutions.

The chemical trait of alkene or alkyne moieties suggested increased rigidity of the side arms and wherefore introduced to CLR01. Interestingly, C3 and C4 alkene or alkyne tweezer displayed similar results in regard to antiviral activity and cytotoxicity as the C3 alkyl tweezer CP037 and the C4 alkyl tweezer p-CH205 (Figure 14 and Figure 15). The C5 to C7 alkyl tweezers (CP018, CP019 and CP020) harbor an increased activity in contrast to their alkene or alkyne counterparts and the cytotoxicity of the C5 to C7 alkene tweezers was equal to, whereas the cytotoxicity of alkyne tweezers was lower than that of alkyl tweezers. The reduced antiviral effect observed for alkene or alkyne tweezers might be due to stiffness in the side arms decreasing membrane insertion. This hypothesis can be accessed by computational modelling. The coupling of aromatic moieties to tweezers is based on cholesterol, which is a part of the phospholipid bi-layer. Aromatic moieties are electron enriched, flat and have a rigid π-system and proposed to undergo extensive interactions inside the membrane by London dispersion forces[224], similar to steroids. Furthermore, cholesterol is reported to increase the rigidity in the membrane[225,226]. The proposed increased membrane interaction might explain the elevated antiviral activity of aromatic tweezers against lentiviral SARS-CoV-2 pseudoparticles and several enveloped viruses, but also the relatively high cytotoxicity. Nevertheless, SI values are > 200 (figure 16), arguing that the rigid π-system of the aromatic arms interacts preferentially with the viral membrane leading to a high degree of destabilization.

As stated above, advanced tweezers are effective SARS-CoV-2 inhibitors. During the pandemic, new variants of SARS-CoV-2 emerged and outcompeted previous variants. The so-called variants of concern (VOC) alpha, beta, gamma, delta and omicron showed high transmissibility and/or the potential to evade the immune response[227]. Antibodies induced by COVID-19 vaccines or previous exposure to SARS-CoV-2 showed lower neutralization towards the VOCs, especially against omicron[69,227]. These phenotypes are caused by mutations in the SARS-CoV-2 genome that change the viral proteins, but neither affect the integrity of the host cell membrane, nor the composition of the viral envelope. Consequently, tweezers demonstrated inhibition of SARS-CoV-2 VOC alpha, beta, and delta, which suggests that also future emerging variants will be still targeted and destroyed by tweezers (Figure 16). Furthermore, advanced tweezers are broadly active and inhibit infection of several enveloped viruses such as HIV-1, IAV, MeV, RSV, ZIKV, herpesviruses and hCoVs supporting the utilization of molecular tweezers as broad-spectrum antiviral for all enveloped viruses (Figure 22). Altogether, this features the simple and fast repurposing of

the tweezers to target upcoming pathogens and a negligible chance for resistance development by the virus[228].

Taken together, the structure activity relationship study revealed an increased antiviral activity of the advanced tweezers. C6 and C7 alkyl tweezers CP019 and CP020 demonstrated IC_{50} values in the high nanomolar to low micromolar range and low cytotoxicity. The resulting SI on genuine SARS-CoV-2 reaches 208 and 532, respectively. Moreover, aromatic tweezers are able to abolish SARS-CoV-2 infection even at a lower concentration, but the CC_{50} were also decreased. Nevertheless, both groups seem promising and warrant further characterization.

4.3 Application of molecular tweezers *in vivo*

4.3.1 Activity of molecular tweezers in body fluids

The preferred application for molecular tweezers is as a therapeutic or prophylactic drug. The first barrier for the application of the tweezers is to ensure its activity and retention at the site of action. As previously reported, the tweezer CLR01 fails to remain active in presence of serum, which applies also to the advanced tweezers (Supplementary Figure 4)[146]. CLR01 binds to serum albumin, a highly abundant protein in human blood[229], preferably by interaction with lysine or arginine, as preliminary unpublished findings suggest. Furthermore, the total protein concentration of serum is many times higher than in other body fluids[126]. Further analyses are required to clarify, if the overall protein amount or the presence of specific proteins is responsible for the loss of tweezer activity in serum. Two possibilities should be addresses to evaluate this phenomenon. Firstly, the affinity of advanced tweezers to arginine and lysine residues of serum proteins should be quantified. Second, the accessibility of viruses in serum should be investigated. Nanoparticles, including viruses are covered by proteins of the respective body fluids, building up the so-called protein corona[230,231]. This might shield the virus membrane from tweezer binding. To tackle this question, viruses that were incubated in different amount of protein-solutions and body-fluids should be tested for their susceptibility to tweezers. Furthermore, antivirally active tweezer CLR05 is unable to bind lysine and arginine[147], implicating that the molecule is not scavenged by proteins and should retain the antiviral activity in serum. If this holds true, selected side arms of advanced tweezers can be coupled to CLR05 for improved antiviral activity.

Although tweezers are not antiviral active in serum, they might be applied topically for the treatment of respiratory or sexually transmitted viruses in the respiratory tract or on

anogenital surfaces, respectively. Molecular tweezers showed no loss of activity in presence of mucus derived from primary airway epithelia cells (Figure 17), suggesting that tweezers applied on airway tissue are still antivirally active. The protein concentration in the mucus was determined to be 165 µg/ml, which is approximately 780-fold lower than in serum (Supplementary Figure 5)[126]. This suggest that advanced tweezers can be applied as nasal or oral spray.

4.3.2 Antiviral activity of tweezers *in vivo*

In an *in vivo* study, advanced tweezers were tested against SARS-CoV-2 in mice and showed antiviral activity and complete abrogation of infection, when tweezers were applied intranasally and directly after mixing with the virus and an additional tweezer application after 7 hours (Figure 18). In a prophylactic set-up, no antiviral activity of tweezers was observed (Figure 19). This could have different reasons and should be addressed from various point of views. Firstly, the used K18-ACE2 mouse model is transgenically modified to allow SARS-CoV-2 infection by the expression of human ACE2 under the cytokeratin-18 (K18) gene promotor[232]. The infection leads to fast replication in the lungs, with high viral loads peaking 2 dpi and is followed by viral spread into other organs such as the brain, heart, kidney, gut and spleen[233]. As a consequence, pulmonary functions are impaired by viral infection, immune cell infiltration and high levels of cytokine and chemokines. The model features a fast and simple evaluation of antivirals *in vivo* and is highly susceptible, however the elevated viral loads and ectopic ACE2 expression inducing a changed cellular tropism of the virus, and does not reflect the pathology in COVID-19 patients[234]. Furthermore, the fast SARS-CoV-2 replication might overlay entry inhibitory effects.

Secondly, pharmacological aspects of the tweezer *in vivo* need to be analyzed. Until today, the tweezer´s stability, half-life and cellular uptake or interaction with the mucosal tissue, which can affect its activity *in vivo*, is unknown. A previous study, demonstrated internalization of molecular tweezer CLR01 into neuronal cells, astrocytes and commonly used HEK293 cells by dynamin-mediated endocytosis[235]. CLR01 is found to a small extend in early and late endosomes and enriched in lysosomes and autophagosomes, already after 30 min incubation time. Nevertheless, downstream aspects, such as the metabolization or degradation of the tweezers are matter of future investigations. These results suggest cellular uptake of molecular tweezers accompanied by the removal from the site of viral infection. However, the data shows an accumulation of tweezer in the intracellular space over time, arguing that tweezers remain in the extracellular space for a certain time[235]. Furthermore,

the tweezer accumulating in autophagosomes can inactivate viruses that enter the cells by an endocytotic route. These *in vitro* experiments provide first insights in the pharmacokinetic of tweezers, but data on the half-life in the airways or the distribution in the body are still required. Attar et al. reported previously a plasma half-life from CLR01 of around 2.5 h when applied subcutaneously or intravenously and only low concentration when administered orally[236].

Taken together, the establishment of molecular tweezers as antiviral drug of respiratory viruses requires comprehensive investigations in regard to cellular metabolization, half-life, distribution and stability in the mucosa of the airways. This obtained knowledge might than help to improve the tweezers specificity and *in vivo* activity.

4.4 Viral budding route influences the tweezer activity

4.4.1 Characteristics of cellular membranes affect the viral envelope composition and structure

During the budding process, many viruses get equipped with an envelope, which consists of a phospholipid membrane decorated with viral glycoproteins that are required for entry of another host cell[115]. The lipid composition of the viral envelope depends on the budding site. Viruses are known to bud directly from the plasma membrane (PM) releasing the virions into the extracellular space[237]. Budding can also occur at intracellular membranes from the nuclear envelope, the ER, the endosome, the endoplasmic-reticulum Golgi intermediate complex (ERGIC) and the Golgi requiring transport through the cell and the release into the extracellular environment by fusion of the PM and the vesicular membrane, the virus is captured in. The viruses investigated in this study are described to bud through the ER[198,199] (ZIKV), Golgi[200] (HSV-1 and HSV-2), ERGIC[22,34,188,194] (*Coronaviridae*) and the PM[195–197] (HIV-1, MeV, RSV and lentiviral pseudoparticles) (Figure 32). Little is known about the lipid composition of viral envelops. Cellular membranes are mainly composed of different sorts of phospholipids, sphingolipids and sterols[238]. However, their ratios and distribution differ hugely between different membranes, thus influencing the membrane properties. Investigations on the lipid membranes of eukaryotic cells revealed that phospholipids make up the majority of membrane lipids, whereby phospholipids with unsaturated fatty acid chains are preferably found at the ER and the Golgi[114]. The main phospholipids found in eukaryotic membranes are PC and PE, followed by PI and PS[201,239]. PA is a minor membrane phospholipid with an amount of 1 – 4 %[201,240]. The overall phospholipid concentration decreases along the secretory pathway, only PS is enriched in the PM[239]. Vice

versa, levels of SM and Chol increase along the secretory pathway and reach the highest concentration in the PM (Figure 32).

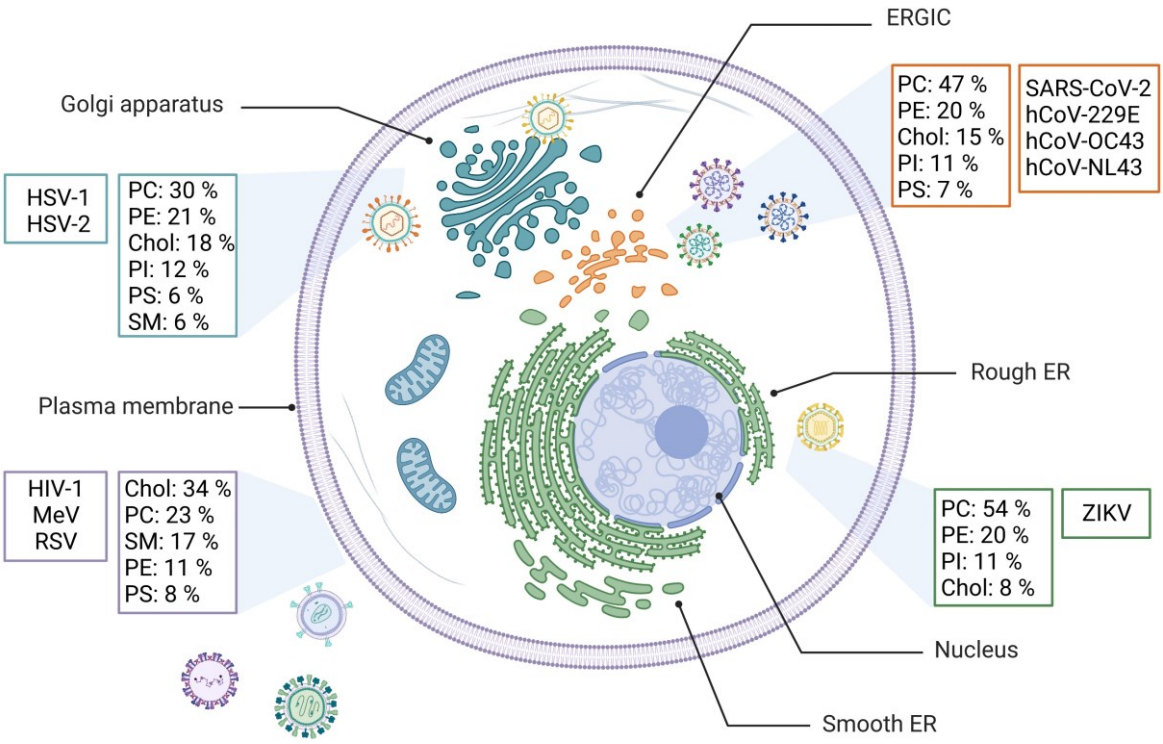

Figure 32. Lipid composition of cellular membranes that serve as viral budding sites. Budding of viruses occurs from different locations including the plasma membrane and membranes from organelles. Each membrane is composed of different lipids influencing the envelope identity of the virus. PC: phosphatidylcholine, PE: phosphatidylethanolamine, PS: phosphatidylserine, PI: phosphatidylinositol, SM: sphingomyelin, Chol: cholesterol. Values of lipid content and compositions of each organelle were used from Casares et al.[201] and Casalino et al.[241]. Figure was created with BioRender.com. Printed with permission according to Biorender Academic License Terms (https://biorender.com/terms/).

The PM is the best studied cellular membrane. It is described to hold more sphingolipids compromising long saturated fatty acid chains that makes the membrane less mobile. Furthermore, Chol itself is reported to reduce membrane fluidity [225,226,240,242].Altogether, the PM contains high levels of saturated lipids, SM, and Chol, which are linked to each other by a strong hydrogen bonding[113,238] making the membrane thicker, tightly packed, robust and less fluid. This organization is described as a liquid-ordered domain L_o[238,243], whose properties strengthen the PM and feature a higher resistance against mechanical stress from the environment[114,244]. Through accumulation of these lipids by interactions, specific nanodomains, so-called lipid rafts assemble in the PM, which contain high concentrations of Chol, SM and saturated lipids and are described as heterologous, dynamic liquid-ordered L_o nanodomains (10-200 nm) (Figure 33)[113,201,245]. These domains are present in both, the inner and outer leaflet of membranes and build up a lateral heterogenicity within their leaflet[113,238]. Viruses take advantage of lipid rafts as a preferred budding place, since the

ordered-lipid state L_o strengthens and increase the rigidity of viral membranes. HIV-1 lipidome studies revealed high levels of saturated lipids, sphingolipids and Chol in the envelope, even higher in comparison to the producer cells[246,247], enabling the specific targeting by membrane acting antivirals as the molecular tweezers. Moreover, the HIV-1 glycoprotein gp41 contains a cholesterol binding motif, which regulates its membrane distribution confirming the budding route through lipid rafts (Figure 33)[113].

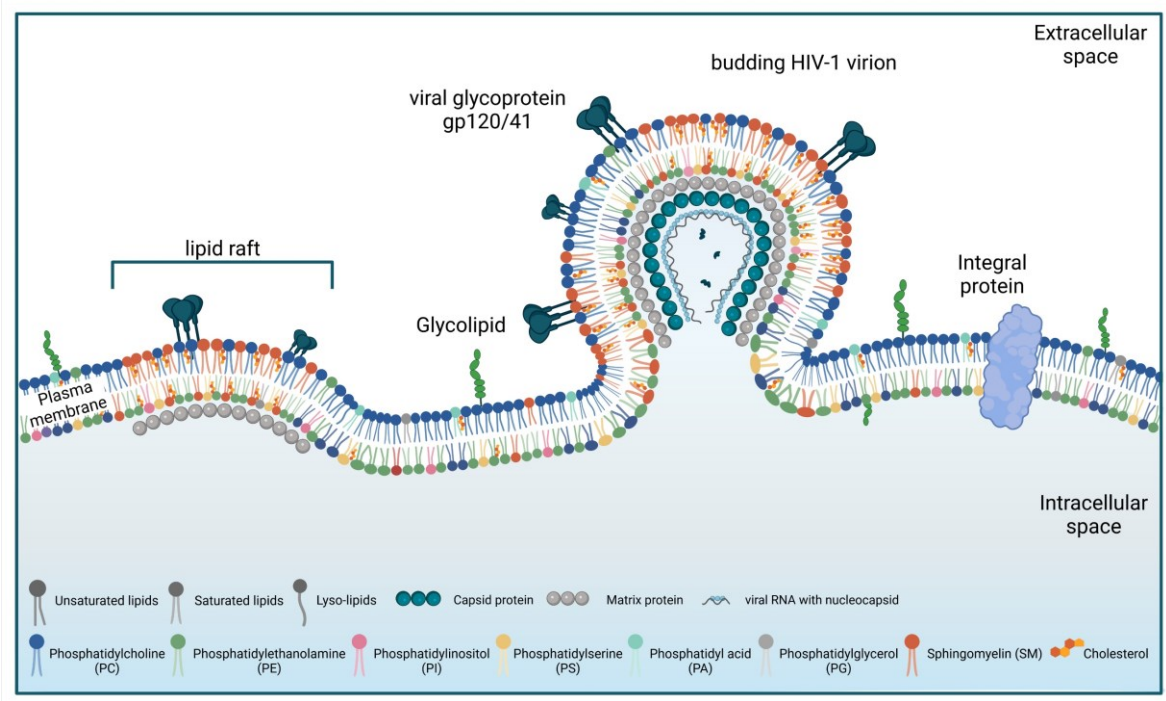

Figure 33. Illustrated viral budding process of HIV-1 through the plasma membrane. During the budding process, viruses gets surrounded by the envelope consisting of a phospholipid bi-layer. The PM is an asymmetric and heterologous membrane and contains phospholipids, sphingolipids and sterols. Budding of HIV-1 is favoured through lipid rafts, which are enriched in sphingomyelin and cholesterol. Modified from Weil and Münch 2023[248] (CC BY 4.0; https://creativecommons.org/licenses/by/4.0/, Copyright© The Authors, permission to remix and transform was obtained from the creator). Figure was created with BioRender.com. Printed with permission according to Biorender Academic License Terms (https://biorender.com/terms/).

In contrast to the lipid-ordered domains L_o, unsaturated lipids in membranes cause an opposite effect due to acyl-chain kinks, thereby preventing a tight packing resulting in greater fluidity and a so-called liquid-disordered domain L_d[238,243]. This state makes the membrane relatively thin and flexible, and is found in membranes with high unsaturated phospholipid amount, such as the ER[249].

Furthermore, membranes are asymmetric structures (Figure 33). The phospholipids PE, PS and PI are enriched in the inner/cytoplasmic leaflet of the PM and Golgi[114,201,239,250], while in the outer/luminal leaflet PC and sphingolipids are mostly present[226]. The sterol Chol can be found in both, the inner and outer leaflet due to a high propensity to flip between both leaflets, but its enriched in the outer leaflet[243]. This asymmetry is accomplished by

ATP-dependent flippases (lipid transport from the extracellular/luminal to cytosolic side), floppases (lipid transport from cytosolic to the luminal leaflet) and ATP-independent scramblases (a bi-directional transport randomizing the asymmetry)[114,239,251]. However, viruses inactivate flippases and activate scramblases, which results in an increased level of PS in the outer leaflet of the viral envelope[252], providing an option to specify viral membrane targeting.

Besides the lipid distribution and composition of membranes, the chemical and physical abilities such as lipid charge and shape influence the membrane integrity. As a short recapitulation, only PC and PE have neutral head groups, whereas PS, PG, PA and PI lipids contain negatively charged head groups[203]. Furthermore, Chol and SM were described to lower the zeta potential of a membrane[204,205]. Additionally, the shape of a lipid has a strong impact on the membrane structure by induction of a positive or negative curvature (Figure 34). The most abundant phospholipid PC and the lipids PG and PS are cylindrical, forming nearly flat lipid layers without curvature formation under physiological conditions[238,240]. The head groups of PA and PE are relatively small, in comparison to the headgroup of PC. Thus, the lipids together with Chol have a cone shape inducing spontaneous negative curvature, which is important in fusion and fission processes[238,240,251,253]. On the contrary, lyso-lipids harbouring only one lipid tail possess an inverted cone shape and, hence, induce a positive spontaneous curvature[206].

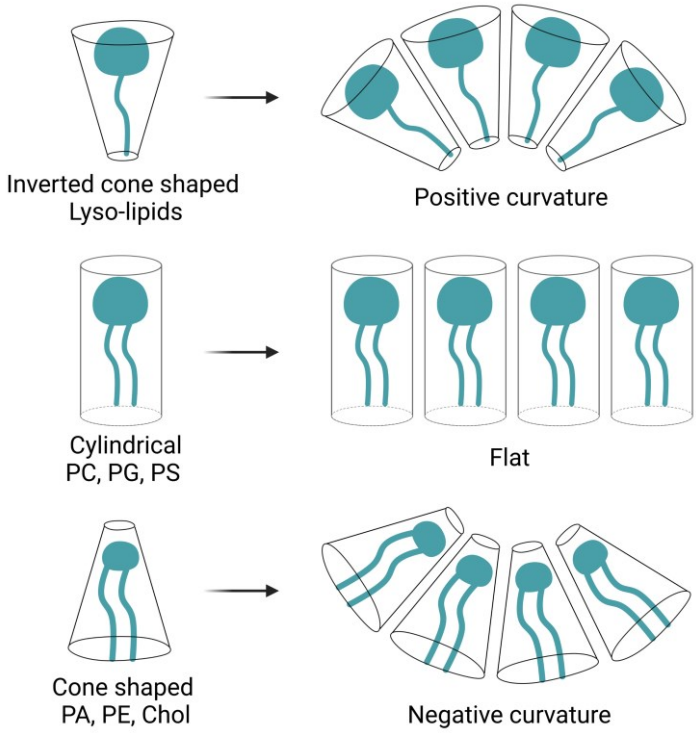

Figure 34. The shape of lipids influences the membrane structure. Lyso-lipids contain only one lipid tail, which results in an inverted cone shaped structure and formation of positive curvature. On the contrary, lipids

with relatively small head groups such as PE, PA or Chol possess a cone shape and induce negative curvature formation. Phospholipids PC, PG and PS are cylindrical lipids exhibit no curvature. Figure was created with BioRender.com. Printed with permission according to Biorender Academic License Terms (https://biorender.com/terms/). Adapted from Peeters and Piët et al. 2022[254] (Department of Cell Biology, Erasmus MC, Rotterdam, The Netherlands; CC BY 4.0; https://creativecommons.org/licenses/by/4.0/, Copyright© The Authors¸ https://doi.org/10.3390/cells11030469).

The shapes of lipids have been reported to not only influence curvature formation but also packing of lipids. Cone-shaped lipids such as PA can induce packing defects in the membrane leading to a higher exposure of the hydrophobic region of the membrane towards the aqueous environment[255]. This effect can also be promoted by monounsaturated lipids in the membrane or induced mechanical bending.

In sum, cellular membranes are composed by different lipid composition, which can influence the structure over their charge, shape, interactions, packing density and fluidity. These properties will cause viruses to have differently composed envelopes according to their defined budding route and can influence the activity of molecular tweezers.

4.4.2 Improved membranolytic activity of advanced tweezers

In a previous study, the molecular mechanism by which molecular tweezers CLR01 and CLR05 disrupt the viral membrane was elucidated[147]. Each tweezer captures a lipid head group present in the outer layer of the viral envelope into its cavity. This induces an orientation change of the lipid, which allows penetration of the tweezer into the external layer of the membrane, resulting in increased surface tension, destabilization of the membrane and abrogation of infectivity[147]. With this knowledge, the mechanism of advanced tweezers was analyzed, since they displayed an enhanced antiviral activity, especially the C6/C7 alkyl and aromatic tweezers. The liposome dye leakage assay showed that the advanced tweezers still bind to the viral membrane and disrupt small vesicles with higher efficiency than CLR01 and CLR05 (Figure 20). Computational modelling of advanced tweezers displayed an altered orientation of the bound lipid head group similar to CLR01, leading to penetration of the tweezers into the membrane (Figure 21). Additionally, the simulations revealed that one or both side arms of advanced tweezers are inserted into the membrane, thus increasing the membrane tension further, explaining the increased activity (Figure 21 and Figure 35). Elongation of the alkyl side arms resulted in a steadily increasing activity (Figure 15), which might be explained due to deeper side arm insertion into the membrane and increased tension. However, this requires extended computational modelling analysis.

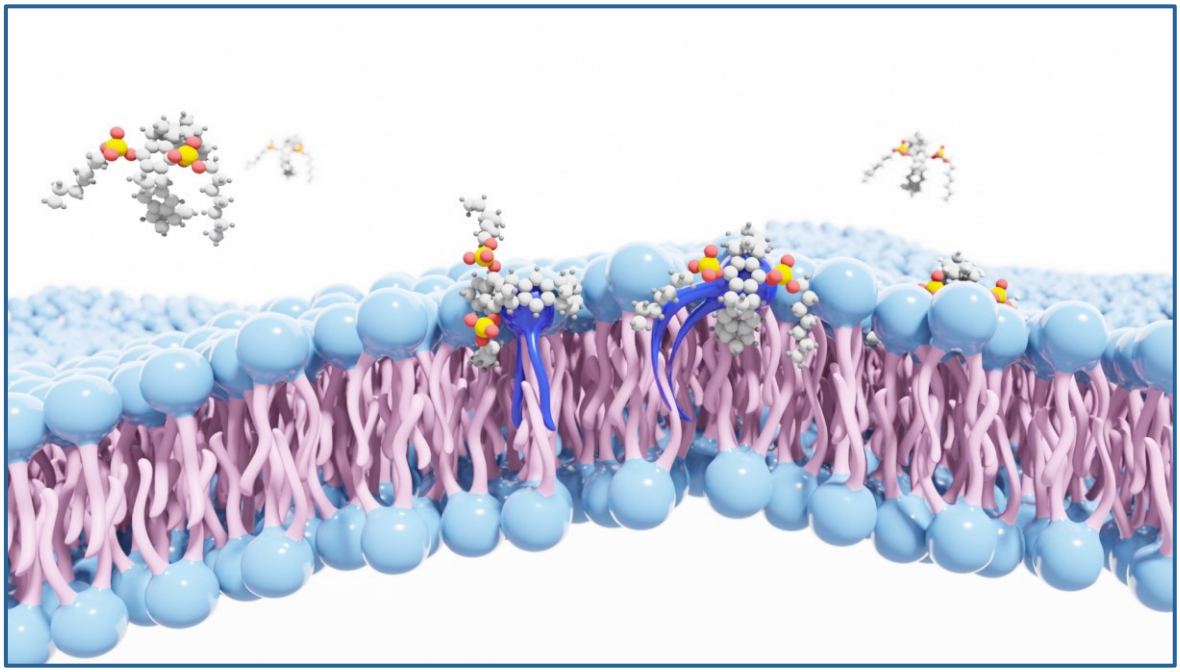

Figure 35. Antiviral mechanism of advanced molecular tweezers. Binding of tweezers to lipid head groups in the viral envelope and subsequent insertion into the lipid bilayer results in increased surface tension and membrane disruption. Addition of aliphatic or aromatic ester groups on CLR01 increases the antiviral activity by broad binding to various lipids and additional insertion of the side arms into the membrane. Figure was created by Joel Mieres-Perez (Institute of Computational Biochemistry, University of Duisburg-Essen). Obtained from Weil et al. 2022[159] (CC BY-NC-ND 4.0; https://creativecommons.org/licenses/by-nc-nd/4.0/, Copyright© The Authors, permission to remix and transform was obtained from the creator).

Furthermore, the side arms of advanced tweezers enable the binding to a broader panel of phospholipids, except for C6 alkyne tweezer CP021 (Figure 29). This novel ability expands the mode of action, postulated for CLR01. As a short recapitulation, lipid binding through ancestor tweezers was possible by inclusion of the entire choline head group of SM or DOPC into the tweezer cavity[147]. This is confirmed by CLR03 which lacks the cavity and thus is unable to bind to head groups. Choline head group inclusion was demonstrated for ancestor tweezers CLR01, CLR05 and PC. Furthermore, the interaction between tweezer and SM was shown to be more stable than with DOPC, due to a strong intramolecular hydrogen bond within SM[256], diminishing the desolvation cost and stabilizing the tweezer-SM complex[147]. Advanced tweezers also show the highest membranolytic activity towards SM containing liposomes in the dye leakage assay (Figure 29). However, interaction of advanced tweezers takes also place with lipids lacking the choline head group, as PA, PS, PG, PI and PE. These phospholipids are neutral (PE) or negatively charged (PS, PG, PA and PI), have varying lipid shapes (PA, PE, Chol: cone, lyso-lipids: inverted cone and PC, PS, PG: cylindrical) and carry various head groups. Investigation to clarify how the advanced tweezers bind to these lipids need to be performed. For example, biomolecular modelling

can be used to simulate the behaviour of advanced tweezers on uniform phospholipid membrane layers with varying composition. The results could resolve how the side arms evoke the binding potential to other lipid head groups than choline, and if the cavity of the tweezers is still necessary for membrane disruption. Investigating the membranolytic activity of CLR03 coupled to various side arms might further help to answer this question.
Preliminary unpublished NMR experiments were conducted to investigate the interaction of aromatic or C6/C7 alkyl tweezers to SM in methanol. The affinity of C7 alkyl tweezer CP020 was 15 mM, whereas aromatic tweezers demonstrated similar values as CLR01 (K_D = 8 mM[147,159]) suggesting not only the binding affinity to SM is responsible for increased membranolytic activity. Other factors such as the degree of side arm intercalation or the ratio of destabilization inside the membrane might play a role. Additionally, binding affinities in an aqueous environment or on multi-lipid vesicles might differ. To analyse the binding affinities of advanced tweezers further, more tweezers and lipid types should be included in NMR analysis or tested in Langmuir film balance measurements[257], which might give insight in the degree of induced tension on membranes by each tweezer.

4.4.3 Membranolytic activities of advanced tweezers are influenced by the lipid composition and the particle size

Analyzing the antiviral properties of each tweezer revealed a varying activity pattern against the examined enveloped viruses. For example, when comparing tweezer activity against authentic SARS-CoV-2 and lentiviral pseudoparticles harboring the SARS-CoV-2 S-protein no correlation was observed. For instance, CP025 was the least active aromatic tweezer against lentiviral SARS-CoV-2 pseudoparticles, while it was one of the most active aromatic tweezers against authentic SARS-CoV-2 (Figure 14 and Figure 16). Interestingly, authentic SARS-CoV-2 buds from the ERGIC, while lentiviral pseudoparticles bud from the PM. It is tempting to speculate that the budding route and therefore the lipid composition of the viral envelope impacts the tweezer susceptibility of a virus. When analysing the tweezer activities towards viruses in PCA, it is remarkable, that viruses budding from the ERGIC (*Coronaviridae*) cluster very differently than those budding from the PM (HIV-1, MeV, lentiviral pseudoparticles and RSV) (Figure 25). PM budding viruses may contain high levels of sphingolipids, saturated lipids and Chol in an ordered-state L_o, whereas the ERGIC budding viruses might harbour an increased concentration of unsaturated phospholipids, decreasing the packing density and the rigidity (4.4.1). This goes along with data obtained from uniform or mixed liposomes in the dye leakage assay. Tweezer with high activities

against liposomes made from PS, PI, PA, PG and PC/PE that might be enriched in the ERGIC demonstrated high activity against *Coronaviridae*, whereas tweezers against liposomes with sterols, sphingolipids and PC that represent the PM showed a higher activity to PM budding viruses (Figure 22, Figure 29 and Figure 31). Especially, the aromatic tweezer CP025 revealed an increased activity against phospholipid liposomes and ERGIC budding viruses, but not in the presence of sterol or sphingolipid liposomes, as also be seen for PM budding viruses. Thorough analysis on the lipidome of viruses - which is thus far only known for HIV-1[247] – this hypothesis can be address further. However, these observations must be interpreted with caution, since the tweezer activity was investigated only against liposomes with one or two lipid sources, not representing the complexity of a viral envelope. Moreover, it is highly likely that factors other than the lipid composition in the viral membrane, such as the glycoproteins as well as their density, the surrounding protein-corona, and the size affect the activity of the tweezers.

Besides the overall lipid composition, lipid characteristics such as the shape and related curvature induction might as well influence the membranolytic activity of tweezers. PA and Chol lipids harbouring a cone shape and are known to generate a negative curvature, which causes compression in the membrane (Figure 34)[258]. Additionally, PA is capable of inducing packing defects leading to a higher exposure of hydrophobic fatty acid tails towards the aqueous environment[240,255,259]. Both characteristics seem to impede the lipid head accessibility and as expected, decrease the tweezer activity in the liposome dye leakage assay (Figure 29). A similar effect can be overserved for neutrally charged PC/PE liposomes: The presence of the cone shaped PE results in a reduced efficiency of the tweezers. On the contrary, lyso-lipids with their inverted cone shape increase the permeability and curvature stress of a membrane by formation of a positive curvature[206,240]. Consequently, the tweezer activity in the liposomes dye leakage assay was increased when lyso-lipids were spiked into PC liposomes (Figure 30).

Furthermore, the saturation degree of lipid tails determines the packing density of lipids, thereby controlling the rigidity or fluidity of a membrane[259]. Alkene bonds in monounsaturated lipids, preferably found in the ER and Golgi, form a disordered state L_d with higher fluidity, while saturated lipids (enriched in the PM) are cylindrical and tightly packed[238]. Polyunsaturated lipids are able to shallow the disordered state L_d and increase the packing density[255]. The influence of saturated, unsaturated and polyunsaturated lipids on tweezer activity remains elusive and requests investigation, which can be accomplished in liposome dye leakage assay. This method can also help to clarify the impact of different

lipid tail lengths and membrane asymmetry on the tweezer activity, factors which further complex the membrane organization. The properties of lipids influencing the packing density, fluidity/rigidity and curvature formation that affect the tweezer activity can be further investigated in a biomolecular modelling approach or with the Langmuir film balance.

Besides the lipid composition, the particle size was investigated in regard to the tweezer activity. Viruses are varying in their size, ranging between 20 to 400 nm in diameter, with 100 nm as typical size[260]. Moreover, filoviruses such as the EBOV can reach a length over 1000 nm. Most viruses examined in this study are around 100 to 200 nm in size, whereas ZIKV exhibits only 40 to 60 nm in diameter (Table 4). Interestingly, smaller viruses were more susceptible to tweezers (Figure 22), which is confirmed by liposomes of defined particle sizes ranging from 50 to 800 nm (Figure 23). With an increase of the liposome size in diameter, the activity of the tweezers was reduced and an increased number of tweezer molecules were required for complete membrane disruption.

Table 4. Virus size. Investigated viruses in this study vary in their size in diameter.

Virusfamily	Virus	Size	Source
Flaviviridae	ZIKV	40 - 60 nm	King et al.[191]
Retroviridae	HIV-1	145 ± 25 nm	Briggs et al.[261]
Herpesviridae	HSV-1	170 - 200 nm, average of 186 nm	Grünewald et al. [262]
Herpesviridae	HSV-2	180 – 200 nm	Mundle et al.[263]
Paramyxoviridae	MeV	100 – 250 nm	Azap and Pehlivanoglu[264]
Pneumoviridae	RSV	150 – 250 nm	Utley et al.[265]
Coronaviridae	SARS-CoV-2	91 ± 11 nm	Ke et al.[188]

The analysis of the factor size influencing the tweezer activity was further expanded using GUVs. GUVs of the size of small cells, for example erythrocytes[192,193], were destroyed by tweezers, but a significantly higher number of tweezer molecules was required to do so (Figure 24). Rupture of GUVs might explain the cytotoxic effect on cells by tweezers when applied at high concentrations. However, cells possess a membrane repair mechanism allowing the fixation of small gaps[266,267]. Interestingly, when normalized to the total lipid

number, tweezers displayed even a 260-fold increased activity towards liposomes than towards GUVs. This shows that not only the amount of lipids, but also the curvature of the membrane impacts the tweezer activity. Viruses as nanoparticles exhibit a highly curved membrane leading to an increased positive bending in comparison to cells[258,268]. This suggests that the membrane, being highly curved, is under significant stress and more vulnerable to being disrupted by tweezers. The enhanced disruption of highly curved particles was observed across all tweezers, with the C6/C7 alkyl and alkyne tweezer being the most effective among them (Figure 24e). These insights might open another way for increasing the specificity of tweezers towards viruses.

In sum, the tweezer activity against enveloped viruses originating from different budding sites shows overlap with the tweezers lipid specificity and accompanying lipid characteristics. Besides the lipid specificity, the size and the corresponding curvature of a virus also impacts the tweezer activity. This study shows that C6/C7 alkyl and aromatic tweezers display the most promising antiviral and membranolytic activities of the advanced tweezers and the insight herein can be used to improve the tweezer as membrane targeting antivirals.

5 Summary

The frequent occurrences of viral outbreaks and the ongoing transmission of zoonotic viruses highlight the threat posed by emerging and re-emerging viruses. Pandemics, characterized by widespread and global infection waves with high mortality rates, present a significant challenge for the human health. The emergence of SARS-CoV-2 in late 2019 necessitated the rapid characterization of the virus and the development of targeted countermeasures. Swiftly approved vaccines helped to reduce hospitalization rates and severe disease progression, but new SARS-CoV-2 variants have emerged that can evade immunity, leading to contagion and new infection waves. Recently approved drug regimens protect against severe COVID-19 progression, but only when administered early. These events and the risk from other zoonotic spillovers emphasize the need for broad-spectrum antivirals that can be readily used when encountering a novel virus as a measure of pandemic preparedness.

In this study, high-throughput methodologies like flow cytometry and in-cell ELISA were established to quantify hCoV infection, enabling antiviral testing and identification of new inhibitors, including broad-spectrum antivirals. The study's second part focused on enhancing the antiviral activity of a group of broad-spectrum antivirals called molecular tweezers. Molecular tweezers are known to inhibit various respiratory viruses and offer potential for repurposing against newly emerged viruses. The incorporation of a lipid head group into the tweezer's cavity causes an orientation change of the lipid, allowing the tweezer to penetrate the viral membrane's outer layer. This increases tension and subsequently disrupts the viral membrane, enabling tweezers to inhibit enveloped viruses. By chemically introducing aliphatic or aromatic side chains that mimic lipid components and function as lipid anchors, the antiviral activity of advanced tweezers was improved. A structure-activity relationship study identified C6/C7 alkyl and aromatic tweezers as promising lead candidates for further preclinical development. This was confirmed against authentic SARS-CoV-2 in immunodetection assays and TEM analysis. *In vivo* studies in mice showed complete viral abrogation of SARS-CoV-2 infection by advanced tweezers when mixed with the virus and directly administered, but not in a prophylactic setting, indicating a need for further pharmacokinetic analysis in the upper respiratory tract. Mechanistic studies of the advanced tweezers showed increased membranolytic activity against virus-like liposomes. Unlike ancestral tweezers, advanced tweezers were not limited to binding exclusively to lipids with a choline head group (phosphatidylcholine and sphingomyelin) and exhibited therefore a broader lytic activity. Additionally, advanced tweezers not only incorporated lipid head

groups into their cavity but also inserted their introduced side arms into membranes, further elevating viral membrane tension, as demonstrated by computational modeling.

Principal component analysis during the characterization of advanced tweezers suggested that the viral budding site and thus the lipid composition of the viral envelope influence the antiviral activity of tweezers. Viral membranes are proposed to contain different lipid head groups that serve as tweezer target, and each lipid species can alter the membrane characteristics in charge, shape, packing density, and fluidity, which may also affect the efficacy of tweezers. To simplify the biological membrane for tweezer investigations, uniform or two-lipid liposomes representing the most abundant lipid types in the membrane were generated and exposed to advanced tweezers. The study revealed a lipid specificity of tweezers, influenced by lipid characteristics and overlapped with the antiviral activity of tweezers against viruses from distinct budding sites and their assumed lipid composition. Additionally, investigations with differently sized vesicles showed that particle size and curvature also impacted the tweezer activity. Tweezers disrupted highly curved liposomes, mimicking viruses with higher efficiency than giant unilamellar vesicles, which represent small cells in size. The C6/C7 alkyl and alkyne tweezers were most effective on small, highly curved particles, increasing their specificity towards viruses.

In summary, molecular tweezers as broad-spectrum antivirals presented here are promising candidates for treating known or emerging enveloped viruses. The molecular tweezers were enhanced and characterized to specify their activity against viruses from distinct budding sites.

6 References

1. Kreuder Johnson, C., Hitchens, P. L., Smiley Evans, T., Goldstein, T., Thomas, K., Clements, A., Joly, D. O., Wolfe, N. D., Daszak, P., Karesh, W. B. & Mazet, J. K. Spillover and pandemic properties of zoonotic viruses with high host plasticity. *Sci Rep* **5**, 14830 (2015).
2. Simpson, S., Kaufmann, M. C., Glozman, V. & Chakrabarti, A. Disease X: accelerating the development of medical countermeasures for the next pandemic. *The Lancet Infectious Diseases* **20**, e108–e115 (2020).
3. Trilla, A., Trilla, G. & Daer, C. The 1918 "Spanish Flu" in Spain. *Clinical Infectious Diseases* **47**, 668–673 (2008).
4. Deeks, S. G., Overbaugh, J., Phillips, A. & Buchbinder, S. HIV infection. *Nat Rev Dis Primers* **1**, 1–22 (2015).
5. Jacob, S. T., Crozier, I., Fischer, W. A., Hewlett, A., Kraft, C. S., Vega, M.-A. de L., Soka, M. J., Wahl, V., Griffiths, A., Bollinger, L. & Kuhn, J. H. Ebola virus disease. *Nat Rev Dis Primers* **6**, 1–31 (2020).
6. Drosten, C., Günther, S., Preiser, W., van der Werf, S., Brodt, H.-R., Becker, S., Rabenau, H., Panning, M., Kolesnikova, L., Fouchier, R. A. M., Berger, A., Burguière, A.-M., Cinatl, J., Eickmann, M., Escriou, N., Grywna, K., Kramme, S., Manuguerra, J.-C., Müller, S., Rickerts, V., Stürmer, M., Vieth, S., Klenk, H.-D., Osterhaus, A. D. M. E., Schmitz, H. & Doerr, H. W. Identification of a novel coronavirus in patients with severe acute respiratory syndrome. *N Engl J Med* **348**, 1967–1976 (2003).
7. Zaki, A. M., van Boheemen, S., Bestebroer, T. M., Osterhaus, A. D. M. E. & Fouchier, R. A. M. Isolation of a novel coronavirus from a man with pneumonia in Saudi Arabia. *N Engl J Med* **367**, 1814–1820 (2012).
8. Zhu, N., Zhang, D., Wang, W., Li, X., Yang, B., Song, J., Zhao, X., Huang, B., Shi, W., Lu, R., Niu, P., Zhan, F., Ma, X., Wang, D., Xu, W., Wu, G., Gao, G. F. & Tan, W. A Novel Coronavirus from Patients with Pneumonia in China, 2019. *N Engl J Med* **382**, 727–733 (2020).
9. Markotter, W., Coertse, J., De Vries, L., Geldenhuys, M. & Mortlock, M. Bat-borne viruses in Africa: a critical review. *Journal of Zoology* **311**, 77–98 (2020).
10. El-Sayed, A. & Kamel, M. Coronaviruses in humans and animals: the role of bats in viral evolution. *Environ Sci Pollut Res* **28**, 19589–19600 (2021).

11. Letko, M., Seifert, S. N., Olival, K. J., Plowright, R. K. & Munster, V. J. Bat-borne virus diversity, spillover and emergence. *Nat Rev Microbiol* **18**, 461–471 (2020).
12. Pierson, T. C. & Diamond, M. S. The continued threat of emerging flaviviruses. *Nat Microbiol* **5**, 796–812 (2020).
13. Disease Outbreak News. https://www.who.int/emergencies/disease-outbreak-news.
14. Yoon, B. K., Jeon, W.-Y., Sut, T. N., Cho, N.-J. & Jackman, J. A. Stopping Membrane-Enveloped Viruses with Nanotechnology Strategies: Toward Antiviral Drug Development and Pandemic Preparedness. *ACS Nano* **15**, 125–148 (2021).
15. Leung, N. H. L. Transmissibility and transmission of respiratory viruses. *Nat Rev Microbiol* **19**, 528–545 (2021).
16. Zhou, Z., Qiu, Y. & Ge, X. The taxonomy, host range and pathogenicity of coronaviruses and other viruses in the Nidovirales order. *Animal Diseases* **1**, 5 (2021).
17. Chen, B., Tian, E.-K., He, B., Tian, L., Han, R., Wang, S., Xiang, Q., Zhang, S., El Arnaout, T. & Cheng, W. Overview of lethal human coronaviruses. *Sig Transduct Target Ther* **5**, 1–16 (2020).
18. Hamre, D. & Procknow, J. J. A new virus isolated from the human respiratory tract. *Proc Soc Exp Biol Med* **121**, 190–193 (1966).
19. McIntosh, K., Dees, J. H., Becker, W. B., Kapikian, A. Z. & Chanock, R. M. Recovery in tracheal organ cultures of novel viruses from patients with respiratory disease. *Proc Natl Acad Sci U S A* **57**, 933–940 (1967).
20. van der Hoek, L., Pyrc, K., Jebbink, M. F., Vermeulen-Oost, W., Berkhout, R. J. M., Wolthers, K. C., Wertheim-van Dillen, P. M. E., Kaandorp, J., Spaargaren, J. & Berkhout, B. Identification of a new human coronavirus. *Nat Med* **10**, 368–373 (2004).
21. Woo, P. C. Y., Lau, S. K. P., Chu, C., Chan, K., Tsoi, H., Huang, Y., Wong, B. H. L., Poon, R. W. S., Cai, J. J., Luk, W., Poon, L. L. M., Wong, S. S. Y., Guan, Y., Peiris, J. S. M. & Yuen, K. Characterization and complete genome sequence of a novel coronavirus, coronavirus HKU1, from patients with pneumonia. *J Virol* **79**, 884–895 (2005).
22. Liu, D. X., Liang, J. Q. & Fung, T. S. Human Coronavirus-229E, -OC43, -NL63, and -HKU1 (Coronaviridae). *Encyclopedia of Virology* 428–440 (2021).
23. Killerby, M. E., Biggs, H. M., Haynes, A., Dahl, R. M., Mustaquim, D., Gerber, S. I. & Watson, J. T. Human coronavirus circulation in the United States 2014-2017. *J Clin Virol* **101**, 52–56 (2018).

24. Li, Y., Wang, X. & Nair, H. Global Seasonality of Human Seasonal Coronaviruses: A Clue for Postpandemic Circulating Season of Severe Acute Respiratory Syndrome Coronavirus 2? *J Infect Dis* jiaa436 (2020).
25. Park, S., Lee, Y., Michelow, I. C. & Choe, Y. J. Global Seasonality of Human Coronaviruses: A Systematic Review. *Open Forum Infect Dis* **7**, ofaa443 (2020).
26. Corman, V. M., Muth, D., Niemeyer, D. & Drosten, C. Hosts and Sources of Endemic Human Coronaviruses. *Adv Virus Res* **100**, 163–188 (2018).
27. Dhama, K., Khan, S., Tiwari, R., Sircar, S., Bhat, S., Malik, Y. S., Singh, K. P., Chaicumpa, W., Bonilla-Aldana, D. K. & Rodriguez-Morales, A. J. Coronavirus Disease 2019-COVID-19. *Clin Microbiol Rev* **33**, e00028-20 (2020).
28. Cui, J., Li, F. & Shi, Z.-L. Origin and evolution of pathogenic coronaviruses. *Nat Rev Microbiol* **17**, 181–192 (2019).
29. Ye, Z.-W., Yuan, S., Yuen, K.-S., Fung, S.-Y., Chan, C.-P. & Jin, D.-Y. Zoonotic origins of human coronaviruses. *Int J Biol Sci* **16**, 1686–1697 (2020).
30. Chen, Y., Liu, Q. & Guo, D. Emerging coronaviruses: Genome structure, replication, and pathogenesis. *J Med Virol* **92**, 418–423 (2020).
31. Woo, P. C. Y., Lau, S. K. P., Lam, C. S. F., Lau, C. C. Y., Tsang, A. K. L., Lau, J. H. N., Bai, R., Teng, J. L. L., Tsang, C. C. C., Wang, M., Zheng, B.-J., Chan, K.-H. & Yuen, K.-Y. Discovery of seven novel Mammalian and avian coronaviruses in the genus deltacoronavirus supports bat coronaviruses as the gene source of alphacoronavirus and betacoronavirus and avian coronaviruses as the gene source of gammacoronavirus and deltacoronavirus. *J Virol* **86**, 3995–4008 (2012).
32. Su, S., Wong, G., Shi, W., Liu, J., Lai, A. C. K., Zhou, J., Liu, W., Bi, Y. & Gao, G. F. Epidemiology, Genetic Recombination, and Pathogenesis of Coronaviruses. *Trends Microbiol* **24**, 490–502 (2016).
33. Fehr, A. R. & Perlman, S. Coronaviruses: an overview of their replication and pathogenesis. *Methods Mol Biol* **1282**, 1–23 (2015).
34. V'kovski, P., Kratzel, A., Steiner, S., Stalder, H. & Thiel, V. Coronavirus biology and replication: implications for SARS-CoV-2. *Nat Rev Microbiol* **19**, 155–170 (2021).
35. Tortorici, M. A. & Veesler, D. Structural insights into coronavirus entry. *Adv Virus Res* **105**, 93–116 (2019).
36. Li, F. Structure, Function, and Evolution of Coronavirus Spike Proteins. *Annu Rev Virol* **3**, 237–261 (2016).

37. Letko, M., Marzi, A. & Munster, V. Functional assessment of cell entry and receptor usage for SARS-CoV-2 and other lineage B betacoronaviruses. *Nat Microbiol* **5**, 562–569 (2020).
38. Li, Z., Tomlinson, A. C., Wong, A. H., Zhou, D., Desforges, M., Talbot, P. J., Benlekbir, S., Rubinstein, J. L. & Rini, J. M. The human coronavirus HCoV-229E S-protein structure and receptor binding. *eLife* **8**, e51230 (2019).
39. Hoffmann, M., Kleine-Weber, H., Schroeder, S., Krüger, N., Herrler, T., Erichsen, S., Schiergens, T. S., Herrler, G., Wu, N.-H., Nitsche, A., Müller, M. A., Drosten, C. & Pöhlmann, S. SARS-CoV-2 Cell Entry Depends on ACE2 and TMPRSS2 and Is Blocked by a Clinically Proven Protease Inhibitor. *Cell* **181**, 271-280.e8 (2020).
40. Li, W., Moore, M. J., Vasilieva, N., Sui, J., Wong, S. K., Berne, M. A., Somasundaran, M., Sullivan, J. L., Luzuriaga, K., Greenough, T. C., Choe, H. & Farzan, M. Angiotensin-converting enzyme 2 is a functional receptor for the SARS coronavirus. *Nature* **426**, 450–454 (2003).
41. Raj, V. S., Mou, H., Smits, S. L., Dekkers, D. H. W., Müller, M. A., Dijkman, R., Muth, D., Demmers, J. A. A., Zaki, A., Fouchier, R. A. M., Thiel, V., Drosten, C., Rottier, P. J. M., Osterhaus, A. D. M. E., Bosch, B. J. & Haagmans, B. L. Dipeptidyl peptidase 4 is a functional receptor for the emerging human coronavirus-EMC. *Nature* **495**, 251–254 (2013).
42. Wettstein, L., Kirchhoff, F. & Münch, J. The Transmembrane Protease TMPRSS2 as a Therapeutic Target for COVID-19 Treatment. *International Journal of Molecular Sciences* **23**, 1351 (2022).
43. Artika, I. M., Dewantari, A. K. & Wiyatno, A. Molecular biology of coronaviruses: current knowledge. *Heliyon* **6**, e04743 (2020).
44. Neuman, B. W., Kiss, G., Kunding, A. H., Bhella, D., Baksh, M. F., Connelly, S., Droese, B., Klaus, J. P., Makino, S., Sawicki, S. G., Siddell, S. G., Stamou, D. G., Wilson, I. A., Kuhn, P. & Buchmeier, M. J. A structural analysis of M protein in coronavirus assembly and morphology. *J Struct Biol* **174**, 11–22 (2011).
45. Nal, B., Chan, C., Kien, F., Siu, L., Tse, J., Chu, K., Kam, J., Staropoli, I., Crescenzo-Chaigne, B., Escriou, N., van der Werf, S., Yuen, K.-Y. & Altmeyer, R. Differential maturation and subcellular localization of severe acute respiratory syndrome coronavirus surface proteins S, M and E. *J Gen Virol* **86**, 1423–1434 (2005).
46. Nieto-Torres, J. L., DeDiego, M. L., Verdiá-Báguena, C., Jimenez-Guardeño, J. M., Regla-Nava, J. A., Fernandez-Delgado, R., Castaño-Rodriguez, C., Alcaraz, A., Torres,

J., Aguilella, V. M. & Enjuanes, L. Severe acute respiratory syndrome coronavirus envelope protein ion channel activity promotes virus fitness and pathogenesis. *PLoS Pathog* **10**, e1004077 (2014).

47. Chang, C., Sue, S.-C., Yu, T., Hsieh, C.-M., Tsai, C.-K., Chiang, Y.-C., Lee, S., Hsiao, H., Wu, W.-J., Chang, W.-L., Lin, C.-H. & Huang, T. Modular organization of SARS coronavirus nucleocapsid protein. *J Biomed Sci* **13**, 59–72 (2006).
48. Sheikh, A., Al-Taher, A., Al-Nazawi, M., Al-Mubarak, A. I. & Kandeel, M. Analysis of preferred codon usage in the coronavirus N genes and their implications for genome evolution and vaccine design. *J Virol Methods* **277**, 113806 (2020).
49. Hartenian, E., Nandakumar, D., Lari, A., Ly, M., Tucker, J. M. & Glaunsinger, B. A. The molecular virology of coronaviruses. *J Biol Chem* **295**, 12910–12934 (2020).
50. Hemida, M. G. Middle East Respiratory Syndrome Coronavirus and the One Health concept. *PeerJ* **7**, e7556 (2019).
51. Wang, L.-F. & Eaton, B. T. Bats, Civets and the Emergence of SARS. *Wildlife and Emerging Zoonotic Diseases: The Biology, Circumstances and Consequences of Cross-Species Transmission* **315**, 325–344 (2007).
52. Corman, V. M., Baldwin, H. J., Tateno, A. F., Zerbinati, R. M., Annan, A., Owusu, M., Nkrumah, E. E., Maganga, G. D., Oppong, S., Adu-Sarkodie, Y., Vallo, P., da Silva Filho, L. V. R. F., Leroy, E. M., Thiel, V., van der Hoek, L., Poon, L. L. M., Tschapka, M., Drosten, C. & Drexler, J. F. Evidence for an Ancestral Association of Human Coronavirus 229E with Bats. *J Virol* **89**, 11858–11870 (2015).
53. van Doremalen, N., Bushmaker, T., Morris, D. H., Holbrook, M. G., Gamble, A., Williamson, B. N., Tamin, A., Harcourt, J. L., Thornburg, N. J., Gerber, S. I., Lloyd-Smith, J. O., de Wit, E. & Munster, V. J. Aerosol and Surface Stability of SARS-CoV-2 as Compared with SARS-CoV-1. *N Engl J Med* **382**, 1564–1567 (2020).
54. MERS-CoV worldwide overview. European Centre for Disease Prevention and Control https://www.ecdc.europa.eu/en/middle-east-respiratory-syndrome-coronavirus-mers-cov-situation-update.
55. COVID-19 Map. *Johns Hopkins Coronavirus Resource Center* https://coronavirus.jhu.edu/map.html.
56. Hoffmann, M., Kleine-Weber, H. & Pöhlmann, S. A Multibasic Cleavage Site in the Spike Protein of SARS-CoV-2 Is Essential for Infection of Human Lung Cells. *Mol Cell* **78**, 779-784.e5 (2020).

57. Walls, A. C., Park, Y.-J., Tortorici, M. A., Wall, A., McGuire, A. T. & Veesler, D. Structure, Function, and Antigenicity of the SARS-CoV-2 Spike Glycoprotein. *Cell* **181**, 281-292.e6 (2020).
58. Zheng, J. SARS-CoV-2: an Emerging Coronavirus that Causes a Global Threat. *Int J Biol Sci* **16**, 1678–1685 (2020).
59. Zou, L., Ruan, F., Huang, M., Liang, L., Huang, H., Hong, Z., Yu, J., Kang, M., Song, Y., Xia, J., Guo, Q., Song, T., He, J., Yen, H.-L., Peiris, M. & Wu, J. SARS-CoV-2 Viral Load in Upper Respiratory Specimens of Infected Patients. *N Engl J Med* **382**, 1177–1179 (2020).
60. World Health Organization. Consensus document on the epidemiology of severe acute respiratory syndrome (SARS). https://apps.who.int/iris/handle/10665/70863 (2003).
61. Robson, F., Khan, K. S., Le, T. K., Paris, C., Demirbag, S., Barfuss, P., Rocchi, P. & Ng, W.-L. Coronavirus RNA Proofreading: Molecular Basis and Therapeutic Targeting. *Mol Cell* **79**, 710–727 (2020).
62. Choi, J. Y. & Smith, D. M. SARS-CoV-2 Variants of Concern. *Yonsei Med J* **62**, 961–968 (2021).
63. Plante, J. A., Liu, Y., Liu, J., Xia, H., Johnson, B. A., Lokugamage, K. G., Zhang, X., Muruato, A. E., Zou, J., Fontes-Garfias, C. R., Mirchandani, D., Scharton, D., Bilello, J. P., Ku, Z., An, Z., Kalveram, B., Freiberg, A. N., Menachery, V. D., Xie, X., Plante, K. S., Weaver, S. C. & Shi, P.-Y. Spike mutation D614G alters SARS-CoV-2 fitness. *Nature* **592**, 116–121 (2021).
64. Davies, N. G., Abbott, S., Barnard, R. C., Jarvis, C. I., Kucharski, A. J., Munday, J. D., Pearson, C. A. B., Russell, T. W., Tully, D. C., Washburne, A. D., Wenseleers, T., Gimma, A., Waites, W., Wong, K. L. M., van Zandvoort, K., Silverman, J. D., Diaz-Ordaz, K., Keogh, R., Eggo, R. M., Funk, S., Jit, M., Atkins, K. E. & Edmunds, W. J. Estimated transmissibility and impact of SARS-CoV-2 lineage B.1.1.7 in England. *Science* **372**, eabg3055 (2021).
65. Starr, T. N., Greaney, A. J., Hilton, S. K., Ellis, D., Crawford, K. H. D., Dingens, A. S., Navarro, M. J., Bowen, J. E., Tortorici, M. A., Walls, A. C., King, N. P., Veesler, D. & Bloom, J. D. Deep Mutational Scanning of SARS-CoV-2 Receptor Binding Domain Reveals Constraints on Folding and ACE2 Binding. *Cell* **182**, 1295-1310.e20 (2020).
66. Andeweg, S. P., Vennema, H., Veldhuijzen, I., Smorenburg, N., Schmitz, D., Zwagemaker, F., van Gageldonk-Lafeber, A. B., Hahné, S. J. M., Reusken, C., Knol, M. J., Eggink, D., SeqNeth Molecular surveillance group, & RIVM COVID-19

MOLECULAR EPIDEMIOLOGY GROUP. Elevated risk of infection with SARS-CoV-2 Beta, Gamma, and Delta variant compared to Alpha variant in vaccinated individuals. *Science Translational Medicine* **0**, eabn4338 (2022).

67. Mlcochova, P., Kemp, S. A., Dhar, M. S., Papa, G., Meng, B., Ferreira, I. A. T. M., Datir, R., Collier, D. A., Albecka, A., Singh, S., Pandey, R., Brown, J., Zhou, J., Goonawardane, N., Mishra, S., Whittaker, C., Mellan, T., Marwal, R., Datta, M., Sengupta, S., Ponnusamy, K., Radhakrishnan, V. S., Abdullahi, A., Charles, O., Chattopadhyay, P., Devi, P., Caputo, D., Peacock, T., Wattal, C., Goel, N., Satwik, A., Vaishya, R., Agarwal, M., Mavousian, A., Lee, J. H., Bassi, J., Silacci-Fegni, C., Saliba, C., Pinto, D., Irie, T., Yoshida, I., Hamilton, W. L., Sato, K., Bhatt, S., Flaxman, S., James, L. C., Corti, D., Piccoli, L., Barclay, W. S., Rakshit, P., Agrawal, A. & Gupta, R. K. SARS-CoV-2 B.1.617.2 Delta variant replication and immune evasion. *Nature* **599**, 114–119 (2021).
68. Jung, C., Kmiec, D., Koepke, L., Zech, F., Jacob, T., Sparrer, K. M. J. & Kirchhoff, F. Omicron: What Makes the Latest SARS-CoV-2 Variant of Concern So Concerning? *J Virol* **96**, e0207721 (2022).
69. Tian, D., Sun, Y., Xu, H. & Ye, Q. The emergence and epidemic characteristics of the highly mutated SARS-CoV-2 Omicron variant. *J Med Virol* **94**, 2376–2383 (2022).
70. Wolter, N., Jassat, W., Walaza, S., Welch, R., Moultrie, H., Groome, M., Amoako, D. G., Everatt, J., Bhiman, J. N., Scheepers, C., Tebeila, N., Chiwandire, N., du Plessis, M., Govender, N., Ismail, A., Glass, A., Mlisana, K., Stevens, W., Treurnicht, F. K., Makatini, Z., Hsiao, N., Parboosing, R., Wadula, J., Hussey, H., Davies, M.-A., Boulle, A., von Gottberg, A. & Cohen, C. Early assessment of the clinical severity of the SARS-CoV-2 omicron variant in South Africa: a data linkage study. *The Lancet* **399**, 437–446 (2022).
71. Paules, C. I., Marston, H. D. & Fauci, A. S. Coronavirus Infections-More Than Just the Common Cold. *JAMA* **323**, 707–708 (2020).
72. Corman, V. M., Muth, D., Niemeyer, D. & Drosten, C. Chapter Eight - Hosts and Sources of Endemic Human Coronaviruses. in *Advances in Virus Research* (eds. Kielian, M., Mettenleiter, T. C. & Roossinck, M. J.) vol. 100 163–188 (Academic Press, 2018).
73. Pyrc, K., Berkhout, B. & van der Hoek, L. Antiviral strategies against human coronaviruses. *Infect Disord Drug Targets* **7**, 59–66 (2007).
74. Zhu, Z., Lian, X., Su, X., Wu, W., Marraro, G. A. & Zeng, Y. From SARS and MERS to COVID-19: a brief summary and comparison of severe acute respiratory infections

caused by three highly pathogenic human coronaviruses. *Respiratory Research* **21**, 224 (2020).

75. Lamers, M. M. & Haagmans, B. L. SARS-CoV-2 pathogenesis. *Nat Rev Microbiol* **20**, 270–284 (2022).
76. Peiris, J. S. M., Guan, Y. & Yuen, K. Y. Severe acute respiratory syndrome. *Nat Med* **10**, S88-97 (2004).
77. Parasa, S., Desai, M., Thoguluva Chandrasekar, V., Patel, H. K., Kennedy, K. F., Roesch, T., Spadaccini, M., Colombo, M., Gabbiadini, R., Artifon, E. L. A., Repici, A. & Sharma, P. Prevalence of Gastrointestinal Symptoms and Fecal Viral Shedding in Patients With Coronavirus Disease 2019. *JAMA Netw Open* **3**, e2011335 (2020).
78. Middle East respiratory syndrome coronavirus (MERS-CoV). https://www.who.int/health-topics/middle-east-respiratory-syndrome-coronavirus-mers.
79. van den Brand, J. M., Smits, S. L. & Haagmans, B. L. Pathogenesis of Middle East respiratory syndrome coronavirus. *The Journal of Pathology* **235**, 175–184 (2015).
80. Huang, J., Hume, A. J., Abo, K. M., Werder, R. B., Villacorta-Martin, C., Alysandratos, K.-D., Beermann, M. L., Simone-Roach, C., Lindstrom-Vautrin, J., Olejnik, J., Suder, E. L., Bullitt, E., Hinds, A., Sharma, A., Bosmann, M., Wang, R., Hawkins, F., Burks, E. J., Saeed, M., Wilson, A. A., Mühlberger, E. & Kotton, D. N. SARS-CoV-2 Infection of Pluripotent Stem Cell-Derived Human Lung Alveolar Type 2 Cells Elicits a Rapid Epithelial-Intrinsic Inflammatory Response. *Cell Stem Cell* **27**, 962-973.e7 (2020).
81. Lamers, M. M., van der Vaart, J., Knoops, K., Riesebosch, S., Breugem, T. I., Mykytyn, A. Z., Beumer, J., Schipper, D., Bezstarosti, K., Koopman, C. D., Groen, N., Ravelli, R. B. G., Duimel, H. Q., Demmers, J. A. A., Verjans, G. M. G. M., Koopmans, M. P. G., Muraro, M. J., Peters, P. J., Clevers, H. & Haagmans, B. L. An organoid-derived bronchioalveolar model for SARS-CoV-2 infection of human alveolar type II-like cells. *EMBO J* **40**, e105912 (2021).
82. Schäfer, A., Martinez, D. R., Won, J. J., Meganck, R. M., Moreira, F. R., Brown, A. J., Gully, K. L., Zweigart, M. R., Conrad, W. S., May, S. R., Dong, S., Kalla, R., Chun, K., Du Pont, V., Babusis, D., Tang, J., Murakami, E., Subramanian, R., Barrett, K. T., Bleier, B. J., Bannister, R., Feng, J. Y., Bilello, J. P., Cihlar, T., Mackman, R. L., Montgomery, S. A., Baric, R. S. & Sheahan, T. P. Therapeutic treatment with an oral prodrug of the remdesivir parental nucleoside is protective against SARS-CoV-2 pathogenesis in mice. *Science Translational Medicine* **14**, eabm3410 (2022).

83. CDC. COVID-19 and Your Health. Centers for Disease Control and Prevention https://www.cdc.gov/coronavirus/2019-ncov/your-health/treatments-for-severe-illness.html (2020).
84. REMAP-CAP Investigators, ACTIV-4a Investigators, ATTACC Investigators, Goligher, E. C., Bradbury, C. A., McVerry, B. J., Lawler, P. R., Berger, J. S., Gong, M. N., Carrier, M., Reynolds, H. R., Kumar, A., Turgeon, A. F., Kornblith, L. Z., Kahn, S. R., Marshall, J. C., Kim, K. S., Houston, B. L., Derde, L. P. G., Cushman, M., Tritschler, T., Angus, D. C., Godoy, L. C., McQuilten, Z., Kirwan, B.-A., Farkouh, M. E., Brooks, M. M., Lewis, R. J., Berry, L. R., Lorenzi, E., Gordon, A. C., Ahuja, T., Al-Beidh, F., Annane, D., Arabi, Y. M., Aryal, D., Baumann Kreuziger, L., Beane, A., Bhimani, Z., Bihari, S., Billett, H. H., Bond, L., Bonten, M., Brunkhorst, F., Buxton, M., Buzgau, A., Castellucci, L. A., Chekuri, S., Chen, J.-T., Cheng, A. C., Chkhikvadze, T., Coiffard, B., Contreras, A., Costantini, T. W., de Brouwer, S., Detry, M. A., Duggal, A., Džavík, V., Effron, M. B., Eng, H. F., Escobedo, J., Estcourt, L. J., Everett, B. M., Fergusson, D. A., Fitzgerald, M., Fowler, R. A., Froess, J. D., Fu, Z., Galanaud, J. P., Galen, B. T., Gandotra, S., Girard, T. D., Goodman, A. L., Goossens, H., Green, C., Greenstein, Y. Y., Gross, P. L., Haniffa, R., Hegde, S. M., Hendrickson, C. M., Higgins, A. M., Hindenburg, A. A., Hope, A. A., Horowitz, J. M., Horvat, C. M., Huang, D. T., Hudock, K., Hunt, B. J., Husain, M., Hyzy, R. C., Jacobson, J. R., Jayakumar, D., Keller, N. M., Khan, A., Kim, Y., Kindzelski, A., King, A. J., Knudson, M. M., Kornblith, A. E., Kutcher, M. E., Laffan, M. A., Lamontagne, F., Le Gal, G., Leeper, C. M., Leifer, E. S., Lim, G., Gallego Lima, F., Linstrum, K., Litton, E., Lopez-Sendon, J., Lother, S. A., Marten, N., Saud Marinez, A., Martinez, M., Mateos Garcia, E., Mavromichalis, S., McAuley, D. F., McDonald, E. G., McGlothlin, A., McGuinness, S. P., Middeldorp, S., Montgomery, S. K., Mouncey, P. R., Murthy, S., Nair, G. B., Nair, R., Nichol, A. D., Nicolau, J. C., Nunez-Garcia, B., Park, J. J., Park, P. K., Parke, R. L., Parker, J. C., Parnia, S., Paul, J. D., Pompilio, M., Quigley, J. G., Rosenson, R. S., Rost, N. S., Rowan, K., Santos, F. O., Santos, M., Santos, M. O., Satterwhite, L., Saunders, C. T., Schreiber, J., Schutgens, R. E. G., Seymour, C. W., Siegal, D. M., Silva, D. G., Singhal, A. B., Slutsky, A. S., Solvason, D., Stanworth, S. J., Turner, A. M., van Bentum-Puijk, W., van de Veerdonk, F. L., van Diepen, S., Vazquez-Grande, G., Wahid, L., Wareham, V., Widmer, R. J., Wilson, J. G., Yuriditsky, E., Zhong, Y., Berry, S. M., McArthur, C. J., Neal, M. D., Hochman, J. S., Webb, S. A. & Zarychanski, R. Therapeutic

Anticoagulation with Heparin in Critically Ill Patients with Covid-19. *N Engl J Med* **385**, 777–789 (2021).

85. Clinical Management of Adults Summary. COVID-19 Treatment Guidelines https://www.covid19treatmentguidelines.nih.gov/management/clinical-management-of-adults/clinical-management-of-adults-summary/.
86. Prescott, H. C. & Rice, T. W. Corticosteroids in COVID-19 ARDS: Evidence and Hope During the Pandemic. *JAMA* **324**, 1292–1295 (2020).
87. Warren, T. K., Jordan, R., Lo, M. K., Ray, A. S., Mackman, R. L., Soloveva, V., Siegel, D., Perron, M., Bannister, R., Hui, H. C., Larson, N., Strickley, R., Wells, J., Stuthman, K. S., Van Tongeren, S. A., Garza, N. L., Donnelly, G., Shurtleff, A. C., Retterer, C. J., Gharaibeh, D., Zamani, R., Kenny, T., Eaton, B. P., Grimes, E., Welch, L. S., Gomba, L., Wilhelmsen, C. L., Nichols, D. K., Nuss, J. E., Nagle, E. R., Kugelman, J. R., Palacios, G., Doerffler, E., Neville, S., Carra, E., Clarke, M. O., Zhang, L., Lew, W., Ross, B., Wang, Q., Chun, K., Wolfe, L., Babusis, D., Park, Y., Stray, K. M., Trancheva, I., Feng, J. Y., Barauskas, O., Xu, Y., Wong, P., Braun, M. R., Flint, M., McMullan, L. K., Chen, S.-S., Fearns, R., Swaminathan, S., Mayers, D. L., Spiropoulou, C. F., Lee, W. A., Nichol, S. T., Cihlar, T. & Bavari, S. Therapeutic efficacy of the small molecule GS-5734 against Ebola virus in rhesus monkeys. *Nature* **531**, 381–385 (2016).
88. Williamson, B. N., Feldmann, F., Schwarz, B., Meade-White, K., Porter, D. P., Schulz, J., van Doremalen, N., Leighton, I., Yinda, C. K., Pérez-Pérez, L., Okumura, A., Lovaglio, J., Hanley, P. W., Saturday, G., Bosio, C. M., Anzick, S., Barbian, K., Cihlar, T., Martens, C., Scott, D. P., Munster, V. J. & de Wit, E. Clinical benefit of remdesivir in rhesus macaques infected with SARS-CoV-2. *Nature* **585**, 273–276 (2020).
89. Niknam, Z., Jafari, A., Golchin, A., Danesh Pouya, F., Nemati, M., Rezaei-Tavirani, M. & Rasmi, Y. Potential therapeutic options for COVID-19: an update on current evidence. *Eur J Med Res* **27**, 6 (2022).
90. Sheahan, T. P., Sims, A. C., Graham, R. L., Menachery, V. D., Gralinski, L. E., Case, J. B., Leist, S. R., Pyrc, K., Feng, J. Y., Trantcheva, I., Bannister, R., Park, Y., Babusis, D., Clarke, M. O., Mackman, R. L., Spahn, J. E., Palmiotti, C. A., Siegel, D., Ray, A. S., Cihlar, T., Jordan, R., Denison, M. R. & Baric, R. S. Broad-spectrum antiviral GS-5734 inhibits both epidemic and zoonotic coronaviruses. *Science Translational Medicine* **9**, eaal3653 (2017).
91. Tao, K., Tzou, P. L., Nouhin, J., Bonilla, H., Jagannathan, P. & Shafer, R. W. SARS-CoV-2 Antiviral Therapy. *Clin Microbiol Rev* **34**, e0010921 (2021).

92. Malone, B., Urakova, N., Snijder, E. J. & Campbell, E. A. Structures and functions of coronavirus replication-transcription complexes and their relevance for SARS-CoV-2 drug design. *Nat Rev Mol Cell Biol* **23**, 21–39 (2022).
93. Wang, Y., Li, P., Solanki, K., Li, Y., Ma, Z., Peppelenbosch, M. P., Baig, M. S. & Pan, Q. Viral polymerase binding and broad-spectrum antiviral activity of molnupiravir against human seasonal coronaviruses. *Virology* **564**, 33–38 (2021).
94. Commissioner, O. of the. Coronavirus (COVID-19) Update: FDA Authorizes First Oral Antiviral for Treatment of COVID-19. *FDA* https://www.fda.gov/news-events/press-announcements/coronavirus-covid-19-update-fda-authorizes-first-oral-antiviral-treatment-covid-19 (2021).
95. EMA. Paxlovid. *European Medicines Agency* https://www.ema.europa.eu/en/medicines/human/EPAR/paxlovid (2022).
96. Owen, D. R., Allerton, C. M. N., Anderson, A. S., Aschenbrenner, L., Avery, M., Berritt, S., Boras, B., Cardin, R. D., Carlo, A., Coffman, K. J., Dantonio, A., Di, L., Eng, H., Ferre, R., Gajiwala, K. S., Gibson, S. A., Greasley, S. E., Hurst, B. L., Kadar, E. P., Kalgutkar, A. S., Lee, J. C., Lee, J., Liu, W., Mason, S. W., Noell, S., Novak, J. J., Obach, R. S., Ogilvie, K., Patel, N. C., Pettersson, M., Rai, D. K., Reese, M. R., Sammons, M. F., Sathish, J. G., Singh, R. S. P., Steppan, C. M., Stewart, A. E., Tuttle, J. B., Updyke, L., Verhoest, P. R., Wei, L., Yang, Q. & Zhu, Y. An oral SARS-CoV-2 Mpro inhibitor clinical candidate for the treatment of COVID-19. *Science* **374**, 1586–1593 (2021).
97. Schütz, D., Ruiz-Blanco, Y. B., Münch, J., Kirchhoff, F., Sanchez-Garcia, E. & Müller, J. A. Peptide and peptide-based inhibitors of SARS-CoV-2 entry. *Adv Drug Deliv Rev* **167**, 47–65 (2020).
98. Gunst, J. D., Staerke, N. B., Pahus, M. H., Kristensen, L. H., Bodilsen, J., Lohse, N., Dalgaard, L. S., Brønnum, D., Fröbert, O., Hønge, B., Johansen, I. S., Monrad, I., Erikstrup, C., Rosendal, R., Vilstrup, E., Mariager, T., Bove, D. G., Offersen, R., Shakar, S., Cajander, S., Jørgensen, N. P., Sritharan, S. S., Breining, P., Jespersen, S., Mortensen, K. L., Jensen, M. L., Kolte, L., Frattari, G. S., Larsen, C. S., Storgaard, M., Nielsen, L. P., Tolstrup, M., Sædder, E. A., Østergaard, L. J., Ngo, H. T. T., Jensen, M. H., Højen, J. F., Kjolby, M. & Søgaard, O. S. Efficacy of the TMPRSS2 inhibitor camostat mesilate in patients hospitalized with Covid-19-a double-blind randomized controlled trial. *EClinicalMedicine* **35**, 100849 (2021).

99. Ono Pharmaceutical Co. Ltd. A Placebo-controlled, Multicenter, Double-blind, Randomized, Parallel-group Comparative Study in SARS-CoV-2 Infection (COVID-19). https://clinicaltrials.gov/ct2/show/NCT04657497 (2021).

100. Focosi, D., McConnell, S., Casadevall, A., Cappello, E., Valdiserra, G. & Tuccori, M. Monoclonal antibody therapies against SARS-CoV-2. *Lancet Infect Dis* **22**, e311–e326 (2022).

101. VanBlargan, L. A., Errico, J. M., Halfmann, P. J., Zost, S. J., Crowe, J. E., Purcell, L. A., Kawaoka, Y., Corti, D., Fremont, D. H. & Diamond, M. S. An infectious SARS-CoV-2 B.1.1.529 Omicron virus escapes neutralization by therapeutic monoclonal antibodies. *Nat Med* **28**, 490–495 (2022).

102. Polack, F. P., Thomas, S. J., Kitchin, N., Absalon, J., Gurtman, A., Lockhart, S., Perez, J. L., Pérez Marc, G., Moreira, E. D., Zerbini, C., Bailey, R., Swanson, K. A., Roychoudhury, S., Koury, K., Li, P., Kalina, W. V., Cooper, D., Frenck, R. W., Hammitt, L. L., Türeci, Ö., Nell, H., Schaefer, A., Ünal, S., Tresnan, D. B., Mather, S., Dormitzer, P. R., Şahin, U., Jansen, K. U. & Gruber, W. C. Safety and Efficacy of the BNT162b2 mRNA Covid-19 Vaccine. *N Engl J Med* **383**, 2603–2615 (2020).

103. Voysey, M., Clemens, S. A. C., Madhi, S. A., Weckx, L. Y., Folegatti, P. M., Aley, P. K., Angus, B., Baillie, V. L., Barnabas, S. L., Bhorat, Q. E., Bibi, S., Briner, C., Cicconi, P., Collins, A. M., Colin-Jones, R., Cutland, C. L., Darton, T. C., Dheda, K., Duncan, C. J. A., Emary, K. R. W., Ewer, K. J., Fairlie, L., Faust, S. N., Feng, S., Ferreira, D. M., Finn, A., Goodman, A. L., Green, C. M., Green, C. A., Heath, P. T., Hill, C., Hill, H., Hirsch, I., Hodgson, S. H. C., Izu, A., Jackson, S., Jenkin, D., Joe, C. C. D., Kerridge, S., Koen, A., Kwatra, G., Lazarus, R., Lawrie, A. M., Lelliott, A., Libri, V., Lillie, P. J., Mallory, R., Mendes, A. V. A., Milan, E. P., Minassian, A. M., McGregor, A., Morrison, H., Mujadidi, Y. F., Nana, A., O'Reilly, P. J., Padayachee, S. D., Pittella, A., Plested, E., Pollock, K. M., Ramasamy, M. N., Rhead, S., Schwarzbold, A. V., Singh, N., Smith, A., Song, R., Snape, M. D., Sprinz, E., Sutherland, R. K., Tarrant, R., Thomson, E. C., Török, M. E., Toshner, M., Turner, D. P. J., Vekemans, J., Villafana, T. L., Watson, M. E. E., Williams, C. J., Douglas, A. D., Hill, A. V. S., Lambe, T., Gilbert, S. C. & Pollard, A. J. Safety and efficacy of the ChAdOx1 nCoV-19 vaccine (AZD1222) against SARS-CoV-2: an interim analysis of four randomised controlled trials in Brazil, South Africa, and the UK. *Lancet* **397**, 99–111 (2021).

104. Baden, L. R., El Sahly, H. M., Essink, B., Kotloff, K., Frey, S., Novak, R., Diemert, D., Spector, S. A., Rouphael, N., Creech, C. B., McGettigan, J., Khetan, S., Segall, N.,

Solis, J., Brosz, A., Fierro, C., Schwartz, H., Neuzil, K., Corey, L., Gilbert, P., Janes, H., Follmann, D., Marovich, M., Mascola, J., Polakowski, L., Ledgerwood, J., Graham, B. S., Bennett, H., Pajon, R., Knightly, C., Leav, B., Deng, W., Zhou, H., Han, S., Ivarsson, M., Miller, J. & Zaks, T. Efficacy and Safety of the mRNA-1273 SARS-CoV-2 Vaccine. *N Engl J Med* **384**, 403–416 (2021).

105. Hoffmann, M., Krüger, N., Schulz, S., Cossmann, A., Rocha, C., Kempf, A., Nehlmeier, I., Graichen, L., Moldenhauer, A.-S., Winkler, M. S., Lier, M., Dopfer-Jablonka, A., Jäck, H.-M., Behrens, G. M. N. & Pöhlmann, S. The Omicron variant is highly resistant against antibody-mediated neutralization: Implications for control of the COVID-19 pandemic. *Cell* **185**, 447-456.e11 (2022).

106. Hoffmann, M., Arora, P., Groß, R., Seidel, A., Hörnich, B. F., Hahn, A. S., Krüger, N., Graichen, L., Hofmann-Winkler, H., Kempf, A., Winkler, M. S., Schulz, S., Jäck, H.-M., Jahrsdörfer, B., Schrezenmeier, H., Müller, M., Kleger, A., Münch, J. & Pöhlmann, S. SARS-CoV-2 variants B.1.351 and P.1 escape from neutralizing antibodies. *Cell* **184**, 2384-2393.e12 (2021).

107. Tseng, C.-T., Sbrana, E., Iwata-Yoshikawa, N., Newman, P. C., Garron, T., Atmar, R. L., Peters, C. J. & Couch, R. B. Immunization with SARS coronavirus vaccines leads to pulmonary immunopathology on challenge with the SARS virus. *PLoS One* **7**, e35421 (2012).

108. Folegatti, P. M., Bittaye, M., Flaxman, A., Lopez, F. R., Bellamy, D., Kupke, A., Mair, C., Makinson, R., Sheridan, J., Rohde, C., Halwe, S., Jeong, Y., Park, Y.-S., Kim, J.-O., Song, M., Boyd, A., Tran, N., Silman, D., Poulton, I., Datoo, M., Marshall, J., Themistocleous, Y., Lawrie, A., Roberts, R., Berrie, E., Becker, S., Lambe, T., Hill, A., Ewer, K. & Gilbert, S. Safety and immunogenicity of a candidate Middle East respiratory syndrome coronavirus viral-vectored vaccine: a dose-escalation, open-label, non-randomised, uncontrolled, phase 1 trial. *Lancet Infect Dis* **20**, 816–826 (2020).

109. Doms, R. W. & Moore, J. P. HIV-1 Membrane Fusion: Targets of Opportunity. *Journal of Cell Biology* **151**, F9–F14 (2000).

110. Dou, D., Revol, R., Östbye, H., Wang, H. & Daniels, R. Influenza A Virus Cell Entry, Replication, Virion Assembly and Movement. *Frontiers in Immunology* **9**, (2018).

111. Burrell, C. J., Howard, C. R. & Murphy, F. A. Coronaviruses. *Fenner and White's Medical Virology* 437–446 (2017).

112. Alberts, B., Johnson, A., Lewis, J., Raff, M., Roberts, K. & Walter, P. The Lipid Bilayer. *Molecular Biology of the Cell. 4th edition* (2002).

113. Sezgin, E., Levental, I., Mayor, S. & Eggeling, C. The mystery of membrane organization: composition, regulation and roles of lipid rafts. *Nat Rev Mol Cell Biol* **18**, 361–374 (2017).

114. van Meer, G., Voelker, D. R. & Feigenson, G. W. Membrane lipids: where they are and how they behave. *Nat Rev Mol Cell Biol* **9**, 112–124 (2008).

115. Rheinemann, L. & Sundquist, W. I. Virus Budding. *Encyclopedia of Virology* 519–528 (2021).

116. Jackman, J. A., Shi, P.-Y. & Cho, N.-J. Targeting the Achilles Heel of Mosquito-Borne Viruses for Antiviral Therapy. *ACS Infect. Dis.* **5**, 4–8 (2019).

117. Vigant, F., Santos, N. C. & Lee, B. Broad-spectrum antivirals against viral fusion. *Nat Rev Microbiol* **13**, 426–437 (2015).

118. Prochnow, H., Rox, K., Birudukota, N. V. S., Weichert, L., Hotop, S.-K., Klahn, P., Mohr, K., Franz, S., Banda, D. H., Blockus, S., Schreiber, J., Haid, S., Oeyen, M., Martinez, J. P., Süssmuth, R. D., Wink, J., Meyerhans, A., Goffinet, C., Messerle, M., Schulz, T. F., Kröger, A., Schols, D., Pietschmann, T. & Brönstrup, M. Labyrinthopeptins Exert Broad-Spectrum Antiviral Activity through Lipid-Binding-Mediated Virolysis. *J Virol* **94**, e01471-19 (2020).

119. Park, S., Jackman, J. A. & Cho, N.-J. Comparing the Membrane-Interaction Profiles of Two Antiviral Peptides: Insights into Structure–Function Relationship. *Langmuir* **35**, 9934–9943 (2019).

120. Jackman, J. A., Zan, G. H., Zhdanov, V. P. & Cho, N.-J. Rupture of Lipid Vesicles by a Broad-Spectrum Antiviral Peptide: Influence of Vesicle Size. *J. Phys. Chem. B* **117**, 16117–16128 (2013).

121. Fokkens, M., Schrader, T. & Klärner, F.-G. A Molecular Tweezer for Lysine and Arginine. *J. Am. Chem. Soc.* **127**, 14415–14421 (2005).

122. Dutt, S., Wilch, C., Gersthagen, T., Talbiersky, P., Bravo-Rodriguez, K., Hanni, M., Sánchez-García, E., Ochsenfeld, C., Klärner, F.-G. & Schrader, T. Molecular Tweezers with Varying Anions: A Comparative Study. *J. Org. Chem.* **78**, 6721–6734 (2013).

123. Talbiersky, P., Bastkowski, F., Klärner, F.-G. & Schrader, T. Molecular Clip and Tweezer Introduce New Mechanisms of Enzyme Inhibition. *J. Am. Chem. Soc.* **130**, 9824–9828 (2008).

124. Shahpasand-Kroner, H., Siddique, I., Malik, R., Linares, G., Ivanova, M. I., Ichida, J., Weil, T., Münch, J., Sanchez-Garcia, E., Klärner, F.-G., Schrader, T. & Bitan, G.

Molecular tweezers - supramolecular hosts with broad-spectrum biological applications. *Pharmacol Rev* (2022).

125. Schrader, T., Bitan, G. & Klärner, F.-G. Molecular Tweezers for Lysine and Arginine – Powerful Inhibitors of Pathologic Protein Aggregation. *Chem Commun (Camb)* **52**, 11318–11334 (2016).

126. Röcker, A. E. Mechanistic insights into amyloid-mediated enhancement of viral infection and its antagonization by molecular tweezers. (Universität Ulm, 2018).

127. Lump, E., Castellano, L. M., Meier, C., Seeliger, J., Erwin, N., Sperlich, B., Stürzel, C. M., Usmani, S., Hammond, R. M., von Einem, J., Gerold, G., Kreppel, F., Bravo-Rodriguez, K., Pietschmann, T., Holmes, V. M., Palesch, D., Zirafi, O., Weissman, D., Sowislok, A., Wettig, B., Heid, C., Kirchhoff, F., Weil, T., Klärner, F.-G., Schrader, T., Bitan, G., Sanchez-Garcia, E., Winter, R., Shorter, J. & Münch, J. A molecular tweezer antagonizes seminal amyloids and HIV infection. *eLife* **4**, e05397 (2015).

128. Soto, C. & Pritzkow, S. Protein misfolding, aggregation, and conformational strains in neurodegenerative diseases. *Nat Neurosci* **21**, 1332–1340 (2018).

129. Kayed, R., Dettmer, U. & Lesné, S. E. Soluble endogenous oligomeric α-synuclein species in neurodegenerative diseases: Expression, spreading, and cross-talk. *J Parkinsons Dis* **10**, 791–818 (2020).

130. Verma, M., Vats, A. & Taneja, V. Toxic species in amyloid disorders: Oligomers or mature fibrils. *Ann Indian Acad Neurol* **18**, 138–145 (2015).

131. Lasagna-Reeves, C. A., Castillo-Carranza, D. L., Sengupta, U., Clos, A. L., Jackson, G. R. & Kayed, R. Tau oligomers impair memory and induce synaptic and mitochondrial dysfunction in wild-type mice. *Mol Neurodegener* **6**, 39 (2011).

132. Goedert, M. NEURODEGENERATION. Alzheimer's and Parkinson's diseases: The prion concept in relation to assembled Aβ, tau, and α-synuclein. *Science* **349**, 1255555 (2015).

133. Jucker, M. & Walker, L. C. Self-propagation of pathogenic protein aggregates in neurodegenerative diseases. *Nature* **501**, 45–51 (2013).

134. Sinha, S., Lopes, D. H. J. & Bitan, G. A key role for lysine residues in amyloid β-protein folding, assembly, and toxicity. *ACS Chem Neurosci* **3**, 473–481 (2012).

135. Bier, D., Rose, R., Bravo-Rodriguez, K., Bartel, M., Ramirez-Anguita, J. M., Dutt, S., Wilch, C., Klärner, F.-G., Sanchez-Garcia, E., Schrader, T. & Ottmann, C. Molecular tweezers modulate 14-3-3 protein–protein interactions. *Nature Chem* **5**, 234–239 (2013).

136. Sinha, S., Lopes, D. H. J., Du, Z., Pang, E. S., Shanmugam, A., Lomakin, A., Talbiersky, P., Tennstaedt, A., McDaniel, K., Bakshi, R., Kuo, P.-Y., Ehrmann, M., Benedek, G. B., Loo, J. A., Klärner, F.-G., Schrader, T., Wang, C. & Bitan, G. Lysine-Specific Molecular Tweezers Are Broad-Spectrum Inhibitors of Assembly and Toxicity of Amyloid Proteins. *J. Am. Chem. Soc.* **133**, 16958–16969 (2011).

137. Attar, A., Ripoli, C., Riccardi, E., Maiti, P., Li Puma, D. D., Liu, T., Hayes, J., Jones, M. R., Lichti-Kaiser, K., Yang, F., Gale, G. D., Tseng, C., Tan, M., Xie, C.-W., Straudinger, J. L., Klärner, F.-G., Schrader, T., Frautschy, S. A., Grassi, C. & Bitan, G. Protection of primary neurons and mouse brain from Alzheimer's pathology by molecular tweezers. *Brain* **135**, 3735–3748 (2012).

138. Despres, C., Di, J., Cantrelle, F.-X., Li, Z., Huvent, I., Chambraud, B., Zhao, J., Chen, J., Chen, S., Lippens, G., Zhang, F., Linhardt, R., Wang, C., Klärner, F.-G., Schrader, T., Landrieu, I., Bitan, G. & Smet-Nocca, C. Major Differences between the Self-Assembly and Seeding Behavior of Heparin-Induced and in Vitro Phosphorylated Tau and Their Modulation by Potential Inhibitors. *ACS Chem. Biol.* **14**, 1363–1379 (2019).

139. Bengoa-Vergniory, N., Faggiani, E., Ramos-Gonzalez, P., Kirkiz, E., Connor-Robson, N., Brown, L. V., Siddique, I., Li, Z., Vingill, S., Cioroch, M., Cavaliere, F., Threlfell, S., Roberts, B., Schrader, T., Klärner, F.-G., Cragg, S., Dehay, B., Bitan, G., Matute, C., Bezard, E. & Wade-Martins, R. CLR01 protects dopaminergic neurons in vitro and in mouse models of Parkinson's disease. *Nat Commun* **11**, 4885 (2020).

140. Prabhudesai, S., Sinha, S., Attar, A., Kotagiri, A., Fitzmaurice, A. G., Lakshmanan, R., Lakshmanan, R., Ivanova, M. I., Loo, J. A., Klärner, F.-G., Schrader, T., Stahl, M., Bitan, G. & Bronstein, J. M. A novel 'molecular tweezer' inhibitor of α-synuclein neurotoxicity in vitro and in vivo. *Neurotherapeutics* **9**, 464–476 (2012).

141. Münch, J., Rücker, E., Ständker, L., Adermann, K., Goffinet, C., Schindler, M., Wildum, S., Chinnadurai, R., Rajan, D., Specht, A., Giménez-Gallego, G., Sánchez, P. C., Fowler, D. M., Koulov, A., Kelly, J. W., Mothes, W., Grivel, J.-C., Margolis, L., Keppler, O. T., Forssmann, W.-G. & Kirchhoff, F. Semen-derived amyloid fibrils drastically enhance HIV infection. *Cell* **131**, 1059–1071 (2007).

142. Roan, N. R., Münch, J., Arhel, N., Mothes, W., Neidleman, J., Kobayashi, A., Smith-McCune, K., Kirchhoff, F. & Greene, W. C. The Cationic Properties of SEVI Underlie Its Ability To Enhance Human Immunodeficiency Virus Infection. *J Virol* **83**, 73–80 (2009).

143. Usmani, S. M., Zirafi, O., Müller, J. A., Sandi-Monroy, N. L., Yadav, J. K., Meier, C., Weil, T., Roan, N. R., Greene, W. C., Walther, P., Nilsson, K. P. R., Hammarström, P., Wetzel, R., Pilcher, C. D., Gagsteiger, F., Fändrich, M., Kirchhoff, F. & Münch, J. Direct visualization of HIV-enhancing endogenous amyloid fibrils in human semen. *Nat Commun* **5**, 3508 (2014).

144. Arnold, F., Schnell, J., Zirafi, O., Stürzel, C., Meier, C., Weil, T., Ständker, L., Forssmann, W.-G., Roan, N. R., Greene, W. C., Kirchhoff, F. & Münch, J. Naturally Occurring Fragments from Two Distinct Regions of the Prostatic Acid Phosphatase Form Amyloidogenic Enhancers of HIV Infection. *Journal of Virology* **86**, 1244–1249 (2012).

145. Roan, N. R., Müller, J. A., Liu, H., Chu, S., Arnold, F., Stürzel, C. M., Walther, P., Dong, M., Witkowska, H. E., Kirchhoff, F., Münch, J. & Greene, W. C. Peptides released by physiological cleavage of semen coagulum proteins form amyloids that enhance HIV infection. *Cell Host Microbe* **10**, 541–550 (2011).

146. Röcker, A. E., Müller, J. A., Dietzel, E., Harms, M., Krüger, F., Heid, C., Sowislok, A., Riber, C. F., Kupke, A., Lippold, S., von Einem, J., Beer, J., Knöll, B., Becker, S., Schmidt-Chanasit, J., Otto, M., Vapalahti, O., Zelikin, A. N., Bitan, G., Schrader, T. & Münch, J. The molecular tweezer CLR01 inhibits Ebola and Zika virus infection. *Antiviral Research* **152**, 26–35 (2018).

147. Weil, T., Groß, R., Röcker, A., Bravo-Rodriguez, K., Heid, C., Sowislok, A., Le, M.-H., Erwin, N., Dwivedi, M., Bart, S. M., Bates, P., Wettstein, L., Müller, J. A., Harms, M., Sparrer, K., Ruiz-Blanco, Y. B., Stürzel, C. M., von Einem, J., Lippold, S., Read, C., Walther, P., Hebel, M., Kreppel, F., Klärner, F.-G., Bitan, G., Ehrmann, M., Weil, T., Winter, R., Schrader, T., Shorter, J., Sanchez-Garcia, E. & Münch, J. Supramolecular Mechanism of Viral Envelope Disruption by Molecular Tweezers. *J. Am. Chem. Soc.* **142**, 17024–17038 (2020).

148. Jasper, C., Schrader, T., Panitzky, J. & Klärner, F.-G. Selective Complexation of N-Alkylpyridinium Salts: Recognition of NAD+ in Water. *Angewandte Chemie International Edition* **41**, 1355–1358 (2002).

149. Klingelhöfer, D., Braun, M., Brüggmann, D. & Groneberg, D. A. Coronavirus: An insight into global research until outbreak of COVID-19 and its implications for the future. *J Glob Health* **10**, 020508.

150. Grifoni, A., Sidney, J., Zhang, Y., Scheuermann, R. H., Peters, B. & Sette, A. A Sequence Homology and Bioinformatic Approach Can Predict Candidate Targets for Immune Responses to SARS-CoV-2. *Cell Host & Microbe* **27**, 671-680.e2 (2020).

151. Dai, W., Zhang, B., Jiang, X.-M., Su, H., Li, J., Zhao, Y., Xie, X., Jin, Z., Peng, J., Liu, F., Li, C., Li, Y., Bai, F., Wang, H., Cheng, X., Cen, X., Hu, S., Yang, X., Wang, J., Liu, X., Xiao, G., Jiang, H., Rao, Z., Zhang, L.-K., Xu, Y., Yang, H. & Liu, H. Structure-based design of antiviral drug candidates targeting the SARS-CoV-2 main protease. *Science* **368**, 1331–1335 (2020).

152. Carbajo-Lozoya, J., Ma-Lauer, Y., Malešević, M., Theuerkorn, M., Kahlert, V., Prell, E., von Brunn, B., Muth, D., Baumert, T. F., Drosten, C., Fischer, G. & von Brunn, A. Human coronavirus NL63 replication is cyclophilin A-dependent and inhibited by non-immunosuppressive cyclosporine A-derivatives including Alisporivir. *Virus Research* **184**, 44–53 (2014).

153. Hirose, R., Watanabe, N., Bandou, R., Yoshida, T., Daidoji, T., Naito, Y., Itoh, Y. & Nakaya, T. A Cytopathic Effect-Based Tissue Culture Method for HCoV-OC43 Titration Using TMPRSS2-Expressing VeroE6 Cells. *mSphere* **6**, e00159-21 (2021).

154. Hsu, H.-Y., Yang, C.-W., Lee, Y.-Z., Lin, Y.-L., Chang, S.-Y., Yang, R.-B., Liang, J.-J., Chao, T.-L., Liao, C.-C., Kao, H.-C., Wu, S.-H., Chang, J.-Y., Sytwu, H.-K., Chen, C.-T. & Lee, S.-J. Remdesivir and Cyclosporine Synergistically Inhibit the Human Coronaviruses OC43 and SARS-CoV-2. *Frontiers in Pharmacology* **12**, (2021).

155. García-Serradilla, M., Risco, C. & Pacheco, B. Drug repurposing for new, efficient, broad spectrum antivirals. *Virus Research* **264**, 22–31 (2019).

156. Hansasuta, P. & Rowland-Jones, S. L. HIV-1 transmission and acute HIV-1 infection. *British Medical Bulletin* **58**, 109–127 (2001).

157. Gregory, C. J., Oduyebo, T., Brault, A. C., Brooks, J. T., Chung, K.-W., Hills, S., Kuehnert, M. J., Mead, P., Meaney-Delman, D., Rabe, I., Staples, E. & Petersen, L. R. Modes of Transmission of Zika Virus. *The Journal of Infectious Diseases* **216**, S875–S883 (2017).

158. Graham, F. L., Smiley, J., Russell, W. C. & Nairn, R. Characteristics of a human cell line transformed by DNA from human adenovirus type 5. *J Gen Virol* **36**, 59–74 (1977).

159. Weil, T., Kirupakaran, A., Le, M.-H., Rebmann, P., Mieres-Perez, J., Issmail, L., Conzelmann, C., Müller, J. A., Rauch, L., Gilg, A., Wettstein, L., Groß, R., Read, C., Bergner, T., Pålsson, S. A., Uhlig, N., Eberlein, V., Wöll, H., Klärner, F.-G., Stenger, S., Kümmerer, B. M., Streeck, H., Fois, G., Frick, M., Braubach, P., Spetz, A.-L.,

Grunwald, T., Shorter, J., Sanchez-Garcia, E., Schrader, T. & Münch, J. Advanced Molecular Tweezers with Lipid Anchors against SARS-CoV-2 and Other Respiratory Viruses. *JACS Au* **2**, 2187–2202 (2022).

160. Braun, E., Hotter, D., Koepke, L., Zech, F., Groß, R., Sparrer, K. M. J., Müller, J. A., Pfaller, C. K., Heusinger, E., Wombacher, R., Sutter, K., Dittmer, U., Winkler, M., Simmons, G., Jakobsen, M. R., Conzelmann, K.-K., Pöhlmann, S., Münch, J., Fackler, O. T., Kirchhoff, F. & Sauter, D. Guanylate-Binding Proteins 2 and 5 Exert Broad Antiviral Activity by Inhibiting Furin-Mediated Processing of Viral Envelope Proteins. *Cell Reports* **27**, 2092-2104.e10 (2019).
161. Villenave, R., Broadbent, L., Douglas, I., Lyons, J. D., Coyle, P. V., Teng, M. N., Tripp, R. A., Heaney, L. G., Shields, M. D. & Power, U. F. Induction and Antagonism of Antiviral Responses in Respiratory Syncytial Virus-Infected Pediatric Airway Epithelium. *J Virol* **89**, 12309–12318 (2015).
162. Driggers, R. W., Ho, C.-Y., Korhonen, E. M., Kuivanen, S., Jääskeläinen, A. J., Smura, T., Rosenberg, A., Hill, D. A., DeBiasi, R. L., Vezina, G., Timofeev, J., Rodriguez, F. J., Levanov, L., Razak, J., Iyengar, P., Hennenfent, A., Kennedy, R., Lanciotti, R., du Plessis, A. & Vapalahti, O. Zika Virus Infection with Prolonged Maternal Viremia and Fetal Brain Abnormalities. *N Engl J Med* **374**, 2142–2151 (2016).
163. Papkalla, A., Münch, J., Otto, C. & Kirchhoff, F. Nef enhances human immunodeficiency virus type 1 infectivity and replication independently of viral coreceptor tropism. *J Virol* **76**, 8455–8459 (2002).
164. Schwegmann-Weßels, C., Glende, J., Ren, X., Qu, X., Deng, H., Enjuanes, L. & Herrler, G. Comparison of vesicular stomatitis virus pseudotyped with the S proteins from a porcine and a human coronavirus. *J Gen Virol* **90**, 1724–1729 (2009).
165. Wettstein, L., Weil, T., Conzelmann, C., Müller, J. A., Groß, R., Hirschenberger, M., Seidel, A., Klute, S., Zech, F., Prelli Bozzo, C., Preising, N., Fois, G., Lochbaum, R., Knaff, P. M., Mailänder, V., Ständker, L., Thal, D. R., Schumann, C., Stenger, S., Kleger, A., Lochnit, G., Mayer, B., Ruiz-Blanco, Y. B., Hoffmann, M., Sparrer, K. M. J., Pöhlmann, S., Sanchez-Garcia, E., Kirchhoff, F., Frick, M. & Münch, J. Alpha-1 antitrypsin inhibits TMPRSS2 protease activity and SARS-CoV-2 infection. *Nat Commun* **12**, 1726 (2021).
166. Weil, T., Lawrenz, J., Seidel, A., Münch, J. & Müller, J. A. Immunodetection assays for the quantification of seasonal common cold coronaviruses OC43, NL63, or 229E

infection confirm nirmatrelvir as broad coronavirus inhibitor. *Antiviral Res* **203**, 105343 (2022).

167. REED, L. J. & MUENCH, H. A SIMPLE METHOD OF ESTIMATING FIFTY PER CENT ENDPOINTS12. *American Journal of Epidemiology* **27**, 493–497 (1938).
168. Conzelmann, C., Groß, R., Zou, M., Krüger, F., Görgens, A., Gustafsson, M. O., El Andaloussi, S., Münch, J. & Müller, J. A. Salivary extracellular vesicles inhibit Zika virus but not SARS-CoV-2 infection. *J Extracell Vesicles* **9**, 1808281.
169. Groß, R., Dias Loiola, L. M., Issmail, L., Uhlig, N., Eberlein, V., Conzelmann, C., Olari, L., Rauch, L., Lawrenz, J., Weil, T., Müller, J. A., Cardoso, M. B., Gilg, A., Larsson, O., Höglund, U., Pålsson, S. A., Tvilum, A. S., Løvschall, K. B., Kristensen, M. M., Spetz, A., Hontonnou, F., Galloux, M., Grunwald, T., Zelikin, A. N. & Münch, J. Macromolecular Viral Entry Inhibitors as Broad-Spectrum First-Line Antivirals with Activity against SARS-CoV-2. *Adv Sci (Weinh)* **9**, 2201378 (2022).
170. Groß, R., Bauer, R., Krüger, F., Rücker-Braun, E., Olari, L.-R., Ständker, L., Preising, N., Rodríguez, A. A., Conzelmann, C., Gerbl, F., Sauter, D., Kirchhoff, F., Hagemann, B., Gačanin, J., Weil, T., Ruiz-Blanco, Y. B., Sanchez-Garcia, E., Forssmann, W.-G., Mankertz, A., Santibanez, S., Stenger, S., Walther, P., Wiese, S., Spellerberg, B. & Münch, J. A Placenta Derived C-Terminal Fragment of β-Hemoglobin With Combined Antibacterial and Antiviral Activity. *Frontiers in Microbiology* **11**, (2020).
171. Kresse, K. M., Xu, M., Pazzi, J., García-Ojeda, M. & Subramaniam, A. B. Novel Application of Cellulose Paper As a Platform for the Macromolecular Self-Assembly of Biomimetic Giant Liposomes. *ACS Appl. Mater. Interfaces* **8**, 32102–32107 (2016).
172. R Core Team. R: A language and environment for statistical computing. R Foundation for Statistical Computing. https://www.r-project.org/ (2021).
173. Josse, J. & Husson, F. missMDA: A Package for Handling Missing Values in Multivariate Data Analysis. *Journal of Statistical Software* **70**, 1–31 (2016).
174. Lê, S., Josse, J. & Husson, F. FactoMineR: An R Package for Multivariate Analysis. *Journal of Statistical Software* **25**, 1–18 (2008).
175. Kassambara, A. & Mundt, F. factoextra: Extract and Visualize the Results of Multivariate Data Analyses. (2020).
176. Wickham, H., Averick, M., Bryan, J., Chang, W., McGowan, L. D., François, R., Grolemund, G., Hayes, A., Henry, L., Hester, J., Kuhn, M., Pedersen, T. L., Miller, E., Bache, S. M., Müller, K., Ooms, J., Robinson, D., Seidel, D. P., Spinu, V., Takahashi,

K., Vaughan, D., Wilke, C., Woo, K. & Yutani, H. Welcome to the Tidyverse. *Journal of Open Source Software* **4**, 1686 (2019).

177. Herzog, P., Drosten, C. & Müller, M. A. Plaque assay for human coronavirus NL63 using human colon carcinoma cells. *Virology Journal* **5**, 138 (2008).

178. Hu, Y., Ma, C. & Wang, J. Cytopathic Effect Assay and Plaque Assay to Evaluate in vitro Activity of Antiviral Compounds Against Human Coronaviruses 229E, OC43, and NL63. *Bio-protocol* **12**, e4314–e4314 (2022).

179. Freymuth, F., Vabret, A., Rozenberg, F., Dina, J., Petitjean, J., Gouarin, S., Legrand, L., Corbet, S., Brouard, J. & Lebon, P. Replication of respiratory viruses, particularly influenza virus, rhinovirus, and coronavirus in HuH7 hepatocarcinoma cell line. *Journal of Medical Virology* **77**, 295–301 (2005).

180. Brown, A. J., Won, J. J., Graham, R. L., Dinnon, K. H., Sims, A. C., Feng, J. Y., Cihlar, T., Denison, M. R., Baric, R. S. & Sheahan, T. P. Broad spectrum antiviral remdesivir inhibits human endemic and zoonotic deltacoronaviruses with a highly divergent RNA dependent RNA polymerase. *Antiviral Res* **169**, 104541 (2019).

181. Wang, Y., Li, P., Rajpoot, S., Saqib, U., Yu, P., Li, Y., Li, Y., Ma, Z., Baig, M. S. & Pan, Q. Comparative assessment of favipiravir and remdesivir against human coronavirus NL63 in molecular docking and cell culture models. *Sci Rep* **11**, 23465 (2021).

182. Parang, K., El-Sayed, N. S., Kazeminy, A. J. & Tiwari, R. K. Comparative Antiviral Activity of Remdesivir and Anti-HIV Nucleoside Analogs against Human Coronavirus 229E (HCoV-229E). *Molecules* **25**, 2343 (2020).

183. Conzelmann, C., Gilg, A., Groß, R., Schütz, D., Preising, N., Ständker, L., Jahrsdörfer, B., Schrezenmeier, H., Sparrer, K. M. J., Stamminger, T., Stenger, S., Münch, J. & Müller, J. A. An enzyme-based immunodetection assay to quantify SARS-CoV-2 infection. *Antiviral Research* **181**, 104882 (2020).

184. Müller, J. A., Harms, M., Schubert, A., Mayer, B., Jansen, S., Herbeuval, J.-P., Michel, D., Mertens, T., Vapalahti, O., Schmidt-Chanasit, J. & Münch, J. Development of a high-throughput colorimetric Zika virus infection assay. *Med Microbiol Immunol* **206**, 175–185 (2017).

185. Tang, B. S. F., Chan, K., Cheng, V. C. C., Woo, P. C. Y., Lau, S. K. P., Lam, C. C. K., Chan, T., Wu, A. K. L., Hung, I. F. N., Leung, S. & Yuen, K. Comparative Host Gene Transcription by Microarray Analysis Early after Infection of the Huh7 Cell Line

by Severe Acute Respiratory Syndrome Coronavirus and Human Coronavirus 229E. *Journal of Virology* **79**, 6180–6193 (2005).

186. Tsai, Y.-C., Lee, C.-L., Yen, H.-R., Chang, Y.-S., Lin, Y.-P., Huang, S.-H. & Lin, C.-W. Antiviral Action of Tryptanthrin Isolated from Strobilanthes cusia Leaf against Human Coronavirus NL63. *Biomolecules* **10**, 366 (2020).

187. Taylor, P. C., Adams, A. C., Hufford, M. M., de la Torre, I., Winthrop, K. & Gottlieb, R. L. Neutralizing monoclonal antibodies for treatment of COVID-19. *Nat Rev Immunol* **21**, 382–393 (2021).

188. Ke, Z., Oton, J., Qu, K., Cortese, M., Zila, V., McKeane, L., Nakane, T., Zivanov, J., Neufeldt, C. J., Cerikan, B., Lu, J. M., Peukes, J., Xiong, X., Kräusslich, H.-G., Scheres, S. H. W., Bartenschlager, R. & Briggs, J. A. G. Structures and distributions of SARS-CoV-2 spike proteins on intact virions. *Nature* **588**, 498–502 (2020).

189. Forbester, J. L. & Humphreys, I. R. Genetic influences on viral-induced cytokine responses in the lung. *Mucosal Immunol* **14**, 14–25 (2021).

190. Brügger, B., Glass, B., Haberkant, P., Leibrecht, I., Wieland, F. T. & Kräusslich, H.-G. The HIV lipidome: a raft with an unusual composition. *Proc Natl Acad Sci U S A* **103**, 2641–2646 (2006).

191. Family - Flaviviridae. in *Virus Taxonomy* (eds. King, A. M. Q., Adams, M. J., Carstens, E. B. & Lefkowitz, E. J.) 1003–1020 (Elsevier, 2012).

192. Vömel, T., Platt, D. & Strobelt, W. Diameters of erythrocytes of different ages measured by scanning electron-microscopy. *Mechanisms of Ageing and Development* **13**, 357–365 (1980).

193. Auerswald, J. & Knapp, H. F. Quantitative assessment of dielectrophoresis as a micro fluidic retention and separation technique for beads and human blood erythrocytes. *Microelectronic Engineering* **67–68**, 879–886 (2003).

194. Klein, S., Cortese, M., Winter, S. L., Wachsmuth-Melm, M., Neufeldt, C. J., Cerikan, B., Stanifer, M. L., Boulant, S., Bartenschlager, R. & Chlanda, P. SARS-CoV-2 structure and replication characterized by in situ cryo-electron tomography. *Nat Commun* **11**, 5885 (2020).

195. Sundquist, W. I. & Kräusslich, H.-G. HIV-1 Assembly, Budding, and Maturation. *Cold Spring Harb Perspect Med* **2**, a006924 (2012).

196. Manié, S. N., Debreyne, S., Vincent, S. & Gerlier, D. Measles Virus Structural Components Are Enriched into Lipid Raft Microdomains: a Potential Cellular Location for Virus Assembly. *J Virol* **74**, 305–311 (2000).

197. Marty, A., Meanger, J., Mills, J., Shields, B. & Ghildyal, R. Association of matrix protein of respiratory syncytial virus with the host cell membrane of infected cells. *Arch Virol* **149**, 199–210 (2004).

198. Sirohi, D. & Kuhn, R. J. Zika Virus Structure, Maturation, and Receptors. *The Journal of Infectious Diseases* **216**, S935–S944 (2017).

199. Cortese, M., Goellner, S., Acosta, E. G., Neufeldt, C. J., Oleksiuk, O., Lampe, M., Haselmann, U., Funaya, C., Schieber, N., Ronchi, P., Schorb, M., Pruunsild, P., Schwab, Y., Chatel-Chaix, L., Ruggieri, A. & Bartenschlager, R. Ultrastructural Characterization of Zika Virus Replication Factories. *Cell Rep* **18**, 2113–2123 (2017).

200. Mettenleiter, T. C. Budding events in herpesvirus morphogenesis. *Virus Res* **106**, 167–180 (2004).

201. Casares, D., Escribá, P. V. & Rosselló, C. A. Membrane Lipid Composition: Effect on Membrane and Organelle Structure, Function and Compartmentalization and Therapeutic Avenues. *Int J Mol Sci* **20**, 2167 (2019).

202. van der Veen, J. N., Kennelly, J. P., Wan, S., Vance, J. E., Vance, D. E. & Jacobs, R. L. The critical role of phosphatidylcholine and phosphatidylethanolamine metabolism in health and disease. *Biochimica et Biophysica Acta (BBA) - Biomembranes* **1859**, 1558–1572 (2017).

203. Kraft, J. C., Freeling, J. P., Wang, Ziyao. & Ho, R. J. Y. Emerging Research and Clinical Development Trends of Liposome and Lipid Nanoparticle Drug Delivery Systems. *Journal of Pharmaceutical Sciences* **103**, 29–52 (2014).

204. Magarkar, A., Dhawan, V., Kallinteri, P., Viitala, T., Elmowafy, M., Róg, T. & Bunker, A. Cholesterol level affects surface charge of lipid membranes in saline solution. *Sci Rep* **4**, 5005 (2014).

205. Tokudome, Y., Uchida, R., Yokote, T., Todo, H., Hada, N., Kon, T., Yasuda, J., Hayashi, H., Hashimoto, F. & Sugibayashi, K. Effect of topically applied sphingomyelin-based liposomes on the ceramide level in a three-dimensional cultured human skin model. *Journal of Liposome Research* **20**, 49–54 (2010).

206. Arouri, A. & Mouritsen, O. G. Membrane-perturbing effect of fatty acids and lysolipids. *Progress in Lipid Research* **52**, 130–140 (2013).

207. Bramley, T. J., Lerner, D. & Sarnes, M. Productivity Losses Related to the Common Cold. *Journal of Occupational and Environmental Medicine* **44**, 822 (2002).

208. Fendrick, A. M., Monto, A. S., Nightengale, B. & Sarnes, M. The Economic Burden of Non–Influenza-Related Viral Respiratory Tract Infection in the United States. *Archives of Internal Medicine* **163**, 487–494 (2003).

209. Ljubin-Sternak, S., Meštrović, T., Lukšić, I., Mijač, M. & Vraneš, J. Seasonal Coronaviruses and Other Neglected Respiratory Viruses: A Global Perspective and a Local Snapshot. *Front Public Health* **9**, 691163 (2021).

210. Pyrc, K., Sims, A. C., Dijkman, R., Jebbink, M., Long, C., Deming, D., Donaldson, E., Vabret, A., Baric, R., van der Hoek, L. & Pickles, R. Culturing the Unculturable: Human Coronavirus HKU1 Infects, Replicates, and Produces Progeny Virions in Human Ciliated Airway Epithelial Cell Cultures. *Journal of Virology* **84**, 11255–11263 (2010).

211. Bracci, N., Pan, H.-C., Lehman, C., Kehn-Hall, K. & Lin, S.-C. Improved plaque assay for human coronaviruses 229E and OC43. *PeerJ* **8**, e10639 (2020).

212. von Brunn, A., Ciesek, S., von Brunn, B. & Carbajo-Lozoya, J. Genetic deficiency and polymorphisms of cyclophilin A reveal its essential role for Human Coronavirus 229E replication. *Current Opinion in Virology* **14**, 56–61 (2015).

213. Gerna, G., Campanini, G., Rovida, F., Percivalle, E., Sarasini, A., Marchi, A. & Baldanti, F. Genetic variability of human coronavirus OC43-, 229E-, and NL63-like strains and their association with lower respiratory tract infections of hospitalized infants and immunocompromised patients. *Journal of Medical Virology* **78**, 938–949 (2006).

214. Schirtzinger, E. E., Kim, Y. & Davis, A. S. Improving human coronavirus OC43 (HCoV-OC43) research comparability in studies using HCoV-OC43 as a surrogate for SARS-CoV-2. *Journal of Virological Methods* **299**, 114317 (2022).

215. Kawase, M., Shirato, K., van der Hoek, L., Taguchi, F. & Matsuyama, S. Simultaneous Treatment of Human Bronchial Epithelial Cells with Serine and Cysteine Protease Inhibitors Prevents Severe Acute Respiratory Syndrome Coronavirus Entry. *Journal of Virology* **86**, 6537–6545 (2012).

216. Hu, Y., Ma, C., Szeto, T., Hurst, B., Tarbet, B. & Wang, J. Boceprevir, Calpain Inhibitors II and XII, and GC-376 Have Broad-Spectrum Antiviral Activity against Coronaviruses. *ACS Infect. Dis.* **7**, 586–597 (2021).

217. Huang, Y., Yang, C., Xu, X., Xu, W. & Liu, S. Structural and functional properties of SARS-CoV-2 spike protein: potential antivirus drug development for COVID-19. *Acta Pharmacol Sin* **41**, 1141–1149 (2020).

218. Hicks, J., Klumpp-Thomas, C., Kalish, H., Shunmugavel, A., Mehalko, J., Denson, J.-P., Snead, K. R., Drew, M., Corbett, K. S., Graham, B. S., Hall, M. D., Memoli, M.

J., Esposito, D. & Sadtler, K. Serologic Cross-Reactivity of SARS-CoV-2 with Endemic and Seasonal Betacoronaviruses. *J Clin Immunol* **41**, 906–913 (2021).

219. Huang, I.-C., Bosch, B. J., Li, F., Li, W., Lee, K. H., Ghiran, S., Vasilieva, N., Dermody, T. S., Harrison, S. C., Dormitzer, P. R., Farzan, M., Rottier, P. J. M. & Choe, H. SARS Coronavirus, but Not Human Coronavirus NL63, Utilizes Cathepsin L to Infect ACE2-expressing Cells*. *Journal of Biological Chemistry* **281**, 3198–3203 (2006).
220. Esumi, M., Ishibashi, M., Yamaguchi, H., Nakajima, S., Tai, Y., Kikuta, S., Sugitani, M., Takayama, T., Tahara, M., Takeda, M. & Wakita, T. Transmembrane serine protease TMPRSS2 activates hepatitis C virus infection. *Hepatology* **61**, 437 (2015).
221. Shirato, K., Kawase, M. & Matsuyama, S. Wild-type human coronaviruses prefer cell-surface TMPRSS2 to endosomal cathepsins for cell entry. *Virology* **517**, 9–15 (2018).
222. Shirato, K., Kanou, K., Kawase, M. & Matsuyama, S. Clinical Isolates of Human Coronavirus 229E Bypass the Endosome for Cell Entry. *Journal of Virology* **91**, e01387-16 (2016).
223. Kawase, M., Shirato, K., Matsuyama, S. & Taguchi, F. Protease-Mediated Entry via the Endosome of Human Coronavirus 229E. *Journal of Virology* **83**, 712–721 (2009).
224. Wenz, J. J. Molecular properties of steroids involved in their effects on the biophysical state of membranes. *Biochimica et Biophysica Acta (BBA) - Biomembranes* **1848**, 2448–2459 (2015).
225. Subczynski, W. K., Pasenkiewicz-Gierula, M., Widomska, J., Mainali, L. & Raguz, M. High Cholesterol/Low Cholesterol: Effects in Biological Membranes: A Review. *Cell Biochem Biophys* **75**, 369–385 (2017).
226. Munro, S. Lipid Rafts: Elusive or Illusive? *Cell* **115**, 377–388 (2003).
227. Chi, W.-Y., Li, Y.-D., Huang, H.-C., Chan, T. E. H., Chow, S.-Y., Su, J.-H., Ferrall, L., Hung, C.-F. & Wu, T.-C. COVID-19 vaccine update: vaccine effectiveness, SARS-CoV-2 variants, boosters, adverse effects, and immune correlates of protection. *Journal of Biomedical Science* **29**, 82 (2022).
228. Park, S. & Cho, N.-J. Lipid Membrane Interface Viewpoint: From Viral Entry to Antiviral and Vaccine Development. *Langmuir* **39**, 1–11 (2023).
229. Merlot, A. M., Kalinowski, D. S. & Richardson, D. R. Unraveling the mysteries of serum albumin—more than just a serum protein. *Frontiers in Physiology* **5**, (2014).
230. Cai, R. & Chen, C. The Crown and the Scepter: Roles of the Protein Corona in Nanomedicine. *Advanced Materials* **31**, 1805740 (2019).

231. Ezzat, K., Pernemalm, M., Pålsson, S., Roberts, T. C., Järver, P., Dondalska, A., Bestas, B., Sobkowiak, M. J., Levänen, B., Sköld, M., Thompson, E. A., Saher, O., Kari, O. K., Lajunen, T., Sverremark Ekström, E., Nilsson, C., Ishchenko, Y., Malm, T., Wood, M. J. A., Power, U. F., Masich, S., Lindén, A., Sandberg, J. K., Lehtiö, J., Spetz, A.-L. & EL Andaloussi, S. The viral protein corona directs viral pathogenesis and amyloid aggregation. *Nat Commun* **10**, 2331 (2019).

232. Chu, H., Chan, J. F.-W. & Yuen, K.-Y. Animal models in SARS-CoV-2 research. *Nat Methods* **19**, 392–394 (2022).

233. Winkler, E. S., Bailey, A. L., Kafai, N. M., Nair, S., McCune, B. T., Yu, J., Fox, J. M., Chen, R. E., Earnest, J. T., Keeler, S. P., Ritter, J. H., Kang, L.-I., Dort, S., Robichaud, A., Head, R., Holtzman, M. J. & Diamond, M. S. SARS-CoV-2 infection of human ACE2-transgenic mice causes severe lung inflammation and impaired function. *Nat Immunol* **21**, 1327–1335 (2020).

234. Caldera-Crespo, L. A., Paidas, M. J., Roy, S., Schulman, C. I., Kenyon, N. S., Daunert, S. & Jayakumar, A. R. Experimental Models of COVID-19. *Frontiers in Cellular and Infection Microbiology* **11**, (2022).

235. Li, Z., Siddique, I., Hadrović, I., Kirupakaran, A., Li, J., Zhang, Y., Klärner, F.-G., Schrader, T. & Bitan, G. Lysine-selective molecular tweezers are cell penetrant and concentrate in lysosomes. *Commun Biol* **4**, 1–15 (2021).

236. Attar, A., Chan, W.-T. C., Klärner, F.-G., Schrader, T. & Bitan, G. Safety and pharmacological characterization of the molecular tweezer CLR01 – a broad-spectrum inhibitor of amyloid proteins' toxicity. *BMC Pharmacology and Toxicology* **15**, 23 (2014).

237. Welsch, S., Müller, B. & Kräusslich, H.-G. More than one door – Budding of enveloped viruses through cellular membranes. *FEBS Letters* **581**, 2089–2097 (2007).

238. Harayama, T. & Riezman, H. Understanding the diversity of membrane lipid composition. *Nat Rev Mol Cell Biol* **19**, 281–296 (2018).

239. Leventis, P. A. & Grinstein, S. The Distribution and Function of Phosphatidylserine in Cellular Membranes. *Annual Review of Biophysics* **39**, 407–427 (2010).

240. Zhukovsky, M. A., Filograna, A., Luini, A., Corda, D. & Valente, C. Phosphatidic acid in membrane rearrangements. *FEBS Letters* **593**, 2428–2451 (2019).

241. Casalino, L., Gaieb, Z., Goldsmith, J. A., Hjorth, C. K., Dommer, A. C., Harbison, A. M., Fogarty, C. A., Barros, E. P., Taylor, B. C., McLellan, J. S., Fadda, E. & Amaro,

R. E. Beyond Shielding: The Roles of Glycans in the SARS-CoV-2 Spike Protein. *ACS Cent. Sci.* **6**, 1722–1734 (2020).

242. Chakraborty, S., Doktorova, M., Molugu, T. R., Heberle, F. A., Scott, H. L., Dzikovski, B., Nagao, M., Stingaciu, L.-R., Standaert, R. F., Barrera, F. N., Katsaras, J., Khelashvili, G., Brown, M. F. & Ashkar, R. How cholesterol stiffens unsaturated lipid membranes. *Proceedings of the National Academy of Sciences* **117**, 21896–21905 (2020).

243. Ingólfsson, H. I., Melo, M. N., van Eerden, F. J., Arnarez, C., Lopez, C. A., Wassenaar, T. A., Periole, X., de Vries, A. H., Tieleman, D. P. & Marrink, S. J. Lipid Organization of the Plasma Membrane. *J. Am. Chem. Soc.* **136**, 14554–14559 (2014).

244. Bui, T. T., Suga, K. & Umakoshi, H. Roles of Sterol Derivatives in Regulating the Properties of Phospholipid Bilayer Systems. *Langmuir* **32**, 6176–6184 (2016).

245. Sezgin, E. & Schwille, P. Model membrane platforms to study protein-membrane interactions. *Molecular Membrane Biology* **29**, 144–154 (2012).

246. Lorizate, M., Sachsenheimer, T., Glass, B., Habermann, A., Gerl, M. J., Kräusslich, H.-G. & Brügger, B. Comparative lipidomics analysis of HIV-1 particles and their producer cell membrane in different cell lines. *Cellular Microbiology* **15**, 292–304 (2013).

247. Mücksch, F., Citir, M., Lüchtenborg, C., Glass, B., Traynor-Kaplan, A., Schultz, C., Brügger, B. & Kräusslich, H.-G. Quantification of phosphoinositides reveals strong enrichment of PIP2 in HIV-1 compared to producer cell membranes. *Sci Rep* **9**, 17661 (2019).

248. Weil, T. & Münch, J. Molekulare Pinzetten als Breitbandinhibitor viraler Infektionen. *Biospektrum* **29**, 150–152 (2023).

249. Jacquemyn, J., Cascalho, A. & Goodchild, R. E. The ins and outs of endoplasmic reticulum-controlled lipid biosynthesis. *EMBO reports* **18**, 1905–1921 (2017).

250. London, E. Membrane Structure–Function Insights from Asymmetric Lipid Vesicles. *Acc. Chem. Res.* **52**, 2382–2391 (2019).

251. Sprong, H., van der Sluijs, P. & van Meer, G. How proteins move lipids and lipids move proteins. *Nat Rev Mol Cell Biol* **2**, 504–513 (2001).

252. Acciani, M. D. & Brindley, M. A. Scrambled or flipped: 5 facts about how cellular phosphatidylserine localization can mediate viral replication. *PLoS Pathog* **18**, e1010352 (2022).

253. Yang, S.-T., Kreutzberger, A. J. B., Lee, J., Kiessling, V. & Tamm, L. K. The role of cholesterol in membrane fusion. *Chem Phys Lipids* **199**, 136–143 (2016).

254. Peeters, B. W. A., Piët, A. C. A. & Fornerod, M. Generating Membrane Curvature at the Nuclear Pore: A Lipid Point of View. *Cells* **11**, 469 (2022).

255. Antonny, B., Vanni, S., Shindou, H. & Ferreira, T. From zero to six double bonds: phospholipid unsaturation and organelle function. *Trends in Cell Biology* **25**, 427–436 (2015).

256. de la Arada, I., González-Ramírez, E. J., Alonso, A., Goñi, F. M. & Arrondo, J.-L. R. Exploring polar headgroup interactions between sphingomyelin and ceramide with infrared spectroscopy. *Sci Rep* **10**, 17606 (2020).

257. Ramsden, J. J. Chapter 6 - Nanomaterials and their Production. in *Nanotechnology* (ed. Ramsden, J. J.) 101–124 (William Andrew Publishing, 2011).

258. Lipowsky, R. Remodeling of Membrane Shape and Topology by Curvature Elasticity and Membrane Tension. *Advanced Biology* **6**, 2101020 (2022).

259. Vanni, S., Hirose, H., Barelli, H., Antonny, B. & Gautier, R. A sub-nanometre view of how membrane curvature and composition modulate lipid packing and protein recruitment. *Nat Commun* **5**, 4916 (2014).

260. Louten, J. Virus Structure and Classification. *Essential Human Virology* 19–29 (2016).

261. Briggs, J. A. G., Wilk, T., Welker, R., Kräusslich, H.-G. & Fuller, S. D. Structural organization of authentic, mature HIV-1 virions and cores. *The EMBO Journal* **22**, 1707–1715 (2003).

262. Grünewald, K., Desai, P., Winkler, D. C., Heymann, J. B., Belnap, D. M., Baumeister, W. & Steven, A. C. Three-Dimensional Structure of Herpes Simplex Virus from Cryo-Electron Tomography. *Science* **302**, 1396–1398 (2003).

263. Mundle, S. T., Hernandez, H., Hamberger, J., Catalan, J., Zhou, C., Stegalkina, S., Tiffany, A., Kleanthous, H., Delagrave, S. & Anderson, S. F. High-Purity Preparation of HSV-2 Vaccine Candidate ACAM529 Is Immunogenic and Efficacious In Vivo. *PLOS ONE* **8**, e57224 (2013).

264. Azap, A. & Pehlivanoglu, F. Chapter 26 - Measles. in *Emerging Infectious Diseases* (eds. Ergönül, Ö., Can, F., Madoff, L. & Akova, M.) 347–357 (Academic Press, 2014).

265. Utley, T. J., Ducharme, N. A., Varthakavi, V., Shepherd, B. E., Santangelo, P. J., Lindquist, M. E., Goldenring, J. R. & Crowe, J. E. Respiratory syncytial virus uses a

Vps4-independent budding mechanism controlled by Rab11-FIP2. *Proceedings of the National Academy of Sciences* **105**, 10209–10214 (2008).

266. Blazek, A. D., Paleo, B. J. & Weisleder, N. Plasma Membrane Repair: A Central Process for Maintaining Cellular Homeostasis. *Physiology (Bethesda)* **30**, 438–448 (2015).

267. Cooper, S. T. & McNeil, P. L. Membrane Repair: Mechanisms and Pathophysiology. *Physiol Rev* **95**, 1205–1240 (2015).

268. Roos, W. H., Bruinsma, R. & Wuite, G. J. L. Physical virology. *Nature Phys* **6**, 733–743 (2010).

7 Appendix

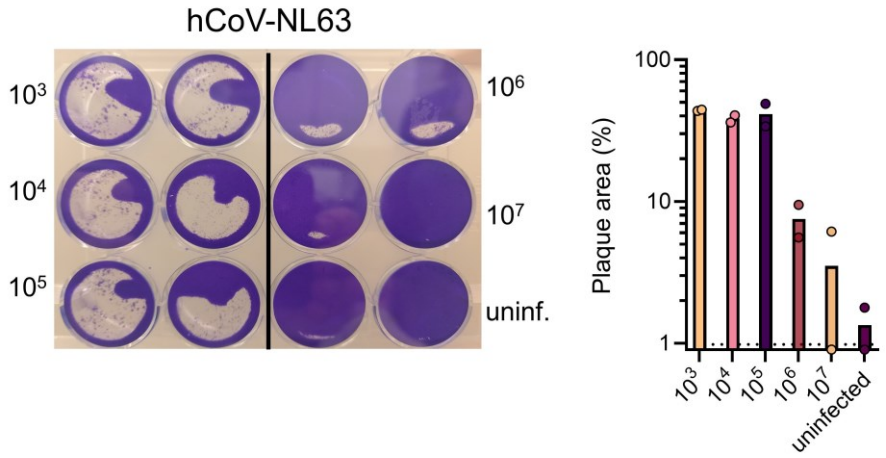

Supplementary Figure 1. Quantification of hCoV-NL63 infectiousness by plaque analysis. Serial dilution of hCoV-NL63 was added on LLC-MK2 cells. After incubation of 2 hours at 33 °C cells were overlaid with cellulose containing medium and incubated for 5 dpi. After removal of cellulose containing medium and washing, remaining cells were stained with crystal violet. Plaques were quantified with ImageJ. Shown are mean from a single experiment performed in duplicates. Dashed lines indicate limit of detection. Data was generated together with Jan Lawrenz, Institute of Molecular Virology, Ulm University Medical Center. Obtained from the master thesis of Jan Lawrenz and from Weil and Lawrenz et al. 2022[166] (CC BY-NC-ND 4.0; https://creativecommons.org/licenses/by-nc-nd/4.0/, Copyright© The Authors, permission to remix and transform was obtained from the creator).

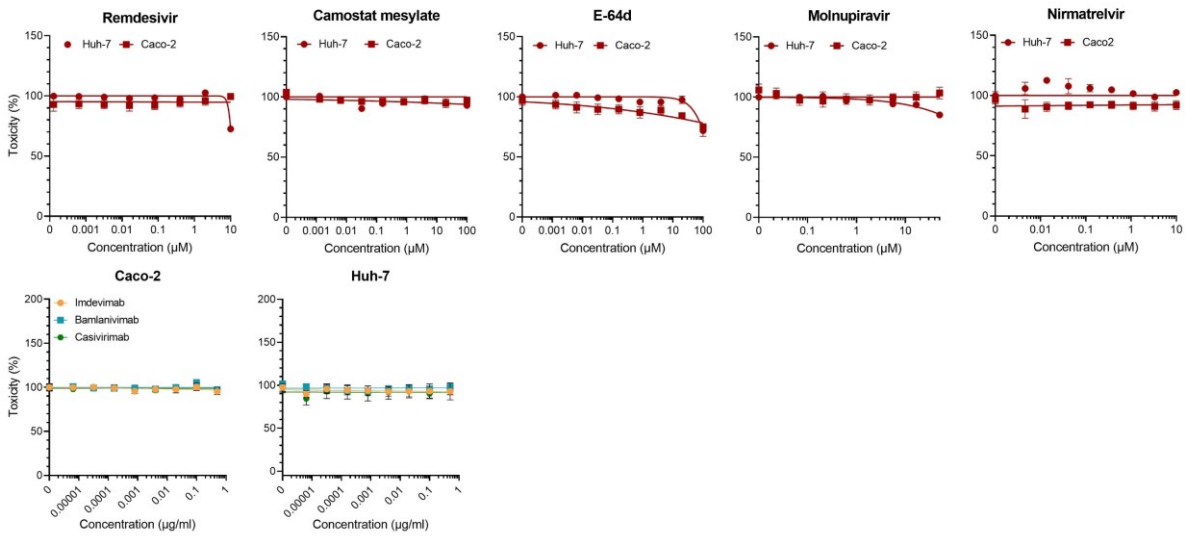

Supplementary Figure 2. Cytotoxicity of antiviral compounds on Caco-2 and Huh-7 cells. Compounds were added to Caco-2 or Huh-7 cells at indicated concentrations. Three or four days later, cell viability was assessed by measuring ATP level in cell lysates with CellTiterGlo Luminescence Cell Viability Assay. Shown are mean values ± SD from one experiment performed in triplicates. Data was generated together with Jan Lawrenz, Institute of Molecular Virology, Ulm University Medical Center. Obtained from the master thesis of Jan Lawrenz and from Weil and Lawrenz et al. 2022[166] (CC BY-NC-ND 4.0; https://creativecommons.org/licenses/by-nc-nd/4.0/, Copyright© The Authors, permission to remix and transform was obtained from the creator).

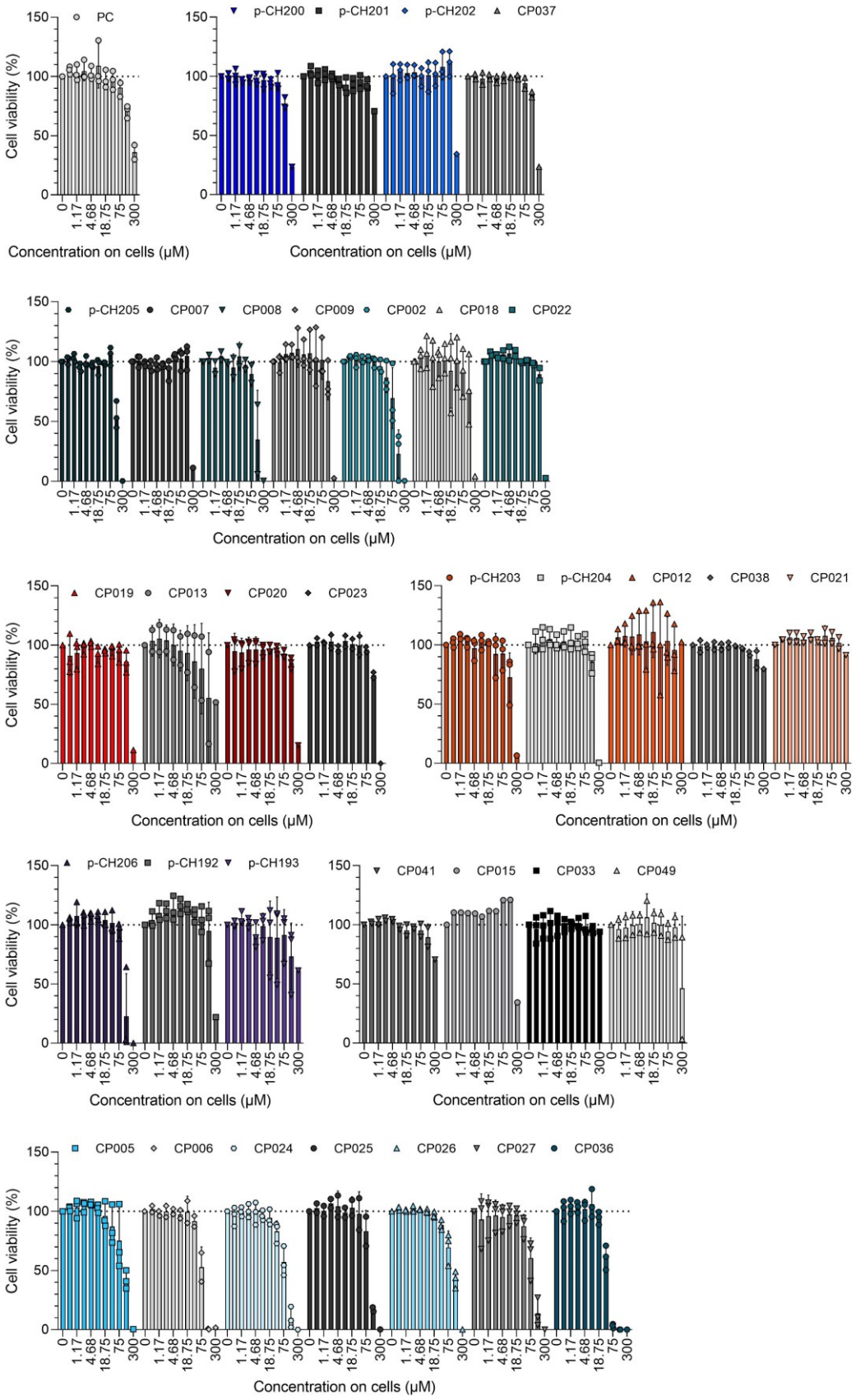

Supplementary Figure 3. Cytotoxicity of tweezers on Caco-2 cells. Tweezer were added to Caco-2 cells at indicated concentrations. Two days later, cell viability was assessed by measuring ATP level in cell lysates with CellTiterGlo Luminescence Cell Viability Assay. Shown are mean values ± SD from three independent experiments performed in duplicates. Modified from Weil et al. 2022[159] (CC BY-NC-ND 4.0;

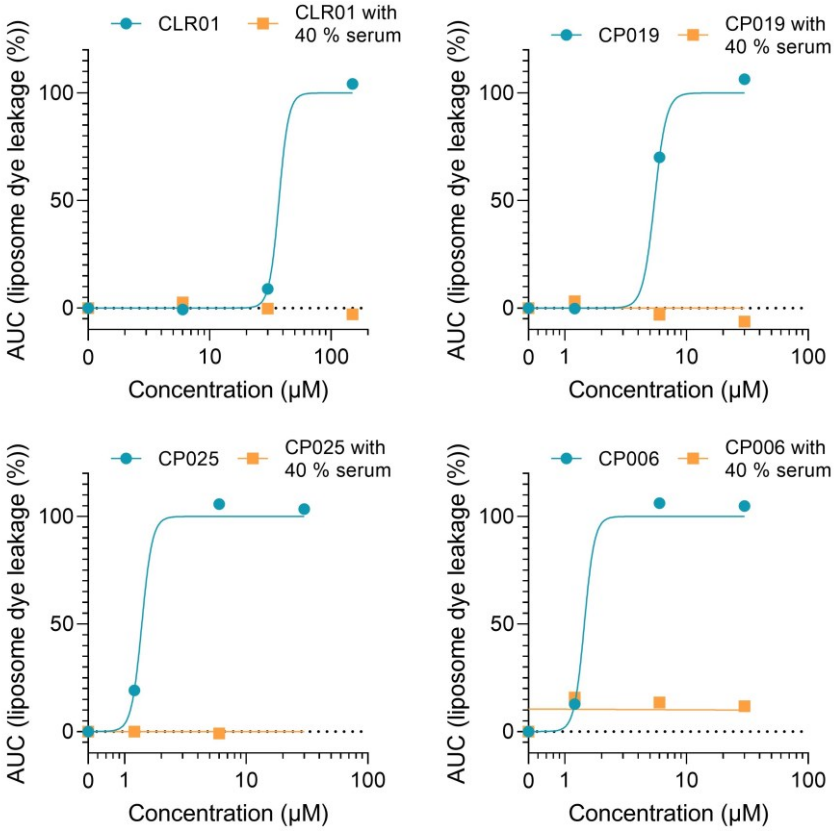

Supplementary Figure 4. Serum interfere with the activity of molecular tweezers. 100 nm sized virus-like liposomes (DOPC/SM/Chol (45/25/30 mol%)) filled with carboxyfluorescein (2.5 x 10^{10} particles/ml and 50 µl/well) were incubated for 10 min with 40 µl of serum. Fluorescence was recorded every minute at 485 nm excitation and 528 nm emission. Afterwards, rising concentrations of tweezers were added and incubated for 30 min while fluorescence was recorded again. Baseline was measured for 5 min in absence of serum and tweezers and maximum fluorescence was recorded after addition of 1 % Triton X-100 to liposomes with serum and tweezer. Shown values were corrected for baseline, normalized to maximum fluorescence and area under the curve calculated. Experiment was performed once in triplicates.

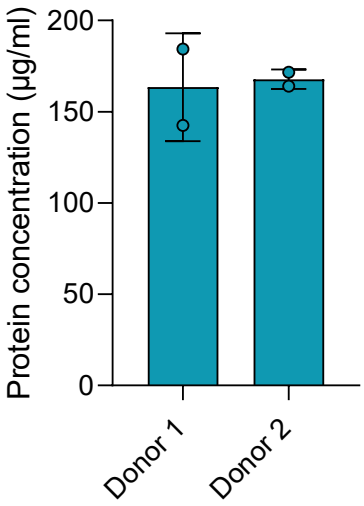

Supplementary Figure 5. Protein concentration of mucus derived from primary airway epithelia cells (HAEC). Protein concentration of mucus used in Figure 17 was determined in a Pierce™ Rapid Gold BCA Protein Assay. Graph represents mean values ± SD of one experiment performed in duplicates.

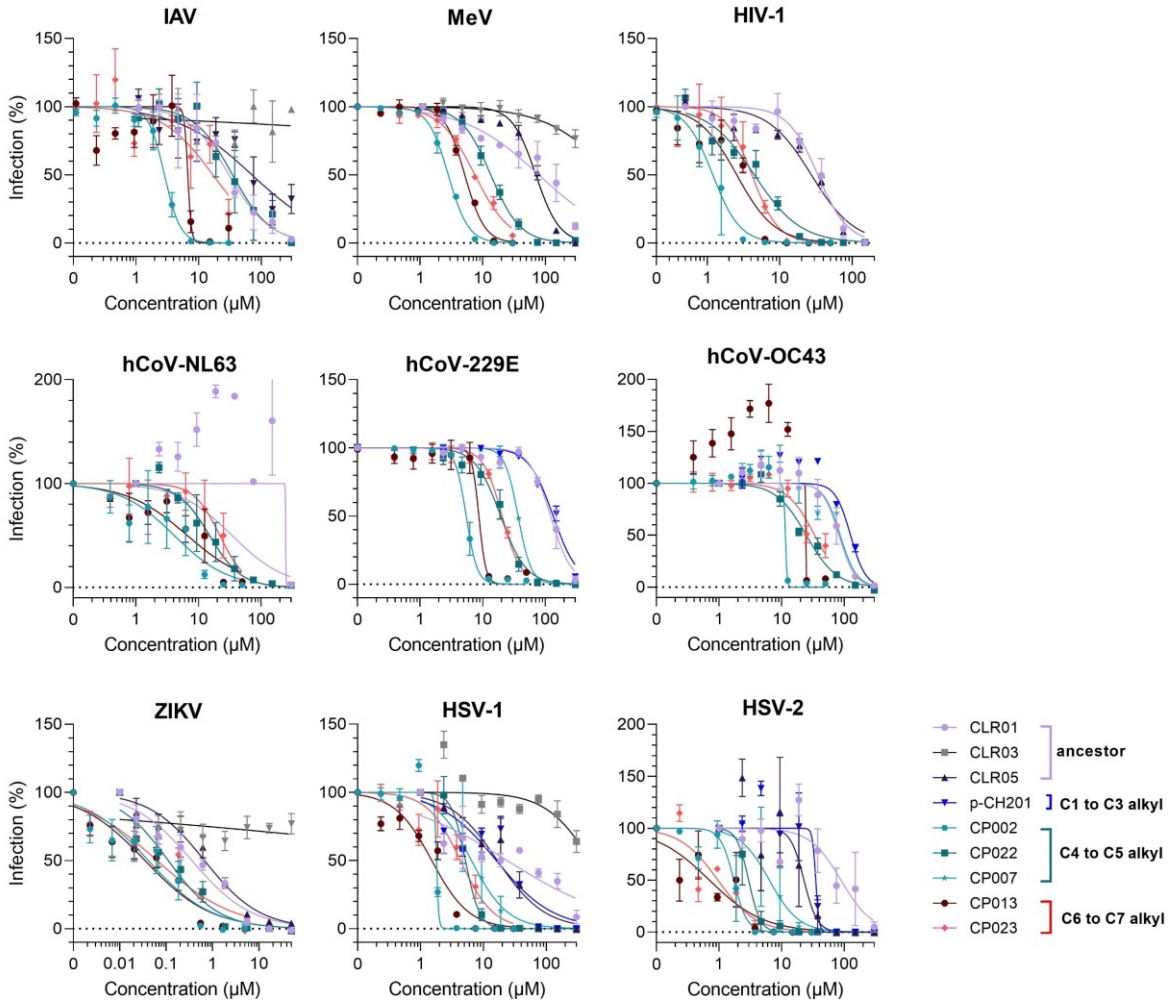

Supplementary Figure 6. Broad-spectrum antiviral activity of advanced tweezers. a) To investigate activity of tweezers against IAV, titrated tweezers were mixed with IAV (MOI 0.0007), incubated for 30 min at 37 °C and added on Caco-2 cells. Infection rates were determined two days later by measuring neuraminidase activity in cellular lysates with a MUNANA assay. For MeV (MOI 0.1) GFP reporter virus, tweezers were incubated with the viruses for 30 min at 37 °C and added on A549 cells. Two dpi, infection rate was measured with flow cytometry. Escalating concentrations of tweezers were incubated with hCoV-NL63 (MOI 0.01), hCoV-OC43 (MOI 0.006), hCoV-229E (MOI 0.002) for 30 min at 33 °C before inoculation onto Caco-2 (hCoV-NL63) or Huh-7 cells (hCoV-OC43 and -229E). Infection rate was measured by in-cell ELISA analyzing N protein expression 2 (-229E), 3 (-OC43) or 6 (-NL63) dpi. ZIKV (MOI 0.15) was incubated for 30 min at 37 °C with titrated tweezers. Mixture was added on Vero E6 cells and two days later in-cell ELISA detecting flavivirus protein E was performed. For testing of tweezers on HSV-1 (MOI 0.05), HSV-2 (MOI 0.05) or HIV-1, viruses were incubated together with tweezers at indicated concentrations for 10 (in case of HIV-1) or 15 min at 37 °C and inoculated onto TZM-bl (for HIV-1) or ELVIS reporter cells. Infections rates were determined two days later by quantification of β-galactosidase activity in cellular lysates. Shown are mean values ± SEM of two (in case of MeV, HSV-1 and HSV-2) or three independent experiments conducted in triplicates. Data of IAV and MeV was generated by Lena Rauch-Wirth and Andrea Gilg (Institute of Molecular Virology, Ulm University Medical Center), respectively. Data of tweezers on hCoV-229E, -NL63 and ZIKV was generated by Jan Lawrenz (Master thesis), Institute of Molecular Virology, Ulm University Medical Center. Modified from Weil et al. 2022[159] (CC BY-NC-ND 4.0; https://creativecommons.org/licenses/by-nc-nd/4.0/, Copyright© The Authors, permission to remix and transform was obtained from the creator).

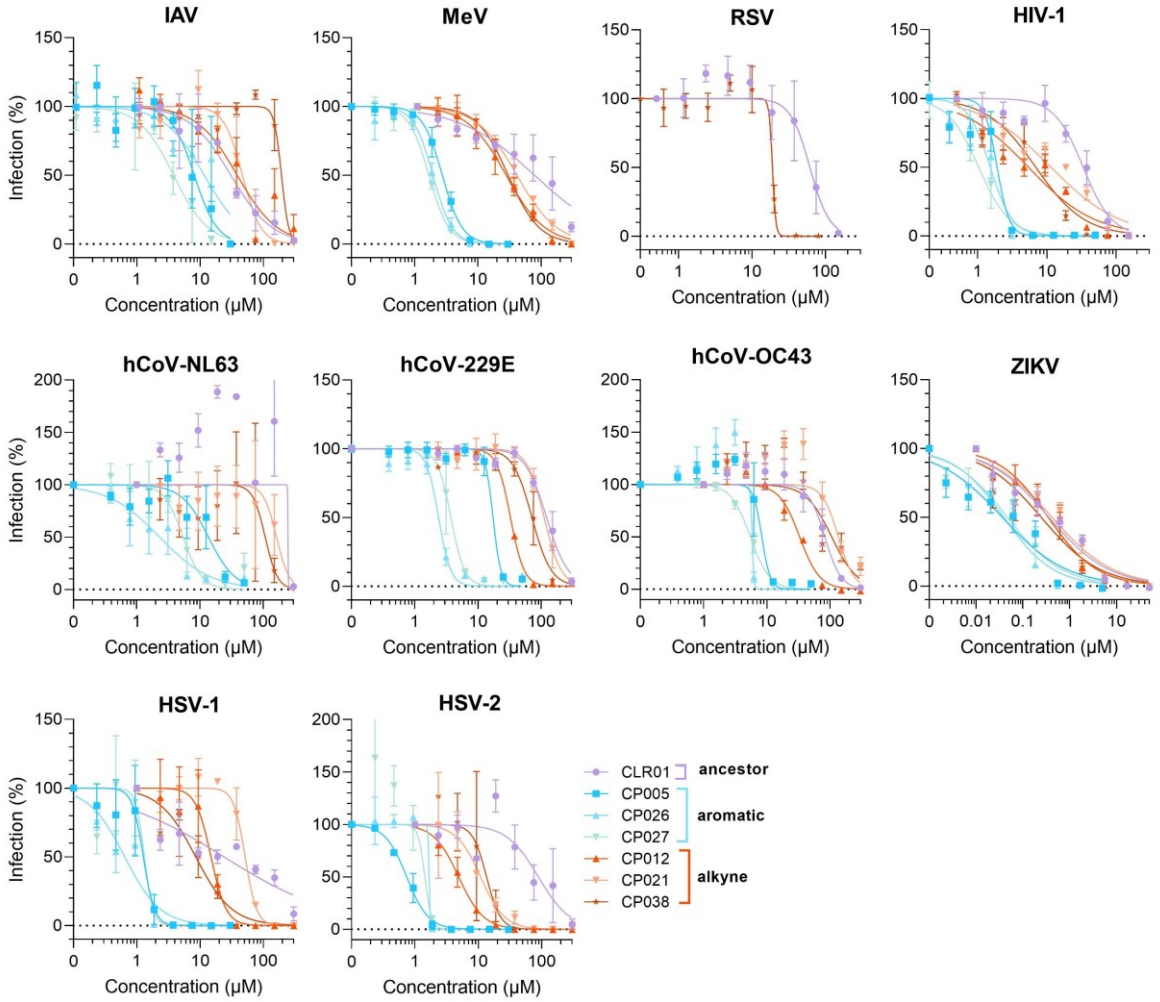

Supplementary Figure 7. Broad-spectrum antiviral activity of advanced tweezers. a) To investigate activity of tweezers against IAV, titrated tweezers were mixed with IAV (MOI 0.0007), incubated for 30 min at 37 °C and added on Caco-2 cells. Infection rates were determined two days later by measuring neuraminidase activity in cellular lysates with a MUNANA assay. For MeV (MOI 0.1) and RSV (MOI 1) GFP reporter viruses, tweezers were incubated with the viruses for 30 min at 37 °C and added on A549 cells. One (for RSV) or two (for MeV) dpi, infection rate was measured with flow cytometry. Escalating concentrations of tweezers were incubated with hCoV-NL63 (MOI 0.01), hCoV-OC43 (MOI 0.006), hCoV-229E (MOI 0.002) for 30 min at 33 °C before inoculation onto Caco-2 (hCoV-NL63) or Huh-7 cells (hCoV-OC43 and -229E). Infection rate was measured by in-cell ELISA analyzing N protein expression 2 (-229E), 3 (-OC43) or 6 (-NL63) dpi. ZIKV (MOI 0.15) was incubated for 30 min at 37 °C with titrated tweezers. Mixture was added on Vero E6 cells and two days later in-cell ELISA detecting flavivirus protein E was performed. For testing of tweezers on HSV-1 (MOI 0.05), HSV-2 (MOI 0.05) or HIV-1, viruses were incubated together with tweezers at indicated concentrations for 10 (in case of HIV-1) or 15 min at 37 °C and inoculated onto TZM-bl (for HIV-1) or ELVIS reporter cells. Infections rates were determined two days later by quantification of β-galactosidase activity in cellular lysates. Shown are mean values ± SEM of two (in case of MeV, HSV-1 and HSV-2) or three independent experiments conducted in triplicates. Data of IAV, MeV, RSV was generated by Lena Rauch-Wirth (Institute of Molecular Virology, Ulm University Medical Center), Andrea Gilg (Institute of Molecular Virology, Ulm University Medical Center) and Sandra Axberg Pålsson (Department of Molecular Bioscience, Stockholm University), respectively. Data of tweezers on hCoV-229E, -NL63 and ZIKV was generated by Jan Lawrenz (Master thesis), Institute of Molecular Virology, Ulm University Medical Center. Modified from Weil et al. 2022[159] (CC BY-NC-ND 4.0; https://creativecommons.org/licenses/by-nc-nd/4.0/, Copyright© The Authors, permission to remix and transform was obtained from the creator).

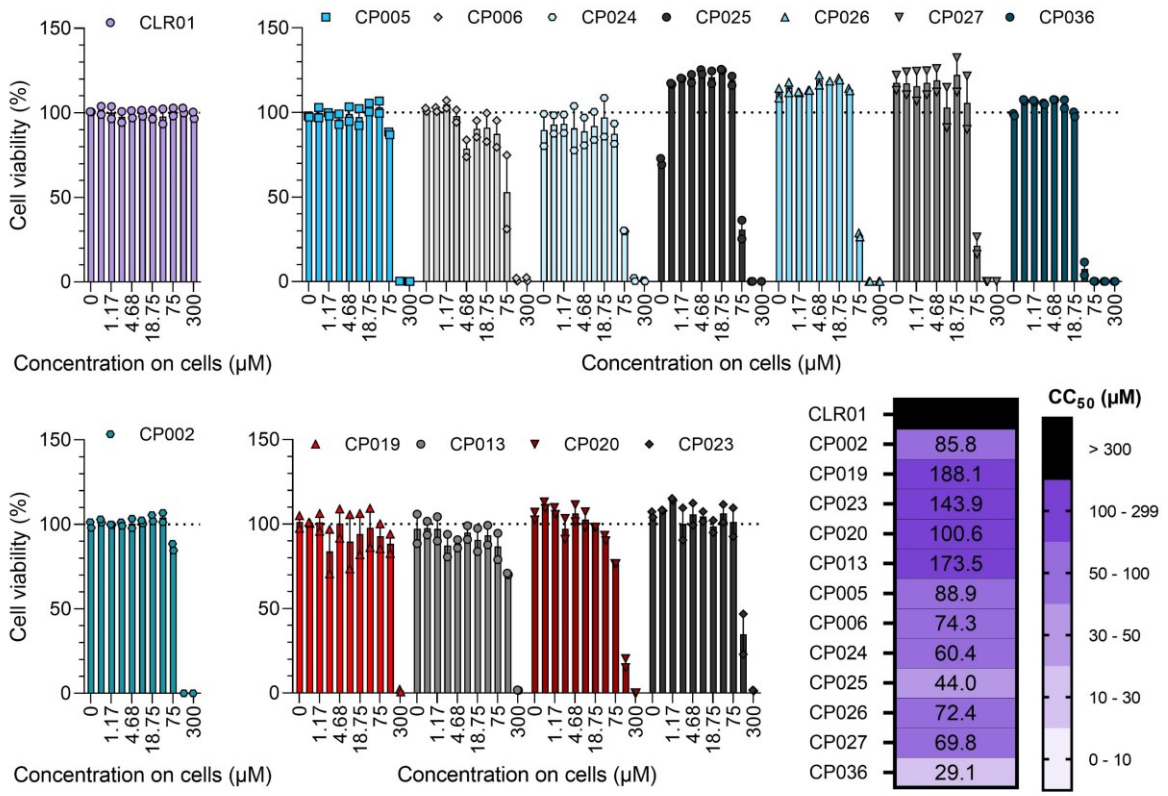

Supplementary Figure 8. Cytotoxicity of tweezers on TZM-bl reporter cells. Tweezer were added to TZM-bl cells at indicated concentrations. Three days later, cell viability was assessed by measuring ATP level in cell lysates with CellTiterGlo Luminescence Cell Viability Assay. Shown are mean values ± range from one experiment performed in duplicates. Modified from Weil et al. 2022[159] (CC BY-NC-ND 4.0; https://creativecommons.org/licenses/by-nc-nd/4.0/, Copyright© The Authors, permission to remix and transform was obtained from the creator).

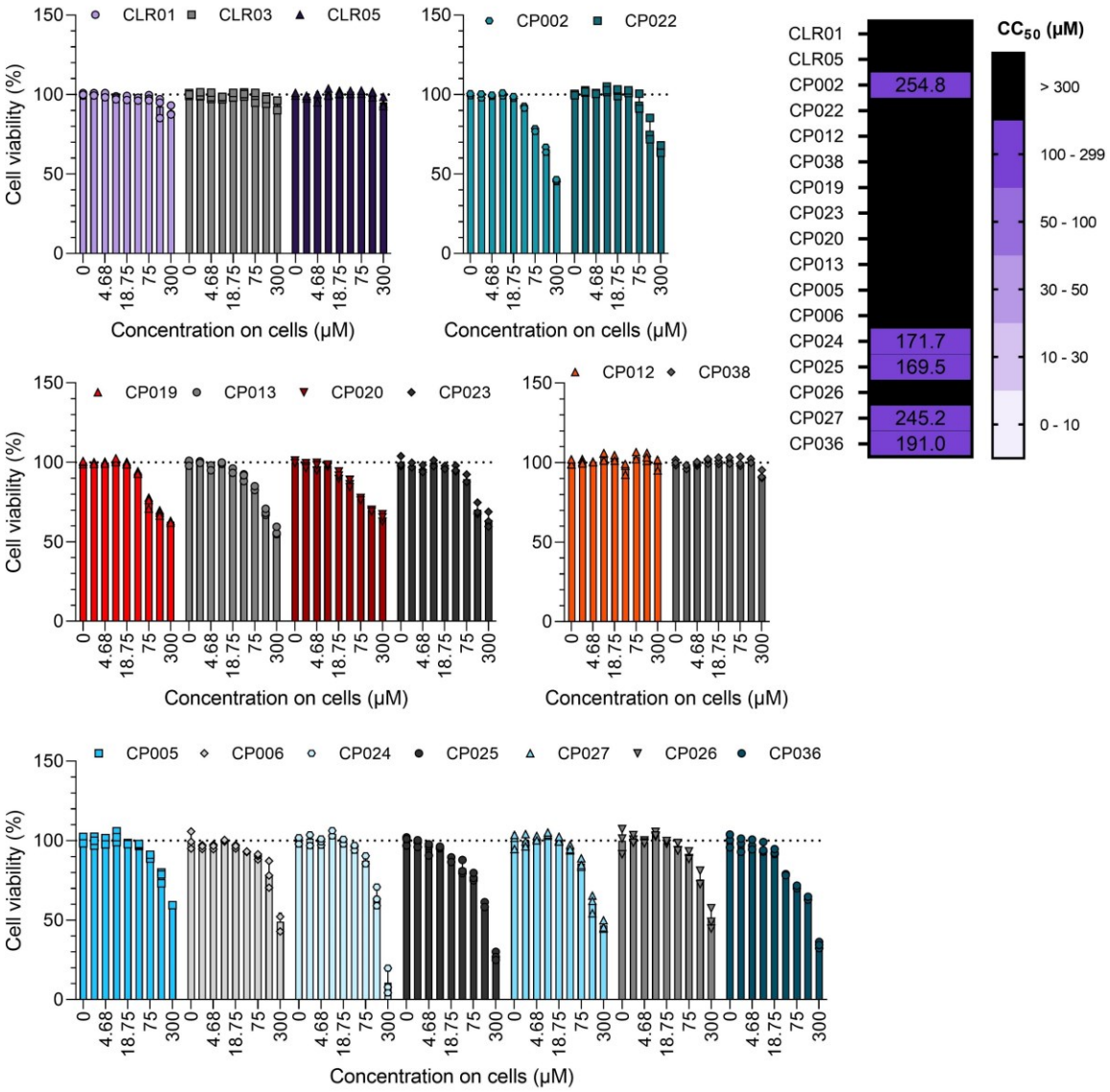

Supplementary Figure 9. Cytotoxicity of tweezers on A549 cells. Tweezer were added to A549 cells at indicated concentrations. Two days later, cell viability was assessed by measuring ATP level in cell lysates with CellTiterGlo Luminescence Cell Viability Assay. Shown are mean values ± SD from one experiment performed in triplicates. Modified from Weil et al. 2022[159] (CC BY-NC-ND 4.0; https://creativecommons.org/licenses/by-nc-nd/4.0/, Copyright© The Authors, permission to remix and transform was obtained from the creator).

8 List of publications

Chronological order; * indicates (co)-first authorship

1. Weil, T. & Münch, J. **Molekulare Pinzetten als Breitbandinhibitor viraler Infektionen.** *Biospektrum* 29, 150–152 (2023). doi:10.1007/s12268-023-1906-y
2. Seidel, A., Jacobsen, E.-M., Fabricius, D., Class, M., Zernickel, M., Blum, C., Conzelmann, C., Weil, T., Groß, R., Bode, S. F. N., Renk, H., Elling, R., Stich, M., Kirchhoff, F., Debatin, K.-M., Münch, J. & Janda, A. **Serum neutralizing capacity and T-cell response against the omicron BA.1 variant in seropositive children and their parents one year after SARS-CoV-2 infection.** *Frontiers in Pediatrics* 11, (2023). https://doi.org/10.3389/fped.2023.1020865
3. Shahpasand-Kroner, H., Siddique, I., Malik, R., Linares, G., Ivanova, M. I., Ichida, J., Weil, T., Münch, J., Sanchez-Garcia, E., Klärner, F.-G., Schrader, T. & Bitan, G. **Molecular tweezers - supramolecular hosts with broad-spectrum biological applications.** *Pharmacol Rev* (2022) doi:10.1124/pharmrev.122.000654
4. Weil, T., Kirupakaran, A., Le, M.-H., Rebmann, P., Mieres-Perez, J., Issmail, L., Conzelmann, C., Müller, J. A., Rauch, L., Gilg, A., Wettstein, L., Groß, R., Read, C., Bergner, T., Pålsson, S. A., Uhlig, N., Eberlein, V., Wöll, H., Klärner, F.-G., Stenger, S., Kümmerer, B. M., Streeck, H., Fois, G., Frick, M., Braubach, P., Spetz, A.-L., Grunwald, T., Shorter, J., Sanchez-Garcia, E., Schrader, T. & Münch, J. **Advanced Molecular Tweezers with Lipid Anchors against SARS-CoV-2 and Other Respiratory Viruses**. *JACS Au* 2, 2187–2202 (2022). https://doi.org/10.1021/jacsau.2c00220
5. Wettstein, L., Immenschuh, P., Weil, T., Conzelmann, C., Almeida-Hernández, Y., Hoffmann, M., Kempf, A., Nehlmeier, I., Lotke, R., Petersen, M., Stenger, S., Kirchhoff, F., Sauter, D., Pöhlmann, S., Sanchez-Garcia, E. & Münch, J. **Native and activated antithrombin inhibits TMPRSS2 activity and SARS-CoV-2 infection.** *Journal of Medical Virology* 95, e28124 (2022). https://doi.org/10.1002/jmv.28124
6. Seidel, A., Zanoni, M., Groß, R., Krnavek, D., Erdemci-Evin, S., von Maltitz, P., Albers, D. P. J., Conzelmann, C., Liu, S., Weil, T., Mayer, B., Hoffmann, M., Pöhlmann, S., Beil, A., Kroschel, J., Kirchhoff, F., Münch, J. & Müller, J. A. **BNT162b2 booster after heterologous prime-boost vaccination induces potent neutralizing antibodies and T cell reactivity against SARS-CoV-2 Omicron BA.1 in young adults.** *Front Immunol* 13, 882918 (2022). https://doi.org/10.3389/fimmu.2022.882918

7. Wettstein, L., Knaff, P. M., Kersten, C., Müller, P., Weil, T., Conzelmann, C., Müller, J. A., Brückner, M., Hoffmann, M., Pöhlmann, S., Schirmeister, T., Landfester, K., Münch, J. & Mailänder, V. **Peptidomimetic inhibitors of TMPRSS2 block SARS-CoV-2 infection in cell culture.** *Commun Biol* 5, 1–12 (2022). https://doi.org/10.1038/s42003-022-03613-4
8. Mezger, M. C., Conzelmann, C., Weil, T., von Maltitz, P., Albers, D. P. J., Münch, J., Stamminger, T. & Schilling, E.-M. **Inhibitors of Activin Receptor-like Kinase 5 Interfere with SARS-CoV-2 S-Protein Processing and Spike-Mediated Cell Fusion via Attenuation of Furin Expression.** *Viruses* 14, 1308 (2022). https://doi.org/10.3390/v14061308
9. Weil, T*., Lawrenz, J*., Seidel, A., Münch, J. & Müller, J. A. **Immunodetection assays for the quantification of seasonal common cold coronaviruses OC43, NL63, or 229E infection confirm nirmatrelvir as broad coronavirus inhibitor.** *Antiviral Res* 203, 105343 (2022). https://doi.org/10.1016/j.antiviral.2022.105343
10. Groß, R., Dias Loiola, L. M., Issmail, L., Uhlig, N., Eberlein, V., Conzelmann, C., Olari, L., Rauch, L., Lawrenz, J., Weil, T., Müller, J. A., Cardoso, M. B., Gilg, A., Larsson, O., Höglund, U., Pålsson, S. A., Tvilum, A. S., Løvschall, K. B., Kristensen, M. M., Spetz, A., Hontonnou, F., Galloux, M., Grunwald, T., Zelikin, A. N. & Münch, J. **Macromolecular Viral Entry Inhibitors as Broad-Spectrum First-Line Antivirals with Activity against SARS-CoV-2.** *Adv Sci* (Weinh) 9, 2201378 (2022). https://doi.org/ 10.1002/advs.202201378
11. Lawrenz, J., Xie, Q., Zech, F., Weil, T., Seidel, A., Krnavek, D., van der Hoek, L., Münch, J., Müller, J. A. & Kirchhoff, F. **Severe Acute Respiratory Syndrome Coronavirus 2 Vaccination Boosts Neutralizing Activity Against Seasonal Human Coronaviruses.** *Clinical Infectious Diseases* (2022). https://doi.org/10.1093/cid/ciac057
12. Conzelmann, C*., Weil, T*., Olari, L.-R., Gilg, A., Rauch, L., Albers, D. P. J., Groß, R., Müller, J. A. & Münch, J. **Virucidal activity of SARS-CoV-2 rapid antigen extraction buffers.** *Journal of Clinical Virology* 147, 105062 (2022). https://doi.org/10.1016/j.jcv.2021.105062
13. Brenner, S., Braun, B., Read, C., Weil, T., Walther, P., Schrader, T., Münch, J. & von Einem, J. **The Molecular Tweezer CLR01 Inhibits Antibody-Resistant Cell-to-Cell Spread of Human Cytomegalovirus.** *Viruses* 13, 1685 (2021). https://doi.org/10.3390/v13091685

14. Prelli Bozzo, C., Nchioua, R., Volcic, M., Koepke, L., Krüger, J., Schütz, D., Heller, S., Stürzel, C. M., Kmiec, D., Conzelmann, C., Müller, J., Zech, F., Braun, E., Groß, R., Wettstein, L., Weil, T., Weiß, J., Diofano, F., Rodríguez Alfonso, A. A., Wiese, S., Sauter, D., Münch, J., Goffinet, C., Catanese, A., Schön, M., Boeckers, T. M., Stenger, S., Sato, K., Just, S., Kleger, A., Sparrer, K. M. J. & Kirchhoff, F. **IFITM proteins promote SARS-CoV-2 infection and are targets for virus inhibition in vitro.** *Nat Commun* 12, 4584 (2021). https://doi.org/10.1038/s41467-021-24817-y
15. Wettstein, L*., Weil, T*., Conzelmann, C*., Müller, J. A., Groß, R., Hirschenberger, M., Seidel, A., Klute, S., Zech, F., Prelli Bozzo, C., Preising, N., Fois, G., Lochbaum, R., Knaff, P. M., Mailänder, V., Ständker, L., Thal, D. R., Schumann, C., Stenger, S., Kleger, A., Lochnit, G., Mayer, B., Ruiz-Blanco, Y. B., Hoffmann, M., Sparrer, K. M. J., Pöhlmann, S., Sanchez-Garcia, E., Kirchhoff, F., Frick, M. & Münch, J. **Alpha-1 antitrypsin inhibits TMPRSS2 protease activity and SARS-CoV-2 infection.** *Nat Commun* 12, 1726 (2021). https://doi.org/10.1038/s41467-021-21972-0
16. Schütz, D., Conzelmann, C., Fois, G., Groß, R., Weil, T., Wettstein, L., Stenger, S., Zelikin, A., Hoffmann, T. K., Frick, M., Müller, J. A. & Münch, J. **Carrageenan-containing over-the-counter nasal and oral sprays inhibit SARS-CoV-2 infection of airway epithelial cultures.** *American Journal of Physiology-Lung Cellular and Molecular Physiology* 320, L750–L756 (2021). https://doi.org/10.1152/ajplung.00552.2020
17. Müller, J. A., Groß, R., Conzelmann, C., Krüger, J., Merle, U., Steinhart, J., Weil, T., Koepke, L., Bozzo, C. P., Read, C., Fois, G., Eiseler, T., Gehrmann, J., van Vuuren, J., Wessbecher, I. M., Frick, M., Costa, I. G., Breunig, M., Grüner, B., Peters, L., Schuster, M., Liebau, S., Seufferlein, T., Stenger, S., Stenzinger, A., MacDonald, P. E., Kirchhoff, F., Sparrer, K. M. J., Walther, P., Lickert, H., Barth, T. F. E., Wagner, M., Münch, J., Heller, S. & Kleger, A. **SARS-CoV-2 infects and replicates in cells of the human endocrine and exocrine pancreas.** *Nat Metab* 3, 149–165 (2021). https://doi.org/10.1038/s42255-021-00347-1
18. Krüger, J., Groß, R., Conzelmann, C., Müller, J. A., Koepke, L., Sparrer, K. M. J., Weil, T., Schütz, D., Seufferlein, T., Barth, T. F. E., Stenger, S., Heller, S., Münch, J. & Kleger, A. **Drug Inhibition of SARS-CoV-2 Replication in Human Pluripotent Stem Cell–Derived Intestinal Organoids.** *Cellular and Molecular Gastroenterology and Hepatology* 11, 935–948 (2021). https://doi.org/10.1016/j.jcmgh.2020.11.003

19. Weil, T*., Groß, R*., Röcker, A*., Bravo-Rodriguez, K*., Heid, C., Sowislok, A., Le, M.-H., Erwin, N., Dwivedi, M., Bart, S. M., Bates, P., Wettstein, L., Müller, J. A., Harms, M., Sparrer, K., Ruiz-Blanco, Y. B., Stürzel, C. M., von Einem, J., Lippold, S., Read, C., Walther, P., Hebel, M., Kreppel, F., Klärner, F.-G., Bitan, G., Ehrmann, M., Weil, T., Winter, R., Schrader, T., Shorter, J., Sanchez-Garcia, E. & Münch, J. **Supramolecular Mechanism of Viral Envelope Disruption by Molecular Tweezers.** *J. Am. Chem. Soc.* 142, 17024–17038 (2020). https://doi.org/10.1021/jacs.0c06400

20. Gauttam, R., Seibold, G. M., Mueller, P., Weil, T., Weiß, T., Handrick, R. & Eikmanns, B. J. **A simple dual-inducible CRISPR interference system for multiple gene targeting in Corynebacterium glutamicum.** *Plasmid* 103, 25–35 (2019). https://doi.org/10.1016/j.plasmid.2019.04.001

9 Acknowledgements

I would like to thank Jan Münch for giving me the opportunity to perform my PhD at the Institute of Molecular Virology. Thank you for the interesting discussions, possibilities and support for the projects and during my PhD.

Further, I would like to thank Frank Kirchhoff for the great and constructive scientific input during presentations.

Thanks also to my thesis advisory committee, Holger Barth and Tanja Weil, for your contribution to this project and input, for your constructive feedback in my intermediate evaluations and for taking the time to evaluate this thesis.

Thanks to all collaborators, especially to the group of Thomas Schrader together with Estelle Taghuo Kaptouom, My-Hue Le, Abbna Kirupakaran and Philipp Rebmann for providing me all the tweezers molecules that built the foundation of my work and for the chemical expertise. Thanks to Elsa Sánchez-García and Joel Mieres-Perez for their contribution and expertise on biomolecular modelling. Clarissa Read and Tim Bergner for their contribution in TEM analysis, the group of Thomas Grunwald for conducting the mice experiments and Sandra Axberg Pålsson together with Anna-Lena Spetz for testing the tweezers against RSV.

Thanks to all co-workers and friends that contributed to my work and moreover supported me. Special thanks to Carina and Janis for introducing me to the work in the BSL-3 and for their contributions. A big thank you to Lena, Lukas, Jan, Andrea, Alina and Rüdiger for their contributions to this work and I want to highlight the extensive contribution of my former hardworking master student Jan. Together with Lia, Mirja, Pascal, Marta, Desiree and Dan, you created a lovely, caring and supportive working environment, which also extended outside of the lab. This goes also to all members of the Institute of Molecular Virology. Special thanks to Nicola Schrott, Daniela Krnavek and Dré van der Merwe for technical support.

Lastly, but very importantly, I want to thank my boyfriend Lukas for pushing and motivating me, for taking care and for his constant love and my family for making this possible, their love and support throughout my whole life.

10 Statutory declaration

I hereby declare that I wrote the present dissertation with the topic:

”Advanced molecular tweezers as broad-spectrum antivirals”

independently and used no other aids that those cited. In each individual case, I have clearly identified the source of the passages that are taken word for word or paraphrased from other works.
I also hereby declare that I have carried out my scientific work according to the principles of good scientific practice in accordance with the current „Satzung der Universität Ulm zur Sicherung guter wissenschaftlicher Praxis“ [Rules of the University of Ulm for Assuring Good Scientific Practice].

Ulm, _____

_____

Tatjana Weil